FACULTY OF SCIENCES

Department of Astrophysics, Geophysics and Oceanography

UR SPHERES

Groupe Infra-Rouge de Physique Atmosphérique et Solaire (GIRPAS)

Stratospheric circulation changes: investigations using multidecadal observations and simulations of inorganic fluorine

A thesis submitted for the partial fulfilment of the requirements for the academic degree of *Philosophiae Doctor* in Sciences at the University of Liege (College of Spatial Sciences) by

MAXIME PRIGNON

Academic year 2020-2021

JURY MEMBERS:

Denis Grodent	President	ULiège, Belgium
Emmanuel Mahieu	Promoter	ULiège, Belgium
Louis François	Secretary	ULiège, Belgium
Bertrand Calpini		MeteoSwiss, Switzerland
Simon Chabrillat		BIRA-IASB, Belgium
Andreas Engel		Goethe University Frankfurt, Germany
Xavier Fettweis		ULiège, Belgium

This work was supported by the Fonds de la Recherche Scientifique – FNRS
under grant no. PDR.T.0040.16

Remerciements

Il m'est impossible de débuter cette section sans pensées émues envers la personne qui a fait naitre ma passion, qui m'a élevé de « bébé » à « jeune climatologue », Michel Erpicum. « Qui peut le plus peut le moins » disiez-vous, j'espère maintenant avoir fait le plus à vos yeux, même si cela m'étonnerait, votre esprit critique me poussant toujours à l'amélioration.

Ce travail n'aurait jamais été accompli sans le soutien inépuisable de mon promoteur, Emmanuel Mahieu. Il m'a tout d'abord permis de réaliser ce projet puisqu'il est, avec Simon Chabrillat, l'auteur de sa proposition. Merci donc de m'avoir fait confiance il y a de ça quatre ans et demi déjà. Ton regard bienveillant, ta disponibilité à tout instant (week-end et « congés » compris) mais aussi l'indépendance que tu m'as laissée m'ont permis d'évoluer tout au long de ce travail. Tu auras repris le flambeau laissé par Michel Erpicum dans mon éducation *climatologique*. Je suis peut-être maintenant grâce à toi un jeune adulte climatologue, s'apprêtant à prendre un peu, mais sûrement pas trop, d'indépendance.

Je tiens également à remercier Simon Chabrillat, mon *co-promoteur non officiel* de thèse. Merci pour tout le temps que tu m'auras accordé. Tes corrections pertinentes m'auront peut-être fait souffrir mais qu'est-ce qu'elles auront été bénéfiques au travail accompli ici. Merci également de m'avoir prêté les clés de BASCOE pour ce projet et pour ta disponibilité quant à mes questions sur son fonctionnement.

Mes pensées vont ensuite aux collègues du GIRPAS. Il y a Diane Zander, qui s'est toujours montrée à l'écoute, attentive à tous mes besoins professionnels ou autres. Je pense que peu de doctorants ont pu bénéficier d'une telle personne dans leur entourage, alors merci pour tout ça Diane. Il y a également Olivier Flock (Flock pour les intimes), qui est d'une aide indispensable quant aux observations et à l'infrastructure informatique du laboratoire et qui est, surtout, devenu un ami. Je tiens également à remercier Christian Servais et Ginette Roland pour leur contribution précieuse aux observations et donc sans qui cette thèse ne serait pas la même. Merci également à tous les collègues croisés durant ces quatre années (dans l'ordre d'apparition) : Benoit Bovy, Whitney Bader, Rodriguez Yombo Phaka, Arpita Verma et Irene Pardo Cantos.

Parallèlement aux collègues du GIRPAS, je tiens à remercier les collègues de l'Institut royal d'Aéronomie Spatiale de Belgique pour leur aide concernant BASCOE ou de manière plus générale concernant le projet. Merci à Yves Christophe et Quentin Errera. Mes pensées vont également à Daniele Minganti avec qui j'ai partagé cette expérience du doctorat mais aussi celle des quatre semaines de l'école doctorale ERCA à Grenoble. Merci également d'avoir enrichi mon vocabulaire italien.

Il me faut ensuite remercier Dan Smale (NIWA, Nouvelle-Zélande). Sans son travail méticuleux, nous n'aurions pu analyser les séries temporelles de Lauder pourtant indispensables aux conclusions tirées à la fin de ce manuscrit.

Merci chers parents et chères sœurs pour votre soutien pendant ces quatre années de thèse. Il est temps pour vous de découvrir le travail accompli, rassurez-vous, je ne vous demanderai pas de tout lire. Je remercie aussi ma belle-famille pour leur présence. Merci également Deborah pour ta contribution à parfaire ce travail, GG pour la relecture. Je ne peux citer ici tous mes proches ayant contribué de près

ou de loin à ce projet mais je pense également à vous les amis faisant partie de la *nomenklatura* ou des *gros tas*.

Enfin, je voulais garder le dernier paragraphe pour toi, Laura. Il y a quatre ans et demi, j'ai débuté cette aventure mais nous avons aussi débuté notre vie à deux, chez nous. Merci d'y avoir directement accueilli une troisième personne, cette thèse. Elle aura par moment accompagné tous nos faits et gestes, jours et nuits. Une thèse écrase parfois tout sur son passage, y compris la personne avec qui on partage sa vie. Merci d'avoir eu le recul nécessaire durant cette épreuve que pour pouvoir m'encourager et me supporter. Sans toi je suis certain que je n'aurais jamais écrit cette section. Tu es une personne formidable et personne ne devrait t'en laisser penser le contraire.

Summary

The intense human activity of the past two hundred years has perturbed the subtle balance existing between the spheres of the Earth system. The atmospheric composition has been modified with massive emissions of greenhouse gases and substances depleting the life-essential ozone layer (ODSs). The most known to the general public resulting changes are certainly the global warming of the troposphere and the dramatic formation of the Antarctic ozone hole. However, it is less generally known that the most robustly modelled response to the increase of greenhouse gases, and the resulting global warming, is a speeding-up of the transport circulation occurring in the stratosphere, the atmospheric layer that is situated well above our head, between 10 and 50 km. This transport circulation, referred to as the Brewer-Dobson circulation (BDC), controls the distribution of ozone and other long-lived gaseous constituents of the stratosphere. Therefore, it is crucial to characterize the BDC and its changes to assess precisely the healing of the ozone layer, expected to occur gradually in the twenty-first century as most of ODS emissions have been successfully phased out by the Montreal Protocol on Substances that Deplete the Ozone Layer, including its Amendments and Adjustments.

In this work, we investigated BDC changes through their impact on multidecadal time-series of stratospheric fluorine. To this end, we include ground-based Fourier transform infrared time-series from Jungfraujoch (Switzerland, 46°N) and Lauder (New Zealand, 45°S), Atmospheric Chemistry Experiment – Fourier Transform Spectrometer (ACE-FTS) satellite time-series and five simulations performed by the BASCOE chemical-transport model (CTM). These simulations are driven by the five modern meteorological reanalyses of the atmosphere. Thus, we assess the representation of the investigated BDC changes in state-of-the-art reanalyses which are designed to represent at best the atmospheric state over the past 30 years.

We first improved the retrieval strategy of HCFC-22 (CHF_2Cl), the most abundant hydrochlorofluorocarbon (HCFC) and the second source of fluorine in the stratosphere, using infrared solar spectra recorded at Jungfraujoch. We showed that HCFC-22 accumulation rates are progressively decreasing in the last decade, highlighting the success of the Montreal Protocol. Furthermore, this first step allowed us to demonstrate the validity of our BASCOE CTM set-up. Indeed, it is the first time that this model is used for such simulations, hence new features were implemented just before and during this thesis project and needed to be validated.

The investigations on the impact of BDC changes on the time-series of stratospheric fluorine showed that, for the past twenty years, the BDC has been changing asymmetrically, with the Southern Hemisphere branch getting stronger relative to that of the Northern Hemisphere. Observational datasets and all of the five reanalyses are qualitatively in agreement with this change. However, this important finding is opposed to all model projections, notably used to project ozone recovery, modelling a weakening of the southern branch, in response to increases in greenhouse gases and to decreases in ODSs, calling for further investigations. Superimposed to this 20 year-trend, we have further confirmed a 5-to-7-year variability of the stratosphere, a feature which allows to put into perspective recent studies questioning specific stratospheric variabilities and associated hemispheric asymmetries.

Résumé

Au cours des 200 dernières années, l'activité humaine a perturbé l'équilibre subtil qui existait entre les sphères de notre système planétaire. Notamment, la composition atmosphérique a été altérée par des émissions massives de gaz à effet de serre et de substances réduisant la couche d'ozone qui, pourtant, est essentielle à la vie. Les conséquences les plus connues du grand public sont certainement le réchauffement global de la troposphère et la formation du trou d'ozone au-dessus de l'Antarctique. Par contre, la réponse atmosphérique à l'augmentation des gaz à effet de serre, et au réchauffement climatique en résultant, reste très largement méconnue, en particulier la projection unanime par les modèles d'une accélération de la circulation de transport de la stratosphère, la couche atmosphérique se situant entre 10 et 50 km. Cette circulation, appelée la circulation de Brewer-Dobson (BDC), contrôle la distribution d'ozone ainsi que celle d'autres constituants à longue durée de vie dans la stratosphère. Il est donc crucial de caractériser au mieux la BDC et ses changements afin d'évaluer précisément le rétablissement de la couche d'ozone. Son recouvrement progressif est effectivement attendu avant la fin du 21ème siècle grâce à la suppression par le Protocole de Montréal, ainsi que ses Amendements et Ajustements, des émissions de la plupart des substances qui appauvrissent la couche d'ozone.

Dans ce travail, nous avons investigué, à l'aide de séries temporelles multidécennales, les changements de la BDC à travers leur impact sur la distribution du fluor dans la stratosphère. Dans ce but, nous incluons des séries temporelles générées par des spectromètres par transformée de Fourier (FTS) situés au Jungfraujoch (Suisse, 46°N) et à Lauder (Nouvelle-Zélande, 45°S), des séries temporelles d'un senseur satellitaire (ACE-FTS) ainsi que cinq simulations réalisées par le modèle de chimie et transport BASCOE (BASCOE CTM). Ces simulations sont conduites par les réanalyses météorologiques de l'atmosphère les plus récentes. Ainsi, il nous est possible d'évaluer leur aptitude à représenter fidèlement les changements de circulation qui ont affecté l'atmosphère terrestre ces 30 dernières années.

Au début de cette thèse, nous avons amélioré la stratégie d'inversion du HCFC-22 (CHF_2Cl), l'hydrochlorofluorocarbure (HCFC) le plus abondant ainsi que la deuxième source actuelle de fluor dans la stratosphère, à l'aide de spectres solaires infrarouges enregistrés au Jungfraujoch. Nous avons alors montré que le HCFC-22 s'accumule moins rapidement dans l'atmosphère durant cette dernière décennie, mettant en exergue le succès du Protocol de Montréal. Cette première étape a aussi permis de démontrer la validité de notre configuration de BASCOE CTM, après implémentation de nouvelles fonctionnalités indispensables à la réalisation de nos simulations.

Nos investigations, fondées sur les séries observationnelles et les simulations du fluor stratosphérique, ont démontré que la BDC a changé de manière asymétrique au cours des vingt dernières années, avec la branche de l'hémisphère Sud s'intensifiant par rapport à celle de l'hémisphère Nord. Il est important de noter que cette conclusion est en contradiction avec nombre de projections qui anticipent un affaiblissement de la branche de l'hémisphère Sud en réponse à l'augmentation des gaz à effet de serre et à la diminution des substances appauvrissant l'ozone. Enfin, nous avons confirmé de manière indépendante que la variabilité pluriannuelle (5 à 7 ans) de la BDC identifiée très récemment est superposée à ce changement multidécennal.

List of acronyms

3D-Var	Three-dimensional variational (assimilation)
4D-Var	Four-dimensional variational (assimilation)
ACE-FTS	Atmospheric Chemistry Experiment-Fourier Transform Spectrometer
AGAGE	Advanced Global Atmospheric Gases Experiment
AoA	Age of air
ARW	Autoregressive wild (bootstrap)
ATMOS	Atmospheric Trace Molecule Spectroscopy
BASCOE	Belgian Assimilation System for Chemical ObsErvations
BRAM	BASCOE reanalysis of AURA-MLS
CAM	Community Atmosphere Model
CCCma	Canadian Centre for Climate Modeling and Analysis
CCM	Chemistry-climate model
CFC	Chlorofluorocarbon
CMAM	Canadian Middle-Atmosphere Model
CTM	Chemical-transport model
DOFS	Degree of freedom for signal
DU	Dobson unit
ECMWF	European Centre for Medium-Range Weather Forecasts
ERA-Interim	ECMWF Interim reanalysis
FFSL	flux-form semi-Lagrangian (transport scheme)
FGAT	First guest at the appropriate time
FTIR	Fourier transform infrared
$\mathbf{F_y}$	Total inorganic fluorine (HF + 2 COF2 + COClF)
$\mathbf{^*F_y}$	Proxy for F_y (HF + 2 COF_2)
GCM	General circulation model
GWP	Global warming potential
HCFC	Hydrochlorofluorocarbon
HGGC	Historical Greenhouse Gas Concentrations (Meinshausen et al., 2017)
HFC	Hydrofluorocarbon
IPCC	Intergovernmental Panel on Climate Change
JFJ	Jungfraujoch
JRA-55	Japanese Meteorological Agency's Japanese 55-year Reanalysis
MERRA	Modern-Era Retrospective analysis for Research and Applications
MERRA-2	Modern-Era Retrospective analysis for Research and Applications Version 2
MHD	Mace Head
MIPAS	Michelson Interferometer for Passive Atmospheric Sounding
MLR	Multiple linear regression model
MLS	Microwave Limb Sounder
NCAR	National Center for Atmospheric Research

NDACC	Network for the Detection of Atmospheric Composition Change
NOAA	National Oceanic and Atmospheric Administration
ODP	Ozone depletion potential
ODS	Ozone depleting substance
OEM	Optimal estimation method
OPD	Optical path difference
PSC	Polar stratospheric clouds
QBO	Quasi-biennial oscillation
SNR	Signal-to-noise-ratio
UV	Ultraviolet
vmr	Volume mixing ratio
WACCM	Whole Atmosphere Community Climate Model
WMO	World Meteorological Organization
ZPD	Zero path difference

Contents

Chapter 1

The Earth's atmosphere:

composition and changes

1.1 Introduction

From its formation 4.6 billion years ago, the Earth system has known dramatic changes, involving biological, physical and chemical processes which altogether have shaped the Earth as we know it today. The Earth system is often considered as five interconnected "spheres": the biosphere, the lithosphere (or geosphere), the hydrosphere, the cryosphere and, last but not least, the atmosphere. Each of these spheres can further be decomposed. For example, the lithosphere consists of the Earth's crust and a deeper layer (the Earth's core and mantle), the former isolating the latter from the other spheres. Before going on with the description of the actual atmosphere structure, composition and "recent" changes, it is important to realize how long are the processes that have been shaping the Earth and more specifically, the atmosphere.

Following the formation of the Earth by accretion of small celestial bodies, a secondary atmosphere began to form, as the very first atmosphere at the early stage of the Earth formation should have rapidly dissipated due to the lack of a strong gravitational field (e.g., Kasting, 1993). It is believed that the secondary atmosphere originated from volatile compounds contained in the celestial bodies that formed the Earth. The progressive release of these compounds has led to the presence of large quantities of carbon dioxide (CO_2), water vapour (H_2O), nitrogen (N_2) and trace amounts of other species in the secondary steam atmosphere (e.g., Kasting, 1993; Brasseur and Solomon, 2005). The Earth system started to cool after the ending of the main accretion phase, causing a strong hydrological cycle, with the condensation of the steam atmosphere into an ocean. The large amount of carbons that remained in the atmosphere after the rain out is believed to have produced such a greenhouse effect that it prevented the Earth to freeze despite the 25% lower radiative energy provided by the sun 4 billion years ago. The "heavy bombardment" of very large impactors (100 km diameter; Kasting, 1993) that ceased about 3.8 billion years ago probably prevented life to develop before then. The emergence of life (between 3.8 and 3.5 billion years ago) has in turn progressively shaped the Earth system. Some of the first living

organisms were indeed able to convert CO_2 in organic carbon forms and to release oxygen (O_2) by photosynthesis (i.e., with the involvement of ultraviolet radiations from the sun). With the development of the photosynthetic organisms, O_2 gradually accumulated in the atmosphere while atmospheric CO_2 decreased by burial of organic carbon. This way, the complex interplay of all "spheres" has finally caused the O_2 sinks to be smaller than its sources ("the great oxidation event", 2.4-2 billion years ago) and O_2 levels comparable as that of today's atmosphere were reached around 500-400 million years ago (e.g., Jacob, 1999), along with the Cambrian explosion (i.e., intense diversification of life forms).

The current geologic period, the Quaternary, starting around 2.5 million years ago, is of great interest for climatologists as it has seen the succession of relatively long glacial and interglacial periods. Ice coring techniques, as performed in the framework of the European Project for Ice Coring in Antarctica (EPICA; EPICA community members, 2004), provide the evolution of atmospheric parameters over timescales reaching 800 000 years (Figure 1-1). Among other parameters, the reconstruction of concentration of CO_2 and temperature time-series, from ice cores collected in Antarctica, highlights the succession of at least eight consecutive glacial cycles (T_x in Figure 1-1). During the last 500 000 years, the glacial cycle had a very strong cycle of 100 000-year length, with temperature anomalies ranging from -9°C to 4°C (relative to the mean temperature of the last millennium; Lüthi et al., 2008). The last and current interglacial period corresponds to the current geological epoch, the Holocene (11 650 years before present).

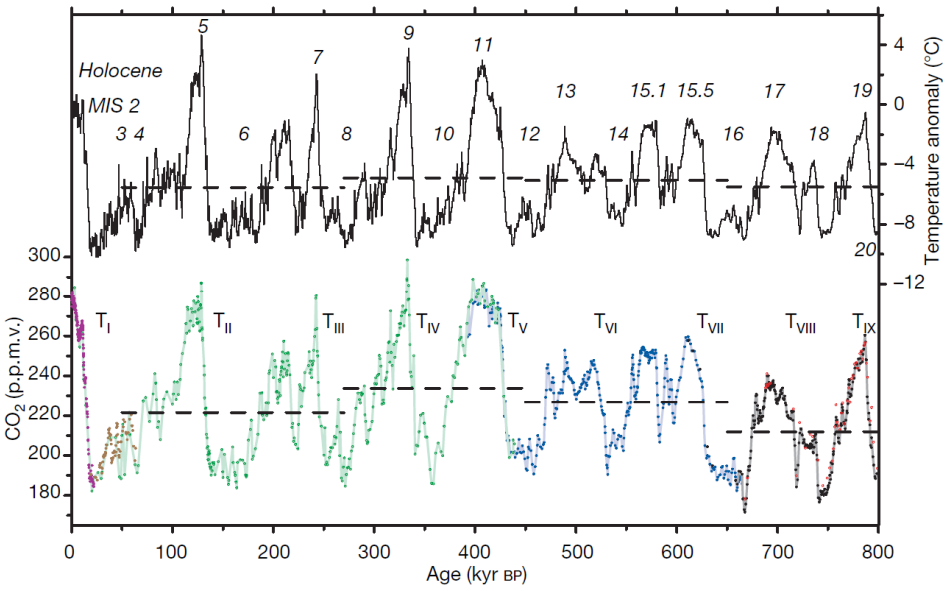

Figure 1-1: Temperature anomalies (top) and CO_2 records (bottom) over the past 800 kyr as reconstructed from EPICA ice core measurements. Temperature anomalies are given with respect to the last millennium. Horizontal lines are the mean temperature anomalies and CO_2 concentrations for the time periods 799–650, 650–450, 450–270 and 270–50 kyr BP. Roman numerals represent glacial terminations. Arabic numbers are not relevant here. From Lüthi et al. (2008).

During the Holocene, successive agricultural revolutions happened and the world population started to grow more and more rapidly, even reaching a quasi-exponential growth by the industrial revolution (nineteenth century). The resulting changes in agricultural practices (e.g., more frequent use of nitrogen fertilizers, growing number of cattle, deforestation or burning of old-growth forests) but also the resulting increasing emission of carbons by the combustion of fossil fuels have perturbed the subtle and very long-term balance between the physical, chemical and biological processes which existed until then. The continuous technological advance in the last century has also led to the synthesis of very

attractive and promising compounds as the well-known chlorofluorocarbons (CFCs). Massively used in the second half of the 20th century, the CFCs offer the advantages to have a relatively low toxicity, a low reactivity and a low flammability. However, as we will see in Sect. 1.4 and Sect. 1.5.1, their stability is also an environmental and public health issue as their resulting long atmospheric lifetime allows them to reach the stratosphere and cause the catalytic destruction of the life-essential ozone layer.

The undeniable relatively short-term (compared to the geological scales approached in this section) human forcings on the Earth system have without a doubt induced global changes. However, the natural forcings and the feedbacks linked to these changes are still today not completely understood or quantified and, consequently, the recent temperature increase (see black lines in Figure 1- 2) cannot be entirely attributed to anthropogenic emissions of greenhouse gases. From 1880 to 2012, temperature has increased by 0.85 (0.65 to 1.06) °C, a period where independently produced datasets exist (IPCC, 2013). From 1951 to 2010, a period where it is virtually certain (i.e., 99-100% probability) that the troposphere has warmed globally, it is extremely likely (i.e., 95-100% probability) that more than the half of the observed increase in the global average surface temperature was caused by the anthropogenic increase in greenhouse gas concentrations and other anthropogenic forcings together (IPCC, 2013). Moreover, we will see, in Sect. 1.3.1, that greenhouse gases are still massively emitted by human activities. As a consequence, the global surface temperature is expected to continue to increase in the twenty-first century. It is likely (i.e., 66-100% probability) that the change of the global surface temperature at the end of the century will exceed 1.5°C relative to 1850-1900 for all of the emission scenarios (except for the most optimistic; IPCC, 2013).

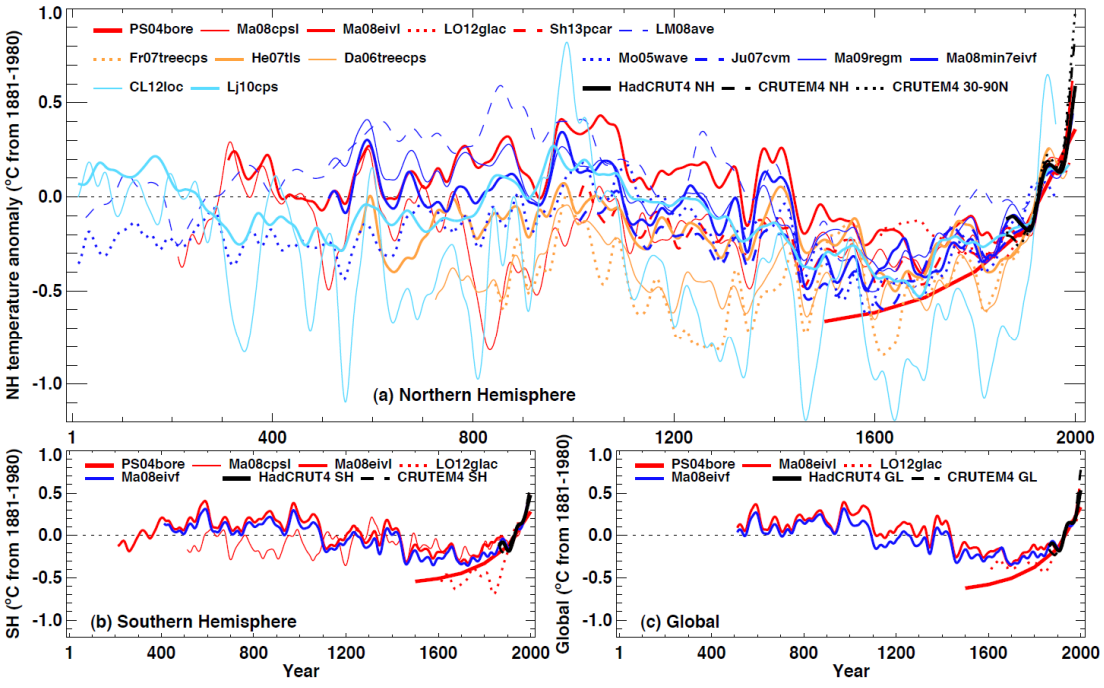

Figure 1- 2: Reconstructed (a) Northern Hemisphere and (b) Southern Hemisphere, and (c) global annual temperature anomalies (with respect to 1881-1980) during the last 2000 years. Lines represent individual temperature reconstructions and are grouped by colour according to their spatial representation (red: land-only all latitudes; orange: land-only extratropical latitudes; light blue: land and sea extra-tropical latitudes; dark blue: land and sea all latitudes). Black lines are instrumental temperature anomalies. See Appendix 5.A.1 in IPCC (2013) for further information about individual reconstructions. From IPCC (2013).

Caused entirely or not by the anthropogenic stresses affecting all "spheres" of the Earth system, our climate system is changing as it always has. However, entire nations are today vulnerable to the climate variability and long-term changes (e.g., IPCC, 2014). Today, key aspects of the climate system are still not sufficiently understood and the scientific community strives to acquire the most thorough knowledge of the Earth system. As we will see in Chapter 2, the stratosphere is also affected by these changes. Indeed, the most robust response to the temperature and greenhouse gases increase, projected by global models, is a speeding up of the stratospheric circulation (Butchart, 2014). In this introductory chapter, after a short reminder on the vertical structure of the atmosphere (Sect. 1.2), an overview of the Earth's atmosphere composition is given in Sect. 1.3, with a focus on greenhouse gases and the ozone layer. The problematic of halogenated compounds is then approached in Sect. 1.4. Finally, Section 1.5 presents the main observed and projected stratospheric ozone changes due to the increase and decrease of ozone depleting substances.

1.2 Vertical structure of the atmosphere

The atmosphere as observed today can be subdivided in vertical layers following two main criteria, the vertical profile of temperature and the atmospheric composition. Figure 1- 3 depicts the typical vertical profile of the atmospheric temperature and the different atmospheric layers described in this section.

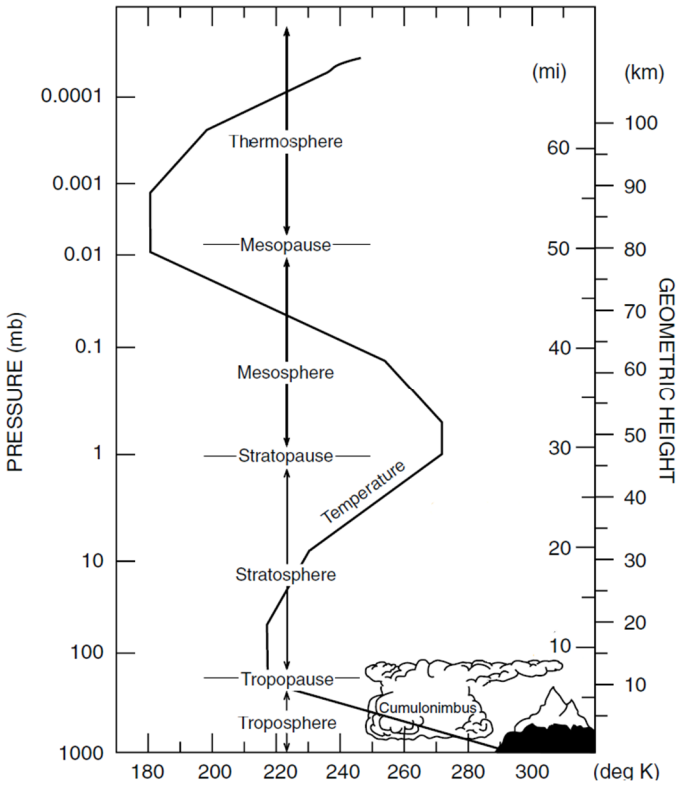

Figure 1- 3: Schematic of the vertical structure of the atmosphere and its typical temperature profile, representing the opposite gradients of temperature from one layer to the other. Adapted from Brasseur and Solomon (2005).

Looking at the vertical temperature gradient, one can distinguish successive atmospheric layers with opposed vertical gradients (Figure 1- 3). Starting from the Earth's surface and gaining in altitude, the first layer is characterized by a negative vertical temperature gradient, it is the **troposphere**. It can be approximated that the negative gradient of the troposphere is due to the fact that the Earth's surface is

the main source of heat in the troposphere, through ultraviolet (UV) absorption and resulting upward heat fluxes. The apparent unstable condition of the troposphere is actually not seen through most of the layer. In fact, convective instability is mainly observable in the lowest few kilometres of the troposphere (Shepherd, 2003). As a moving-upward parcel undergoes adiabatic (i.e., without exchange of heat) expansion and therefore cooling, it often goes back to its initial altitude level. However, if the air temperature is decreasing more rapidly than the dry adiabatic lapse rate (~10 K/km), the upward motion is not counterbalanced by the adiabatic cooling and the density of the air parcel will stay smaller than the surrounding air, conserving this way its positive buoyancy and upward motion. Moreover, considering that the warm and humid warm air rises and adiabatically cools, the convective instability often causes the water vapour, within the air parcel, to reach saturation and condensate, thus forming clouds and rain. The condensation, releasing latent heat, warms the air and allows the convection to penetrate higher heights. If this effect of the latent heat is accounted for in convective instability calculation, the atmospheric condition becomes instable when the air temperature is decreasing more rapidly than the moist adiabatic lapse rate (6.5K/km; Shepherd, 2003). At altitudes from 7-8 km at the poles, to 16-17 km at the tropics, a minimum is reached in air temperatures and the vertical temperature gradient becomes close to zero. This region, the tropopause, marks the boundary between the troposphere and the next upper layer. In addition to latitudes, the tropopause height is also a function of the season. At the tropical tropopause, temperatures as low as 190 K are reached –making it one of the coldest point of the entire atmosphere– and the convective phenomena described above ceases.

Above the tropopause, the vertical temperature gradient is positive and maximal temperatures are reached at altitudes around 50 km (i.e., the stratopause), defining this way the vertical extent of the **stratosphere**. Significant absorption of UV solar radiations occurs in the stratosphere and is responsible of the positive vertical temperature gradient. Indeed, maximum abundances of ozone (O_3) are encountered in this layer of the atmosphere (see Sect. 1.3.2). As a result of the positive vertical temperature gradient, the stratosphere is strongly stratified and surfaces of constant entropy are getting progressively horizontal. In consequence, vertical motions are strongly hindered and are very slow, if they exist. We will see, in the next chapter dedicated to the stratospheric circulation and its changes, that a slow and constant vertical motion in the tropics, coupled to a meridional transport, actually exists in the stratosphere.

The **mesosphere**, as the troposphere, sees a negative vertical temperature gradient. It is due to the radiative cooling produced by (mostly) CO_2 infrared emissions as well as to the lower UV absorption compared to the underlying stratosphere. The stratosphere and mesosphere taken together are often referred to as the middle atmosphere. The mesosphere is extending to 85-90 km.

Finally, above the minimum temperature of the mesopause, the vertical temperature gradient is again positive and strongly depends on the solar activity. The **thermosphere** temperature gradient is, as the stratosphere, caused by the absorption of UV radiations. However, in the case of the mesosphere, it is the molecular and free oxygen that directly absorb the very short UV wave lengths (<200 nm).

Considering together the first three layers (starting from the ground), the troposphere, the stratosphere and the mesosphere, we note that their two major constituents, N_2 and O_2, represent ~78% and ~21% of the total number density, respectively. As a result, the mean molecular weight of the air is constant with height in these layers, which can be grouped this way by the term **homosphere**. In the thermosphere, the effect of diffusive separation between lighter and heavier compounds becomes significant. In

addition to that, O_2 and N_2 abundances decrease due to the efficient photodissociation taking place above 100 km. As a direct result, the relative abundance of atomic oxygen increases, reaching and overcoming that of O_2 and N_2, and the mean molecular weight of the air is no more constant with height. In contrast to the homosphere, the region above 100 km is consequently referred to as the **heterosphere**.

1.3 Overview of the composition of the Earth's atmosphere

Before going on with the description of the atmospheric composition, it is important to introduce the units commonly used to quantify the abundances of atmospheric constituents. The most commonly used unit is certainly the mixing ratio. It expresses the number of moles of a constituent *X* per mole of air (mole/mole). In the homosphere, the ideal gas law is almost always observed and, consequently, mixing ratios remain constant when the air density changes. The mixing ratio can moreover be directly linked to the volume mixing ratio (vmr) which is expressed in parts per volume (ppv). For readability purpose, volume mixing ratios are often scaled, e.g., parts per million by volume (ppmv = ppv$\times 10^{-6}$), parts per billion by volume (ppbv = ppv$\times 10^{-9}$) or parts per trillion by volume (pptv = ppv$\times 10^{-12}$). Another physical quantity, commonly used in, e.g., the Fourier transform infrared (FTIR) technique, is the column abundance. It expresses the number density (number of particles per unit volume, particles/m^3) of a constituent *X* integrated vertically. In other words, it is generally the total number of molecules of *X* in a vertical column with a horizontal section of 1 cm^2 and with the vertical limits depending on the instrument or model (molecules cm^{-2}). Total columns refer to column abundances integrated from the ground to the top of the atmosphere. For ozone abundances, total columns of ozone (hereafter total ozone) are generally expressed in Dobson units (DU), which correspond to the height (10^{-3} cm) of an ozone column if the gases were at standard temperature and pressure. 1 DU is equivalent to 2.687×10^{16} molecules cm^{-2}.

We just saw in the previous section that N_2 and O_2 taken together represent ~99% of the air composition in total number density or volume. The remaining 1% is almost filled by the noble gas argon (Ar). Thus, these three gases are commonly referred to as the major constituents of the homosphere. The other noble gases and the molecular hydrogen (H_2) taken apart, CO_2, O_3, methane (CH_4) and nitrous oxide (N_2O) represent the minor constituents. They are nonetheless key actors of the climate system through their interaction with infrared (CO_2, CH_4 and N_2O; see Sect. 1.3.1) or UV radiations (O_3, see Sect. 1.3.2). Furthermore, N_2O and CH_4 are also precursors of radicals (i.e., NO and OH, respectively) involved in the catalytic destruction of stratospheric O_3 (Sect. 1.3.2). Water vapour, despite its very high variability, is sometimes included among the minor constituents of the homosphere as it can reach relative abundances of the order of the percent. While its anthropogenic emissions are negligible compared to the natural fluxes, water vapour remains today the primary greenhouse gas in the Earth's atmosphere (IPCC, 2013). As water vapour concentration in the troposphere is mainly controlled by the air temperature through evaporation, condensation and precipitation, its effect on the climate system is more often considered as a feedback agent rather than a forcing to climate change (IPCC, 2013). The minor constituents have typical global surface concentrations reaching hundreds of ppbv (N_2O) to hundreds of ppmv (CO_2). Finally, other important gases, also having significant effects on the climate system, are present in the atmosphere in much smaller abundances. These atmospheric constituents are referred to as trace gases. In this chapter, the considered trace gases are the halogenated compounds of the atmosphere. For the most abundant ones, their global surface concentrations reach several hundreds of

pptv. As we will see in more details in Sect. 1.4, these gases have large ozone depletion and global warming potential and have been very strictly regulated for several decades now.

1.3.1 Greenhouse gases

Some of the minor and trace constituents of the homosphere have molecular structures that allow them to interact with the radiation emitted by the sun or the Earth's surface. By radiation we mean the energy that is emitted or transmitted in the form of electromagnetic waves (e.g., the sunlight). The energy carried by these waves is quantized in discrete quantity of energy with zero mass, travelling at the speed of light, i.e., the photons (Jacob, 1999). The electromagnetic waves in the atmosphere are polychromatic and may, therefore, be seen as an ensemble of waves with a continuum of wavelengths (λ, expressed in distance units). The most essential wavelengths in atmospheric sciences are ranging from ultraviolet ($0.01\ \mu m < \lambda < 0.04\ \mu m$) to infrared ($0.7 < \lambda < 100\ \mu m$, including near-infrared and far-infrared). Between these two limits, we have the visible light.

1.3.1.1 Infrared spectroscopy basics

To understand why some gas molecules may interact with radiations of specific wavelengths, it is first necessary to consider the basics of the spectroscopy of gas molecules. Letting apart the kinetic energy due to translational motions of molecules, the internal energy of a molecule is quantized in a series of electronic, vibrational and rotational states. The transition to higher or lower energy states obeys some rules which are derived from the principles of quantum mechanics. Following these rules, a gas molecule absorbs (emits) radiations of a given wavelength only if the corresponding absorbed (emitted) energy can be used to shift the internal energy of the molecule to a higher (lower) state. Considering this last point, electronic state transitions require relatively high energy inputs, corresponding to wavelengths of the ultraviolet ($\lambda < 0.04\ \mu m$). Vibrational transitions require lower energy, corresponding to near-infrared radiation ($0.7 < \lambda < 20\ \mu m$), while rotational transitions require far-infrared radiation ($\lambda > 20\ \mu m$). Vibrational states represent different degrees of stretching or bending of a molecule. Rotating gas molecules with a permanent dipole moment (i.e., a net separation of positive and negative charges) produce an oscillating electric field that may result in radiation absorptions and rotational transitions.

The main source of heat for the Earth, at least for its atmosphere and surface, is the incoming solar energy, transmitted by radiation, absorbed by the surface and converted to heat. To balance this excess of energy, the Earth's surface emits radiation out to space. The Earth's surface emits almost exclusively in the infrared, with maximum emission values corresponding to wavelengths from 5 μm to 20 μm. Therefore, these infrared radiations may be absorbed by gas molecules and cause vibrational and/or vibrational-rotational (i.e., involving changes in both vibrational and rotational states) transitions. Another important rule for vibrational transitions to occur is that the radiation must interact with an oscillating electric field produced by the dipole moment of the vibrating gas molecules. Figure 1- 4 shows the normal vibration modes of CO_2 and N_2. From this figure, we see that CO_2 may only interact with infrared radiations in asymmetric stretching and bending vibrational modes. On the other hand, N_2 has vibrations that will never induce any dipole and, hence, is transparent to infrared radiations. More generally, diatomic homonuclear molecules (e.g., N_2 and O_2, the two most abundant compounds of the Earth's atmosphere) do not undergo vibrational transitions. This leads us to a definition of **greenhouse gases**: gas molecules that can acquire a charge asymmetry by stretching or bending and, therefore, absorb infrared radiations, emitted by the Earth's surface, through vibrational or vibrational-rotational

state transitions. CO_2, H_2O, N_2O, CH_4, tropospheric O_3 and halogenated compounds all meet this definition.

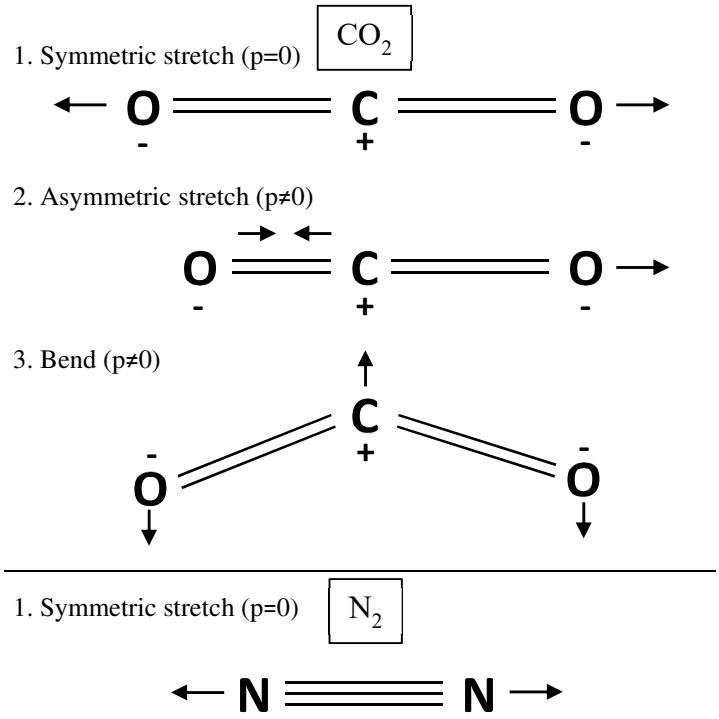

Figure 1- 4: Normal vibrational modes of CO_2 and N_2. "p≠0" indicates that a dipole moment exists. Adapted from Jacob (1999)

1.3.1.2 The greenhouse effect

As already mentioned in this section, the Earth's surface absorbs about the half of the incoming short-wave solar radiation, heats and balances this incoming excess of energy through the emission of longwave radiations (i.e., infrared) back to the atmosphere and space. Greenhouse gases in the troposphere then largely absorb this emitted infrared radiation and emit back infrared radiations in all directions. The net greenhouse effect is a warming of the Earth's surface and the troposphere.

Primary greenhouse gases are H_2O, CO_2, CH_4, N_2O and O_3 (IPCC, 2013). These five gases are naturally present in the Earth's atmosphere and, therefore, the greenhouse effect itself is a natural phenomenon that has always existed. Notably, without this effect, the Earth's surface average temperature would be well under the water freezing point (around -17 °C), which would prevent the existence of life on Earth. However, human activities have led to massive emissions of greenhouse gases (e.g., CO_2, N_2O, CH_4 and halogenated compounds) in the atmosphere and, consequently, increased the intensity of the greenhouse effect (IPCC, 2013). The main expected consequence is an increase of the global temperature (see Sect. 1.1).

To quantify the effect of individual greenhouse gases on the climate system one may use various metrics. The **radiative forcing** definition can be approximated as follows: "the change in the net, downward minus upward, radiative flux (expressed in W m^{-2}) at the tropopause or top of atmosphere due to a change in an external driver of climate change, such as, for example, a change in the concentration of CO_2 or the output of the Sun" (IPCC, 2013). Therefore, a positive radiative forcing implies a positive change of the downward radiative flux compared to the upward flux. It, consequently, implies an excess of energy in the Earth system that may result in a global warming. In addition to the

radiative forcing, one may also use a relative index to quantify the potential impact of individual greenhouse gases on the atmosphere: the **global warming potential** (GWP). GWP "measures the radiative forcing following a pulse emission of a unit mass of a given greenhouse gas in the present-day atmosphere integrated over a chosen time horizon, relative to that of CO_2." (IPCC, 2013). The GWP thus accounts for the radiative forcing effectiveness and the lifetime of the given gas.

1.3.1.3 Past evolution of greenhouse gas concentrations

Figure 1- 5 and Table 1- 1 illustrate the past evolution of the greenhouse gases CO_2, CH_4, N_2O and sulphur hexafluoride (SF_6) from FTIR measurements performed at the station of the Jungfraujoch (see Chapter 4).

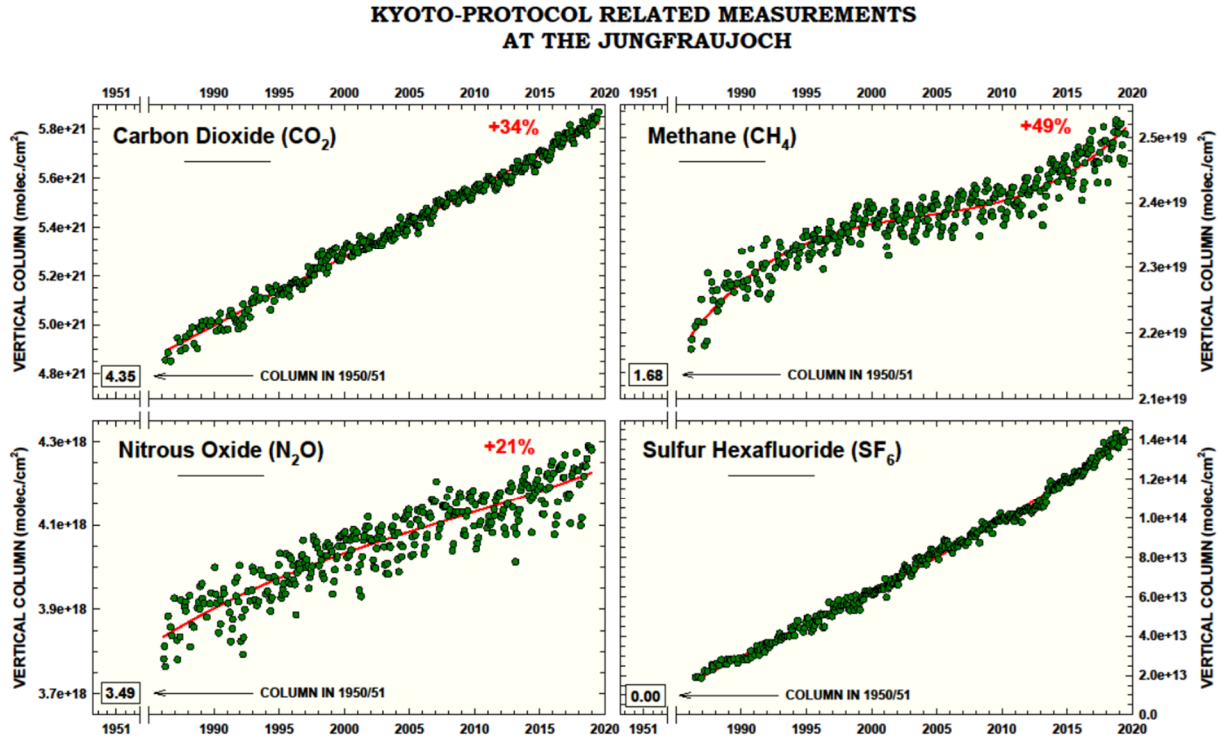

Figure 1- 5: Ground-based FTIR time-series of CO_2, CH_4, N_2O and SF_6 above Jungfraujoch. Column values in the early 1950s are derived from pioneering IR observations performed at the same site by Pr M. Migeotte (Mahieu et al., 2019).

Major CO_2 sources are fossil fuel combustion and land use change. From 1980 to 2011, the average global annual increase was 1.7 ± 0.5 ppm yr^{-1} (1 standard deviation, σ; IPCC, 2013). Time-series of CO_2 show a strong annual cycle. It is due to the photosynthesis and respiration by the terrestrial biosphere (predominantly in the Northern Hemisphere).

CH_4 has more complex sources and sinks. Anthropogenic emissions are originating from the agriculture (livestock and rice cultivation) and from the fossil fuel exploitation (including transport), while the natural sources are dominated by wetlands. The major atmospheric sink for CH_4 is its oxidation by OH. Global and Jungfraujoch (Figure 1- 5) time-series show that CH_4 growth rates have not been constant. CH_4 was rising sharply in the 1990s and then stabilized between 2000 and 2005. Since then, CH_4 has been rising again (Bader et al., 2017, and references therein). It is still no clear what has been influencing the recent CH_4 increase (IPCC, 2013; Bader et al., 2017).

Since the late 1970s, N_2O has increased at an average rate of ~0.75 ppb yr^{-1} (IPCC, 2013). The major contributor to this increase is the agriculture with the use of nitrogen fertilizers.

SF_6 is extremely stable in the atmosphere, hence it has a very long lifetime of 3200 years (WMO, 2018). SF_6 is so stable that more than 96-99% of its emissions accumulate in the atmosphere (Levin et al., 2010). Therefore, SF_6 emissions can be estimated from its atmospheric abundance (top-down method). The industrial production of SF_6 started in the 1950s. Major emissions are related to the electricity sector (used as an insulator in high voltage installations; Levin et al., 2010). SF_6 global atmospheric abundance increased from near zero in the 1970s (Levin et al., 2010) to 9.96 ppt by the end of 2019 (Table 1- 1). SF_6 accumulation rates are more or less constant but periods with higher or lower trends (e.g., from 1995 to 1998) are depicted.

Table 1- 1: Greenhouse gases targeted by the Kyoto Protocol (see below). Surface abundances for 2019 were downloaded from https://www.esrl.noaa.gov/gmd/aggi/aggi.html (last access 2021/04/09). Total lifetime and GWP are from WMO (2018). [a] Etheridge et al. (1996). [b] Etheridge et al. (1998) and Dlugokencky et al. (2005). [c] Prather et al. (2012).

	1750 atmospheric abundance	2019 atmospheric abundance	Total lifetime (years)	GWP	Anthropogenic emission
CO_2	278 ± 2 ppm[a]	409.8 ppm		1	-fossil fuel combustion -land use change
CH_4	722 ± 25 ppb[b]	1866.6 ppb	12.4	28	-agriculture (livestock, rice cultivation) -fossil fuel exploitation
N_2O	270 ± 7 ppb[c]	331 ppb	123	265	-use of nitrogen fertilizers
SF_6	NA	9.96 ppt	3200	23500	-electricity distribution -magnesium production -semi-conductor manufacturing

1.3.1.4 International efforts to reduce greenhouse gas emissions

Following the first Synthesis Report of the Intergovernmental Panel on Climate Change (IPCC) in 1990, which highlighted the increase in greenhouse gases and their role in climate change, the United Nations Framework Convention on Climate Change (UNFCCC) was adopted in 1992. It entered into force in 1994. The UNFCCC itself does not contain any quantified objectives of greenhouse gas emission reduction but it rather sets up a framework for upcoming protocols. In 1997, the Kyoto protocol to the UNFCCC was signed. Following the Russian and Canadian ratifications, marking that parties to the treaty were accounting for at least 55% of the CO_2 emissions for 1990, it entered into force in 2005 and the first commitment expired in 2012. The main objective of this first commitment was to reduce by at least 5% (reference level taken in 1990) the emissions of CO_2, CH_4, N_2O, hydrofluorocarbons, perfluorocarbons and sulphur hexafluoride (SF_6) during the 2005-2012 period. At its end, new negotiations started and it was decided, at the Doha's 18th Conference of the Parties (COP) in 2012, to extend the commitment period to 2020. However, some parties have objected to further take part in the international effort if primary polluting countries as China or India did not also join the effort. Consequently, Japan, New Zealand and Russia stepped down. Accounting also for the withdraw of Canada in 2012 and the fact that the United States did not ratified the Kyoto Protocol, the remaining parties were only accounting for less than 15% of the global emission of greenhouse gases. Finally, new negotiations occurred in 2015 at the 21st COP in Paris and led to the signature of the Paris Agreement. The main objective of the Paris Agreement is to limit the global warming well below 2 °C, preferably

to 1.5 °C, compared to pre-industrial levels. Opened for signature in April 2016, the Paris Agreement obtained enough ratifications (55 countries producing at least 55% of the global greenhouse gas emissions) in November 2016, making the Paris Agreement the most rapidly adopted international treaty.

1.3.2 Stratospheric ozone

In its cycle of formation and destruction, stratospheric ozone interacts with UV photons. This phenomenon is essential for life at the Earth's surface as it filters out the harmful UV radiations emitted by the Sun. The first theory for the formation and destruction of ozone was proposed by Chapman (1930). The so-called Chapman mechanism describes how the ozone is formed:

$$O_2 + h\nu \rightarrow O + O \qquad (\lambda < 240 \text{ nm}), \tag{1.1}$$

$$O + O_2 + M \rightarrow O_3 + M, \tag{1.2}$$

$$O + O + M \rightarrow O_2 + M. \tag{1.3}$$

From Eq. 1.1, we see that UV photons (hν) of wavelengths shorter than 240 nm, corresponding to a higher energy than that of the bound of the O_2 molecule, photodissociate molecular oxygen (O_2) to yield two oxygen atoms (O). Equation 1.2 further depicts the ozone formation by the rapid combination of the oxygen molecule with the highly reactive oxygen atom and the presence of a third body *M*. It should be noted that the oxygen atoms released in Eq. 1.1 may also recombine in a three-body collision process following Eq. 1.3.

The Chapman mechanism further describes how ozone is depleted:

$$O_3 + h\nu \rightarrow O_2 + O, \tag{1.4}$$

$$O_3 + O \rightarrow 2O_2. \tag{1.5}$$

We see that ozone is jointly depleted by photolysis involving lower-energy photos (Eq. 1.4) and a reaction with atomic oxygen (Eq. 1.5).

Grouping O and O_3 in the *odd oxygen* chemical family ($O_x \equiv O_3 + O$), we see that the reaction in Eq. 1.1 produces O_x while the reactions in Eq. 1.3 and Eq. 1.5 consume it. The fast reactions of Eq. 1.2 and 1.4 (several minutes) do not induce any net production or loss of O_x but rather modify the partitioning among members of the O_x chemical family. Moreover, it can be shown that, in the stratosphere, the abundance of O is negligible compared to that of O_3 so that $[O_x] \approx [O_3]$ and thus that Eq. 1.1 and Eq. 1.5 are the reactions controlling the O_3 abundance in the stratosphere.

From a chemical steady-state analysis of the Chapman mechanism (see, e.g., Chapter 10 in Jacob, 1999), the maximum of O_3 concentrations between 20 and 30 km altitude can be explained qualitatively. However, the Chapman mechanism fails at explaining quantitatively the corresponding observed O_3 concentrations, which in practice are smaller by, at least, a factor of 2. If differences are indeed expected in the lower stratosphere due to transport, the upper stratospheric differences are not, as the lifetime of O_x should be short compared to the transport timescales. Thus, it suggests that the sources in the Chapman mechanism are overestimated or that the sinks are underestimated.

During the second half of the twentieth century, a series of catalytic loss cycles, representing significant sinks of O_3, were discovered. The catalytic destruction of O_3 in the stratosphere can be summarized as follows:

$$O_3 + X \rightarrow O_2 + XO, \quad (1.6)$$

$$XO + O \rightarrow O_2 + X, \quad (1.7)$$

$$\text{net: } O_3 + O \rightarrow 2O_2, \quad (1.8)$$

with X corresponding to a catalyst returned at the end of the reaction cycle, thus able to effectively deplete O_3 even in relatively small concentrations. The above mentioned discoveries of the twentieth century have shown that X can either be the hydrogen atom and the hydrogen oxide radicals (HO_x; Bates and Nicolet, 1950), the nitrogen oxide radicals (NO_x; Crutzen, 1970; Johnston, 1971), the chlorine radicals (ClO_x; Molina and Rowland, 1974; Stolarski and Cicerone, 1974) and the bromine radicals (BrO_x; Wofsy et al., 1975).

Total ozone abundances have now been observed for several decades with the help of satellite remote sensors probing the Earth atmosphere. Therefore, the general spatial (meridional distribution) and seasonal behaviours of stratospheric ozone are very well known. It is now common knowledge that stratospheric ozone finds its maximum abundance in region of the least production. Indeed, the tropics are characterized by relatively low O_3 concentrations while high latitudes see relatively high concentrations. This global picture of ozone distribution can be explained by considering a slow meridional transport from the tropics, region of the most O_3 production, to the high latitudes, as was first proposed by Dobson (1930). This global stratospheric circulation is now referred to as the Brewer-Dobson circulation (BDC) and will be more deeply described in Chapter 2.

The stratospheric ozone at high latitudes also shows a large annual cycle, particularly over the Antarctica where the smallest O_3 abundances are observed during the austral spring. This spring minimum is referred to as the ozone hole and is due to very cold temperatures and activation of chlorine through heterogeneous chemistry at surface of polar stratospheric clouds (PSC). The formation of the ozone hole and its link with anthropogenic emissions of chlorinated compounds will be further discussed in Sect. 1.5.1.

1.4 Halogenated compounds in the atmosphere

1.4.1 Halogenated sources and their regulation by the Montreal Protocol

Halogenated compounds (i.e., containing chlorine, fluorine, bromine and to a lesser extent iodine) emitted at the Earth's surface by natural or anthropogenic processes can reach the stratosphere if they are long-lived enough (i.e., lifetime reaching the order of month). In the stratosphere, these compounds eventually break up and release halogen atoms that may be involved in the catalytic destruction of stratospheric O_3. Main halogenated compounds and their surface concentrations, lifetime, ozone depletion potential and global warming potential at 100-year time horizon are provided in Table 1- 2.

A few naturally emitted halogenated compounds are present in relatively high abundances (compared to the other trace gas abundances considered in this section) in the atmosphere. Methyl chloride (CH_3Cl), emitted by the ocean and by biomass burning, is the largest natural source of chlorine in the atmosphere (555 ppt in 2016; WMO, 2018). Methyl bromide (CH_3Br) is emitted by the ocean and biomass burning

and is also produced for agricultural purposes. Methyl bromide is certainly the most abundant bromine reservoir in the troposphere (6.8 ppt in 2016; WMO, 2018).

Table 1- 2: Major anthropogenic halogenated compounds in the atmosphere. Abundance, lifetime, ozone depletion potential (ODP) and GWP data are taken from Appendix Table A-1 in WMO (2018). The total sums also account for secondary contributors of each family.

Industrial designation	Chemical formula	2016 atmospheric abundance (ppt)	Total lifetime (years)	ODP	100-yr GWP
Chlorofluorocarbons					
CFC-12	CCl_2F_2	516	102	0.75	10300
CFC-11	CCl_3F	230	52	1.0	5160
CFC-113	CCl_2FCClF_2	72	93	0.8	6080
CFC-114	$CClF_2CClF_2$	15	189	0.5	8580
CFC-115	$CClF_2CF_3$	8.5	540	0.25	7310
Total		846.5			
Hydrochlorofluorocarbons					
HCFC-22	CHF_2Cl	253.5	12	0.025-0.035	1780
HCFC-141b	CH_3CCl_2F	24.5	9.5	0.07-0.1	800
HCFC-142b	CH_3CClF_2	22	18	0.02-0.06	2070
Total		301.5			
Hydrofluorocarbons					
HFC-134a	CH_2FCF_3	90	14	0	1360
HFC-23	CHF_3	29	228	0	12690
HFC-125	CHF_2CF_3	20.5	30	0	3450
HFC-143a	CH_3CF_3	19	51	0	5080
HFC-32	CH_2F_2	10	5.5	0	705
HFC-152a	CH_3CHF_2	6.5	1.5	0	148
Total		180			
Perfluorocarbons					
PFC-14	CF_4	83	50000	0	6630
PFC-116	C_2F_6	4.5	10000	0	11100
Total		89.5			
Halons					
Halon-1211	$CBrClF_2$	3.6	16	6.9-7.7	1750
Halon-1301	$CBrF_3$	3.3	72	15-19	6670
Total		7.3			

The most abundant halogenated compounds, methyl chloride excluded, have exclusively anthropogenic emissions. Discovered in the 1930's, CFCs have advantageous physical and chemical properties that have led to their intensive and extensive production. CFCs have, indeed, a low flammability, a low toxicity and a low reactivity (i.e., they are extremely stable; see their lifetime in Table 1- 2). CFCs are composed of carbon, chlorine and fluorine atoms and their general chemical

formula is $C_nCl_mF_q$, with $m + q = 2n + 2$. Main usages of these anthropogenic compounds are as refrigerants (CFC-11, CFC-12, CFC-114), solvents (CFC-113), inflating agents (CFC-11, CFC-12), aerosol propellants and in the manufacturing of foams. CFCs started to be largely emitted in the 1950s and their concentrations rapidly increased. Their extreme stability, that was sought by the industries producing or using them, makes them very long-lived in the atmosphere (from 52 to 540 years for the most abundant CFCs; see Table 1- 2). Large quantities of chlorine and fluorine were thus transported into the stratosphere. Two decades later, Molina and Rowland (1974) and Stolarski and Cicerone (1974) stated, almost simultaneously, the hypothesis that CFCs were decomposed in the stratosphere, leading to the release of chlorine atoms and the destruction of ozone through the catalytic cycle of ClO_x radicals. About simultaneously, the presence of hydrogen fluoride (HF) in the stratosphere was demonstrated for the first time by the infrared measurements performed on board the stratospheric gondola of the University of Liège (Zander, 1975). This observation was soon confirmed using spectra recorded from the ground at the Jungfraujoch station (Zander et al., 1977). The impact of the chlorine atoms, released in the stratosphere from the decomposition of CFCs, was later confirmed by the first observation of the occurrence of the ozone hole over Antarctica (Farman et al., 1985).

Facing the recent and worrying discoveries related to CFCs and their role in the ozone hole formation, the international authorities had to rapidly adopt measures to protect the ozone layer by phasing out CFC emissions. In March 1985, the Vienna Convention for the Protection of the Ozone Layer initiated and laid the foundation of an international framework to regulate the production and emission of ozone-depleting substances (ODSs). Two years later, the Montreal Protocol on Substances that Deplete the Ozone Layer was signed by 46 countries and entered into force in 1989. Today, the Montreal Protocol has been ratified by all United Nations Member and Non-member States. The complex framework set up by the Protocol facilitates the scientific and technical cooperation between States to achieve more rapidly its objectives. Moreover, it includes mechanisms of flexibility to further modify the Protocol as the global scientific knowledge progresses. Subsequent Amendments and Adjustments were thus ratified to accelerate the phase out of CFCs and their replacement by other chemical species such as hydrochlorofluorocarbons (HCFCs) and hydrofluorocarbons (HFCs). Figure 1- 6 synthetizes the control measures of the Montreal Protocol to phase out ODS (and HFCs, see below) production and consumption. The global success of the Montreal Protocol and its further Amendments – which is certainly the most successful international cooperation of all time – has implemented a rapid suppression of CFC production and consumption (Figure 1- 6**a**). In the wake of the international awareness on the harmful impacts of anthropogenic chlorinated source gases and the first observations of the ozone hole, the World Meteorological Organization (WMO) and the United Nations Environment Programme (UNEP) conducted, in 1985, the first "state-of-science" assessment of processes controlling the ozone layer and its changes, with additional supports of the National Aeronautics and Space Administration (NASA), the National Oceanic and Atmospheric Administration (NOAA) and the European Commission. Nowadays, WMO assessments of ozone depletion are published every four years, with the last one published in 2018 (WMO, 2018). As it was originally planned by the Montreal Protocol, these reports guide policymakers in future regulations of production and consumption of ODSs and their replacement products.

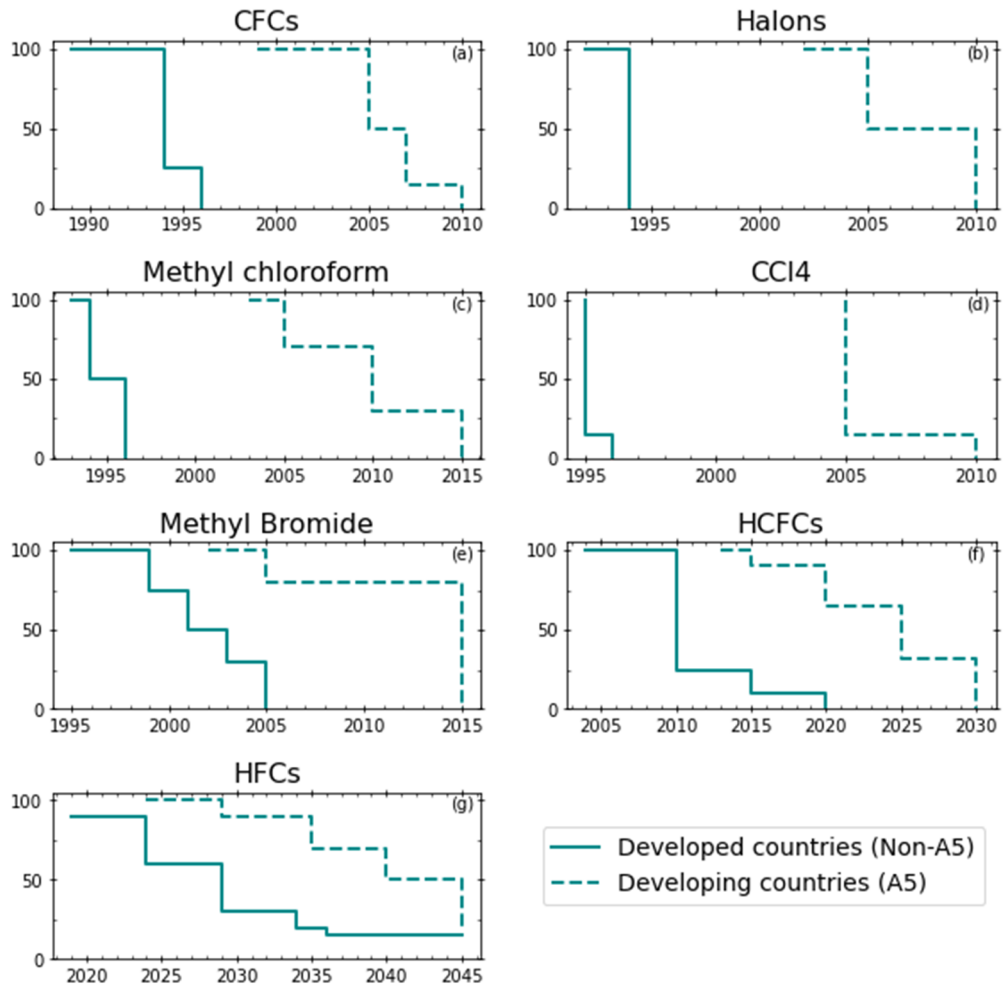

Figure 1- 6: Reduction schedules for the production and consumption of substances targeted by the Montreal Protocol and its amendments and adjustments. Hydrobromofluorocarbons (HBFCs) and bromochloromethane are not showed here. See https://ozone.unep.org/treaties/montreal-protocol/summary-control-measures-under-montreal-protocol (last access: 2021/04/09) for more information (e.g., adopted base level).

As a consequence to the rapid and strong regulation of CFC consumption and production, HCFCs have been, in turn, massively produced and consumed in the past decades. While HCFCs also contain chlorine atoms, their atmospheric lifetime is much lower to that of CFCs (e.g., 12 years for HCFC-22; see Table 1- 2). Indeed, HCFCs contain C-H bounds that make them vulnerable to the oxidation by OH in the troposphere. Consequently, the fluxes of chlorine compounds from the troposphere to the stratosphere, originating from HCFCs, are reduced; hence they have lower ozone depletion potential than CFCs. HCFCs were not included in the original text of the Montreal Protocol but were further added with the ratification of the Copenhagen Amendment in 1992. Following the 2007 Adjustment to the Montreal Protocol, the HCFCs overall production and consumption are now totally phased out in developed countries (1st January 2020) while the phase out is planned to 2030 for developing countries (i.e., Article 5 Parties; Figure 1- 6**f**).

The production of HFCs was initially quite limited due to their higher manufacturing costs, but following the progressive ban of ODSs, the overall production and consumption of HFCs have been strongly on the rise. For example, HFC-134 (CH_2FCF_3) had negligible surface concentrations until 1995 and, then, strongly increased to reach 90 ppt in 2016 (Table 1- 2). HFCs do not contain any chlorine

atoms and are, therefore, harmless to the ozone layer. However, all species considered in this section have very large GWP (see Table 1- 2). In other words, if HFCs do not represent a threat to the ozone layer, their atmospheric concentrations should be monitored and limited in order to support the international efforts mitigating the global warming (Sect 1.3.1.4). The HFC contribution to the overall radiative forcing of all long-lived greenhouse gases is estimated to be currently around 1% (WMO, 2018). In the face of this issue, the Kigali Amendment to the Montreal Protocol was adopted in 2016 and entered into force on 1st January 2019 (Figure 1- 6**g**). The main objective of this Amendment is to reduce the dependency on high-GWP alternatives (i.e., HFCs) as part of the HCFC phase out process by increasing the adoption of low-GWP and energy-efficient technologies. It should be finally noted that the Kigali Amendment does not exclude HFCs from the engagements relative to the Kyoto Protocol.

1.4.2 The degradation of halogens in the stratosphere and their role in the ozone depletion

In the section above, we saw that the most abundant halogenated source gases have long enough lifetime to reach the stratosphere. In the stratosphere, the availability of higher energy UV photons (λ<~250 nm) makes the photodissociation a significant sink for these gases. For example, CFC-12 (CCl_2F_2), the most abundant CFC, is photochemically destructed following the reaction pathway:

$$CCl_2F_2 + h\nu \rightarrow CClF_2 + Cl \qquad (\lambda < 215\ \text{nm}), \tag{1.9}$$

$$CClF_2 + O_2 + M \rightarrow CClF_2O_2 + M, \tag{1.10}$$

$$CClF_2O_2 + NO \rightarrow CClF_2O + NO_2, \tag{1.11}$$

$$CClF_2O + M \rightarrow COF_2 + Cl + M. \tag{1.12}$$

Similarly, CFC-11 (CCl_3F), the second most abundant CFC, is photochemically destructed following the reaction pathway:

$$CCl_3F + h\nu \rightarrow CCl_2F + Cl \qquad (\lambda < 226\ \text{nm}), \tag{1.13}$$

$$CCl_2F + O_2 + M \rightarrow CCl_2FO_2 + M, \tag{1.14}$$

$$CCl_2FO_2 + NO \rightarrow CCl_2FO + NO_2, \tag{1.15}$$

$$CCl_2FO + M \rightarrow COClF + Cl + M. \tag{1.16}$$

In addition to the destruction by photodissociation, the reaction with the electronically excited oxygen atom $O(^1D)$ is also an important sink of halogenated source gases in the stratosphere. For example, for CFC-12 we have:

$$CCl_2F_2 + O(^1D) \rightarrow CClF_2 + ClO. \tag{1.17}$$

Other reaction pathways leading to the release of Cl or Cl_2 are also possible.

The decomposition of HCFCs is similar to that of CFCs but, as written in Sect. 1.4.1, OH is also an important sink for these source gases, with the breaking of a C-H bound. For HCFC-22 ($CHClF_2$), by far the most abundant HCFC, we have:

$$CHClF_2 + OH \rightarrow CClF_2 + H_2O, \tag{1.18}$$

with the reaction pathway continuing with reactions of Eq. 1.10-1.12.

As for HCFCs, the degradation of HFCs starts with the attack by OH radicals (e.g., Bednarek et al., 1996; Burkholder et al., 2015). In the case of HFC-134a (CF_3CFH_2), the most abundant HFC, we have:

$$CF_3CFH_2 + OH \rightarrow CF_3CFH + H_2O, \quad (1.19)$$

CF_3CFH further reacts with O_2 and NO to finally yield the halogenated products CF_3CFO and CFHO. These products are, in turn, photolysed or chemically degraded to eventually release fluorine atoms or hydrogen fluoride (HF).

From all these reaction pathways, we see that the degradation of CFCs and HCFCs in the stratosphere releases chlorine, either directly into chlorine atoms or indirectly through the COClF reservoir. For fluorine, we see that it is mainly released into two main reservoirs, COF_2 and COClF. COF_2 is released by source gases containing at least two fluorine atoms (e.g., CFC-12 or HCFC-22) while COClF is mainly released by CFCs and HCFCs containing a single fluorine atom (e.g., CFC-11). These two reservoirs are in turn photolysed (e.g., Harrison et al., 2016):

$$COF_2 + h\nu \rightarrow FCO + F, \quad (1.20)$$

$$COClF + h\nu \rightarrow FCO + Cl, \quad (1.21)$$

$$FCO + O_2 + M \rightarrow FC(O)O_2 + M, \quad (1.22)$$

$$FC(O)O_2 + NO \rightarrow FCO_2 + NO_2, \quad (1.23)$$

$$FCO_2 + h\nu \rightarrow F + CO_2. \quad (1.24)$$

The fluorine atoms, thus released, finally quickly react with water, CH_4 or molecular hydrogen (H_2) to form HF. This last fluorine reservoir is very stable and prevents any significant catalytic destruction of O_3 by fluorine atoms.

If the fluorine atoms contained in halogenated source gases do not represent a threat to the ozone layer, we know that the chlorine atoms do (see also Eq. 1.6-1.8). Indeed, chlorine is involved in catalytic cycles destructing O_3, through the ClO_x chemistry:

$$ClO + O \rightarrow Cl + O_2, \quad (1.25)$$

$$Cl + O_3 \rightarrow ClO + O_2, \quad (1.26)$$

$$\text{net: } O + O_3 \rightarrow 2O_2. \quad (1.27)$$

However, further destruction pathways are encountered in the stratosphere with the coupling of the ClO_x, HO_x and NO_x cycles:

$$OH + O_3 \rightarrow HO_2 + O_2, \quad (1.28)$$

$$ClO + HO_2 \rightarrow HOCl + O_2, \quad (1.29)$$

$$HOCl + h\nu \rightarrow OH + Cl, \quad (1.30)$$

$$\text{net: } 2O_3 \rightarrow 3O_2, \quad (1.31)$$

and,

$$NO + O_3 \rightarrow NO_2 + O_2, \quad (1.32)$$

$$ClO + NO_2 + M \rightarrow ClONO_2 + M, \quad (1.33)$$

$$ClONO_2 + h\nu \rightarrow Cl + NO_3, \quad (1.34)$$

$$NO_3 + h\nu \rightarrow NO + O_2, \quad (1.35)$$

$$\text{net: } 2O_3 \rightarrow 3O_2. \quad (1.36)$$

From this set of equations, we see the occurrence of two other stable chlorine reservoirs, HOCl (Eq. 1.29) and $ClONO_2$ (Eq. 1.33). Active chlorine atoms can also react with other species (e.g., CH_4 or H_2) to form another stable chlorine reservoir, hydrogen chloride (HCl). Together, these three reservoirs (i.e., HCl, $ClONO_2$ and HOCl), and COClF, prevent the infinite destruction of the ozone layer (see that Cl and NO are free to react again at the end of their respective catalytic cycle; Eq. 1.30 and Eq. 1.35, respectively). We will see, however, in Sect. 1.5.1, that chlorine can be reactivated from these reservoirs through heterogeneous chemistry in the very cold stratosphere above Antarctica and cause a dramatic depletion of the ozone layer, i.e., the ozone hole.

1.4.3 Monitoring the success of the Montreal Protocol

To scrutinize the success of the Montreal Protocol and prevent the ozone layer to be further depleted, it is important to assess how ODS abundances are evolving through time. In addition to the direct scrutinizing of their accumulation rates in the troposphere, one may also assess how chlorine is evolving directly in the stratosphere, where the ozone depletion takes place. To do so, one may group the chlorine reservoirs into a single quantity (e.g., Nassar et al., 2006):

$$[Cl_y] = [HCl] + [ClONO_2] + [COClF] + [ClO] + 2[ClOOCl] + [HOCl] + 2[COCl_2]. \quad (1.37)$$

Note that abundances of ClOOCl and $COCl_2$ are multiplied by two in order to account for their two chlorine atoms. Cl_y is referred to as the **total inorganic chlorine**. In atmospheric chemistry, the *inorganic* term refers to the chemical products resulting from the atmospheric degradation of source gases emitted in the troposphere. Similarly, all source gases containing chlorine atoms may be grouped into the **total organic chlorine** (CCl_y). Furthermore, the sum of Cl_y and CCl_y represents the **total chlorine** (Cl_{TOT}). Due to chemistry and transport, the relative contribution of each inorganic chlorine reservoir to the Cl_y budget varies with altitude and latitude. HCl exhibits a constant increase with altitude and thus also its contribution to Cl_y. At the stratopause, it accounts for nearly all the Cl_{TOT} budget (i.e., [HCl] > 98% [Cl_{TOT}]; e.g, Zander et al., 1992, 1996; Nassar et al., 2006). $ClONO_2$ vertical profile peaks at altitudes ranging from 23km at southern high latitudes to 28km in the tropics (Nassar et al., 2006a). At its peak $ClONO_2$ accounts for 25% of the chlorine budget. For most seasons and latitudes, ClO vertical profile shows a single peak in the upper stratosphere but it can also show enhanced values in the lower stratosphere of winter poles, particularly in the Southern Hemisphere. At the upper stratospheric peak, near 40 km, ClO accounts for 20% of Cl_{TOT} (Nassar et al., 2006a). Figure 1- 7 depicts the evolution of Cl_y total columns above the Jungfraujoch (Switzerland, 46°N) as computed from FTIR observations of HCl and $ClONO_2$ (see Chapter 4 for the basics of the FTIR method). Cl_y total columns

as computed for Figure 1- 7 are a good approximation to Eq. 1.37 as they should represent ~90% of the closed Cl_y total column budget (Zander et al., 1996; Mahieu et al., 2004).

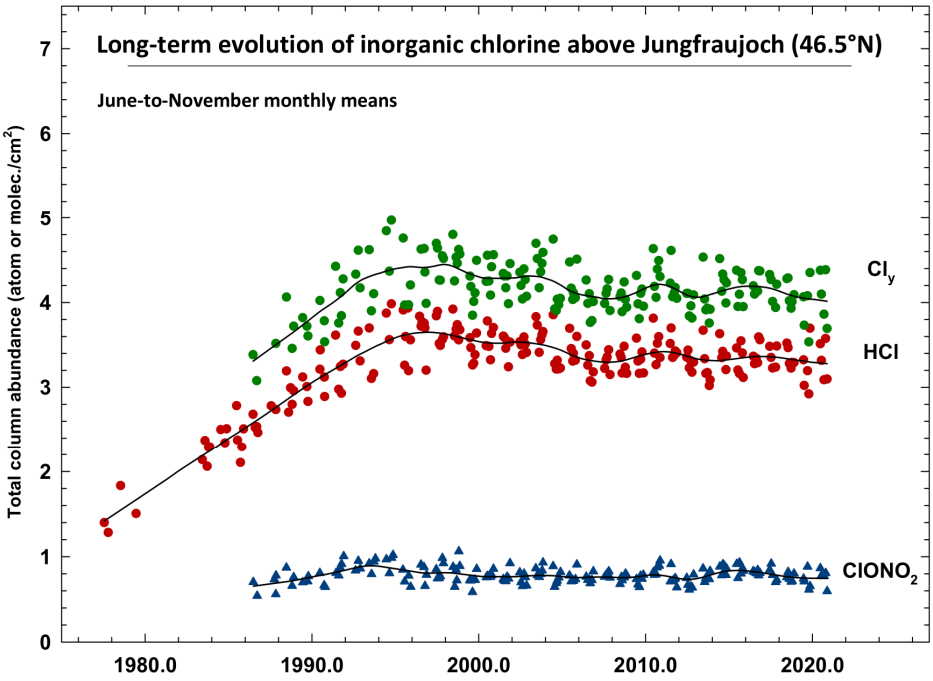

Figure 1- 7: Time-series of $ClONO_2$, HCl and their summation, Cl_y, as obtained from infrared solar spectra recorded at Jungfraujoch (Switzerland). These time-series are restricted to the June to November months in order to limit the dynamical variability caused by transport and subsidence.

Similarly to Cl_y, we define the **total inorganic fluorine** as:

$$[F_y] = [HF] + 2[COF_2] + [COClF]. \quad (1.38)$$

F_y will be used in this work to investigate stratospheric transport circulation changes. Our results concerning F_y sources and trends are further detailed in Chapters 5 and 6.

Another commonly used metric to describe the combined impact of chlorine and bromine on stratospheric ozone is the equivalent effective stratospheric chlorine (EESC). EESC is expressed as the equivalent amount of inorganic chlorine in the stratosphere based on the abundances of chlorinated and brominated tropospheric source gases. In this chapter, as this work focuses on the inorganic fluorine, we did not tackle the impact of bromine on the ozone layer. However, bromine has a much higher ozone depleting efficiency than chlorine due to less stable reservoirs (e.g., Daniel et al., 1999; Newman et al., 2007; see also ODPs of halons in Table 1- 2). With respect to that, inorganic bromine is weighted by a factor of 60 in the calculation of EESC values (Newman et al., 2007; Engel et al., 2018). Basically, the EESC accounts for the transit time of source gases from the troposphere to the stratosphere and inside the stratosphere (i.e., the age of air metric; detailed in the next chapter). Furthermore, it accounts for the release of inorganic halogens (i.e., chlorine and bromine) from the source gases as a function of the transit time (i.e., the fractional release). Different approaches to derive the EESC exist (e.g., Newman et al., 2007; Engel et al., 2018) but are not further detailed here. The key aspect to retain here, is that the EESC is function of the tropospheric source gas trends, the transit time, the fractional release or chemical loss during the transport. With respect to that, EESC values are larger under polar winter conditions in comparison to midlatitude conditions (WMO, 2018). Figure 1- 8 depicts the evolution of the EESC in

polar winter (Figure 1- 8a) and midlatitude (Figure 1- 8b) conditions. From this figure, we see that the EESC peak values were reached in 2000 in polar winter conditions, meaning that the Montreal Protocol has been successfully decreasing the harmful impact of ODSs since then.

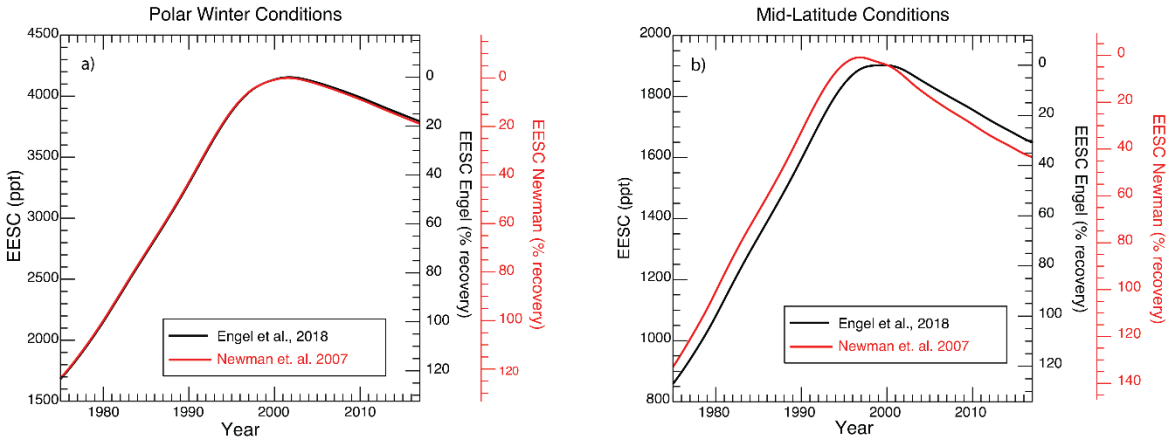

Figure 1- 8: EESC (ppt; left axis) and EESC level of recovery from maximum values towards 1980 benchmark values (right axis), representative of polar winter conditions (5.5 years mean age of air; **a**) and midlatitudes conditions (3 years mean age of air; **b**). EESC values computed following the methods of Newman et al. (2007; red) and Engel et al. (2018; black). From WMO (2018).

1.5 Long-term stratospheric ozone change

1.5.1 The Antarctic ozone hole

1.5.1.1 Destruction mechanisms

We evoked, in Sect. 1.3.2 and Sect. 1.4.2, the existence of catalytic cycles destructing efficiently the stratospheric O_3. However, we also saw that chlorine atoms are ultimately captured in stable reservoirs, preventing the stratospheric O_3 to be entirely destructed by the ClO_x, HO_x and NO_x cycles. The dramatic O_3 decrease above Antarctic occurring in austral spring, firstly observed by Farman et al. (1985), hence suggests that other chemical pathways must be at play in this region of the stratosphere. Solomon et al. (1986) suggested that heterogeneous chemistry (i.e., chemical reaction between reactants in distinct phases), occurring on the surface of PSCs, could reactivate chlorine atoms from the inactive inorganic chlorine reservoirs. PSCs are formed in the very cold conditions of the stratosphere during winter above Antarctica (T<200K), despite the well-known dryness of the stratosphere. These clouds can either consist of a supercooled liquid ternary solution of sulphuric acid or of solid nitric acid trihydrate particles (NAT; e.g., Solomon et al., 2015; Müller et al., 2018). Several important reactions were identified:

$$ClONO_2 + HCl \rightarrow Cl_2 + HNO_3, \quad (1.39)$$

$$N_2O_5 + H_2O \rightarrow 2HNO_3, \quad (1.40)$$

$$ClONO_2 + H_2O \rightarrow HNO_3 + HOCl, \quad (1.41)$$

$$HOCl + HCl \rightarrow H_2O + Cl_2. \quad (1.42)$$

Chlorine molecules yield by reactions of Eq. 1.39 and Eq. 1.42 dissociate to release chlorine atoms when the sunlight reaches again the polar region of the Southern Hemisphere in spring, finally leading to a

dramatic depletion of the ozone layer above the South Pole. Another key consequence of these pathways is the denitrification of the polar stratosphere by the reaction of Eq. 1.40, preventing ClO to be recaptured in $ClONO_2$. Indeed, the HNO_3 molecules thus produced are captured by PSCs through their sedimentation in NAT. Finally, it should be noted that this set of equations only constitutes a limited picture of all the chemical processes occurring in the polar night and later in spring. Indeed, additional pathways should be considered to, for example, explain the fact that the active chlorine is not rapidly deactivated through the formation of HCl molecules in spring (Müller et al., 2018).

1.5.1.2 Trends

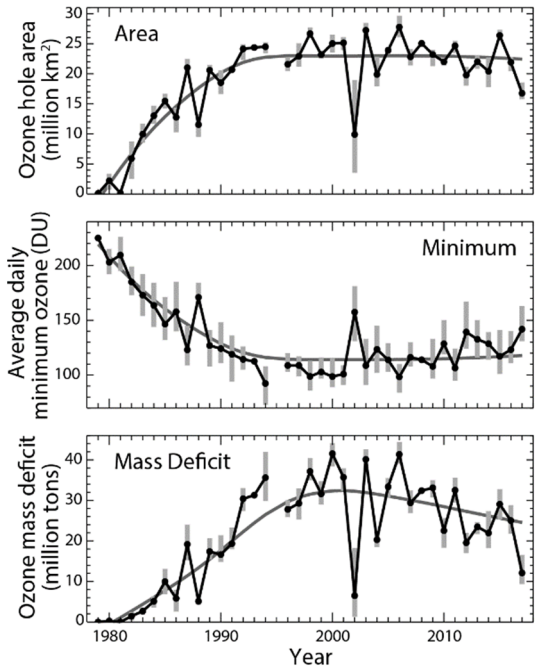

Figure 1- 9: "(top) Area of the Antarctic ozone hole for 1979–2017, averaged from daily total ozone area values contained by the 220 DU contour for 21–30 September. (middle) An average of daily minimum ozone values over Antarctica during the period from 21 September to 16 October. (bottom) Ozone mass deficit averaged over the 21–30 September period. For all three panels, the vertical gray bars indicate the range of values over the same time period. The EESC has a mean age of 5.5 years, an age spectrum width of 2.75 years, and a bromine-scaling factor of 65." From WMO (2018).

Figure 1- 9 depicts the long-term evolution of the three metrics commonly used to report on the state of the ozone hole (WMO, 2018), i.e., the area of the ozone hole (million km^2; upper frame), the average daily minimum ozone (DU; middle frame) and the mass deficit (million tons; lower frame). We see that all three metrics show a clear stabilization after the year 2000, when EESC peaked in Southern Hemisphere high latitudes (see Figure 1- 8 and Figure 1- 9). All three metrics also exhibit a year-to-year variability, with the year 2002 outstanding in the three time-series due to an unprecedented major sudden stratospheric warming.

Similarly to these metrics, total ozone time-series above Antarctica also show contrasted trends before and after the year 2000. Figure 1- 10 shows total ozone trends for the periods 1979-1996 and 1997-2016 for the months of September (top) and October (bottom; Weber et al., 2018). From this figure, it is clear that the Antarctic ozone layer underwent a strong ozone depleting period before 1997. Since then, the intensity of the depletion decreased and the onset of the ozone recovery is statistically significant in September, with total ozone trend of 8.2% per decade. However, it should be noted that trend estimations are influenced by various parameters as the chosen time-period (i.e., sensitivity to the dynamical variability), trend estimation methods (e.g., formulation of regression models), use of different proxies, drifts in the observational datasets and spatial representativeness of sparse ground-based data (see Chapter 4 in WMO, 2018, and references therein). In consequence, studies estimating Antarctic total ozone trends do not show the exact same values. Most studies show, nonetheless, a positive September

trend for the first decades of the twenty-first century, with estimated values ranging from 5% to 10% per decade, corresponding approximately to 1 to 2 DU per year (see Chapter 4 in WMO, 2018, and references therein).

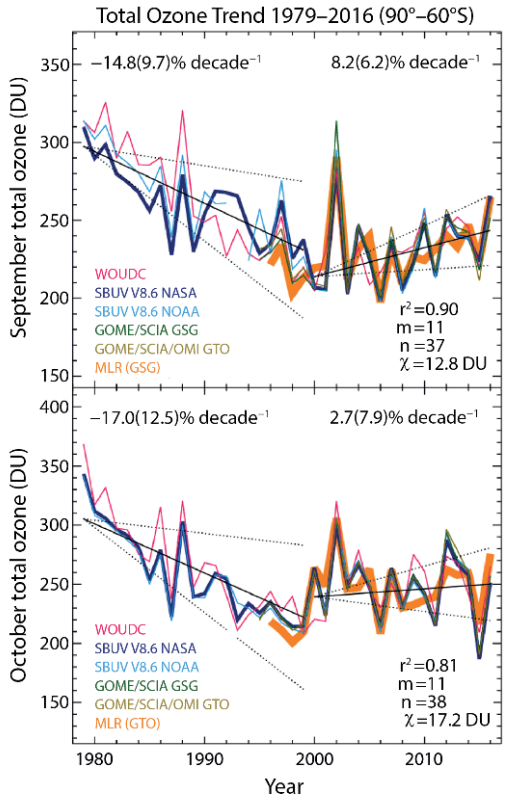

Figure 1- 10: "Total ozone time series for Antarctica (60°–90°S) in the months of September (top) and October (bottom), derived from five long-term observational data sets. In each panel, one data set has been chosen as labelled to show the results of applying a multiple linear regression with independent linear trends analysis (orange). Regressor terms include the solar cycle, QBO, ENSO, volcanic aerosol, and the strength of the Brewer-Dobson circulation." From Weber et al. (2018) and WMO (2018).

Climate models as chemistry-climate models, with full chemistry modules, are commonly used to project the health of the ozone layer as ODS abundances are expected to continue to decrease in the twenty-first century. Using scenarios, based on full compliance with the Montreal Protocol and following the baseline scenario (RCP-6.0) for greenhouse gases future evolution, these models are able to assess the probable evolution of the ozone hole in the twenty-first century. From these simulations, the ozone hole is expected to gradually heal in the twenty-first century, with ozone total columns returning to 1980 values in Antarctica between 2055 and 2066 (Dhomse et al., 2018; WMO, 2018).

1.5.2 Global ozone

Near global total ozone trends (60°S-60°N) are smaller than that above Antarctica (Figure 1- 11). Ground-based and satellites datasets show an increase of between 0.3% to 1.2% per decade, with uncertainties of about 1% per decade (WMO, 2018). The large estimated uncertainties compared to the estimated trends hinder any conclusion about the global ozone recovery. Moreover, these trends, around 1% per decade, are relatively small compared to the dynamical forced year-to-year variations, estimated to be around 5% (WMO, 2018). The sources of variations are, e.g., the solar variability, the quasi-biennial oscillation (detailed in the next chapter), the El Niño–Southern Oscillation (ENSO), stratospheric aerosols (e.g., large volcanic eruptions) and change in the BDC. This last source of variability can, indeed, induces large variations in trends of stratospheric long-lived tracers and ozone (e.g., Nedoluha et al., 2015). In the next chapter we will see that this interannual variability of the stratosphere cannot be only explained by the QBO, ENSO or stratospheric aerosols. In consequence, its

impact on total ozone trends cannot be properly captured by MLR models, thus increasing the estimated uncertainty around estimated trend values. A better characterization of the stratospheric circulation changes could, therefore, improve the estimation of global ozone trends. This last sentence is one of the key motivations of our work on stratospheric circulation trends and changes.

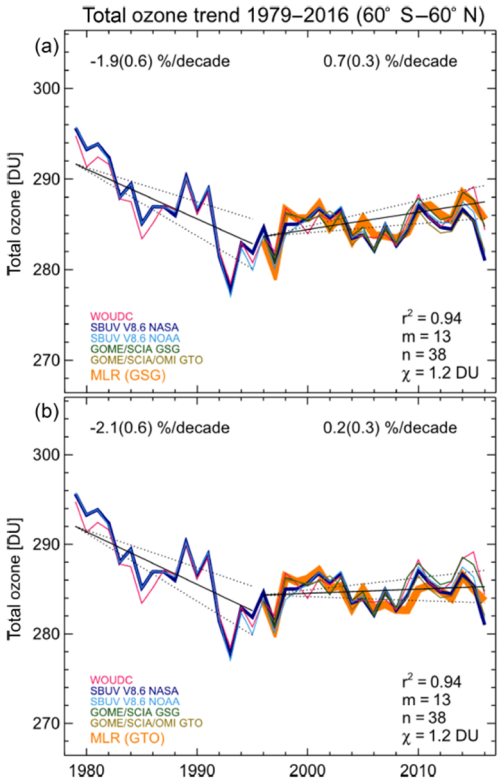

Figure 1- 11: Annual and near-global ozone time series (60°S–60°N). In each panel, one data set has been chosen as labelled to show the results of applying a multiple linear regression with independent linear trends analysis (orange). Regressor terms include the solar cycle, QBO, ENSO, volcanic aerosol, and the strength of the Brewer-Dobson circulation. From Weber et al. (2018).

Chapter 2

The BDC and its changes

In this chapter, after a theoretical overview of the BDC (Sect. 2.1 and Sect. 2.2) and its quasi-biennial oscillation (Sect. 2.3), we propose a review of the metrics commonly used (Sect. 2.4) to investigate the BDC changes addressed in Sect. 2.5.

The theoretical part of this chapter is primarily based on the books of Brasseur and Solomon (2005) and Holton and Hakim (2013), and the excellent BDC review of Butchart (2014).

2.1 The Brewer-Dobson circulation

Earliest theoretical models of stratospheric transport were proposed in the first half of the twentieth century in order to explain the spatial distribution of chemical species in the middle atmosphere. Dobson (1930) was among the firsts to suggest a slow poleward drift of the air in the high stratosphere, followed by an air descent in midlatitude and polar regions, to explain the high ozone concentrations above the Arctic in spring (Butchart, 2014). Later on, Brewer (1949) and Dobson (1956) came up with the same theoretical circulation concept, deduced from water vapour and ozone observations, respectively. The first calculation of the mean circulation was proposed by Murgatroyd and Singleton (1961). Using a radiative heating rate analysis, they computed a mean circulation for the middle atmosphere which was well in agreement with the former proposed concepts. These authors, as well as Brewer (1949), were however concerned by the resulting non-conservation of the angular momentum. For Murgatroyd and Singleton (1961), this was owing to the fact they neglected important eddy processes (fluctuations around the zonal mean). Several studies (Reed et al., 1963; Julian and Labitzke, 1965; Vincent, 1968), including this time the contribution of eddies, then suggested a quite different global circulation in the stratosphere, with two cells in one hemisphere, the additional cell having an ascent branch in the polar region and a descent branch in the midlatitudes (similar to the tropospheric Ferrel cell). The troubling difference between the first tracer studies of Brewer (1949) and Dobson (1956) and the last cited studies actually comes from the Eulerian (simple zonal mean) framework used to derive the mean circulation. In fact, in the case of a steady (amplitude constant with time) and conservative (no dissipation or wave breaking) planetary wave (Rossby wave) propagating vertically in the stratosphere, it can be shown that the resulting eddy perturbation cannot induce any net vertical transport across isentropic surfaces. The Eulerian mean circulation thus relates to a closed ellipse in the latitude-height plane (i.e., there is no net motion; see Matsuno, 1980, for further details). In order to reconcile tracer based circulation concepts

(i.e., net transport) and computed mean circulation, the transformed Eulerian mean (TEM) approach was developed (Andrews and McIntyre, 1976; Andrews and Mcintyre, 1978). In the TEM, the eddy contribution to the mean transport is, this time, combined into a single quantity, the residual mean circulation, representing well the net mass transport earlier described by Brewer and Dobson. The residual circulation avoids the cancellation of the eddy-mean flow and is very similar to the diabatic circulation, with upward transport where the net diabatic heating is positive (tropics) and downward transport where it is negative (winter pole). Figure 2- 1 (left frame) schematics the BDC following the TEM approach (i.e., the residual circulation).

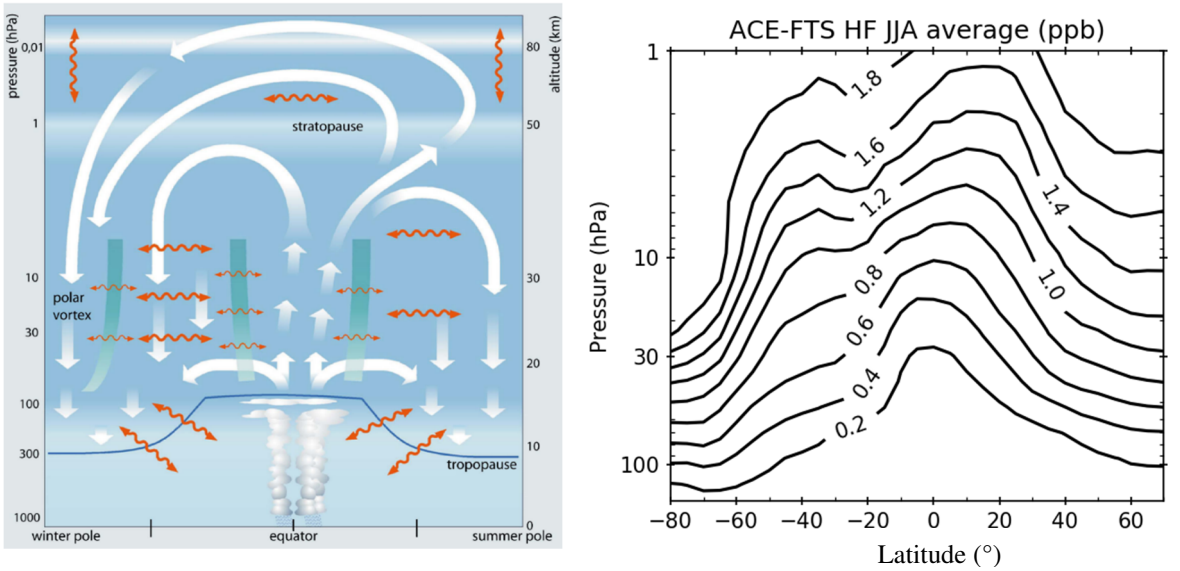

Figure 2- 1: Left frame: "schematic of the BDC as the combined effect of residual circulation and mixing in the stratosphere and mesosphere. The thick white arrows depict the TEM mass streamfunction as representation of the residual circulation whereas the wavy orange arrows indicate two-way mixing processes. The thick green lines represent stratospheric transport and mixing barriers." From Bönisch et al. (2011). Right frame: zonal mean and seasonal mean (June, July and August) of ACE-FTS retrievals (v4.0; Bernath et al., 2020) of HF (black contour lines; ppb).

It emerges from the stratospheric circulation comprehension history addressed above that the now called Brewer-Dobson circulation does not actually conform to a unique or formal definition. However, in the case of tracer transport studies, the BDC is often referring to a two-cell structure (one per hemisphere) with an ascending net transport in the tropics, a poleward drift and a descending net transport in midlatitudes and at the poles (see Figure 2- 1). This broad feature of the transport occurring in the stratosphere can be further divided into transport branches (white arrows in Figure 2- 1; e.g., Plumb, 2002; Birner and Bönisch, 2011; Konopka et al., 2015; Minschwaner et al., 2016). The deep branch (between 70 and 1 hPa) represents the vertical transport from the tropical tropopause to the highest part of the stratosphere, followed by a descent in the winter hemisphere midlatitudes and winter pole. The shallow branches (between 100 and 70 hPa) are all year round transporting air from the tropics to the midlatitudes in the lower stratosphere. It is also worth noticing that a transport is also observed from the summer pole to the winter pole in the high stratosphere/low mesosphere. In addition to these mass transporting branches, the BDC may also include a two-way irreversible mixing. The two-way mixing causes transport of tracers but not of mass. This mixing process is strongly limited in the vicinity of the polar vortex and the tropics by strong potential vorticity gradients, leading to the definition of the transport barriers (green thick vertical lines in Figure 2- 1).

The right frame of Figure 2- 1 shows the average austral winter distribution of HF, obtained from Atmospheric Chemistry Experiment Fourier Transform Spectrometer (ACE-FTS) satellite data. As seen in Chapter 1 (Sect. 1.4.2), HF is formed in the stratosphere through the photodissociation of halogenated sources (e.g., CFCs, HCFCs or HFCs). HF is extremely stable and its lifetime is much larger than the transport timescales in the stratosphere (~years). Consequently, HF is a good chemical tracer of the BDC (e.g., Chipperfield et al., 1997). In the lower tropical stratosphere, low HF values are encountered due to the upward transport advecting HF-poor air from the troposphere. Along the tropical upwelling, halogenated sources are photodissociated and HF mixing ratios increase as the photodissociation gets more efficient. Following the deep branch of the BDC in the high stratosphere, HF-rich air is then transported poleward and downward as it reaches the winter pole. Consequently, high HF mixing ratio values are observed above the winter pole. Indeed, at 25hPa, see the 1.8 ppb values above the winter pole (80°S) compared to ~0.3 ppb at the equator. The transport-inhibiting effect of the transport barriers is also clearly depicted in the right frame of Figure 2- 1, particularly with the very steep gradients in the vicinity of the winter pole. The polar transport barrier is very strongly isolating the polar air from the midlatitude air, it is referred to as the polar vortex. Finally, in the midlatitudes of the summer hemisphere, the quasi-horizontal two-way mixing flattens the HF isopleths (lines of equal mixing ratios) between the subtropical and polar transport barriers. This region of the winter hemisphere is referred to as the surf zone (see Sect. 2.2.3).

2.2 A wave driven stratosphere

In the troposphere, atmospheric waves are formed by the orographic lifting of air masses or by the large scale differential heating of the Earth's surface (e.g., sea-land contrasts). They can be defined "as propagating disturbances of material contours whose acceleration is balanced by a restoring force" (Brasseur and Solomon, 2005). Gravity waves are generated by a vertical displacement of air parcels in a stably stratified fluid. The vertical displacement may be caused by the Earth's surface orography or by large convective systems. The buoyancy force of the air parcel is the restoring force for this type of waves. They have a typical horizontal wavelength of 10 km to 1000 km. Rossby waves are planetary-scale (wavelengths of several thousand kilometres) horizontal waves propagating in the westward direction relative to the mean flow. They owe their existence to the meridional gradient of potential vorticity. They are mainly formed by stationary sources as the large-scale orography and land-sea contrasts.

These waves have the ability to propagate vertically and eventually reach the stratosphere or even the mesosphere. This propagation in the stratosphere is not without consequences, as the induced eddy perturbations drive away the stratosphere from its radiative equilibrium and drive the residual circulations as described above. We will also see that large-scale waves are also responsible of the largest variability modes in the stratosphere as the quasi-biennial oscillation (QBO).

2.2.1 Poleward mass flow in the winter hemisphere

Sometimes referred to as the "extratropical pump" or more adequately as the "Rossby-wave pump", the mechanism driving the poleward mass flow in the winter hemisphere is caused by the vertical propagation and dissipation of Rossby waves. As mentioned above, these planetary waves are generated by land-sea temperature contrasts or by the surface topography. While these forcings are indeed stronger in winter, the seasonal aspect of the deep branch of the BDC is rather caused by the dependence of the

vertical propagation of these waves to the zonal wind profile (Holton, 1980). It can be in fact demonstrated that stationary Rossby waves can only vertically propagate in a westerly air flow and that is, moreover, weaker than a critical value, i.e., the Charney and Drazin criterion. From the thermal wind relation and the depicted hemispheric meridional temperature gradient, it appears that such a westerly zonal flow is only seen in the winter hemisphere.

As explained in Sect. 2.1, the TEM formalism allows for a net meridional circulation (i.e., the residual circulation), with the effect of eddies included through a wave drag (caused by angular momentum transfer), $\mathcal{G}$ (e.g., Brasseur and Solomon, 2005; Haynes, 2005). The set of following simplified equations, expressed in the TEM formalism, illustrates the wave-driven residual circulation:

$$\frac{\partial \bar{u}}{\partial t} - 2\Omega \sin\phi \bar{v}^* = \mathcal{G}, \tag{2.1}$$

$$2\Omega \sin\phi \frac{\partial \bar{u}}{\partial z} + \frac{R}{aH}\frac{\partial \bar{T}}{\partial \phi} = 0, \tag{2.2}$$

$$\frac{\partial \bar{T}}{\partial t} + \bar{w}^* \left(\frac{HN^2}{R}\right) = -\alpha \bar{T}, \tag{2.3}$$

$$\frac{1}{a\cos\phi}\frac{\partial}{\partial \phi}(\bar{v}^* \cos\phi) + \frac{1}{\rho_0}\frac{\partial}{\partial z}(\rho_0 \bar{w}^*) = 0, \tag{2.4}$$

where ϕ is latitude and z is a log-pressure coordinate. a is the radius of the Earth, Ω is the angular frequency of the Earth's rotation, R is the gas constant for dry air, α is a constant rate representing the longwave heating or cooling, H is the constant nominal density scale height used to define the log-pressure coordinates and ρ_0 is the background density in these coordinates. $\bar{u}$ is the zonal velocity, $\bar{T}$ is the temperature and N^2 is the square of the buoyancy frequency (a measure of static stability). $\bar{v}^*$ and $\bar{w}^*$ are the meridional and vertical components of the residual circulation, respectively. Equation 2.1 is the zonal momentum equation and expresses the effect of the wave drag ($\mathcal{G}$) on the zonal flow ($\bar{u}$) as well as the association between the horizontal meridional circulation ($\bar{v}^*$) and the Coriolis torque ($2\Omega \sin\phi \bar{v}^*$). Equation 2.2 is the thermal wind relation between the zonal velocity and the temperature, following the geostrophic and hydrostatic balance. Equation 2.3 is the temperature equation and expresses that the rate of change of temperature ($\frac{\partial \bar{T}}{\partial t}$) is equal to the diabatic heating ($-\alpha \bar{T}$) plus the adiabatic temperature change associated with vertical motion ($\bar{w}^* \left(\frac{HN^2}{R}\right)$). Equation 3.4 is the mass conservation or continuity equation for the meridional circulation. Taken together, these four equations describe the coupled response of the zonal flow, temperature and meridional circulation to an applied wave force ($\mathcal{G}$).

With further simplifications, the vertical residual velocity can be expressed as:

$$\bar{w}^* = -\frac{1}{2\Omega\rho_0(z)\cos\phi}\frac{\partial}{\partial\phi}\left[\frac{\cos\phi}{\sin\phi}\int_z^\infty \rho_0(z')\mathcal{G}(\phi, z')dz'\right]. \tag{2.5}$$

This last equation expresses the important "downward-control principle" which states that the mean mass flow across a particular level is determined only by the wave force above that level.

To summarize, the dissipation of Rossby waves in the stratosphere causes a westward drag, which, in turn, drives the air poleward to conserve the angular momentum (Butchart, 2014). This poleward airflow pumps the air from the tropics and push it down in the middle and high latitudes. To conserve the mass,

upwelling and downwelling are needed. From kinematic considerations, it can be shown that the upwelling must be situated in the tropics and the downwelling in middle and high latitudes.

2.2.2 Shallow branches

While the deep branch of the BDC is mainly driven by planetary-scale Rossby waves, the shallow branches (between 100 and 70 hPa) are also driven by synoptic scale waves, breaking in the upper troposphere/lower stratosphere region (Birner and Bönisch, 2011; Konopka et al., 2015; Minschwaner et al., 2016). These shallow branches are active all year round in both hemispheres, in contrast with the deep branch that is only depicted in the winter hemisphere. Consequently, the deep branch is dominating the transport in the winter hemisphere while the shallow branches have a stronger impact in the summer hemisphere (Birner and Bönisch, 2011; Konopka et al., 2015). Finally, it is also important to note that the shallow branches are characterized by shorter transit times (~1 year) than the deep branch (several years; Birner and Bönisch, 2011).

2.2.3 Surf zone, mixing barriers and polar vortex

As introduced in Sect. 1.2 and clear form its name, the stratosphere is highly stratified and the air density decreases with height. In consequence, Rossby waves gain in amplitude as they propagate vertically in the stratosphere and eventually break, in the manner of gravitational sea waves as they approach the shore (but in the horizontal plane for Rossby waves). The breaking of Rossby waves occurs on relatively large scales and is able to stir air parcels over thousands of kilometres. As already explained before, the Rossby wave vertical propagation is mainly taking place in the winter hemisphere at midlatitudes, limiting this way the impact of wave breaking to this zone. This region of the stratosphere is commonly referred to as the surf zone (e.g., Plumb, 2002). Because of this large scale stirring, potential vorticity and long-lived tracer concentration fields are homogenised and their corresponding zonal mean isopleths are flattened inside the surf zone (see right frame of Figure 2- 1). Sharp potential vorticity gradients are consequently depicted at the surf zone edges which will act as transport or mixing barriers. The mixing barrier at the polar edge of the surf zone is referred to as the polar vortex while the opposite edge is referred to as the subtropical barrier. Finally, for a still not fully understood reason, a second subtropical barrier is observed in the summer hemisphere (Plumb, 2002; Butchart, 2014). Together, these barriers are defining four distinct regions of the stratosphere: the winter polar vortex, the surf zone, the tropics and the summer hemisphere.

2.3 The quasi-biennial oscillation

In the tropical stratosphere, a long period oscillation of zonal winds is observed, with their zonal direction alternating between westerlies and easterlies. It has an average period of 27 months (ranging from 22 to 36 months, e.g., Osprey et al., 2016) and is thus referred to as the quasi-biennial oscillation. Figure 2- 2 depicts the alternating regimes in the time-height section of the zonal wind speed measured above Singapore (1°N, 104°E). The successive regimes first appear above 30 km and slowly propagate downward, without losing amplitude, at rate of 1 km per month. The westerly wind maximum (~15 ms^{-1}) is half of that of the easterly wind (~30 ms^{-1}). The QBO westerly phase descent is more rapid and more uniform than the descent of QBO easterly phases. Easterly winds can occasionally stall above 50 hPa and, in consequence, QBO westerly phases usually last longer than QBO easterly phases at 50 hPa.

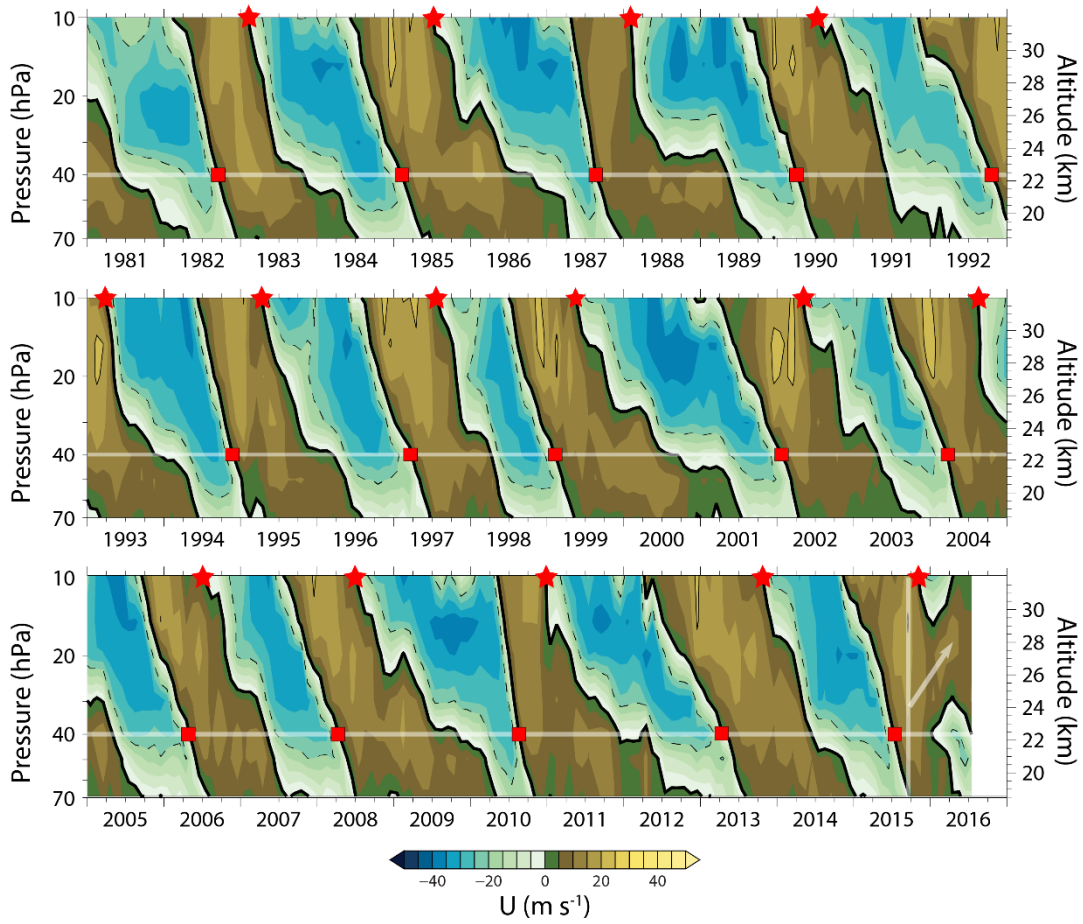

Figure 2- 2: "Monthly mean zonal wind (ms^{-1}) derived from Singapore radiosondes (1°N, 104°E) between 70 and 10 hPa for 1981 through July 2016. The colour scale is on the bottom with 5 ms^{-1} colour increments. Easterlies are shown in cyan blue, while westerlies are in green brown. Contours are every 20 ms^{-1}, with easterlies dashed and westerlies solid, and a thick black zero wind. The red squares show the dates of the 40 hPa easterly-to-westerly transition, while the red stars show the 10 hPa dates of the westerly to easterly transition". From Newman et al. (2016) and WMO (2018).

Baldwin et al. (2001) wrote a comprehensive review of the QBO and its impact on the extratropical stratospheric circulation and chemical composition. Here follows a summary of the key features of the QBO approached by these authors.

A rather simple theory (first proposed and numerically resolved by Lindzen and Holton, 1968), considering a spectrum of westward and eastward waves vertically propagating in the stratosphere, can explain the alternating descending wind regimes of the QBO. This theory is schematically represented in Figure 2- 3. As seen for the deep branch of the BDC (see Sect. 2.2.1), atmospheric waves can only vertically propagate in an opposite mean flow, relative to their phase propagation, which has to be smaller than a critical value. Moreover, remember that dissipating atmospheric waves deposit momentum and tend to accelerate the zonal flow in the direction of their horizontal phase propagation. Now, consider either a small imbalance in the wave spectrum (e.g., a larger contribution of westward waves) or an already existing mean flow in the lower stratosphere (Figure 2- 3**a**). The imbalance lets waves of one zonal phase speed sign drive the mean flow of the tropical lower stratosphere, while the other waves thus have the possibility to propagate farther vertically, eventually dissipate and drive the upper layers in the opposite zonal direction. As the zonal flow of the lowest layer is accelerated by the dissipation of waves, it has to conserve its angular momentum and descend in altitude, eventually

reaching a level where it cannot further descend. The descending upper shear zone will then cause the narrowing of the lower shear zone, the latter getting progressively destroyed by viscous diffusion. The waves that were initially driving the lowest shear zone will thus have again the possibility to propagate vertically through the opposite zonal flow of the lower layer, to reach higher altitudes and to drive the upper layer in the opposite direction (Figure 2- 3**b-c**). Again, the shear zone descends, leading progressively to the destruction of the lowest layer (Figure 2- 3**d**). The full cycle is repeating itself with, as mentioned before, an average period of 27 months.

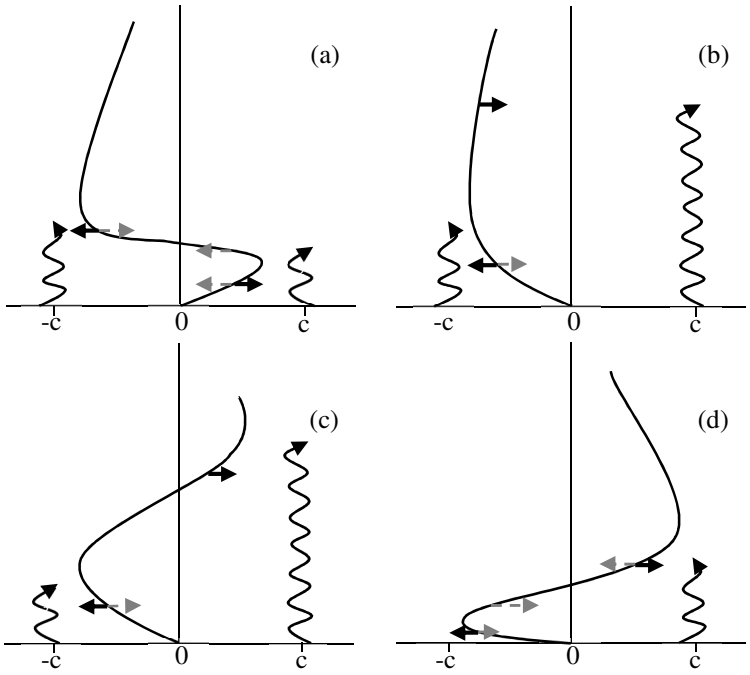

Figure 2- 3: Schematic representation of the theory of Lindzen and Holton (1968), after (Plumb, 1984). Panels **a** to **d** depict the temporal evolution of the mean zonal flow (horizontal axis) during a half cycle of the QBO. Horizontal black arrows represent the wave-driven acceleration and grey arrows represent the viscous diffusion. Wavy black lines indicate vertical propagation of eastward and westward atmospheric waves. This figure is also reproduced in Baldwin et al. (2001).

2.3.1 The QBO-induced secondary meridional circulation

The descending wind anomalies associated with the QBO drive a secondary meridional circulation in low latitudes. It can be summarized as follows (Baldwin et al., 2001; Strahan et al., 2015): a cold perturbation is associated with the descending easterly winds. The descending cold anomaly increases the tropical upwelling, which is balanced by subtropical descent. The secondary circulation is completed by tropical outflows at levels of maximum easterly winds and equatorward convergence at levels of westerly winds. The opposite meridional circulation develops with descending westerly winds. This secondary circulation, induced by the QBO, acts on local trace gas gradients to modify their distributions in low latitudes. As the BDC seasonality is strongly asymmetric, with an enhanced transport in the winter hemisphere by the deep branch, the secondary meridional circulation associated with the QBO is more strongly affecting the winter hemisphere extratropical region.

Figure 2- 4 illustrates the secondary meridional circulation associated with QBO phases (Strahan et al., 2015), using the N_2O tracer. In the lower stratosphere, the enhanced transport from the tropics to the midlatitudes, associated with QBO easterly phases (Figure 2- 4 B and D), induces positive N_2O anomalies in the midlatitudes. During QBO westerly phases, the descent and convergence at levels of

westerly winds creates N_2O negative anomalies in the lower stratosphere (Figure 2- 4 A and C). These N_2O anomalies can be generalized to other chemical tracers or in terms of transit times (or age of air, see Sect. 2.4 below). In a few words, easterly QBO phases generate transport anomalies such as the midlatitudes lower stratosphere air masses are characterized by shorter transit times or lower age of air. In consequence, for a tracer that finds its sources in the stratosphere (e.g., HF, formed by the degradation of halogenated compounds; see Sect. 1.4), the anomalies associated with QBO phases are of opposite signs compared to that of a tracer that is emitted in the troposphere (e.g., N_2O).

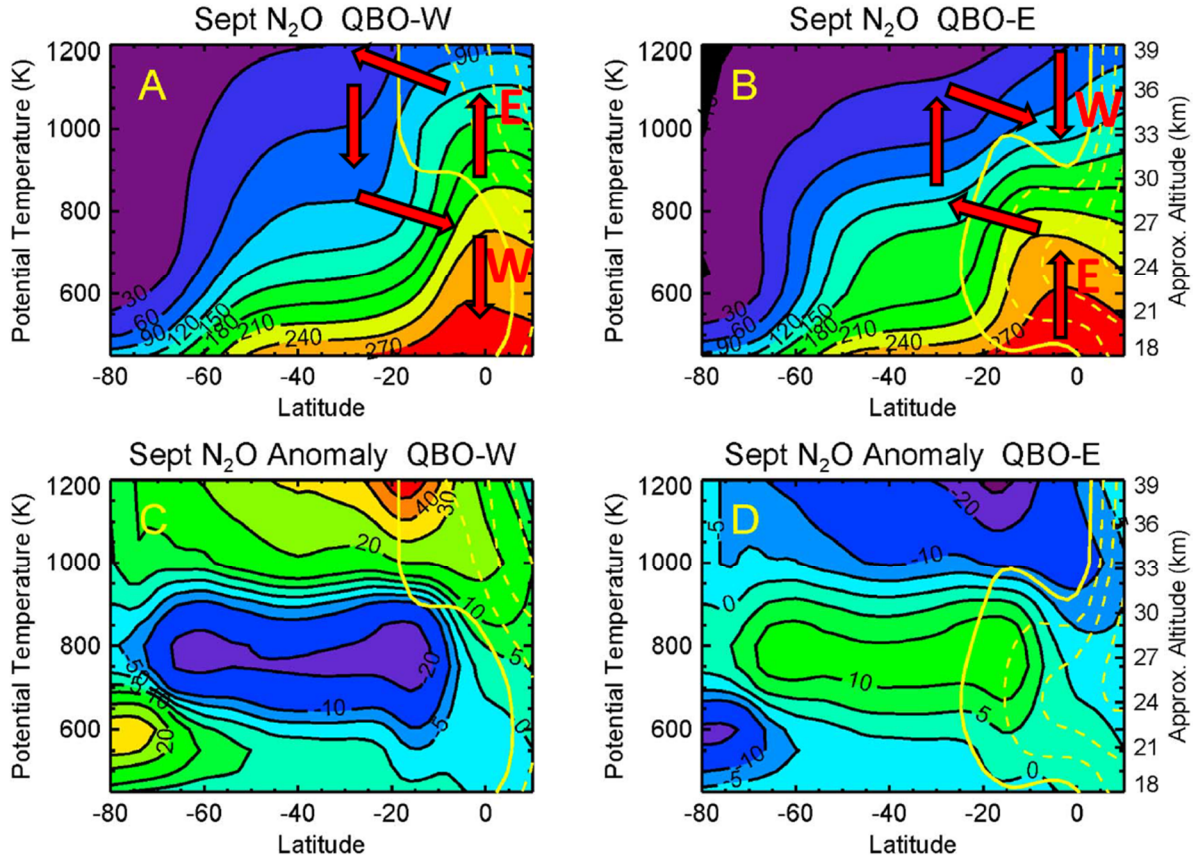

Figure 2- 4: Composites of Microwave Limb Sounder (MLS) September zonal mean N_2O (ppbv) for westerly QBO years (QBO-W, panel A) and easterly QBO years (QBO-E, panel B). Lower panels are the composites of the anomalies associated with QBO westerly and easterly phases for September (panels C and D, respectively). The solid thick yellow line represents the zero wind contour. Easterly zonal winds are shown in yellow dashed lines. Red arrows depict the secondary meridional circulation associated with the QBO phases. From Strahan et al. (2015).

Although the QBO-induced secondary meridional circulation spans the equator to ~30°, we just saw that its effects are depicted at higher latitudes. Strahan et al. (2015) even identified "a transport pathway for QBO-generated trace gas variability to reach the Antarctic lower stratosphere over the course of 1 year". Briefly, the tracer QBO-induced anomalies are mixed and transported in the surf zone (see how the anomalies are "flattened' in Figure 2- 4 C and D). In spring, the Antarctic polar vortex breaks up and the anomaly is further transported to the Antarctic. The next winter, the polar vortex forms again, trapping the anomaly inside. The anomaly finally arrives in the Antarctic lower stratosphere in September, after about 1 year. In the Northern Hemisphere, this transport pathway is less marked than in the Southern Hemisphere. QBO-induced anomalies are also transported in the surf zone and later in the Arctic. However, they do not survive intact during the whole winter as sudden stratospheric

warmings and vortex breakups are more common in the Northern Hemisphere due to the stronger wave activity.

Ploeger and Birner (2016) similarly showed that QBO-induced anomalies were able to persist 2-3 years in the midlatitudes through recirculation in the tropics.

2.4 Observing, modelling and diagnosing the BDC

Observing and diagnosing potential changes in the residual mean circulation as defined by the TEM formalism from direct meteorological observations is still today a challenging task. The difficulty arises from the resulting slow time scale of the TEM residual circulation (on the order of years). Indirect meteorological observations as stratospheric temperatures can, however, be used to diagnose the BDC and its changes (e.g., Fu et al., 2019; and references therein). As this diagnostic of the BDC is indirect and relies on observed stratospheric temperatures, which remain poorly constrained, it does not allow clear conclusions (Ossó et al., 2015). Facing the difficulty to diagnose the BDC from direct meteorological observations, essentially all observational studies rely on indirect measurements of the BDC.

A common diagnostic of the BDC is the age of air. The age of air can be either derived from observations of long-lived tracers or from model simulations. The age of air is the time that a parcel of air takes to be transported from its entry point in the stratosphere (i.e., the tropical tropopause) to a given location in the stratosphere (e.g., Waugh and Hall, 2002). The theoretical concept of the age of air was first proposed by Kida (1983). To derive the age of air from observations, one has to ideally consider a chemical tracer that has a monotonous linear trend at the surface and that has neither sinks nor sources in the middle atmosphere (e.g., Waugh and Hall, 2002; Engel et al., 2009, 2017). Therefore, the chemical species most commonly used to derive the age of air are CO_2 (e.g., Boering et al., 1996; Andrews et al., 2001; Engel et al., 2009, 2017) and SF_6 (e.g., Hall and Waugh, 1998; Engel et al., 2009; Stiller et al., 2012, 2017), even if they do not fulfil completely the ideal requirements. An important aspect of the age of air derived from observations (hereafter observed age of air) is that it includes transport by advection and mixing. In other words, the observed age of air of an air parcel at a given location is not that of an air parcel that would have been only advected; it rather includes the age of other parcels that would have been mixed into the original air parcel. It results that the observed age of air is an average and it is thus commonly referred to as the mean age of air. Atmospheric models, such as chemical-transport models (CTMs), can simulate the age of air from an artificial ideal tracer. Such models do not resolve by themselves the general circulation of the atmosphere and are forced by meteorological fields of reanalyses (see Chapter 3). Consequently, CTMs are appropriate to diagnose the BDC as captured by meteorological reanalyses through age of air simulations. Another advantage that some of CTMs have is that they can separate the individual transit times of fluid elements composing an air parcel and produce a probability density function of their individual transit time, the age of air spectrum. The mean age is related to the full age spectrum as the former is the first moment of the latter. The analysis of the full age of air spectrum is of great interest as it allows for the distinction between transport by advection and the effect of mixing in BDC studies (e.g., Li et al., 2012; Ploeger et al., 2015a, 2015b, 2019).

Beside their utility in the derivation of the age of air, observations of long-lived tracers, with well-known sources and sinks, are also commonly used to diagnose the BDC. The resulting diagnostics are generally rather qualitative but quantitative estimates can however be achieved. One of these

quantitative methods is the well-known water vapour "tape recorder" (e.g., Mote et al., 1996; Minschwaner et al., 2016). Briefly, the annual cycle of the temperature at the tropical tropopause imprints a seasonal cycle in the volume mixing ratios of water vapour entering the stratosphere. Following the imprinted low and high signals of water vapours propagating vertically in the tropical stratosphere, it is possible to derive ascent rates in the tropics and even descent rates outside of the tropics by mass conservation. In addition to the tape recorder methods, studies analysing time-series of long-lived tracers have also successfully detected or confirmed short-term and long-term changes in the BDC. For example, Mahieu et al. (2014) observed an unexpected increase of HCl in the Northern Hemisphere stratosphere from 2007 to 2011, while HCl sources (i.e., mostly CFCs and HCFCs; see Sect. 1.4) were decreasing since about the mid-1990s. They attributed the unexpected increase to a slowing down of the meridional transport in the Northern Hemisphere. We will come back to these BDC changes in Sect. 2.5 below.

The continuous increase of computing power coupled to a better understanding of dynamical and chemical processes of the atmosphere led to the development of a large number of atmospheric models during the last decades. Today, there are two main types of models used to simulate the stratospheric chemistry and dynamics: general circulation models (GCM) and CTMs. GCMs resolve the stratospheric dynamics (generally also including the troposphere) and can be coupled to a chemistry module or to an "on-line" CTM to form a chemistry-climate model (CCM). CCMs are able to produce their own circulation coupled reciprocally to the effect of the atmospheric chemistry. These models tend to reproduce the typical behaviour of the atmosphere but cannot be compared with observations for specific days or years as they are not forced nor nudged towards observations. Thus, their results are compared to observations using climatologies (e.g., seasonal cycle, interannual variability or long-term trends) rather than day to day comparisons. Beside their utility for a better understanding of the climate system, CCMs are also used for climate projections. Using, for example, different greenhouse gas or ODS emission scenarios, it is possible to assess the probable evolution of the global warming or the ozone hole recovery and their coupled effect on the BDC. On the other hand, as already introduced in this section, CTMs do not resolve at all the dynamics of the stratosphere which is actually prescribed to the model. The forcing fields of CTMs are in most cases coming from meteorological reanalyses and these models are therefore convenient for direct comparison with observations. CTMs and meteorological reanalyses are further described in Chapter 3.

2.5 BDC changes

2.5.1 Modelled response to the increase of greenhouse gases

The constant growth of anthropogenic greenhouse gases has modified the radiative budget of the Earth system and, in consequence, undoubtedly induced climate changes (see Sect. 1.1 and Sect. 1.3.1). The radiative effect of the increasing greenhouse gases causes a warming of the troposphere coupled to a cooling of the stratosphere (e.g., IPCC, 2013; Oberländer et al., 2013).

As written in the previous section (Sect. 2.4), a large number of GCMs and CCMs have been developed during the last two decades. Sensitivity tests performed with these models led to one of the most robust result on the impact of growing greenhouse gas concentrations: a projected speed-up of the BDC (Sect. 6.1 in Butchart, 2014, and references therein). Intercomparisons of these studies (e.g., Butchart et al., 2010; Hardiman et al., 2014) showed that the tropical upwelling is projected to speed-up by about 2%

to 3% per decade at 70 hPa, following the medium and the most extreme greenhouse gas concentration scenarios, respectively. A further consistent result, among CCMs, is that the acceleration is occurring in both shallow and deep branches of the BDC and that it is actually stronger in the shallow branches (e.g., Lin and Fu, 2013). Finally, CCMs also simulate a stronger response of the tropical upwelling (and corresponding midlatitudes downwelling) during boreal winter but it remains unclear if this behaviour is not in fact simply driven by the natural seasonality of the BDC (Butchart, 2014; see Sect. 2.2.1 of this chapter for the BDC seasonality).

It is generally accepted that the acceleration of the BDC is a consequence of the tropospheric warming rather than of the stratospheric cooling. As we saw in Sect 2.2, the BDC is primarily driven by the vertical propagation and dissipation of Rossby or gravity waves. Therefore, any change in the BDC strength can directly be attributed to change in the wave drag (Butchart, 2014; see also Sect. 2.2.1 in this chapter). In the troposphere, the global warming, coupled with the stratospheric cooling, causes the tropopause to rise in order for the atmosphere to keep its radiative balance (Santer et al., 2003; Oberländer-Hayn et al., 2016). As a consequence, the subtropical jets are projected, by GCMs, to become stronger and to move upward in response to the climate change, shifting up the critical layer for wave breaking (Shepherd and McLandress, 2011). Rossby waves are thus expected to propagate and break at higher levels, strengthening the BDC at levels above the shifted critical layer. More recently, Oberländer-Hayn et al. (2016) proposed a new interpretation of the conclusion of Shepherd and McLandress (2011): the increase of tropical upward mass flux, projected by GCMs, is actually caused by an upward shift of the BDC, the mass transport in and out of the stratosphere changing a little comparatively. Indeed, as the strength of the overturning circulation decays in height, a rise in the circulation will have an impact on the upward mass flux diagnosed at a fixed pressure level, even if the structure remains otherwise unchanged (Oberländer-Hayn et al., 2016).

The tropical upwelling response to the increase of greenhouse gases has also been investigated through age of air simulations. It is trivial that a BDC speedup leads to decreasing age of air values (see Sect. 2.4). CCMs indeed show decreasing age of air trends for the 21st century (i.e., 2000-2100) in the tropical region as well as in the midlatitudes lower stratosphere (e.g., Li et al., 2012, 2018; Šácha et al., 2019).

2.5.2 Modelled response to ozone depletion and recovery

In chapter 1 (Sect. 1.4 and Sect. 1.5), we saw that ODSs were successfully phased out by the Montreal Protocol on Substances that Depletes the Ozone Layer. As a direct consequence, the ozone layer recovery is expected to occur during the twenty-first century (WMO, 2018). As we also saw in Chapter 1 (Sect. 1.3.2), the ozone layer warms the stratosphere and has, thus, a significant influence on its radiative equilibrium. Therefore, any change in ozone abundances in the stratosphere (depletion and recovery) is expected to impact the dynamics of the BDC.

CCMs indeed simulate a BDC response to the formation of the Antarctic ozone hole in the second half of the twentieth century, with an acceleration of the circulation pairing with decreasing age of air values (Oman et al., 2009; Oberländer-Hayn et al., 2015; Garfinkel et al., 2017; Polvani et al., 2017, 2018, 2019; Li et al., 2018; Morgenstern et al., 2018; Abalos et al., 2019). Moreover, as the global ozone depletion caused by ODSs is asymmetric (due to the Antarctic ozone hole, see Sect. 1.5.1), most of the simulated BDC changes are occurring in the Southern Hemisphere. Accounting for the forcing of both the greenhouse gas and ODS increases, the studies cited in this paragraph further show that ODSs,

through the depletion of the ozone layer, have contributed to about the half of the BDC acceleration in the twentieth century.

With the recovery of the ozone layer, which is expected to occur in the twenty-first century, CCMs project a slowing down of the BDC (Oman et al., 2009; Polvani et al., 2018, 2019). The forcing of the ozone layer recovery will be thus opposed to that of the increase of greenhouse gases (Sect. 2.5.1 above). The forcing of the ozone hole recovery is expected to reduce by a factor of two the greenhouse gas-induced speeding up of the BDC. However, the degree of cancellation between the two forcings will very likely depend on the true evolution of ODS and greenhouse gas concentrations, compared to the scenarios used to perform the CCM projections (Polvani et al., 2019). Finally, as for the depletion period, most of the changes, due to the ozone recovery, are depicted in the Southern Hemisphere, causing hemispheric asymmetries, with the age of air of the Southern Hemisphere decreasing much less than that in the Northern Hemisphere (Polvani et al., 2018, 2019).

2.5.3 Observed long-term changes

In this section, a short review of the observed changes of the BDC is given. The section primarily focuses on BDC global changes related to the forcings of greenhouse gases and ODSs. Here we include observations of stratospheric temperatures and of long-lived tracers (including their use to derive the age of air). Furthermore, we also consider BDC changes as captured by meteorological reanalyses. Indeed, these latter should represent the true state of the atmosphere and its evolution (see also Chapter 3).

From lower-stratospheric temperature data, as retrieved from satellite measurements, a body of studies found observational evidence of a long-term strengthening of the BDC (see Fu et al., 2015, and references therein). However, it has not been clear if these observed changes of the BDC, and their hemispheric contributions, are statistically significant (Fu et al., 2015). More recently, Fu et al. (2019) analysed lower-stratospheric temperatures retrieved from measurements of the Microwave Sounding Unit (MSU/AMSU) satellite for the period 1980-2018. The longer measurement period allowed the authors to further consider two long-term periods of almost 20 years each: 1980-1999 and 2000-2018. To assess the dynamical effect of the BDC on the observed lower-stratospheric temperature changes, Fu et al. (2019) also included eddy heat fluxes taken from the European Centre for Medium-Range Weather Forecasts Interim reanalysis (ERA-Interim; Dee et al., 2011). The authors concluded that the BDC has accelerated for the 1980-2018 period, with statistically significant changes (90% confidence) in the Northern Hemisphere. They furthermore concluded that the BDC has accelerated over 1980-1999 and decelerated over 2000-2018, periods considered by these authors as periods of ozone depletion and recovery, respectively. They also evaluated the hemispheric contribution and showed that, for both periods, most of the change was coming from the Southern Hemisphere, although the trends were not significant at the 90% confidence level. Finally, Fu et al. (2019) also empirically determined the relative acceleration of the BDC in terms of tropical residual vertical velocity at 70 hPa (applying the method of Fu et al., 2015) and found an acceleration of 1.7% per decade. Globally, the results of Fu et al. (2019) are in good agreements with CCM projections in response to the coupled effect of greenhouse gases and ODSs (Polvani et al., 2018, 2019; see Sect. 2.5.2 above).

The longest time-series of observed age of air (i.e., derived from observations of long-lived tracers; see Sect. 2.4) covers the 1975-2016 period (Engel et al., 2009, 2017). It comprises 28 balloon-borne

measurements of SF_6 and CO_2 for the 1975-2005 period. These measurements are representative of altitudes between 24 km and 35 km and of latitudes between 32°N and 51°N. From the 1975-2005 period, Engel et al. (2009) estimated a small but not statistically significant positive trend of 0.24 years per decade. Including five additional balloon-borne "AirCore" (see Karion et al., 2010; Membrive et al., 2017) measurements for the years 2015 and 2016, Engel et al. (2017) expended the 1975-2005 period to 2016 and found a smaller and not statistically significant trend of 0.15 years per decade. In conclusion, trends estimated from this age of air time-series sustain that there is no significant change in mean age of air for the Northern Hemisphere midlatitudes above 24 km (Engel et al., 2017). This result does confirm the BDC acceleration in the Northern Hemisphere as derived from observed lower-stratospheric temperatures (Fu et al., 2019) and simulated by CCMs (Butchart, 2014, and references therein). However, a direct comparison with the study of Fu et al. (2019) is not evident as the MSU/AMSU measurements are sensitive to the lower stratosphere. Moreover, the results of Engel et al. (2009, 2017) do not exclude a strengthening of the tropical upwelling if the latter has resulted in an enhanced BDC in the lower stratosphere only (Engel et al., 2009). Finally, the sparsity of this age of air dataset, inherent to balloon-borne monitoring, should be addressed. Indeed, if the time-series spans 42 years, it includes around thirty profiles representative of the middle stratosphere of the Northern Hemisphere midlatitudes (32°N to 51°N), with a gap of ten years between 2005 and 2015. It was thus argued that the sparsity of the sampling, coupled to the large internal variability of the BDC, could have hindered any trend detection (e.g., Garcia et al., 2011; Hardiman et al., 2017).

Age of air trends were also derived from SF_6 Michelson Interferometer for Passive Atmospheric Sounding (MIPAS) satellite data (Stiller et al., 2012, 2017; Haenel et al., 2015). These global measurements compensated the limited spatial coverage of the balloon-borne measurements of Engel et al. (2009, 2017). The age of air time-series derived from MIPAS is, however, limited to the lifetime of MIPAS (2002-2012). For this period, the age of air trends showed opposite values for the two hemispheres, with positive values for the Northern Hemisphere and negative values for the Southern Hemisphere. Remarkably, the age of air trends for the Northern Hemisphere were well in agreement with those reported by Engel et al. (2009). It is however important to note that the periods considered in these studies are quite different, with only 4 overlapping years. We will particularly see that the short-term period associated with MIPAS age of air time-series is very strongly influenced by a large interannual variability of the BDC (see Sect. 2.5.4).

Recently, Strahan et al. (2020) analysed long time-series (1994-2018) of ground-based and satellite observations of HCl and nitric acid (HNO_3) as well as a CTM simulation driven by MERRA-2 (Modern-Era Retrospective analysis for Research and Applications-2; Gelaro et al., 2017). From these measurements and the CTM simulation, they derived age of air trends. They concluded that the Southern Hemisphere age of air is getting younger by about 1 month per decade compared to that of the Northern Hemisphere for the period 1994-2018. This decreasing age of air trend could correspond to an acceleration of the BDC in the Southern Hemisphere which would be in contrast with the projections of CCMs (Polvani et al., 2018, 2019; see Sect. 2.5.2 above) and the stratospheric temperature study of Fu et al. (2019).

Recent studies employing CTMs also evaluated long-term trends of age of air derived from modern meteorological reanalyses for the period 1989-2015 (Chabrillat et al., 2018; Ploeger et al., 2019). The reanalyses compared were: ERA-Interim (Dee et al., 2011), the Japanese Meteorological Agency's

Japanese 55-year Reanalysis (JRA-55; Kobayashi et al., 2015), MERRA (Rienecker et al., 2011; not included in Ploeger et al., 2019) and MERRA-2 (Gelaro et al., 2017). The study of Ploeger et al. (2019), comparing ERA-Interim, JRA-55 and MERRA-2, showed similar results as CCM studies, with a global decrease of the age of air in the lower stratosphere. However, Chabrillat et al. (2018) found larger disagreements between reanalyses for the same period, precluding any robust conclusions regarding the effect of the greenhouse gas increase. The different results between the two studies are certainly due to the different type of transport model used. In fact, Chabrillat et al. (2018) used a kinematic transport model (see Chapter 3) directly driven by the surface pressure and horizontal wind fields of the reanalyses while Ploeger et al. (2019) used a diabatic model driven also by the heating rates of the reanalyses. It suggests that the reanalysis wind fields are insufficiently constrained by observations in the compared reanalyses, particularly before 2000 (Chabrillat et al., 2018).

2.5.4 Short-term interannual variability

In Section 2.5.3 above, we saw that age of air trends computed over a shorter period (2002-2012) showed opposite hemispheric values, with the age of air increasing in the Northern Hemisphere and decreasing in the Southern Hemisphere (Stiller et al., 2012, 2017; Haenel et al., 2015). A few years after the first results of Stiller et al. (2012), Mahieu et al. (2014) noted an unexpected increase in HCl total columns from 2007 to 2011 in the Northern Hemisphere. Their analysis was based on time-series of ground-based FTIR and satellite measurements and on CTM simulations driven by ERA-Interim. They attributed this increase to circulation changes, i.e., to a deceleration of the BDC in the Northern Hemisphere, as a CTM simulation with perpetually repeating dynamics did not show any positive trends in the time-series. This dipole structure in trends of long-lived tracers (i.e., opposite hemispheric values) was later depicted for N_2O (Nedoluha et al., 2015; Stiller et al., 2017), O_3 (Nedoluha et al., 2015), HF (Harrison et al., 2016), HCFC-22 (Chirkov et al., 2016) and carbonyl sulphide (OCS; Glatthor et al., 2017).

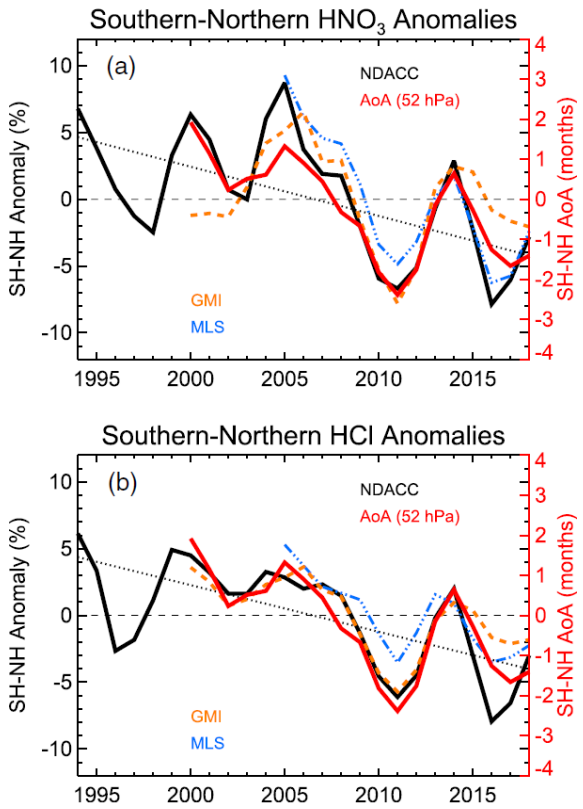

Figure 2- 5: "NDACC ground-based FTIR (black), Microwave Limb Sounder (blue), and Global Modeling Initiative CTM (GMI CTM; orange) interhemispheric difference (Southern Hemisphere – Northern Hemisphere) for (**a**) HNO_3 and (**b**) HCl anomaly time series. The interhemispheric difference of GMI CTM age of air at 52 hPa (red) is plotted in each panel (see the right axis). The dashed line shows the linear trend for the NDACC anomalies". From Strahan et al. (2020).

The results of the recent study of Strahan et al. (2020) also place the previously reported dipole trends in a longer context where a 5-to-7-year BDC interannual variability drives large interhemispheric anomalies in time-series of age of air and of long-lived tracers (Figure 2- 5). The reported hemispheric asymmetry in 2005-2012 in Mahieu et al. (2014) and Stiller et al. (2017) is, for example, located between a large positive interhemispheric anomaly, peaking around 2005 (i.e., older age of air in the Southern Hemisphere relative to the Northern Hemisphere), and a large negative one, peaking around 2011-2012 (younger age of air in the Southern Hemisphere relative to the Northern Hemisphere).

At the present time, there is no clear consensus on what causes the observed and modelled hemispheric asymmetries. While Stiller et al. (2017) showed that a 5° southward shift of the tropical transport barriers could be the cause, Strahan et al. (2020) attributed the hemispheric asymmetries to a variability in the BDC driven by an interaction between the BDC annual cycle and the quasi-biennial oscillation (QBO). This multiyear variability was previously described by Ploeger and Birner (2016) to explain age of air spectrum anomalies in the midlatitude lower stratosphere and may also explain the N_2O and HCl anomalies highlighted in previous works of Strahan et al. (2014 and 2015). Assessing the respective contribution of residual circulation and mixing has also led to conflicting results. Han et al. (2019) found that eddy mixing has a negligible impact on circulation changes compared to the residual circulation and furthermore stated that the southward shift of the upwelling region only partly explains the hemispheric asymmetry. In contrast, Ploeger et al. (2015a) showed that age of air changes (2002-2012) are the result of combined effects of residual circulation and mixing and that the latter is crucial to explain the mean age trends, particularly above 20 km.

2.6 Chapter conclusions

From the short state of the art of observed and modelled BDC changes given in this chapter, we can retain several important conclusions that motivate this research.

While an overall acceleration of the BDC is robustly projected by CCMs in response to the evolution of greenhouse gases and ODSs, trends derived from observations have given contrasted results. It appears that conclusions regarding observed trends highly depend on (1) the type of data considered (lower-stratospheric temperature, observed age of air, long-lived tracers) and (2) the period considered to assess these trends. Moreover, while meteorological reanalyses should represent the true state of the atmosphere and, therefore, provide a good help in the assessment of BDC changes, the substantial differences in age spectra and mean ages among the reanalyses lead to significant uncertainty in their trends.

In consequence, it is still today a challenging task to diagnose the BDC and its changes from observational datasets and, therefore, confirm the CCM simulated changes. Yet, it is important that these models correctly represent the historical climates because these same models are used to project the evolution of the global surface temperature and the health of the ozone layer as greenhouse gases increase and ODSs decrease.

It thus appears that studies based on long-term observations of long-lived tracers, as we propose in this work, are needed to investigate the BDC changes and assess how modern CCMs are performing.

2.7 Objectives and thesis outline

Facing the problematics evoked in these two introductory chapters, we define the **general objective** of this thesis:

Investigate the recently reported BDC changes, including the long-term change and the interannual variability, through an analysis of long-term time-series of observations and CTM simulations of inorganic fluorine.

The observational datasets include ground-based and satellite FTIR measurements. The simulations are performed by the Belgian Assimilation System for Chemical ObsErvations CTM (BASCOE CTM; e.g., Skachko et al., 2016; Chabrillat et al., 2018; Errera et al., 2019). We use BASCOE CTM to evaluate how the observed BDC changes are captured by the main modern reanalyses (see Chapter 3) through their impact on simulated inorganic fluorine time-series. It is the first time that BASCOE CTM is used to perform such long-term historical experiments aiming at the accurate simulation of a long-lived tracer. Therefore, some preliminary evaluations are necessary. To this end, we define a **preliminary objective**:

Develop and evaluate an improved retrieval strategy of HCFC-22, the second source of total inorganic fluorine and by far the most abundant HCFC. Outside the context of the Montreal Protocol, this objective will allow for a first evaluation of our BASCOE CTM simulation set-up regarding a tropospheric source.

Chapter 3

BASCOE CTM and driving reanalyses

CTMs are able to simulate both the effects of chemistry and transport on atmospheric chemical constituents. Unlike GCMs, these models do not solve by themselves the primitive equations of the atmosphere dynamics and, hence, do not resolve the atmospheric circulation. CTMs may be coupled to GCMs in an on-line configuration in order to resolve the chemistry and transport of the atmosphere as the GCM resolves the dynamics. Such a configuration forms a CCM. CTMs can also run in an off-line configuration in which the meteorological fields driving the CTM are pre-calculated by a GCM or are taken from a meteorological reanalysis. Driving a CTM by reanalyses allows for a direct comparison between the observed and simulated distributions of chemical tracers. Indeed, these distributions should reflect the transport as it is truly assimilated by reanalyses. In this work, BASCOE CTM is driven by meteorological reanalyses.

Section 3.1 describes the meteorological reanalyses used to drive BASCOE CTM for this work. Section 3.2 describes the BASCOE CTM transport algorithm. Section 3.3 describes the simulation set-up and the developments which were needed to perform our experiments. Finally, Section 3.4 offers a preview of the F_y simulations that are used and discussed in Chapters 5 and 6.

3.1 Meteorological reanalyses of the atmosphere

To produce the best estimates of past atmospheric states, e.g.., temperature, wind, geopotential height and humidity, a meteorological reanalysis combines observations of these fields, a global forecast model and an assimilation scheme. The forecast model, starting from an initial state or a previous analysis (t_0), propagates information forward in time and space (to t_1). The assimilation scheme then blends the model forecast with observations to produce a new analysis at time t_1 (Fujiwara et al., 2017). The loop starts again with the new analysis used as the initial condition of the next forecast. The difference between the forecasted first-guest and the resulting analysis is defined as the analysis increment. The latter is applied to the forecasted first-guest in order to adjust it closer to the observations. The methods calculating and applying the analysis increment can be seen as the core strategies of the different assimilation methods employed by reanalyses. Table 3- 1 summarizes the basic specifications of the reanalyses used in this work.

Table 3- 1. Basic specifications of the reanalyses used in this work. See Sect. 3.1.1 for the assimilation scheme description.

	Vertical levels, top level	Horizontal grid resolution	Assimilation scheme	Reference
ERA-Interim	60, 0.1 hPa	~79 km	Incremental4D-Var	Dee et al. (2011)
ERA5	137, 0.01 hPa	~31 km	Incremental 4D-Var 10 member-ensemble	Hersbach et al. (2020)
JRA-55	60, 0.1 hPa	~55 km	Incremental 4D-Var	Kobayashi et al. (2015)
MERRA	72, 0.01 hPa	0.5° lat. × 2/3° lon. ~56 km × ~74 km	3D-FGAT + IAU	Rienecker et al. (2011)
MERRA-2	72, 0.01 hPa	0.5° lat. × 0.625° lon. ~56 km × ~69 km	3D-FGAT + IAU	Gelaro et al. (2017)

3.1.1 Assimilation methods

Modern reanalysis systems employ different assimilation methods which may be, at least in part, responsible for the differences depicted between reanalyses (see Sect. 2.5.3). As introduced in this section, an atmospheric analysis includes data from observational datasets and from variables given by a forecasted first-guest background state. Both the observations and the background state may include errors and uncertainties, hence the analysis system should account for the latter when minimizing the differences between the analysis and the true state of the atmosphere. Moreover, analysis systems may ensure consistency with known or assumed physical properties (e.g., hydrostatic or geostrophic balance; Fujiwara et al., 2017). Three different assimilation methods are employed in the reanalyses included and compared in this work (see Table 3- 1). All three methods are based on the variational method. Such a method can be seen as a minimization of a cost function representing the differences between the observations and the background state, taking into account the associated uncertainties. As summarized in Table 3- 1, MERRA and MERRA-2 use a three-dimensional variational assimilation (3D-Var), ERA-Interim, JRA-55 and ERA5 use a four-dimensional variational assimilation (4D-Var). The main difference between these two methods lays in the way observations are handled in the assimilation window used to produce an analysis state and to further compute the analysis increment. The assimilation window is the time window, most often centered at the analysis time, defining the observations influencing the analysis. Bellow follows a cursory overview of these methods (as described in Fujiwara et al., 2017).

3.1.1.1 3D-Var as implemented in MERRA and MERRA-2

In a classic 3D-Var assimilation, the system calculates and applies the analysis increment at discrete analysis times (e.g., 00h, 06h, 12h, 18h). All observations comprised in the analysis window are treated as if they were valid at the analysis time (eventually weighted by the temporal distance). MERRA and MERRA-2 employ a modified 3D-Var method. Indeed, the system evaluates the analysis increment at observation times, rather than at analysis times, through interpolation techniques. This method is referred to as the 3D-FGAT (first guest at the appropriate time). In MERRA and MERRA-2, the products generated strictly following the 3D-FGAT method are labelled “ANA” (“analysis state”). Along with the ANA products, MERRA and MERRA-2 provide a second type of products, unique in reanalysis

systems: the ASM products ("assimilated state"). In this system, the analysis increments (still computed at discrete times) is applied gradually to the forecast model as a tendency term (i.e., forcing term) in the model's equations. This corrector segment, or corrector simulation, is performed 3 hours before analysis time, from a previous saved model state, to 3 hours after. The model is then freely run (i.e., without the incremental forcing) for 3 more hours to the next analysis time (Bloom et al., 1996; Rienecker et al., 2011). This method, the "incremental analysis update" (IAU), presents the major advantage to apply more smoothly the analysis increment to the forecast model compared to other assimilation methods. Ultimately, the MERRA and MERRA-2 ASM products allow for the forecast model to be more consistent with the observations while reducing wind and tracer spurious changes. For this reason, we use MERRA-2 ASM (rather than ANA) products to force BASCOE CTM in this work. For MERRA, the ASM products are only given on constant pressure levels. As we use the native hybrid sigma-pressure vertical grids of reanalyse, we, consequently, use the ANA products of MERRA.

3.1.1.2 4D-Var as implemented in ERA-Interim and JRA-55

In opposition to the 3D-Var methods, a 4D-Var system computes and applies the analysis increment within the full assimilation window and not only at analysis time. However, these systems are vastly more resource consuming than 3D-Var methods and their full implementation remains impossible at present. In the face of this issue, ERA-Interim, JRA-55 and ERA5 employ a simplified incremental 4D-Var method (Courtier et al., 1994). The main objective of a 4D-Var strategy is to iteratively adjust the initial state of the forecast model at the beginning of the assimilation window in order to obtain progressively better fits between the model's trajectory and the observations comprised in the window. It is those iterations, i.e., adjusting the model initial state and evaluating the quality of the fit between the latter and the observations, that are time consuming. In the simplified incremental method, the successive iterations are performed with the same model but using simplified physics on a coarser grid. Once the iteration process has converged, the model state is computed again but using this time the fine resolution and the model full physics.

3.1.1.3 4D-Var ensemble in ERA5

ERA5, the latest reanalysis of the ECMWF, implements the same incremental 4D-Var method. It is of course improved in numerous ways compared to the former reanalysis ERA-Interim (see Hersbach et al., 2020). One of the key improvements is that the assimilation system now provides estimates of analysis and short-range forecast uncertainty, i.e., uncertainties in the reanalysis product. It is achieved through an ensemble component of one control and nine perturbed members. The analysis method is the same for the 10 members of the ensemble. The perturbation method consists in the application of random perturbations to the observations and to the model tendencies. Finally, the resulting spread among the ensemble members is used to assess the uncertainty of the assimilation method.

3.1.2 Reanalysis preprocessing for BASCOE CTM

The transport module of BASCOE CTM (described in Sect. 3.2) requires the input reanalysis fields to be staggered on a relatively low resolution Arakawa-C grid (2°×2.5° latitude-longitude) while the native vertical grid of each reanalysis is kept. In consequence, a pre-processing method to carefully transfer the reanalysis spectral or high resolution fields to the low horizontal grid is needed. Moreover, data assimilation processes used in the elaboration of reanalyses may lead to dynamical imbalances or

spurious surface pressure increments that may, in turn, cause serious deteriorations of the BDC (Chabrillat et al., 2018 and references therein). This step is of crucial importance for the reanalysis comparison conducted in Chapter 6 as we must be sure that the wind fields of the different reanalyses are expressed in a consistent manner for the transport algorithm of BASCOE. The pre-processor used for BASCOE filters out these dynamical imbalances by evaluating the zonal and meridional wind fields on the low resolution grid directly from the primitive variables of the spectral dynamical cores (i.e., vorticity and divergence) while correcting for inconsistencies in the pressure increments compared with the divergence fields. This pre-process is directly applied on ERA-Interim (for which the method was originally developed) and ERA5 spherical harmonic coefficients of vorticity, divergence and surface pressure. For the other reanalyses (JRA-55, MERRA and MERRA-2), we first have to derive these coefficients. For all reanalyses, the spectral coefficients are truncated at wave number 47 to avoid aliasing on the lower resolution grid.

3.2 BASCOE advection module

The advection module of BASCOE CTM is the flux-form semi-Lagrangian (FFSL) scheme (Lin and Rood, 1996).

Lagrangian models solve the advection transport by tracking the tracer particles as they are transported in the atmosphere, i.e., the reference frame is moving with the particles. On the other hand, Eulerian models solve the advection transport on a fixed reference grid, resolving the net transport between entering and exiting tracer quantities. Both approaches have inherent advantages and disadvantages. Eulerian models have regular spatial grids over the entire simulation domain, facilitating result analysis, but are more subject to numerical noise and stability constraints. Lagrangian models do not have such limits but their spatial grids are uneven and the models accumulate errors as the particles are moving away from their original position. Consequently, Lagrangian models are not suited for long-term global simulations. Facing these issues, semi-Lagrangian transport methods, combining advantages of both Eulerian and Lagrangian models, were developed.

In semi-Lagrangian models, the transport algorithm computes backward Lagrangian trajectories of the particles that have reached the Eulerian grid points at time t_{n+1}. The FFSL algorithm, used by BASCOE CTM, is based on a finite volume scheme schematized in Figure 3- 1. Considering a cell of a 2-dimension Eulerian grid at time t_{n+1}, the algorithm computes the backward trajectory of the entire cell to retrieve its position at time t_n. The total mass or mean density of a transported tracer at time t_{n+1} is the one of the retrieved surface at time t_n. As the original volume is distorted by the wind fields during the transport, the method requires interpolation and remapping to derive the tracer quantity in the volume at t_n.

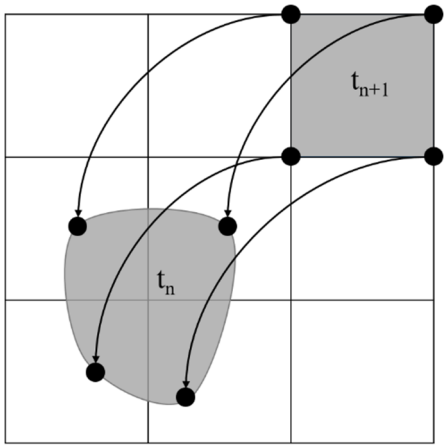

Figure 3- 1. Schematic representation of a finite volume semi-Lagrangian advection scheme. Black arrows represent Lagrangian backward trajectories. Grey areas represent the finite volume (or surface in this 2D case) that is advected to the upper right pixel at time t_{n+1}. Reproduced from Brasseur and Jacob (2017).

The major difference between the semi-Lagrangian and the flux-form semi-Lagrangian transport schemes (SLT and FFSLT, respectively) is that the former does not respect mass conservation inherently. Indeed, the interpolation and remapping steps in the SLT scheme cause mass imbalances which must be fixed to avoid spurious drifts of total tracer mass in multidecadal CTM simulations. Hence SLT schemes require "mass fixers", i.e., numerical workarounds that enforce mass conservation but usually introduce unrealistic long-distance compensations in the tracer distributions (Jablonowski and Williamson, 2011). The FFSLT scheme was designed to address this issue by applying the SLT approach to mass fluxes rather than gridpoint trajectories, thereby inherently ensuring mass conservation.

One important limitation of the FFSL is that, to conserve the mass, the driving winds of the CTM should originate from a GCM where the exact same scheme was applied to solve the equation of momentum (Brasseur and Jacob, 2017). In the case of our off-line configuration, driven by various reanalyses, this is not achievable. Moreover, the analysis increment applied to the dynamical model state in order to match the actual observations (see Sect. 3.1.1) does not respect mass balance (Meijer et al., 2004). In the face of this issue, one may also use a mass or pressure fixer that modifies the horizontal mass fluxes so that they are consistent with the model pressure tendency (e.g., Horowitz et al., 2003). However, this correction may also induce non-physical transport or violate the monotonicity requirement of an advection model (i.e., generate spurious changes of tracer quantities; Brasseur and Jacob, 2017). For BASCOE-CTM, it is the preprocessor of reanalysis high-resolution fields described in the section above (Sect. 3.1.2) that handles the mass conservation by filtering out the inconsistencies brought by the assimilation system of the reanalyses.

The FFSL advection algorithm implemented in BASCOE CTM only requires horizontal winds staggered on a regular horizontal grid. The vertical advection is derived from mass conservation only. Furthermore, it is also important to note that BASCOE CTM does not explicitly represent convection or horizontal diffusion.

3.3 Simulation set-up and model developments

It is the first time that BASCOE CTM is used to perform multidecadal simulations aiming at the accurate modelling of a long-lived tracer such as F_y. Before this project, BASCOE has been mostly used

to perform reanalyses of the stratospheric chemical composition (e.g., Skachko et al., 2016; Errera et al., 2019) or long-term simulations of mean age of air (Chabrillat et al., 2018). Therefore, efforts were made during this PhD thesis to achieve accurate F_y simulations. Here follows a description of the three main developments carried out to this end.

3.3.1 Update of the chemical scheme

The original chemical scheme implemented in BASCOE CTM (version *sb15*), from which we started our developments, was most recently thoroughly described in Ménard et al. (2020). This scheme models the chemistry of the stratosphere solely. In the troposphere, species vulnerable to the oxidation by OH (e.g., HCFCs and HFCs) react through a simple parametrization, using an OH climatology described in Spivakovsky et al. (2000). This parametrization was added just before the start of this PhD project. The chemical scheme includes gas-phase, photolysis and heterogeneous reactions (e.g., chlorine activation on surface of PSCs).

As this research focus on the evolution of inorganic fluorine and one of its main current source, HCFC-22, a particular attention was given to the chemistry related to these species. A first inspection of the chemical scheme showed that some important inorganic fluorine sources and their corresponding degradation schemes were missing. In the original scheme, the included fluorine inorganic sources were CFC-11, CFC-12, CFC-113, CFC-114, CFC-115, HCFC-22, halon-1211 and halon-1301. To support our choice on the species to add, we made use of the lower boundary conditions (LBC) for gas concentrations (see Sect. 3.3.2 below). Major contributors to the total organic fluorine budget (i.e., the sum of fluorine source concentrations weighted by the number of fluorine atoms; CF_y) were thus inspected for two different months, December 1984 (first month of our simulations) and December 2014 (end of the original LBC dataset; see Sect. 3.3.2 below). From this analysis, it was decided to add HFC-134a (~10% of CF_y in December 2014), HFC-23 (~3%), HFC-125 (~2%), HFC-143a (~1%), HCFC-141b (~1%), HCFC-142b (~1%) and halon-2402 (~1%).

Along with these 7 new species, we added 18 gas-phase and 7 photodissociation reactions. Furthermore, we updated the chemical and photodissociation reaction rates of all CF_y species following the Jet Propulsion Laboratory compilation No. 18 (Burkholder et al., 2015b). The chemical scheme updated for this research now includes 65 chemical species interacting through 174 gas-phase reactions, 9 heterogeneous reactions and 60 photolysis reactions (version *sb17c*). The reactions of fluorinated species are provided in Table 3- 2.

Table 3- 2: Reactions implemented in BASCOE CTM for this research (*sb17c* chemical scheme). F_y is the total inorganic fluorine (see Eq. 1.38). The reaction between F_y and $O(^1D)$ was originally implemented for HF.

Gas-phase and photodissociation reactions* for fluorinated species in BASCOE CTM	
CFC-11 + $O(^1D) \rightarrow 3Cl + F_y$	CFC-11 + $h\nu \rightarrow 3Cl + F_y$
CFC-12 + $O(^1D) \rightarrow 2Cl + 2F_y$	CFC-12 + $h\nu \rightarrow 2Cl + 2F_y$
CFC-113 + $O(^1D) \rightarrow 3Cl + 3F_y$	CFC-113 + $h\nu \rightarrow 3Cl + 3F_y$
CFC-114 + $O(^1D) \rightarrow 2Cl + 4F_y$	CFC-114 + $h\nu \rightarrow 2Cl + 4F_y$
CFC-115 + $O(^1D) \rightarrow Cl + 5F_y$	CFC-115 + $h\nu \rightarrow Cl + 5F_y$
HCFC-22 + $O(^1D) \rightarrow Cl + 2F_y$	HCFC-22 + $h\nu \rightarrow Cl + 2F_y$
HCFC-141b + $O(^1D) \rightarrow 2Cl + F_y$	HCFC-141b + $h\nu \rightarrow 2Cl + F_y$
HCFC-142b + $O(^1D) \rightarrow Cl + 2F_y$	HCFC-142b + $h\nu \rightarrow Cl + 2F_y$
HFC-23 + $O(^1D) \rightarrow 3F_y$	HFC-23 + $h\nu \rightarrow 3F_y$
HFC-125 + $O(^1D) \rightarrow 5F_y$	HFC-125 + $h\nu \rightarrow 5F_y$
HFC-134a + $O(^1D) \rightarrow 4F_y$	HFC-134a + $h\nu \rightarrow 4F_y$
HFC-143a + $O(^1D) \rightarrow 3F_y$	HFC-143a + $h\nu \rightarrow 3F_y$
Halon-1211 + $O(^1D) \rightarrow Br + Cl + 2F_y$	Halon-1211 + $h\nu \rightarrow Br + Cl + 2F_y$
Halon-1301 + $O(^1D) \rightarrow Br + 3F_y$	Halon-1301 + $h\nu \rightarrow Br + 3F_y$
Halon-2402 + $O(^1D) \rightarrow 2Br + 4F_y$	Halon-2402 + $h\nu \rightarrow 2Br + 4F_y$
HCFC-22 + OH $\rightarrow Cl + 2F_y + H_2O$	$F_y + O(^1D) \rightarrow$ OH (see caption)
HCFC-22 + Cl $\rightarrow Cl + 2F_y + HCl$	
HCFC-141b + OH $\rightarrow 2Cl + F_y + H_2O$	
HCFC-141b + Cl $\rightarrow 2Cl + F_y + HCl$	
HCFC-142b + OH $\rightarrow Cl + 2F_y + H_2O$	
HCFC-142b + Cl $\rightarrow Cl + 2F_y + HCl$	
HFC-23 + OH $\rightarrow 3F_y + H_2O$	
HFC-125 + OH $\rightarrow 5F_y + H_2O$	
HFC-125 + Cl $\rightarrow 5F_y + HCl$	
HFC-134a + OH $\rightarrow 4F_y + H_2O$	
HFC-134a + Cl $\rightarrow 4F_y + HCl$	
HFC-143a + OH $\rightarrow 3F_y + H_2O$	
HFC-143a + Cl $\rightarrow 3F_y + HCl$	

* Note that these reactions are not closed, they only yield the products that are implemented and handled in the chemical scheme of BASCOE.

From Table 3- 2, we see that the inorganic fluorine chemistry, as implemented in the chemical scheme of BASCOE, is rather simplified. Indeed, the degradation of CF_y species directly leads to a total inorganic fluorine tracer F_y (see Eq. 1.38) and HF, COF_2 and COClF reservoirs are not part of the photochemistry scheme of BASCOE CTM.

3.3.2 Lower boundary conditions

As our simulations will be directly compared to observations and used to investigate observed circulation changes, we need the model lower boundary to be driven by consistent source gas

concentrations derived from accurate observations. With this respect, we use the "Historical Greenhouse Gas Concentrations" (HGGC) dataset described in Meinshausen et al. (2017). This dataset compiles in situ surface measurements performed in the framework of the Advanced Global Atmospheric Gases Experiment (AGAGE) and NOAA networks. It also includes firn and ice core measurements, and other published datasets. This dataset was produced for the Coupled Model Intercomparison Project Phase 6 (CMIP6) and more specifically for the historical experiments. Therefore, Meinshausen et al. (2017) focused their work on the period 1850-2014 but they also provide surface concentrations for 2000 years in the past. Furthermore, the dataset is latitudinally and seasonally resolved. At the beginning of our research in 2016, it was decided that BASCOE CTM would be run over the 30-year period 1985-2014. However, with time passing, it appeared that the extension of the original simulation period to the end of the ERA-Interim reanalysis (August 2019) would be necessary to properly investigate the BDC changes. By then, an extension of the HGGC dataset was produced and described in Meinshausen et al. (2020). This dataset extends the HGGC dataset using AGAGE and NOAA measurements for the years 2015, 2016 and 2017. For the period 2018-2100, it uses shared socio-economic pathway (SSP; established in the framework of CMIP6) emission scenarios to project greenhouse gas surface concentrations. For ODSs, the future concentrations are assumed to follow the baseline scenario A1 as given in WMO (2014).

We use, the "middle of the road" SSP2-4.5 scenario. Nevertheless, the choice of the scenario does not induce large changes in surface concentrations as we only make use of it for the years 2018 and 2019 (August). Indeed, Figure 3- 2 shows that there is only a, if any, negligible spread among the surface concentration time-series following the nine SSPs. However, HFC-134a shows a larger spread (Figure 3- 2), the lower limit is due to the SSP4 "inequality" scenarios which are much lower than the others (not shown). Considering that the difference between the scenarios is relatively small (less than 5% in 2019) and that it is only depicted for less than two years, we assume that our LBC is reasonably well driven during the 2015-2019 extension period.

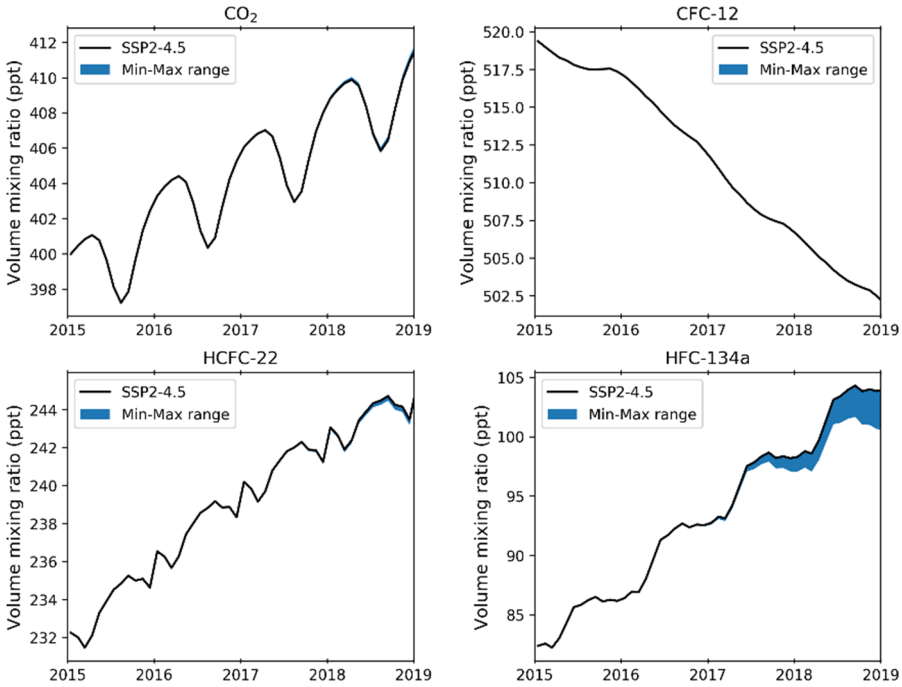

Figure 3- 2: Global mean surface volume mixing ratios as given in Meinshausen et al. (2020). Black lines represent the SSP2-4.5 scenario used to drive the LBC of BASCOE CTM. Blue areas are the spread between the lowest and highest SSP scenarios.

Finally, note that the developments needed to read and to vertically propagate the LBC were implemented, as for the OH oxidation parametrization, just before the start of this project.

3.3.3 Initial state

Our BASCOE CTM simulations start on 1st December, 1984. Since our objective is to compare the simulation outputs to observed atmospheric constituents, either in terms of absolute abundances or trends, we need to establish an initial state, i.e., a model global state at time step 0, which is the closest to the true state of the atmospheric composition on 1st December, 1984. However, global observations at that time are very sparse. In the face of that, we considered three strategies to set up our initial state: (1) create a model state that is mostly composed of N_2 and O_2, the major constituents of the atmosphere (see Sect. 1.3). Then, perform a very long spin-up simulation (probably longer than the actual simulation time-period) with perpetually repeating dynamics and using the HGGC dataset as lower boundary condition; (2) use global outputs from another model; (3) start from a recent analysis, performed by BASCOE, of chemical observations from the Microwave Limb Sounder instrument on board the Aura satellite (hereafter Aura-MLS; see, e.g., Errera et al., 2019) and scale tracer abundances to make them representative of December 1984. Strategy (1) presents the advantage that the initial state thus obtained would be original and not dependent of any other simulations. On the other hand, the long spin-up period is resource demanding and time costly. Strategy (2) is easy to set up but it relies on the quality of the outputs of the other model. Strategy (3) is also rather simple to set up but may not lead to realistic vertical profiles of atmospheric constituents. Seeing respective pros and cons of the three strategies, we finally decided to follow the strategy (3). Strategy (1) was too time consuming and there was no certainty about the final result. For strategy (2), we considered to use outputs of the Canadian Middle-Atmosphere Model (CMAM; e.g., Scinocca et al., 2008) developed by the Canadian Centre for Climate Modeling and Analysis (CCCma). However, preliminary comparisons between CMAM outputs and measurements

from the Atmospheric Trace Molecule Spectroscopy (ATMOS) Fourier transform spectrometer, on board the NASA Space Shuttle Challenger during the Spacelab 3 mission from 29th April to 6th May 1985 (Farmer et al., 1987; Zander et al., 1992), did not give us enough confidence in the validity of CMAM outputs for the year 1985 (not shown).

The key point of the followed strategy is to determine the factors to apply to the BASCOE analysis in order to make it representative of the atmospheric composition in 1985. We used a BASCOE analysis of AURA-MLS valid for 1st December, 2010 (hereafter BRAM). For greenhouse gases and ODSs, we have computed global mean volume mixing ratios at surface for BRAM. Using the global mean volume mixing ratios at surface from December 1984 of the HGGC dataset (see Sect. 3.3.2 above), we have then computed the scaling factors, for each greenhouse gas and ODS, between December 1984 (HGGC) and December 2010 (BRAM). These scaling factor were then applied at all grid points of BRAM. CO_2, CCl_4, CH_4, N_2O, CH_3Br, CH_3CCl_3, CFC-11, CFC-12, CFC-113, CFC-114, CFC-115, HCFC-22, halon-1211 and Halon-1301 were thus scaled from December 2010 to December 1984. For the species we added to the photochemical scheme of BASCOE CTM (i.e., HFC-134a, HFC-23, HFC-125, HFC-143a, HCFC-141b, HCFC-142b and halon-2402), we assumed that their global abundances were negligible in 1984 and, therefore, they were initiated as null in the model initial state. For F_y and HCl, we used measurements from ATMOS performed in 1985. We computed partial columns for ATMOS and BRAM, using the vertical and latitude ranges of ATMOS for the latter. The ratio between the two was then used to scale F_y and HCl. For all the other stratospheric species, we assumed that their lifetime was short enough and their global concentration constant with time. Consequently, for the initial state, we used their abundances as given in BRAM.

3.3.4 General simulation set-up

For this research, we use version 06.07.02 of BASCOE CTM. The photochemical scheme version is *sb17c*. The general set-up is the same as in Chabrillat et al. (2018). The model time step is set to 30 minutes. The horizontal grid is a regular 2°×2.5° latitude-longitude grid. For the vertical grid, we use the native hybrid-sigma pressure grids of each reanalysis. Doing so, we are able to take into account the different vertical resolution of each reanalyses and, furthermore, we avoid to introduce any interferences that could originate from the vertical reridding method. Finally, we use the reanalyses valid at 00h, 06h, 12h and 18h.

3.4 A first glance at the results and on the importance of the added source species to F_y

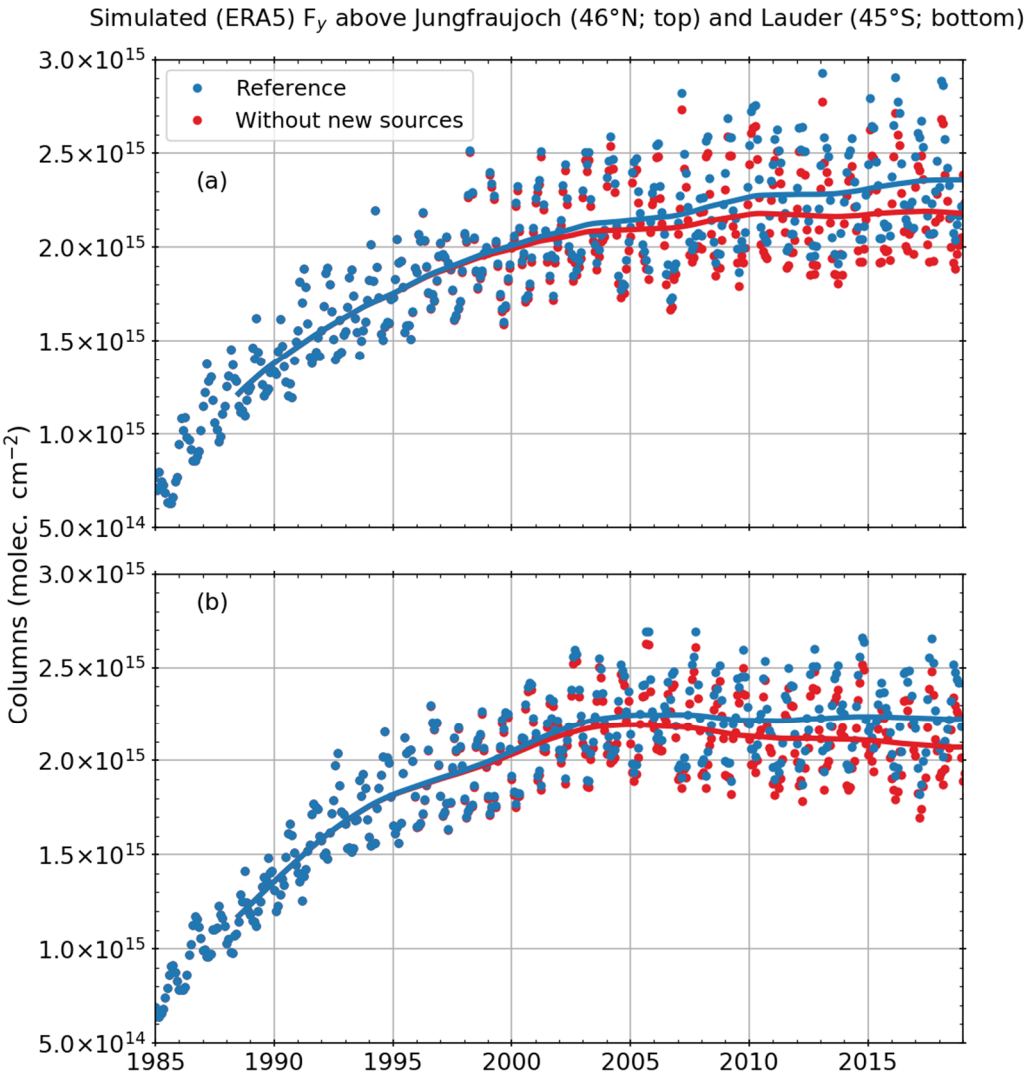

Figure 3- 3: F_y time-series above Jungfraujoch (**a**) and Lauder (**b**) simulated by BASCOE CTM driven by ERA5. Blue dots and lines are the reference run for ERA5 (i.e., these are the time-series showed and analysed in Chapter 6). Red dots and lines are from a run without the species that were added to chemical scheme of BASCOE CTM in the framework of this thesis.

Figure 3- 3 shows the F_y simulated time-series above Jungfraujoch (46°N) and Lauder (45°S) simulated by BASCOE CTM driven by ERA5 (blue dots and lines). The forcing reanalysis is chosen arbitrarily here. From this figure, we see that the first years of the simulation (i.e., 1985-1988) are displaying steeply increasing F_y columns. These F_y trends are probably not realistic as these are shown by all of the five simulations. What we see here is certainly a "spin-up" effect, with the first years being strongly influenced by the model initial state, as we did not perform any explicit spin-ups of the model initial state. As a consequence, we have decided to discard the first five years of our simulations to avoid eventual biases in assessed trends.

The first complete simulations that were performed for this thesis suffered from a misconfiguration regarding the added F_y source species. The sources, for which concentrations were set to null in the initial state (i.e., HFC-134a, HFC-23, HFC-125, HFC-143a, HCFC-141b, HCFC-142b and halon-2402), did not increase during these simulations and, therefore, did not contribute to F_y. While this

misconfiguration was unfortunate, it allowed us to show here the importance of the CFC substitution products in the recent trends of F_y (Figure 3- 3). The major actor here is HFC-134a (see Sect 1.4 and Sect. 6.2). Defining the CF_y of BASCOE CTM as the fluorine atom weighted sum of all F_y source gas included in the chemical scheme, HFC-134a contribution to CF_y is increasing from 0%, in 1995, to ~15% in 2019 (not shown, computed over the LBC dataset).

Chapter 4

Methods

This chapter provides a description of the main methods employed in this work. The two first sections explain how a rather simple measure of light intensity is exploited to retrieve total and partial columns of gaseous constituents of the atmosphere. Section 4.3 describes the method to compare ground-based FTIR products to independent datasets. Section 4.4 briefly presents the techniques of observation of the two main satellites included in this thesis. Finally, Section 4.5 describes the statistical methods used to estimate trend values as well as their uncertainties.

4.1 FTIR basics

The FTIR technique, employed to ultimately derive atmospheric constituent abundances from their infrared solar absorption lines (see Sect. 1.3.1.1), is based on the Michelson interferometer (Figure 4-1). Consisting of fixed and moving mirrors and a semi-reflector beam-splitter, this ostensibly simple interferometer constructs complex interferences which are the essence of the FTIR measurements performed at the Jungfraujoch and at other NDACC (Network for the Detection of Atmospheric Composition Change; De Mazière et al., 2018) sites. Collected through a solar tracker and routed to the instrument by a series of mirrors, the solar incident light firstly falls on the beam-splitter that reflects half of it and transmits the other half. The reflected part then hits a fixed mirror while the transmitted part hits a moving mirror, both being reflected back to the beam-splitter. The light, thus recombined, finally reaches the detector.

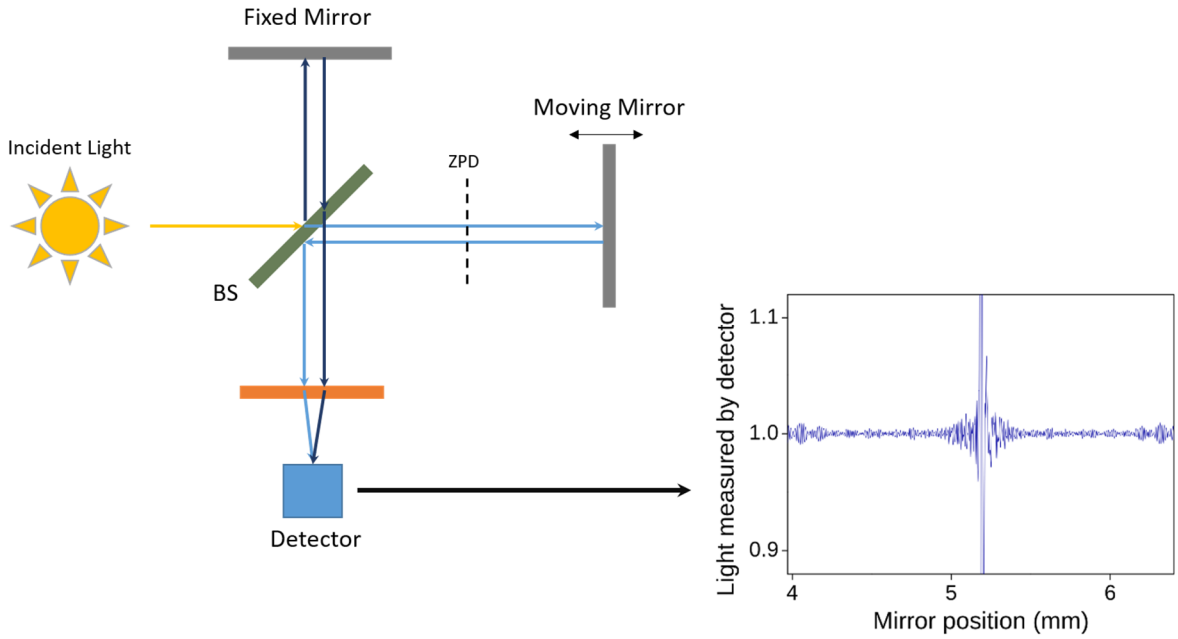

Figure 4- 1: Basic schematic of a Michelson interferometer. Grey thick lines are mirrors. The green thick line is the beam-splitter (BS). The orange thick line is a collimating lens. The dotted line represents the zero path difference position (ZPD). The lower-right frame schematics an interferogram that would be measured by the interferometer.

As depicted in Figure 4- 1, the moving mirror is displaced from the zero path difference position (ZPD), where reflected and transmitted pathways have equal optical lengths, to a maximum distance from the ZPD, *L*. For a displacement of the moving mirror equal to *x*, the optical path difference (OPD), which is defined as the optical path difference between the reflected and the transmitted optical pathways, corresponds to 2*x*. During the displacement of the moving mirror, the detector is recording the light intensity of the recombined beams, building this way an interferogram. At ZPD, the interference between the two beams is constructive and corresponds to the maximum intensity of the interferogram.

If we consider a monochromatic light source with an intensity equal to the unity and if we ignore the instrument optical efficiency, the interferogram is given by:

$$I(x) = \frac{1+\cos(\frac{2\pi x}{\lambda})}{2} = \frac{1+\cos(2\pi\sigma x)}{2}, \quad (4.1)$$

where λ is the wavelength of the source and σ (=1/λ) is its associated wavenumber. From this equation, we see that the intensity is maximal for each OPD (i.e., *x*) corresponding to a round multiple of the wavelength λ, i.e., constructive interferences. On the other hand, the interferences are destructive and the intensity is null for OPDs that are round multiples of $\lambda/2$.

However, in the case of the FTIR solar technique, the light source is of course polychromatic. Each spectral element of the light source has an energy $S(\sigma)d\sigma$ and the interferogram is thus corresponding to the sum of the spectral contributions of the individual spectral elements $d\sigma$, i.e., to:

$$I(x) = \int_0^\infty S(\sigma)\cos(2\pi\sigma x)d\sigma. \quad (4.2)$$

If we define for $x > 0$: $S_e(\sigma) = [S(\sigma) + S(-\sigma)]/2$, to build an even function from the physical function $S(\sigma)$, Eq. 4.2 can be rewritten as:

$$I(x) = \int_{-\infty}^{\infty} S_e(\sigma) \exp(2i\pi\sigma x) d\sigma. \quad (4.3)$$

In fact, noting that $\exp(ix) = \cos(x) + i\sin(x)$ and stating that the imaginary part of Eq. 4.3 is null, the cosine function of Eq. 4.2 can be replaced by an exponential function. As formulated in Eq. 4.3, it appears that the interferogram is actually the Fourier transform of the infinite resolution spectrum $S_e(\sigma)$. Consequently, the observed spectrum is obtained through the inverse Fourier transform of the interferogram:

$$S_e(\sigma) = \int_{-\infty}^{\infty} I(x) \exp(-2i\pi\sigma x) dx. \quad (4.4)$$

This mathematical theory is in practice confronted to physical limitations. The most important one, regarding Eq. 4.4, is certainly that, in practice, the mirror is actually displaced over a finite distance (L), modifying this way the integration interval to $[0; 2L]$. As a result, the observed interferogram is actually the product between an infinite OPD interferogram and a rectangular function with a width of $2L$:

$$I_{obs}(x) = I(x) \prod(x), \quad (4.5)$$

with

$$\prod(x) = \begin{cases} 0, \text{if } x > 2L \\ 1, \text{if } x \leq 2L \end{cases}. \quad (4.6)$$

Applying the Fourier transform to Eq. 4.5, we obtain:

$$S_{obs}(\sigma) = S_e(\sigma) * c\ sinc(c\sigma), \quad (4.7)$$

with c a constant introduced due to mathematical simplifications already used in the rectangular function of Eq. 4.5. Equation 4.7 sees the apparition of a convolution product ($*$), as the Fourier transform of a product of functions is the convolution product of the individual Fourier transform of these functions. Moreover, the right hand-side of the convolution product in Eq. 4.7 is a *sinc* function, as a rectangular function corresponds to a *sinc* function in the spectral domain. From Eq. 4.7, we finally see that the observed spectrum, through the FTIR technique, is actually the convolution product between the spectrum that would be observed in an ideal case and an instrumental *sinc* function. In other words, Dirac delta peaks that would be observed in the case of an infinite mirror displacement are in practice deformed by the instrumental function as depicted in Figure 4- 2. Finally, the spectral definition of the observing system is given by $R = 1/2L$.

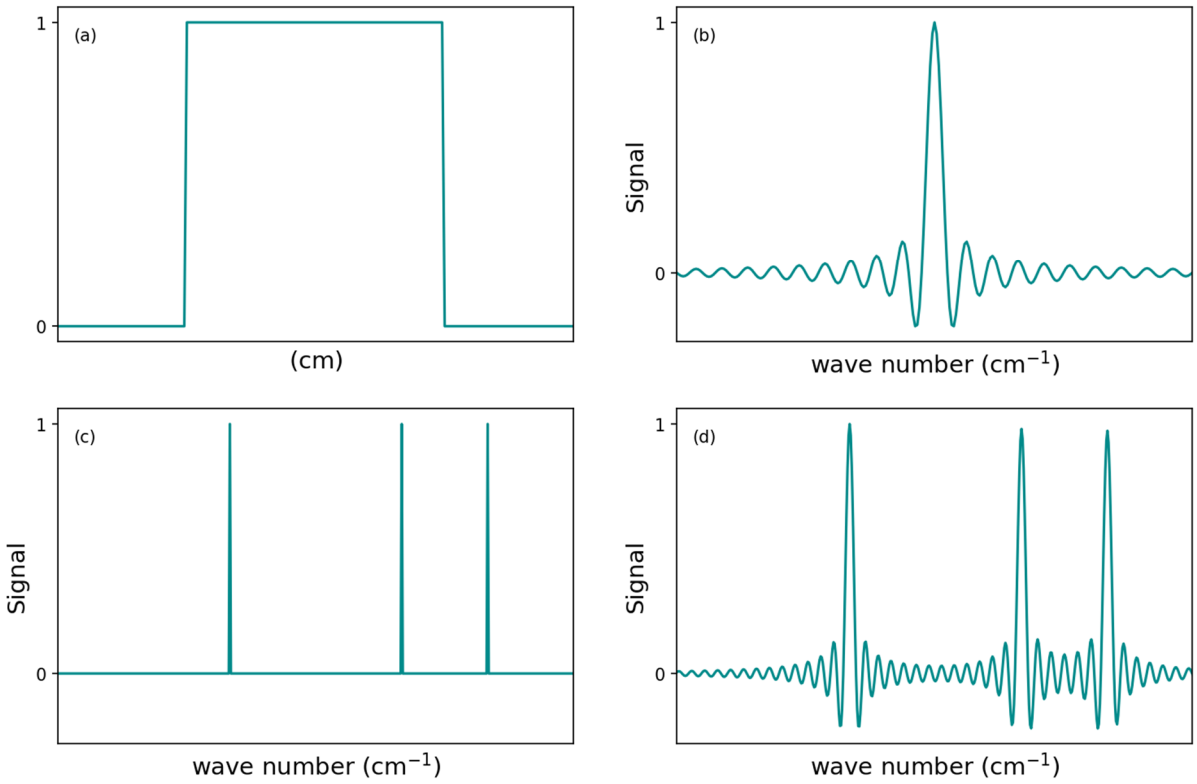

Figure 4- 2: Schematic of a rectangular function (**a**), the Fourier transform of the rectangular function, i.e., a sinc function (**b**), Dirac delta peaks observed in the case of an instrument having an infinite resolution (**c**) and the convolution product between the Dirac delta peaks and the sinc function, i.e., the observed spectrum (**d**). Adapted from Duchatelet (2011).

4.2 The inverse method applied to FTIR observations

Now that we know how a solar FTIR spectrum is obtained from an interferogram measured by our instrument, we will see, in this section, how we are actually able to retrieve atmospheric constituent abundances from the absorption lines observed in the infrared spectrum.

The problem

As we saw in Chapter 1 (Sect. 1.3.1.1), some atmospheric constituents absorb in the infrared region of the solar light spectrum. As a result, absorption lines or signatures specific to the active target species are present in the measured solar spectrum. The shape and the intensity of an absorption line or feature depend on the structure, abundance and vertical distribution of the target species as well as on the state of the atmosphere (e.g., vertical profiles of temperature and pressure). In other words, with a radiative transfer model $\boldsymbol{F}$, we are able to determine an absorption line $\boldsymbol{y}$ of a species from the vertical profile $\boldsymbol{x}$ of the species and other parameters represented in $\boldsymbol{b}$:

$$\boldsymbol{y} = \boldsymbol{F}(\boldsymbol{x}, \boldsymbol{b}) + \boldsymbol{\varepsilon}, \tag{4.8}$$

with $\boldsymbol{\varepsilon}$ the error vector. Source of errors are the measurement errors but also the approximations of the detailed physics in the radiative model. The model $\boldsymbol{F}$ is also more generally called the forward model. It includes the physical theory of the radiative transfer as well as an understanding of the instrument. In our case, the measurement vector $\boldsymbol{y}$ is known while the vertical profile, or state vector, $\boldsymbol{x}$ and some of the parameters in $\boldsymbol{b}$ are not. Consequently, we have to actually inverse the problem and introduce the inverse method.

The inverse method

To inverse the problem and retrieve the best estimator $\hat{\boldsymbol{x}}$ of the state vector $\boldsymbol{x}$, knowing the measurement vector $\boldsymbol{y}$, we have:

$$\hat{\boldsymbol{x}} = \boldsymbol{R}\left(\boldsymbol{y}, \hat{\boldsymbol{b}}, \boldsymbol{x_a}, \boldsymbol{c}\right), \tag{4.9}$$

where **R** is the inverse or retrieval method, $\hat{\boldsymbol{b}}$ an estimation of the parameters of the forward function, $\boldsymbol{x_a}$ the a priori estimation of the state vector (i.e., the a priori vertical profile of the target species) and $\boldsymbol{c}$ the parameters specific to the retrieval method. If we substitute Eq. 4.8 in Eq. 4.9 we have:

$$\hat{\boldsymbol{x}} = \boldsymbol{R}\left(\boldsymbol{F}(\boldsymbol{x}, \boldsymbol{b}) + \boldsymbol{\varepsilon}, \hat{\boldsymbol{b}}, \boldsymbol{x_a}, \boldsymbol{c}\right). \tag{4.10}$$

Equation 4.10 is the transfer function which describes "the operation of the whole observing system, including both the measuring instrument and the retrieval method" (Rodgers, 2000).

Several questions can come to the reader at this point: (1) by introducing an a priori estimation of the solution, how is quantified the independence of the solution to this a priori estimation? (2) how do we get a vertical information and how representative it is? (3) what are the sources of error and how are they quantified? Questions (1) and (2) find their answers in the characterization of the retrieval, leading to the *information content analysis* (Sect. 4.2.1). Question (3) is answered by the *error analysis* (Sect. 4.2.2).

The formalism of Rodgers (2000) allows for the transfer function to be rewritten using matrix operations and, thus, to introduce new terms quantifying the information content and the error estimation. It is decided here to approach the problem in a descriptive way, limiting the mathematical developments leading to the presented equations in the next two sections. The curious reader looking for more developments is advised to find any supplemental information in the book of Rodgers (2000) or in previous PhD manuscripts on the subject (e.g., Barret, 2003; Duchatelet, 2011), which were consulted to write these sections.

4.2.1 Information content

Questions (1) and (2) are related to the same more general question: how is the retrieval related to the true state of the atmosphere?

Following the method of Rodgers (2000), if we linearize the inverse method (Eq. 4.9 and Eq. 4.10) with respect to the measurement vector $\boldsymbol{y}$ and rearrange the terms, we have:

$$\hat{\boldsymbol{x}} - \boldsymbol{x_a} = \boldsymbol{R}\left[\boldsymbol{F}\left(\boldsymbol{x_a}, \hat{\boldsymbol{b}}\right), \hat{\boldsymbol{b}}, \boldsymbol{x_a}, \boldsymbol{c}\right] - \boldsymbol{x_a} + \boldsymbol{A}(\boldsymbol{x} - \boldsymbol{x_a}) + \boldsymbol{G_y}\boldsymbol{\varepsilon_y}. \tag{4.11}$$

The first term of right hand side of Eq. 4.11 expresses the error or the bias, in the absence of measurement error, of the inverse method itself. In the case of a simulated measurement that would perfectly correspond to an a priori known state, we expect from the inverse method to return the a priori. This term is thus expected to be zero in any good inverse method, allowing us to reformulate Eq. 4.11:

$$\hat{\boldsymbol{x}} = \boldsymbol{x_a} + \boldsymbol{A}(\boldsymbol{x} - \boldsymbol{x_a}) + \boldsymbol{G_y}\boldsymbol{\varepsilon_y} = (\boldsymbol{I_n} - \boldsymbol{A})\boldsymbol{x_a} + \boldsymbol{A}\boldsymbol{x} + \boldsymbol{G_y}\boldsymbol{\varepsilon_y}. \tag{4.12}$$

In Eq. (4.11) and Eq. (4.12), $\boldsymbol{A}$ is the sensitivity of the retrieval to the true state and is commonly referred to as the averaging kernel matrix. The averaging kernel matrix is at the centre of the information

content analysis in the formalism of Rodgers (2000). $\boldsymbol{I_n}$ is the identity matrix of dimension n. Therefore, the term $(\boldsymbol{I_n} - \boldsymbol{A})\boldsymbol{x_a}$ represents the contribution of the a priori to the solution. In an ideal inverse method, $\boldsymbol{A}$ would be a unit matrix and in consequence the contribution of the a priori would be null. The term $\boldsymbol{Ax}$, on the other hand, expresses the contribution of the true state to the solution. In the case of the inverse method applied to FTIR measurements, the inverse method is not ideal and the averaging kernel matrix is different from the unit matrix. As a result, the rows of $\boldsymbol{A}$, the individual averaging kernels, can be interpreted as smoothing functions peaking at peculiar levels, with their half-width corresponding to a measure of the vertical resolution of the observing system. Again in other words, the averaging kernel of a particular level, for example the vertical grid level at 30km, "indicates which part of the true state is averaged to produce the retrieval at this level (30km) of the retrieved state" (Rodgers, 2000).

The averaging kernel matrix $\boldsymbol{A}$, as defined in the formalism of Rodgers (2000), also allows for the quantification of the number of independent vertical pieces that can be extracted from the retrieved vertical profile, i.e., the degree of freedom for signal (DOFS). The DOFS is mathematically obtained by computing the trace of the averaging kernel matrix. Another qualification and quantification of the information content, as retrieved by the inverse method from a measured spectrum, is the extraction of the eigenvectors and their respective eigenvalues from the averaging kernel matrix $\boldsymbol{A}$. In fact, a plot of the eigenvectors reveals the altitude ranges of the independent vertical pieces that can be extracted from the whole retrieved profile. More precisely, the shape of the eigenvector and the altitudes where it crosses – or it is close to – the origin, inform on the altitude boundaries of each independent vertical pieces, while its corresponding eigenvalue gives the fraction of information effectively coming from the measurement (in opposition to the a priori) that has contributed to retrieved these pieces of information.

Averaging kernels, eigenvectors and eigenvalues, characterizing the information content are summarized in Figure 4- 3.

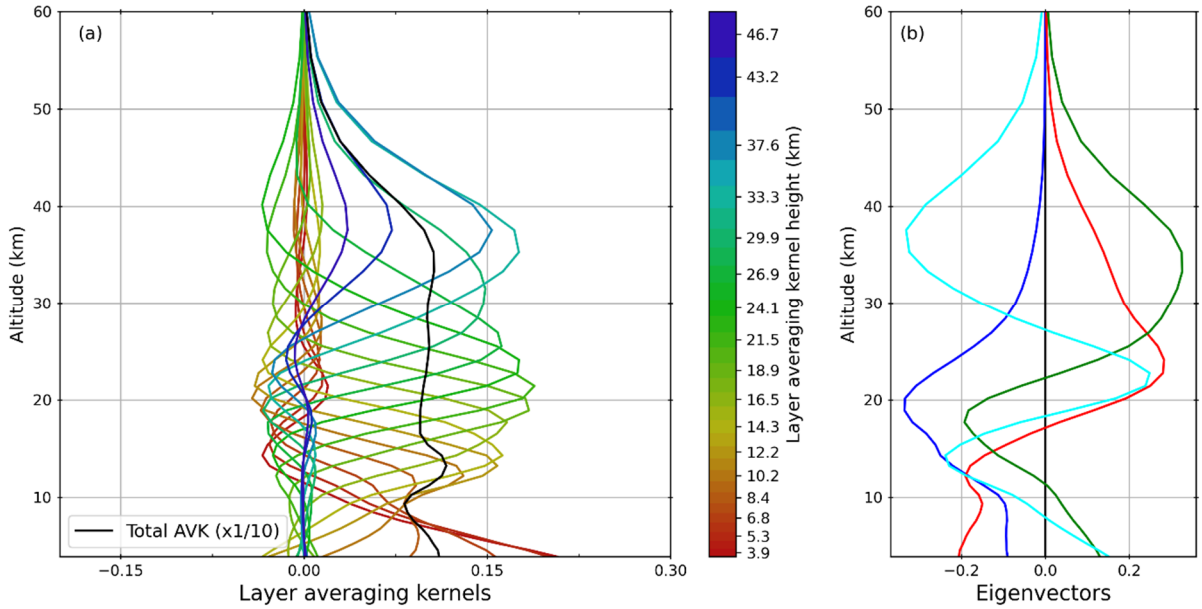

Figure 4- 3: (**a**) Example of individual averaging kernels (unitless) characterizing the retrieval of O_3 from FTIR solar spectra recorded at Jungfraujoch. One in a two layer averaging kernels are displayed for clarity. The black line is the sum of the row of the averaging kernel matrix and represents the vertical sensitivity of the retrieval (scaled by a factor of 10 for clarity). (**b**) Corresponding eigenvectors having eigenvalues greater than 0.98.

O_3 is a good target species to illustrate the averaging kernels and the eigenvectors as its retrieval is characterized by a particularly good information content. Indeed, the DOFS, obtained from the inversion of FTIR solar spectra recorded at Jungfraujoch, is ~4.5, meaning that 4 independent pieces of information can be extracted from the retrieved profiles (as illustrated by the cyan line in Figure 4- 3b). Inspecting the cyan line in Figure 4- 3b, we see that the four pieces of information are defined as follows: the first one is delimited between the ground and 8 km, the second one between 8 km and 18 km, the third one between 18 km and 27 km and the fourth one between 27 and 60 km. This last altitude marks the level above which the retrieval has no sensitivity (black line in Figure 4- 3a)

It is now important for the reader to distinguish between, on the one hand, the resolution of the vertical grid on which the vertical profile is retrieved, i.e., the layer thicknesses of the retrieval grid, and, on the other hand, the number of independent pieces of information that can be retrieved from the spectrum (as defined by the DOFS, eigenvectors and eigenvalues).

4.2.2 Error analysis

As already introduced in linearized Eq. 4.11 and Eq. 4.12, the formalism of Rodgers includes error terms that allow for a full and thorough error analysis. Further rearrangement of Eq. 4.11 leads to:

$$\hat{\boldsymbol{x}} - \boldsymbol{x} = (\boldsymbol{A} - \boldsymbol{I_n})(\boldsymbol{x} - \boldsymbol{x_a}) + \boldsymbol{G_y K_b}(\boldsymbol{b} - \hat{\boldsymbol{b}}) + \boldsymbol{G_y}\Delta\boldsymbol{f}(\boldsymbol{x}, \boldsymbol{b}, \boldsymbol{b'}) + \boldsymbol{G_y}\boldsymbol{\varepsilon}. \quad (4.13)$$

Each term in right hand side of Eq. 4.13 corresponds to an aspect of the total error as characterized by the formalism of Rodgers (2000) and is further described below.

Smoothing error – $(\boldsymbol{A} - \boldsymbol{I_n})(\boldsymbol{x} - \boldsymbol{x_a})$

As revealed by the information content, the retrieval can be regarded as an estimate of the true state, with an error contribution due to the smoothing by the averaging kernels, i.e., the smoothing error. In other words, this error can be interpreted as the error generated by the limited vertical resolution of the observing system or the retrieval.

Because the true state $\boldsymbol{x}$ is not known, the actual smoothing error cannot be estimated. Thus, we seek at the statistics of the error, i.e., the covariance $\boldsymbol{S_s}$ of the smoothing error:

$$\boldsymbol{S_s} = (\boldsymbol{A} - \boldsymbol{I_n})\boldsymbol{S_e}(\boldsymbol{A} - \boldsymbol{I_n})^{\mathrm{T}} \quad (4.14)$$

where $\boldsymbol{S_e}$ is a covariance matrix computed over an ensemble of states and should represent the natural variability of the state vector. To construct $\boldsymbol{S_e}$, one can either use a climatology computed over an independent dataset or, if such a such a dataset is not available, an ad hoc matrix corresponding to the covariance $\boldsymbol{S_a}$ of the a priori.

Forward model parameter error – $\boldsymbol{G_y K_b}(\boldsymbol{b} - \hat{\boldsymbol{b}})$

This error describes the error in the parameters of the forward model. $\boldsymbol{G_y}$ is the sensitivity of the retrieval to the measurement and $\boldsymbol{K_b}$ the sensitivity of the forward model to its parameters. $(\boldsymbol{b} - \hat{\boldsymbol{b}})$ expresses the bias in the estimated parameters.

Forward model error – $\boldsymbol{G_y}\Delta\boldsymbol{f}(\boldsymbol{x}, \boldsymbol{b}, \boldsymbol{b'})$

This error is generated by the forward model itself. In practice, this error is challenging to evaluate as the model with the correct physics is not known. This error is mostly systematic.

Retrieval noise – $\boldsymbol{G_y\varepsilon}$

The retrieval noise is mostly random and easy to evaluate. It represents the measurement noise.

4.2.3 Finding the optimal solution – optimization and regularization types

In the inverse method described above, small perturbations (e.g., measurement noise, instrumental function) introduced in the measured spectrum can lead to large differences in the solution. Moreover, the function relating the vertical profile of the target species and the absorption lines is a continuous function while the measurement and the solution vector are discrete quantities. Therefore, the inverse problem is under-constrained and ill-posed, so that it does not have a unique solution.

It thus implies that an iterative process is needed to reach the optimal solution. In the FTIR inverse method, the forward model is non-linear and, therefore, a non-linear least squares iterative method (i.e., the Gauss-Newton method) is employed. As we saw, the inverse method requires an a priori of the solution, i.e., an estimate of the typical vertical profile of the target species. The iterative process starts with the a priori as the first-guest for the first iteration. At each iteration, the process evaluates the difference between the measurement and the calculated state (i.e., the residuals) and stops when the latter is minimized. In the method of Rodgers (2000), the iterative process is constrained so that the shape of the vertical retrieved profile (i.e., the solution) is not getting too far from that of the a priori. This constraint is applied through a regularization matrix $\boldsymbol{R}$. When the applied constraint is very weak, the iterative process is pushed to its limits and retrieves some information from the measurement noise. Consequently, the DOFS tends to the number of layers and the retrieved profile is unrealistic, with non-realistic oscillations. On the other hand, if the applied constraint is very strong, the retrieved profile corresponds to the a priori and the DOFS is close to 0. Hence, a good constraint, which has to be determined by the user, is situated somewhere between these two extreme cases. The determination of the constraint to apply is one of the key challenges in the elaboration of a retrieval strategy.

Letting apart the simple scaling where the regularization matrix corresponds to the identity matrix and where the a priori is simply scaled in the iterative process, there are two main types of constraints: the climatological and the smoothing constraints.

Climatological regularization

In the climatological regularization, also incorrectly named optimal estimation method[1] (OEM), the regularization matrix is defined as the inverse of the a priori full covariance matrix ($\boldsymbol{S_a^{-1}}$). As introduced in the description of the smoothing error (Sect. 4.2.2), the full covariance matrix should express the natural variability of the target species. The full covariance matrix may be built from a large independent ensemble of profiles, i.e., a climatology covering as much as possible the full range of possible profiles. Satellite datasets can offer such an ensemble. In practice, it is not possible to construct the full covariance matrix, due to the lack of sufficiently large datasets offering profiles in the desired altitude range or temporal coverage. Consequently, it is common to only define the diagonal elements of the a priori covariance matrix. Extra-diagonal elements are then introduced to express the correlation existing

[1] Indeed, the OEM method rather refers to the overall retrieval method as implemented in Rodgers (2000).

between a vertical level and the other nearby levels below and above, i.e., the inter-layer correlation (ILC).

Smoothing regularization

The most commonly used smoothing regularization is the Tikhonov regularization. To summarize and to avoid the need to introduce new equations, the Tikhonov regularization is implemented through a parameter α. This parameter defines the strength of the constraint. The Tikhonov regularization constrains the shape of the retrieved profile but not the absolute values. The absolute values of the target species retrieved profile are thus determined from the information that is located in the measurement. This last sentence marks the difference with the climatological constraint. Indeed, in the latter the determination of the absolute values of the retrieved profile is based on the information of the natural variability of the target species as given by the a priori covariance matrix.

For the extreme cases and as already introduced in this section, if $\alpha = 0$, the constraint is null and the DOFS corresponds to the number of vertical levels but the retrieved profiles will certainly contain unrealistic oscillations. If $\alpha \to \infty$, the DOFS is close to 0 and the retrieved profile merges with the a priori profile. The parameter α can be determined in order to reach the desired DOFS values. The determination of the parameter α can also be done following the method of Steck (2002). Considering that, with increasing α values, the smoothing error increases and the measurement error decreases, the method of Steck (2002) consists in the determination of α so that both errors are minimized.

To summarize, smoothing regularizations are convenient when an independent dataset does not exist to construct a full covariance matrix or when the user wants to avoid unrealistic oscillations in the retrieved profiles. Smoothing regularizations are also employed when a determined DOFS value is aimed at, as in efforts of retrieval harmonization between NDACC sites

4.3 Comparison methods for ground-based FTIR products

We saw in the previous section (Sect. 4.2) that the inverse method applied to FTIR measurement leads to a limited vertical resolution regarding the retrieved profile of the target species (see concluding remark of Sect. 4.2.1). Moreover, the information content analysis reveals that the retrieval is actually sensitive to a limited vertical range of the atmosphere. Therefore, when comparing ground-based FTIR retrievals with independent datasets such as model outputs or satellite data, one has to account for this limited vertical sensitivity of the ground-based FTIR products. In fact, ground-based FTIR measurements convey the poorer vertical resolution and vertical sensitivity (at least in this work). For example, limb sounding satellites (see Sect. 4.4) can benefit from a better geometry of observation and, thus, have a relatively good vertical resolution.

To account for the limited vertical resolution and vertical sensitivity of the ground-based FTIR retrievals, one has to smooth the independent profile (i.e., from model or satellite data) with the averaging kernels of the former (see Sect. 4.3.2 below). To avoid any vertical regridding of these averaging kernels, it is common to first regrid the independent profile on the FTIR retrieval grid (see Sect. 4.3.1 below).

4.3.1 Mass-conservative vertical regridding

In our instrumental case, the fields to be vertically regridded represent gas abundances. Therefore, the employed regridding scheme has to conserve the total mass of the tracer, i.e., one has to consider a mass-conservative regridding scheme. In this work, the scheme used is similar to the one described in Sect. 3.1 of Langerock et al. (2015). It was originally implemented in Python for another CTM by a former colleague, Benoît Bovy. For this work, efforts were made to adapt the Python code for BASCOE CTM ouputs and satellite data. The regridded scheme can be written as follows:

$$\Phi_{dj} = \sum_i p_{ij} \Phi_{si}, \tag{4.15}$$

where Φ is the field to be regridded, Φ_{si} is the value of the field of the i^{th} cell of the source grid (i.e., the vertical grid of the independent profile to be regridded), Φ_{dj} is the value of the field of the j^{th} cell of the destination grid (i.e., the ground-based FTIR vertical grid) and p_{ij} are the coefficients of the sparse interpolation matrix.

For a mass-conservative regridding scheme and an extensive quantity (i.e., whose values change with the grid cell volume as, e.g, number of molecules), p_{ij} is given by:

$$p_{ij} = \frac{V_{si} \cap V_{dj}}{V_{si}}, \tag{4.16}$$

for an intensive quantity (e.g., mixing ratios), we have

$$p_{ij} = \frac{V_{si} \cap V_{dj}}{V_{dj}}, \tag{4.17}$$

where V_{si} and V_{dj} are the volumes of the i^{th} cell of the source grid and of the j^{th} cell of the destination grid, respectively. Thus, $V_{si} \cap V_{dj}$ is the intersection between the two.

Figure 4- 4 schematizes the implemented algorithm. In practice, the regridding algorithm is implemented through the computation of an exchange grid. The exchange grid is defined as all the intersections between the cells of the source grid and the destination grid. Each cell of the source grid is then interpolated on the corresponding cell(s) of the exchange grid (black arrows of Figure 4- 4). The interpolations are weighted following Eq. 4.15-4.17, depending on the nature of the quantity to regrid. Finally, the algorithm identifies, for each cell of the destination grid, the corresponding cells of the exchange grid to sum in order to compute the individual fields of the destination grid (numbers and brackets in Figure 4- 4).

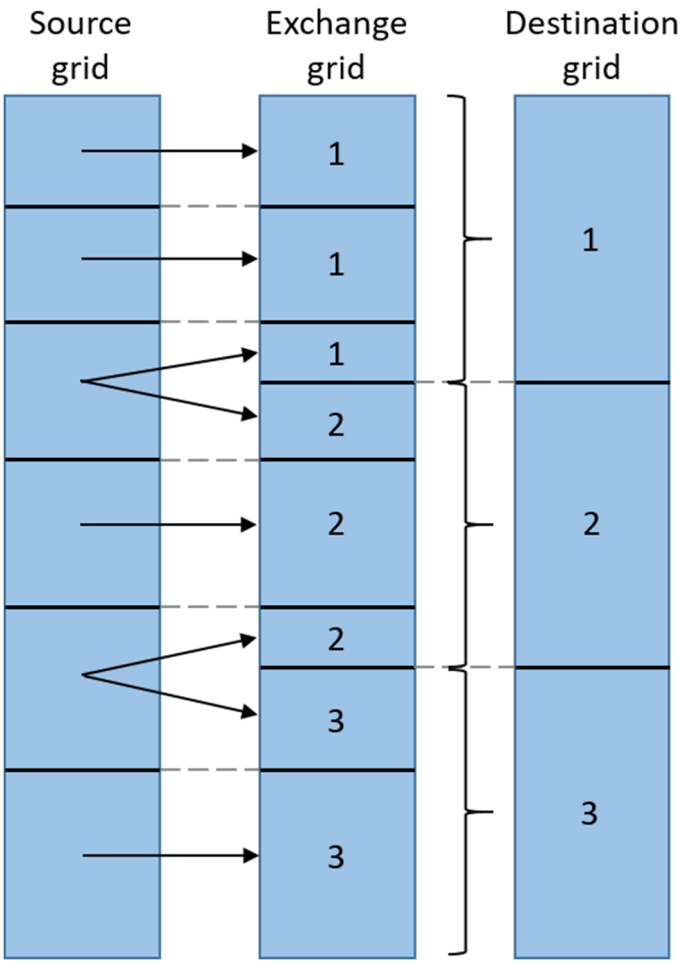

Figure 4- 4: Schematic of the mass-conservative regridding scheme used in this work. The source grid is the vertical profile of the independent dataset to be regridded. The destination grid is the vertical grid on which the source vertical profile is regridded. The cells of the exchange grid are the intersections of that of the source and the destination grids. Black arrows represent the interpolation of the source fields on the exchange grid (following Eq. 4.15-4.17). Finally, the numbers identify the cells summed to compute the regridded fields for a peculiar level of the destination grid. See text for additional comments.

4.3.2 Averaging kernel smoothing

Once the independent profile and the averaging kernels are on the same vertical grid, one may proceed to the averaging kernel smoothing. The smoothing is applied following:

$$\boldsymbol{x_{smooth}} = \boldsymbol{x_a} + \boldsymbol{A}(\boldsymbol{x_m} - \boldsymbol{x_a}), \tag{4.18}$$

where $\boldsymbol{x_a}$ is the a priori profile used for the inversion, $\boldsymbol{x_m}$ is a vertical profile from the independent dataset (e.g., model or satellite data) and $\boldsymbol{A}$ is the averaging kernel matrix (see Sect. 4.2.1).

The averaging kernel smoothing ensures that the independent dataset profile and the ground-based FTIR profile coincide on height levels outside the sensitivity range of the measurement. In other words, it ensures that no biases are depicted between the two profiles outside of the sensitivity range (Langerock et al., 2015).

4.4 Satellite observations

In this work, satellite retrievals of atmospheric constituents are included to support the validation of our FTIR products, for comparison purposes and to provide a global picture. We made use of

measurements performed by the Atmospheric Chemistry Experiment-Fourier Transform Spectrometer (ACE-FTS; Bernath et al., 2005; Bernath, 2017) and MIPAS (Fischer et al., 2008).

ACE-FTS and MIPAS benefit from the same limb viewing geometry. However, ACE-FTS performs solar occultations (similar to ground-based FTIR) while MIPAS measures atmospheric spectral radiances (i.e., atmospheric infrared emissions). In the limb viewing geometry, the satellite probes the atmosphere along tangential optical paths across the horizon (Figure 4- 5). In consequence, the optical path is substantially longer than that of nadir sounders or ground-based FTSs. The longer optical path allows for the absorptions or for the spectral radiances to be stronger in the measured spectra, i.e., it enhances the signal-to-noise ratio (SNR). To give an idea to the reader, the optical path of a limb viewing geometry goes twice in the probed atmospheric layers: once from the entrance in the atmosphere to the tangent point and a second time from the tangent point to the exit of the atmosphere. The limb geometry also allows for a much better vertical resolution compared to satellite nadir sounding or ground-based FTS instruments. ACE-FTS and MIPAS have typical vertical resolutions of 3 km. The counterparts of limb viewing satellites are their relatively coarse horizontal resolution (300 km in the line of sight) and their low sensitivity for the lower troposphere.

Further details regarding satellite data are given in the next chapters when used.

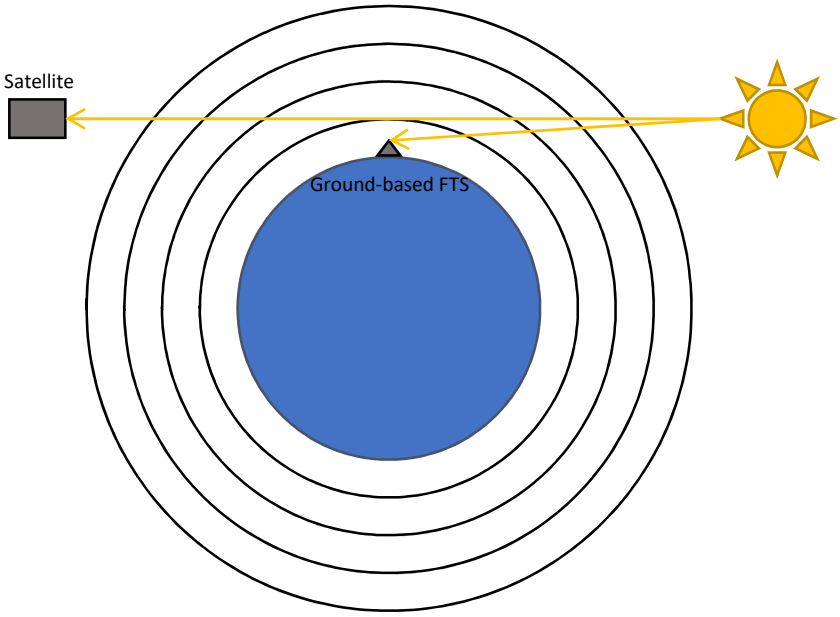

Figure 4- 5: Schematic of satellite limb viewing (solar occultation) and ground-based geometries of observation. Note that the effect of the atmospheric refraction on the optical paths is neglected here.

4.5 Trends assessments

Sections 4.5.1-5 are written following Sect. 3.4 in:

Prignon, M., Chabrillat, S., Friedrich, M., Smale, D., Strahan, S. E., Bernath, P. F., Chipperfield, M. P., Dhomse, S. S., Feng, W., Minganti, D., Servais, C. and Mahieu, E.: Stratospheric fluorine as a tracer of circulation changes: comparison between infrared remote-sensing observations and simulations with five modern reanalyses, J. Geophys. Res. Atmos. (*under review*), 2021.

Note that this study is presented in the Chapter 6 of the present work.

4.5.1 Linear model

Trend estimates presented in this research are obtained from a classic linear trend model accounting for an annual cycle:

$$y_t = d_t + s_t + u_t, \tag{4.18}$$

with

$$d_t = \alpha + \beta t, \tag{4.19}$$

and

$$s_t = \sum_{j=1}^{S} a_j \cos(2j\pi t) + b_j \sin(2j\pi t), \tag{4.20}$$

where y_t are the observation or model values at time t, d_t a simple linear trend model with α its intercept and β the slope we are looking for, s_t is a Fourier series of degree S modelling the annual cycle of the time-series and u_t is a stochastic error term. Accounting for the annual cycle with a Fourier series for atmospheric time-series has already been proposed in a number of previous studies (e.g., Gardiner et al., 2008; Franco et al., 2015; Mahieu et al., 2017; Friedrich et al., 2020a). From these studies it appears that using a third order Fourier series ($S = 3$) allows to correctly capture the intra-annual seasonality of such time-series. Tests with our datasets led us to the same conclusion (not shown). The error term u_t in Eq. (4.18) can exhibit heteroskedasticity (i.e., changing variance over time) and autocorrelation, as often observed in geophysical time-series (Friedrich et al., 2020a). Therefore, once a model such as the one described in Eq. (4.18) is fit to the data, a method to obtain a measure of uncertainty around the resulting estimates has to be found that is valid for this error specification.

Note that the given time periods for trend estimations, performed in this work, include the starting and ending years, e.g., 2004-2018 corresponds to a 15-year period from January 2004 to December 2018.

The three next sections (Sect. 4.5.2-4) describe three methods to assess the uncertainty around trend estimates that were considered in the present work. Section 4.5 describes a nonparametric method to obtain smoothed time-series. Finally, Section 4.5.6 proposes a comparison of the considered trend uncertainty estimation methods.

4.5.2 Bootstrap residual resampling

Gardiner et al. (2008) proposed a bootstrap residual resampling method to assess trend uncertainties that was further applied in subsequent studies (e.g., Mahieu et al., 2014; Franco et al., 2015). Briefly, after fitting the model of Eq. (4.18) to the time-series, the residuals thus obtained are resampled randomly at each time t and a trend is computed again on the new time-series. This process is repeated x times and a distribution of trend values is obtained. Finally, the percentiles of this trend distribution are used to quantify the uncertainty around the trend estimate. While this method is very convenient as it does not require an assumption of normality, it however fails at preserving the potential autocorrelation and heteroskedasticity of the residuals as they are resampled fully at random. Consequently, the bootstrap residual resampling is not used in this work.

4.5.3 A posteriori correction for autocorrelation

Other studies (e.g., Vigouroux et al., 2018; Zhou et al., 2018) applied the method of Santer et al. (2000) in order to correct for autocorrelation when calculating the standard errors of the trend estimates.

This method is based on the standard error for the slope estimate (β in equation Eq. 4.19):

$$S_b = \frac{S_e}{\left[\sum_{t=1}^{n}(t-\bar{t})\right]^{1/2}}, \tag{4.21}$$

with S_e^2 the variance of the residuals *e(t)* about the regression line:

$$S_e^2 = \frac{1}{n-2}\sum_{t=1}^{n} e(t)^2, \tag{4.22}$$

where *n* is the number of data points in the time-series. If the residuals *e(t)* are autocorrelated, the standard error, as estimated in Eq. 4.21, gives results that are too liberal, i.e., trends are estimated too frequently to be statistically significant. To account for the autocorrelation, Santer et al. (2000) proposed to use an "effective" sample size n_e based on the lag-1 autocorrelation coefficient r_1 of the residuals *e(t)*:

$$n_e = n\frac{1-r_1}{1+r_1}. \tag{4.23}$$

The effective sample size is then substituted in Eq. 22 to compute the standard error, accounting for the autocorrelation in the residuals. From Eq. 4.21-4.23, we see that accounting for the autocorrelation reduces the sample size and thus increases the estimated standard error.

This method was initially employed for the trend uncertainty estimations in Chapter 5.

4.5.4 Autoregressive wild bootstrap

Explicitly correcting for autocorrelation following the method described in the previous section (Sect. 4.5.3) normally requires additional estimation uncertainty for the standard error, which is not taken into account by the method of Santer et al. (2000). Indeed, the standard error as estimated in Eq. 4.21 is only an estimator of the true population standard error.

In the face of this issue, we also considered the autoregressive wild (ARW) bootstrap method (e.g., Friedrich et al., 2020b, 2020a). This modified bootstrap method is well-established in the econometric literature and was recently applied to ground-based FTIR retrievals of ethane (Friedrich et al., 2020a). The ARW bootstrap offers three major advantages compared to the previous described methods: it is applicable to (1) heteroskedastic and (2) autocorrelated time-series presenting non-negligible (3) missing observations. This last issue is indeed a common feature in ground-based FTIR observations as the technique requires clear sky conditions, causing the missing data pattern to be unpredictable.

The ARW method is an adaptation of the wild bootstrap (see, e.g., Shao, 2010). Contrary to the residual resampling described in Gardiner et al. (2008), the wild bootstrap does not perform any residual permutations and simply generates bootstrap errors and observations as:

$$z_t^* = \xi_t^* \hat{z}_t, \tag{4.24}$$

$$y_t^* = \hat{y}_t + z_t^*, \tag{4.25}$$

where z_t^* is the bootstrap error at time *t*, $\hat{z}_t$ is the residual of the fit of our linear trend model at time *t*, ξ_t^* is an independent and identically distributed random variable, with an expectation of 0 and a variance of 1, generated for each observations, $\hat{y}_t$ is the value predicted by our linear trend model at time *t* and y_t^* is the bootstrap observation. Bootstrap time-series built this way are again generated a large number of times to obtain a distribution of trends by applying the trend estimator to each of these series. As written above, the wild bootstrap does not involve any resampling of the residuals, therefore, it preserves the original missing data pattern as well as the original heteroskedasticity of the time-series. However, the wild bootstrap method needs to be further modified in situations with autocorrelation since the independence of the random variables $\{\xi_t^*\}$ destroys the dependence pattern which is present in the residuals. Thus, the ARW bootstrap generates the random variables $\{\xi_t^*\}$ as an autoregressive process of order 1 (AR(1)):

$$\xi_t^* = \gamma \xi_{t-1}^* + v_t^*, \tag{4.26}$$

where γ is the AR(1) parameter and v_t^* is an independent and identically distributed random variable with an expectation of 0 and a variance of $1 - \gamma^2$. The bootstrap errors and observations are then generated following Eq. 4.24-26. Since the $\{\xi_t^*\}$ are not independent anymore, this ARW bootstrap method will capture some of the autocorrelation of the time-series while preserving its heteroskedasticity. The choice of γ constitutes a trade-off between allowing for variation in the bootstrap samples (small γ values, falling back to the wild bootstrap) and capturing more autocorrelation ($\gamma \to 1$; Friedrich et al., 2020a). The parameter γ can either be chosen (thus acting as a tuning parameter) or determined as a function of the sample size *n*. We follow the latter case and, as suggested by Smeekes and Urbain (2014) and Friedrich et al. (2020b, 2020a), let $\gamma = 0.01^{1/l}$, with $l = 1.75n^{1/3}$.

The ARW bootstrap was recently developed and applied to Ethane FTIR time-series by Marina Friedrich (Friedrich et al., 2020a) between the research presented in Chapter 5 and Chapter 6. Therefore, this method was only used for the trend estimation of Chapter 6.

4.5.5 Nonparametric trend smoothing

In Chapter 6, several figures display smoothed trend lines. These lines are obtained using the nonparametric trend estimation technique described in Friedrich et al. (2020a, 2020b). While the linear trend model restricts the trend to be of linear shape, the advantage of the nonparametric approach is that it gives an idea of the underlying time trend without requiring such a functional form specification. At each point in the sample, this method locally approximates the underlying trend by calculating a weighted average of neighbouring observations. How many observations are included in this weighted average is determined by a bandwidth parameter *h*. To obtain the desired sensitivity to the interannual variation, the latter parameter can be chosen by the user, depending on the context of the study. Friedrich et al (2020b) also proposed a data-driven procedure to determine the bandwidth parameter. Here, for the time-series in Chapter 6, we manually chose *h*=0.1 in order to reasonably smooth the time-series while preserving the sought multiyear variability.

4.5.6 Comparison of trend uncertainty estimation methods

Table 4- 1 presents a comparison of the trend uncertainty estimation methods described in Sections 4.5.2-4. Taking the residual resampling bootstrap method (Sect. 4.5.2) as the reference, which does not

preserve the autocorrelation and the heteroskedasticity of the residuals, we see that the two other methods (i.e., the a posteriori correction for autocorrelation and the ARW bootstrap) generally widen the estimated confidence interval widths. The widening is more important when applying the a posteriori correction for autocorrelation method (Sect. 4.5.3). We particularly see how the confidence interval width is underestimated for BASCOE CTM daily output time-series when applying the residual resampling bootstrap method. Compared to the residual resampling bootstrap, the two other methods tend to deliver confidence interval widths that are closer to each other (between datasets). The a posteriori correction for autocorrelation method probably lead to overestimated confidence interval widths, which could hinder trend detection or preclude conclusions on changing trends over time.

Table 4- 1: Comparison of confidence interval widths (upper limit minus lower limit) obtained following the residual resampling bootstrap (RR bootstrap; Sect. 4.5.2), the a posteriori correction for autocorrelation (Sect. 4.5.3) and the ARW bootstrap (Sect. 4.5.4) methods. The percentages between brackets represent the widening of the confidence interval width compared to the residual resampling bootstrap. The time-series chosen for this test case are inorganic fluorine time-series from FTIR Jungfraujoch measurements (JFJ), ACE-FTS measurements (zonal mean 40-50°N) and BASCOE CTM (driven by ERA5) daily. "BASCOE sampled" is the BASCOE CTM run sampled as FTIR Jungfraujoch measurements. Observations are daily mean and have missing days of observation. These time-series are shown in Fig. 6-4.

		FTIR JFJ	ACE-FTS	BASCOE	BASCOE sampled
Trend (10^{13} molec. cm^{-2})		2.1	2.1	1.7	2.2
Confidence interval width (10^{13} molec. cm^{-2})	RR bootstrap	0.62	0.79	0.28	0.66
	A posteriori correction	1.0 (+64%)	1.1 (+38%)	0.76 (+171%)	1.1 (+73%)
	ARW bootstrap	0.88 (+42%)	0.62 (-21%)	0.59 (+110%)	0.91 (+38%)

.

Chapter 5

Improved FTIR retrieval strategy for HCFC-22 ($CHClF_2$), comparisons with in situ and satellite datasets with the support of models, and determination of its long-term trend above Jungfraujoch

Numbered sections of this chapter follow:

Prignon, M., Chabrillat, S., Minganti, D., O'Doherty, S., Servais, C., Stiller, G., Toon, G. C., Vollmer, M. K. and Mahieu, E.: Improved FTIR retrieval strategy for HCFC-22 ($CHClF_2$), comparisons with in situ and satellite datasets with the support of models, and determination of its long-term trend above Jungfraujoch, Atmos. Chem. Phys., 19(19), 12309–12324, https://doi.org/10.5194/acp-19-12309-2019, 2019.

Abstract. Hydrochlorofluorocarbons (HCFCs) are the first, but temporary, substitution products to the strong ozone depleting chloroflurocarbons (CFCs). HCFC consumption and production are currently regulated under the Montreal Protocol on Substances that Deplete the Ozone Layer and their emissions have started to stabilize or even decrease. As HCFC-22 ($CHClF_2$) is by far the most abundant HCFC in today's atmosphere, it is crucial to continue to monitor the evolution of its atmospheric concentration. In this study, we describe an improved HCFC-22 retrieval strategy from ground-based high-resolution Fourier Transform InfraRed (FTIR) solar spectra recorded at the high-altitude scientific station of Jungfraujoch (Swiss Alps, 3580 m above mean sea level). This new strategy distinguishes tropospheric and lower-stratospheric partial columns. Comparisons with independent datasets (the Advanced Global Atmospheric Gases Experiment/AGAGE and the Michelson Interferometer for Passive Atmospheric Sounding/MIPAS) supported by models (the Belgian Assimilation System for Chemical ObErvation/BASCOE and the Whole Atmosphere Community Climate Model/WACCM) demonstrate the validity of our tropospheric and lower-stratospheric long-term time-series. A trend analysis on the datasets used here, now spanning thirty years, confirms the last decade's slowing down of the HCFC-22 growth rate. This updated retrieval strategy can be adapted for other ozone-depleting substances (ODSs) as CFC-12, for example. Measuring or retrieving ODS atmospheric concentrations is essential to scrutinise the fulfilment of the globally ratified Montreal Protocol.

Additional discussion elements are given at the end of the chapter. Almost up-to-date total columns and tropospheric time-series are shown. We also reassess the last decade trend to further emphasize the recent slowing down of HCFC-22 accumulation rates.

5.1 Introduction

Chlorodifluoromethane ($CHClF_2$), also known as HCFC-22 (hydrochlorofluorocarbon-22), is an anthropogenic constituent of the atmosphere. It is mainly produced today for domestic and industrial refrigeration systems. As HCFC-22 is a chlorine-containing gas, it is responsible for stratospheric ozone loss and is regulated by the Montreal Protocol on Substances that Deplete the Ozone Layer. HCFC-22 has a global total atmospheric lifetime of 12 years (9.3–18 years; SPARC, 2013) and its ozone depletion potential is 0.034 (WMO, 2014). HCFC-22 also has a significant global warming potential (1760 on a 100-year time horizon; IPCC, 2013).

As HCFCs are the first, but temporary, substitution products for the now banned CFCs, their emissions have been on the rise. Despite the large bank of HCFC-22 remaining in refrigeration systems, HCFC-22 emissions should decrease; this is owing to the fact that the Montreal Protocol and its 2007 adjustment planned a 97.5-100% reduction of the overall production of HCFC by 2030 for all countries. HCFC-22 emissions actually increased before 2007 but have been constant since then (Montzka et al., 2009, 2015; WMO, 2014; Simmonds et al., 2017). In their recent study, Simmonds et al. (2017) determined global HCFC-22 emissions to be 360.6±58.1 Gg yr^{-1} – representing about 79% of total HCFC emissions – and a global mean mole fraction of 234±35 pmol mol^{-1} for the year 2015. These results are in good agreement with previous studies of Montzka et al. (2009, 2015) and the 2014 WMO report on ODS. The 2004–2010 trends (in percent per year relative to 2007) are 3.97±0.06, 3.52±0.08 and 3.7±0.1 derived from in situ, ground-based FTIR and satellite measurements, respectively (WMO, 2014). Yearly global mean growth rates reached a maximum of 8.2 pmol mol^{-1} yr^{-1} in 2007 and decreased by 54% to 3.7 pmol mol^{-1} yr^{-1} in 2015 (Simmonds et al., 2017). Global mean mole fractions of HCFC-22 are predicted to decrease by the year 2025 in the baseline scenario of the 2014 WMO report (see Fig. 5-2 and Table 5A-2 in the WMO report).

Nowadays, two global networks collect and share HCFC-22 in situ and flask measurements: the Advanced Global Atmospheric Gases Experiment (AGAGE) and the National Oceanic and Atmospheric Administration/Halocarbons and other Atmospheric Trace Species Group (NOAA/HATS). Alongside these “in situ” networks, remote-sensing measurements using the FTIR technique also contribute to the monitoring of HCFC-22. FTIR measurements are performed from balloon-borne (e.g. Toon et al., 1999), space-borne and ground-based platforms. MIPAS provided HCFC-22 satellite limb emission measurements from July 2002 to April 2012 (e.g. Chirkov et al., 2016). ACE-FTS is the only other space experiment to retrieve HCFC-22 atmospheric abundance (e.g. Nassar et al., 2006). ACE-FTS has been performing solar occultation since August 2003, although the SCISAT satellite mission was originally planned to last 2 years (Bernath et al., 2005). Finally, in the framework of the NDACC network (De Mazière et al., 2018; http://www.ndacc.org, last access: 30 September 2019), more than 20 ground-based stations, spanning latitudes from pole to pole, record high-resolution solar spectra with FTIR instruments. Note that only a minority of these stations currently retrieve HCFC-22 abundance.

All of these measurement techniques put together enable the atmospheric scientific community to verify the fulfilment of the protocols protecting stratospheric ozone (Montreal Protocol) and reducing greenhouse gas emissions (e.g. the Kyoto Protocol and the Paris Agreement). The necessity of these verifications was most recently highlighted by the detection of an unexpected increase of global emissions of CFC-11 (Montzka et al., 2018).

The purpose of this study is to improve our HCFC-22 retrieval strategy such as to enhance and maximize the information content, in order to retrieve partial columns from high spectral resolution FTIR solar absorption spectra (Sect. 5.3). The resulting tropospheric and lower-stratospheric updated time-series are compared to independent datasets and to models (Sect. 5.4). Moreover, a trend analysis is performed in order to separate distinct HCFC-22 growth rate time periods (Sect. 5.5).

5.2 FTIR observations at Jungfraujoch

The Jungfraujoch scientific station (JFJ), affiliated with the NDACC network, is located on the northern margin of the Swiss Alps at 3580m a.m.s.l. Thanks to its high elevation, the station is usually under free troposphere conditions with less than 45% of air coming from the planetary boundary layer (PBL) on average (Collaud Coen et al., 2011). Consequently, the station can be considered as a "mostly remote site" (Henne et al., 2010) and experiences atmospheric background conditions over central Europe. This peculiar location also enables the study of the mixing of the PBL and the free troposphere (Reimann, 2004). Indeed, the station can receive polluted air during events such as frontal passages, Föhn (Zellweger et al., 2003; Uglietti et al., 2011) or thermal uplift from the surrounding valleys (Baltensperger et al., 1997; Zellweger et al., 2000; Henne et al., 2005).

Since the mid-1980s, very high-resolution (0.003-0.006 cm^{-1}) infrared solar spectra have been regularly recorded at the Jungfraujoch station, under clear-sky conditions using wide band-pass FTIR spectrometers. In this study, spectra from the two JFJ FTIR spectrometers are exploited, i.e. a homemade instrument (1984 to 2008) and a modified Bruker IFS 120HR spectrometer (early 1990s to present). More information on these two instruments is available in Zander et al. (2008). The spectra relevant to our study encompass the 700-1400cm^{-1} range (HgCdTe detectors) and have been recorded at two different spectral resolutions: 0.0061 and 0.004 cm^{-1}, corresponding to maximum optical path differences of 81.97 and 125 cm, respectively.

5.3 HCFC-22 retrieval

5.3.1 Spectroscopy

HCFC-22 presents strong absorption band systems in the infrared spectral region (Harrison, 2016): the main features are the Coriolis-coupled doublets ν_3 (~1108.7 cm^{-1}) and ν_8 (~1127.1 cm^{-1}) and the Q-branches ν_4 (~809.3 cm^{-1}) and $2\nu_6$ (~829.1 cm^{-1}). The well-isolated but unresolved $2\nu_6$ Q- branch is one of the narrowest and most intense features of HCFC-22. Thus, it has been intensively used in FTIR studies from various platforms (e.g., Irion et al., 1994; Zander et al., 1994; Sherlock et al., 1997; Toon et al., 1999; Rinsland, 2005; Nassar et al., 2006; Chirkov et al., 2016; Zhou et al., 2016). As no resolved linelists are available for such relatively heavy molecules, one has to work with laboratory absorption cross-section spectra. In order to interpolate or extrapolate these cross-sections at temperatures and pressures spanning the atmospheric conditions, we use a pseudo-linelist (PLL) developed by one of the authors of this paper (Geoffrey C. Toon, available at: https://mark4sun.jpl.nasa. gov/pseudo.html, last access: 30 September 2019). The PLL used here was built by fitting the cross-sections calculated by McDaniel et al. (1991) and Varanasi et al. (1994). The main interfering species in the windows investigated to establish our retrieval strategy (see next section) are H_2O, CO_2 and O_3, and their line-by-line spectroscopic parameters are taken from HITRAN 2008 (Rothman et al., 2009a).

5.3.2 Strategy

The profile inversions and column retrievals are performed with the SFIT-4 v0.9.4.4 algorithm which implements the optimal estimation method (OEM) developed by Rodgers (2000). This tool corresponds to an upgrade of the SFIT-2 retrieval algorithm Rinsland et al. (1998). We consider a 41-layer atmosphere model (above Jungfraujoch) spanning the 3.58 to 120 km altitude range, with thicknesses progressively increasing from ~0.65 km at the surface up to 14 km for the uppermost layer. The assumed pressure-temperature and a priori water vapour profiles are provided by the National Centers for Environmental Prediction reanalysis (NCEP; Kalnay et al., 1996) and extrapolated above 55km by outputs from the Whole Atmosphere Community Climate Model v4 (WACCM, see Sect. 5.4.1.4). A priori profiles of HCFC-22 and all interfering species, with the exception of water vapour, are also computed from a climatology of WACCM v4 outputs for the 1980-2020 time period. The solar line compilation supplied by Hase et al. (2006) has been assumed for non-telluric absorptions.

Three spectral ranges encompassing the $2\nu_6$ Q-branch (829 cm^{-1}) as well as the ν_4 (809 cm^{-1}) and the ν_3 (near 1100 cm^{-1}) features have been tested for the HCFC-22 retrieval at JFJ. For the latter, it rapidly appeared that the results were not consistent. The corresponding columns were indeed excessively large, by more than 20%, suggesting a discrepancy in intensity in the original cross-section data used to generate the PLL or a missing interference in this window. Thus, two windows were defined: 808.45-809.6 cm^{-1} (window 1) and 828.75-829.4 cm^{-1} (window 2). Moreover, two main regularizations (see Sect. 4.2.3), OEM and a Tikhonov-type L1 regularization (e.g., Steck and Clarmann, 2001; von Clarmann et al., 2003; Sussmann et al., 2009), were tested to optimize the information content while keeping plausible retrieved profiles and minimizing the error budget.

The optimization of the retrieval strategy was performed using a subset of 598 spectra from the Bruker instrument covering the years 1998 and 2015. Window 1 fitted alone gives poor results regardless of the regularization chosen. Considering only the OEM regularization (20% assumed for the diagonal terms of the a priori covariance matrix, Sa), more information is retrieved fitting both windows together. However, this strategy leads to the determination of unrealistic vertical distributions with the maximum concentration located in the lower stratosphere. The Tikhonov regularization leads to substantially better results (i.e. realistic profiles and more information retrieved) than the OEM regularization for any combination of windows. Regarding the choice between fitting only window 2 or both windows together, it appears that the first option enables retrieval of more information and robust vertical distributions, reducing the occurrence of profiles with negative values. The determination of the Tikhonov regularization strength (i.e. alpha parameter) has been performed by minimizing the smoothing and the measurement errors (Steck, 2002), eventually leading to a value of nine. As the homemade instrument has a different point spacing (6.102×10^{-3} cm^{-1}) than the Bruker instrument (3.767×10^{-3} cm^{-1}), the relationship (Eq. 5.1) advised by Sussmann et al. (2009) is applied in order to harmonize the regularization between both instruments:

$$\frac{\alpha_1}{\alpha_2} = \frac{p_2}{p_1}, \tag{5.1}$$

where α_x represents the Tikhonov strength parameters, and p_x represents the instrument point spacings.

Figure 5- 1 shows the selected window and the simulations performed by the SFIT-4 algorithm for HCFC-22 and the interfering species. These fits are typical of the spectral database in terms of signal-

to-noise ratio (SNR), root-mean- square residuals, degree of freedom for signal (DOFS) and solar zenith angle. Note the good results obtained with the homemade instrument (Figure 5- 1a, c) despite the weaker absorption (3%) and noisier spectra when compared to the Bruker results (Figure 5- 1b, d). The final settings include an ozone profile retrieval, whereas the CO_2 and H_2O a priori columns are simply scaled. Note that all of the other interfering species are simulated but not adjusted, and their a priori profiles are also computed from WACCM v4 outputs. Their overall contribution is less than 0.5% and is thus negligible.

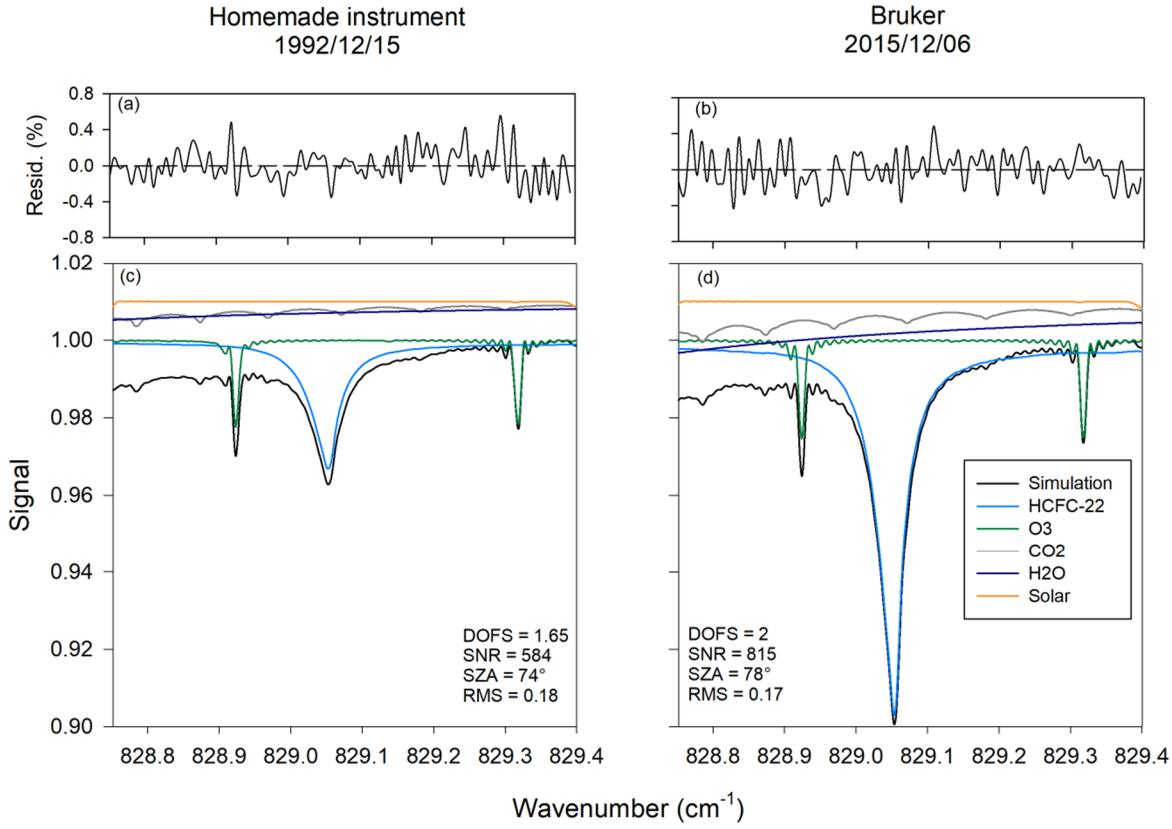

Figure 5- 1: Simulations of the 828.5–829.4 cm^{-1} spectral window from spectra recorded by the homemade (15 December 1992) and the Bruker (6 December 2015) FTIR instruments at Jungfraujoch. CO_2, H_2O and solar spectra are offset vertically for clarity. Panels (**a**) and (**b**) display relative residuals (%) from the fits to the spectra. These fits are typical of the spectra database in terms of signal-to-noise ratio (SNR), root-mean-square error (RMS), degrees of freedom for signal (DOFS) and solar zenith angle (SZA), regarding their respective year. Note that the vertical scales in (**c**) and (**d**) correspond to only 10% of the signal amplitude.

5.3.3 Information content and error budget

The information content obtained from the retrieval processing has been objectively evaluated via the careful inspection of the averaging kernel matrices. The averaging kernel matrix ($\boldsymbol{A}$) describes how the a priori ($\boldsymbol{x_a}$) and the true ($\boldsymbol{x_t}$) vertical profiles contribute to the retrieved vertical distribution ($\boldsymbol{x_r}$), according to Eq. (5.2).

$$\boldsymbol{x_r} = \boldsymbol{x_a} + \boldsymbol{A}(\boldsymbol{x_t} - \boldsymbol{x_a}). \quad (5.2)$$

For the Bruker instrument, the mean column averaging kernel (Figure 5- 2a), as well as the leading eigenvalues and eigenvectors (Figure 5- 2b; see e.g. Barret et al., 2002), have been calculated on the basis of the 2015 retrievals subset. The mean DOFS, the trace of averaging kernel matrix or sum of

eigenvalues, is 1.97, meaning that two pieces of information can be extracted from the retrievals. Moreover, the second eigenvector (Figure 5- 2b), with a value of 0.85, indicates that one can extract tropospheric (from surface to 11.21 km; as defined by the intersection of the eigenvector with the vertical axis) and lower-stratospheric (11.21 to 30 km) columns from the retrieved total columns with 85% of the information coming from the retrieval itself. Concerning the homemade instrument, based on the 1992 retrievals subset, the mean DOFS is 1.73. The eigenvectors are identical to the Bruker's, but the eigenvalue for the second eigenvector is 0.68. Finally, note that the Bruker instrument recorded lower SNR values during the year 2012 (30% lower than 2015). Consequently, a slightly lower DOFS (1.89) and a second individual eigenvalue (0.8) are retrieved for this time period.

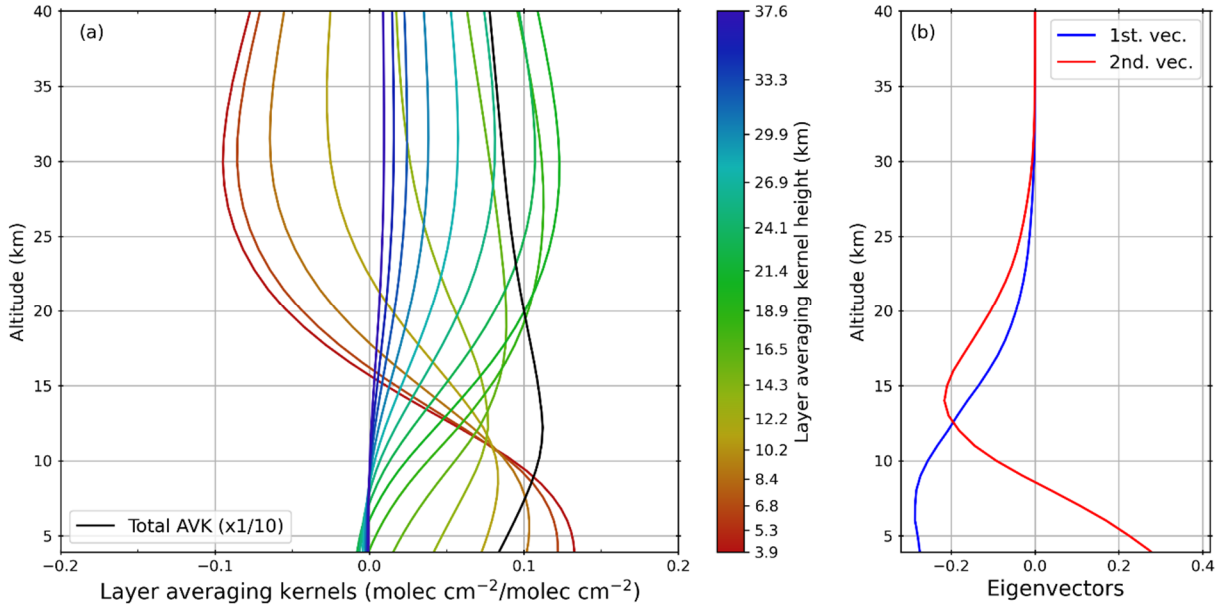

Figure 5- 2: Mean layer averaging kernels (**a**) normalized for partial columns (molec cm–2/molec cm–2) and eigenvectors (**b**) characterizing the FTIR retrievals of HCFC-22 above Jungfraujoch from spectra recorded in 2015 by the Bruker instrument. The ticks on the colour bar are the individual layer averaging kernels represented in the plot. The first eigenvector has a value of 1 for both instruments, and the second eigenvector has a value of 0.68 and 0.85 for the homemade and Bruker instruments, respectively.

As fully described in Zhou et al. (2016), in the formalism of Rodgers (2000), the final state equation can be rewritten in order to express the total error in four components: the smoothing error, the forward model error ε_F, the measurement error ε_y and the forward parameter error $K_b\varepsilon_b$. This last component "comes from the atmospheric (temperature, a priori profiles, pressure, etc.), geometrical and instrumental parameters" (Zhou et al., 2016).

For the computation of the smoothing error components, we created the random part of the $\boldsymbol{S_a}$ matrix by computing the relative standard deviation in HCFC-22 retrievals from MIPAS. The systematic component of the $\boldsymbol{S_a}$ matrix was created using the mean relative difference between ACE-FTS and MIPAS HCFC-22 retrievals. Regarding the off-diagonal elements, the interlayer correlation width has been set to 3 km. We assumed 5% relative systematic uncertainties for the spectroscopic parameters of HCFC-22 as assessed by G. C. Toon. We also assumed 5% for O_3 as reported in the HITRAN 2008 dataset (Rothman et al., 2009a).

Results of the error budget are presented in Table 5- 1. While the systematic errors are commensurate for both instruments (5.5%), the random errors differ significantly from one instrument to the other

(5.6% of total random error for the homemade instrument and 2.7% for the Bruker instrument; this order will be implicit in the following). This difference is mainly due to the random measurement error (4.7%/ 1%). The homemade instrument records lower SNRs than the Bruker instrument (85% of relative difference on coincidences after 2001). Moreover, the homemade instrument was mostly operated over a time period with a lower HCFC- 22 abundance, so the HCFC-22 absorptions are therefore weaker in spectra recorded by the homemade instrument, as is obvious from Figure 5- 1 (median absorption of 3% compared with 7% for the Bruker). For the systematic component of the error budget, HCFC-22 line intensities (5%) as well as temperature (1.8%) stand as the larger sources of uncertainty.

Table 5- 1: Mean relative errors (%) for both instruments (homemade and Bruker) affecting the total column retrievals of HCFC-22 for the years 1992 (homemade instrument) and 2015 (Bruker). See notes and text (Sect. 5.3.3) for more information on the values assumed and the methods.

Error type (%)	Homemade	Bruker	Notes
Random			
Measurement	4.7	1	OEM formalism
Temperature	2		
SZA	1.15		Assuming 0.1° for solar pointing
Zero level offset	1		
Interfering species	0.9	0.3	
Smoothing	0.8	0.3	OEM formalism
Retrieval parameters	0.5	0.1	OEM formalism
Total random	5.6	2.7	
Systematic			
HCFC-22 line intensity	5		Assuming 5% from pseudo-linelist
Temperature	1.85		
Zero level offset	1		
HCFC-22 air-broadening of line width	0.9	0.45	
Retrieved interfering species (i.e., O_3) line intensity	0.43	0.13	Assuming HITRAN 2008 uncertainty
Total systematic	5.5		

Finally, we also investigated the possible effect of a misalignment of the Bruker instrument for the year 2012. We assess the instrumental line shape random error by assuming an effective apodization of 0.9 (a value of 1 corresponds to a perfectly aligned instrument), a value consistent with our HBr cell spectra analysis. We find that such an apodization perturbation has a negligible effect on our retrieved total columns (less than 0.01 %). The error is larger for partial columns: 1.2% and 0.6%, for lower-stratospheric and tropospheric columns, respectively.

5.3.4 Results

Monthly HCFC-22 columns retrieved using the strategy described in the previous section are presented in Figure 5- 3. Due to direct local pollution caused by HCFC-22 leaks after the installation of new elevators in the JFJ scientific station (Zander et al., 2008), observations from the Bruker instrument from 1996 to the end of 2002 have been discarded. The homemade instrument was operated in the dome at the top of the station, almost outdoors, and was, therefore, practically not polluted (Zander et al., 2008). Retrievals with unusually poor residuals, a low SNR, negative values in profiles or that did not converge

have been rejected. This corresponds to less than 8% of the whole dataset. Results include 7302 spectra spanning 1627 days and 272 different months of observations. The overlapping period (2003-2006) in the inset of Figure 5- 3 demonstrates the very good agreement between the two instruments, enabling us to treat our time-series uniformly, without harmonization nor scaling.

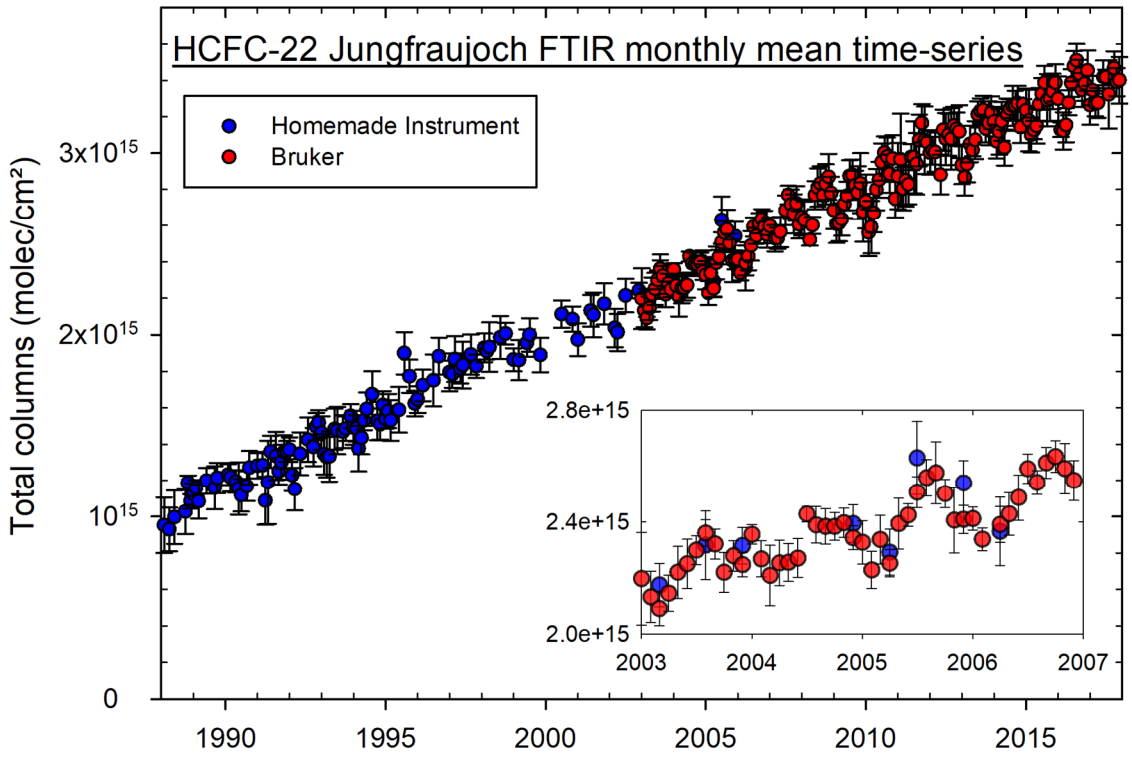

Figure 5- 3: FTIR monthly time-series of HCFC-22 total columns above Jungfraujoch derived from spectra recorded by the homemade FTIR (blue) as well as by the Bruker IFS 120HR (red). Vertical bars are the standard deviations around the monthly means. Due to pollution events starting in 1996 that mainly influenced the Bruker instrument, observations retrieved from the Bruker spectra are discarded before 2003. Note the excellent agreement between the two instruments (inset frame).

5.4 Improved HCFC-22 FTIR time-series above JFJ and comparisons with independent datasets

5.4.1 Description of independent datasets

5.4.1.1 In situ measurements

We include surface AGAGE data from the Mace Head (MHD; 55.33°N, 9.9°W, Ireland) and JFJ stations. At MHD, HCFC-22 measurements were initially carried out by a GC-MS ADS system (gas chromatography-mass spectrometry adsorption/desorption system; Simmonds et al., 1995) from January 1999 to December 2004. In June 2003, a GC-MS Medusa system (Miller et al., 2008) was installed and the sampling frequency was doubled (every 2 h). HCFC-22 measurements at the AGAGE JFJ station have been performed by a GC-MS Medusa system since August 2012. For each measurement, 2L of sample is preconcentrated on a trap filled with HayeSep D and held at ~−160°C. After desorption at 100°C, the compounds are separated and detected by GC-MS. HCFC-22 measurements are reported relative to the Scripps Institution of Oceanography-2005 (SIO-2005) primary calibration scale, leading to an estimated absolute accuracy of 2% (Simmonds et al., 2017). Finally, an iterative AGAGE pollution identification statistical procedure (e.g., O'Doherty et al., 2001; Cunnold et al., 2002) is applied to build

"baseline" mole fraction time-series representative of broad atmospheric regions. This method has excellent performance compared with back trajectory methods as discussed in O'Doherty et al. (2001).

5.4.1.2 Satellite observation

HCFC-22 columns retrieved from MIPAS limb soundings (Fischer et al., 2008) are included for the comparison to our lower-stratospheric time-series. Envisat, the satellite carrying MIPAS, was launched on 1 March 2002 and its mission ended on 8 April 2012 after a loss of communication. Here we use version V5R of MIPAS HCFC-22 retrievals described in Chirkov et al. (2016). All of the spectra included are recorded in the so-called "reduced resolution mode", i.e. 0.12 cm^{-1}. Data are filtered as advised: only observations characterized by a visibility flag of 1 and diagonal terms of the averaging kernel matrix greater than 0.03 are kept.

5.4.1.3 BASCOE CTM

BASCOE CTM and the set-up used for this chapter are described in Sect. 3.2 and Sect. 3.3 of this thesis manuscript. Here BASCOE CTM is driven by ERA-Interim. For this study, we only used the HGGC dataset for the lower boundary conditions of atmospheric constituent concentrations (their extension was not available yet; see Sect. 3.3.2). Therefore, the BASCOE CTM lower-stratospheric time-series showed in this chapter ends in December 2014.

5.4.1.4 WACCM

WACCM is a high-top chemistry climate model developed at NCAR (National Center for Atmospheric Research, Boulder, Colorado). It is a configuration of CAM (Community Atmosphere Model), the atmospheric model of the NCAR coupled Community Earth System Model. For an extensive description, see Garcia et al. (2007) and Garcia et al. (2017) for WACCM and Neale et al. (2013)for CAM.

In this study we use WACCM version 4 (WACCM4), which presents several extensions to the physical parameterization with respect to CAM version 4, such as the addition of the constituent separation velocities to the molecular diffusion, the modification of the gravity wave drag, a new long-wave and solar radiation parameterization above 65 km, and a new ion and neutral chemistry model. WACCM uses a finite volume (FV) dynamical core (Lin and Rood, 1996) for the horizontal discretization. The chemistry scheme used in WACCM4 is MOZART version 3 (Kinnison et al., 2007), which contains 52 neutral species, 1 invariant (N_2), 127 neutral gas-phase reactions, 48 neutral photolysis reactions and 17 heterogeneous reactions. HCFC-22 was not present in the default chemistry scheme and was therefore added. In this study, WACCM is run on a 1.9°×2.5° horizontal grid and on a 66 vertical levels grid, with the default time step of 30 min.

Here, we use a free-running (FR-WACCM) configuration, where the dynamical fields are computed online along with the chemistry and radiation modules. This configuration differs from the specified dynamics (SD-WACCM) option where the dynamical fields are nudged to a meteorological reanalysis (Froidevaux et al., 2018). The simulation covers the 1984-2014 period, starts from the same initial condition as the BASCOE CTM simulation and uses the same HGGC data produced by Meinshausen et al. (2017) as the lower boundary condition.

5.4.2 Data intercomparison methods

We perform the smoothing of MIPAS and model vertical profiles by the averaging kernels of our FTIR retrievals following the method described in Sect. 4.3 of the thesis manuscript. To do so, MIPAS and model vertical profiles are first interpolated on the FTIR retrieval grid using a mass-conservative vertical regridding algorithm (Sect. 4.3.1).

The mean relative differences given in Sect. 5.4.3 and 5.4.4 are reported in terms of fractional differences (FD) along with their 1σ standard deviation:

$$FD = 100\ \% \times \frac{1}{N}\sum_{i}^{N} \frac{O_{x(i)} - O_{y(i)}}{[O_{x(i)} + O_{y(i)}]/2}, \tag{5.3}$$

where N is the number of coincidences between the compared datasets O_x and O_y (Strong et al., 2008), O_x being our FTIR time-series when compared.

5.4.3 Comparison of lower-stratospheric columns

Figure 5- 4 depicts the good agreement between the JFJ Bruker and MIPAS (at ±5◦ latitude around JFJ) lower-stratospheric columns (from 11.21 to 30 km for all data sources). The comparisons of this section are performed on the datasets' common time period, i.e. from 2005 to 2012.

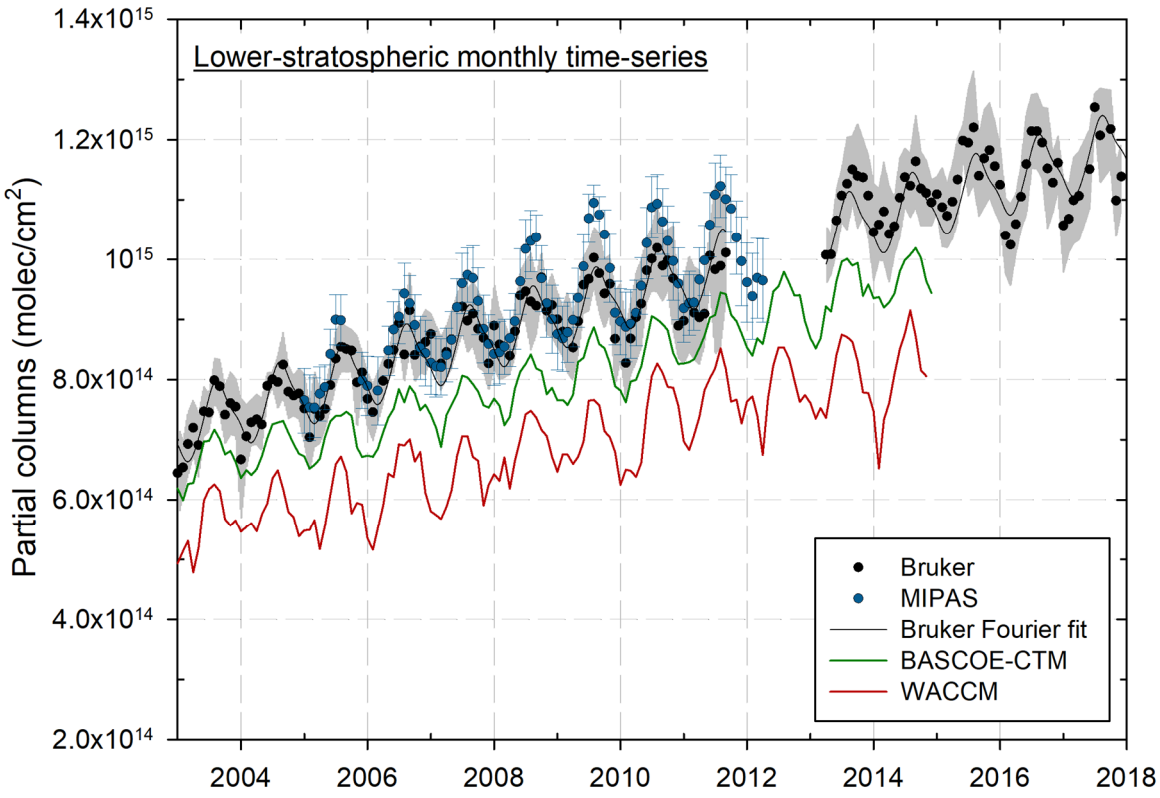

Figure 5- 4: Time-series of lower-stratospheric partial columns (11.21–30 km, as defined by the retrieval information content) above Jungfrau- joch (MIPAS at ±5◦ latitude around JFJ). The grey shaded area and the blue vertical bars depict the standard deviation around the FTIR and the MIPAS monthly means, respectively. A Fourier series fitted to the Bruker time-series (black curve) is also represented (see Sect. 5.5). FTIR partial columns from the middle of 2011 to the middle of 2013 are not displayed because of the lower quality retrievals observed during this time-period (see Sect. 5.3.3).

The mean relative difference between JFJ Bruker and MIPAS is –4.64±6.09%, which is within the range of the systematic error estimated for our measurements (5%; see Sect. 5.3.3). The BASCOE CTM time-series is slightly lower than these two datasets with a 9.80±5.19% mean relative difference to the JFJ Bruker time-series. WACCM lower- stratospheric columns are far too small with respect to the other datasets; the mean relative difference with the JFJ Bruker data is 26.4±9.39 %.

As shown in Figure 5- 5, the four datasets are almost in perfect agreement for the lower-stratospheric seasonality (note that we only use MIPAS measurements performed at a maximum distance of 500km from JFJ station here). The lower-stratospheric annual cycle is computed by subtracting the time-series' calculated linear trend from the monthly mean lower-stratospheric columns. Maximum values of HCFC-22 lower-stratospheric columns are found in August whereas low values are seen in February. This seasonality is also pointed out by Chirkov et al. (2016) and is related to the seasonal cycle of the Brewer–Dobson circulation. The same version of BASCOE CTM was recently used to calculate the mean age of air from ERA-Interim reanalysis (Chabrillat et al., 2018) resulting, for this latitude band of the lower stratosphere, in an annual cycle reaching maximum values in February-March and minimum values at the beginning of August. This result illustrates the young tropical air flooding the extratropical lower stratosphere during boreal summer due to the weaker mixing barrier formed by the subtropical jet (Chirkov et al., 2016).

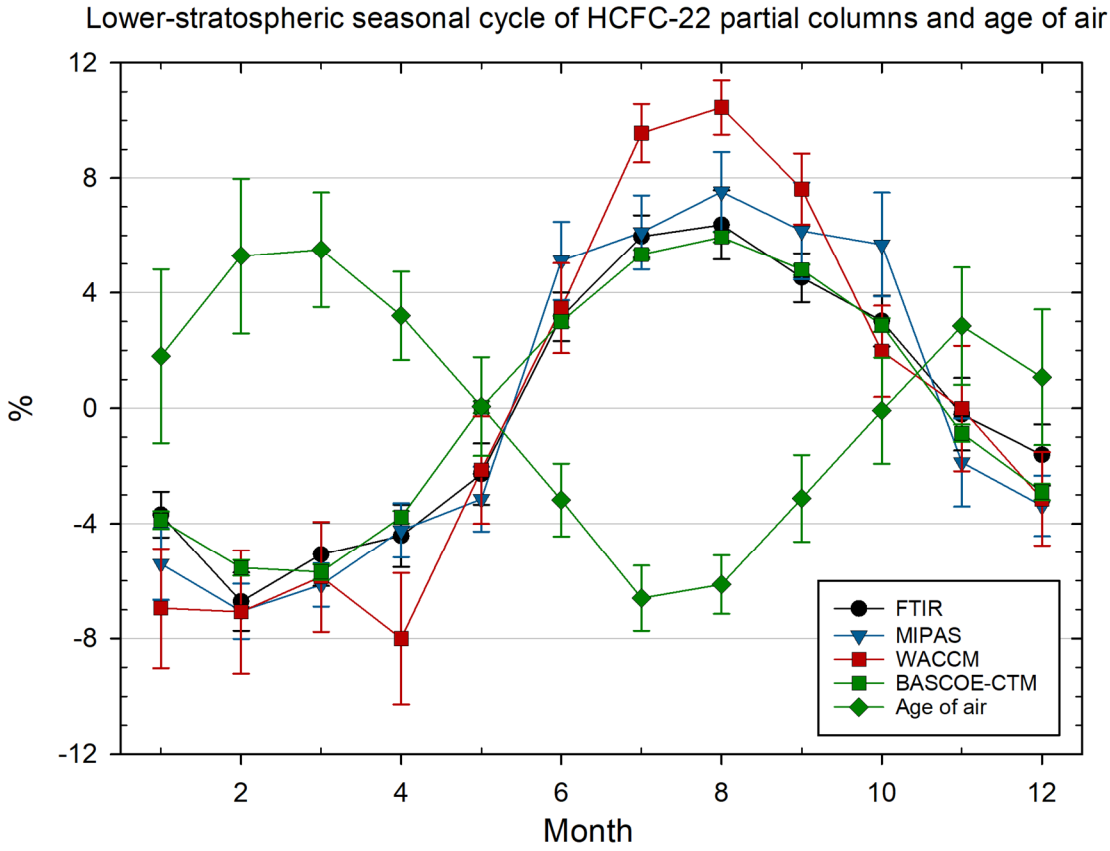

Figure 5- 5: Seasonal cycle of HCFC-22 columns (see Sect. 5.4.3 for method) in the lower stratosphere (11.21–30 km) based on measurements and model outputs (2005-2012). MIPAS measurements are at a maximum distance of 500 km from the JFJ station. Vertical bars depict the 2σ standard error of the means. The age of air simulation is performed by BASCOE-CTM from the ERA-Interim reanalysis. The peak-to-peak amplitude of the age of air cycle is 0.37 years and the mean age of air is 2.96 years.

5.4.4 Comparison of mean tropospheric mixing ratios

Figure 5- 6 compares the averages of all the layers between the surface and 11.21 km altitude of our HCFC-22 retrieved mixing ratio profiles (FTIR mean tropospheric mixing ratio hereafter) with AGAGE in situ time-series. Note that the FTIR-retrieved mixing ratios correspond to moist air values whereas AGAGE measurements are reported as dry air mole fractions. The difference between the two should be insignificantly small because of the very dry air conditions experienced at JFJ (Mahieu et al., 2014b; Lejeune et al., 2017).

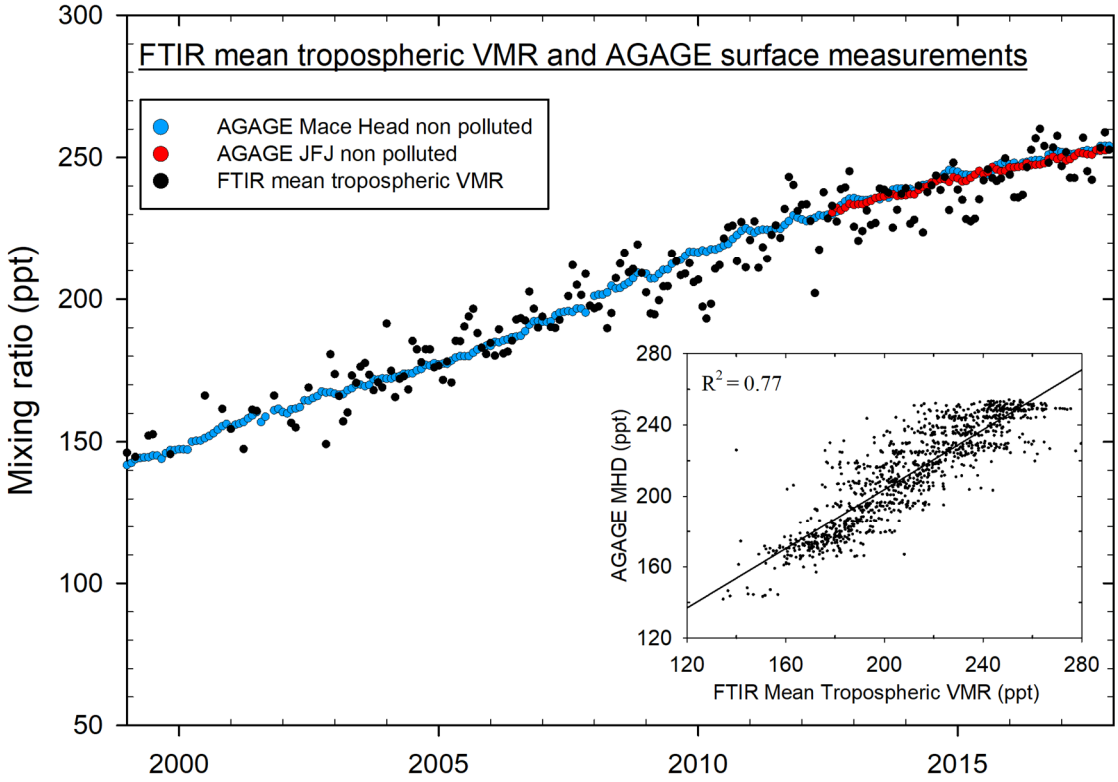

Figure 5- 6: Tropospheric monthly time-series at Jungfraujoch. The FTIR time-series (black) is constructed by taking the average of all of the layers below 11.21 km, the altitude limit objectively defined by the retrieval information content. AGAGE in situ time-series from Mace Head (light blue) and JFJ (red) are baseline measurements (see Sect. 5.4.1.1). Daily coincidences between Mace Head and FTIR are depicted in the inset scatter plot. The coefficient of determination of the linear regression, R2, is 0.77 (R = 0.88).

MHD and JFJ AGAGE baseline data agree very well for their common period (2012-2018) with relative extreme differences ranging from −1.82% to 4.70% and a mean relative difference of 0.50±0.82%, with MHD recording higher concentrations. Unfiltered time-series show similar results, with relative differences ranging from −4.1% to 5% and a mean relative difference of 0.51±0.97%.

Comparisons between the FTIR mean tropospheric mixing ratio and the MHD daily averaged baseline measurements, over the 1999–2018 time period, demonstrate a good consistency between the two datasets. The mean relative difference is −1.11±6.61% with extreme values ranging from −47% to 23%. The scatter plot between the FTIR mean tropospheric mixing ratio and the MHD daily mean coincidences (inset of Figure 5- 6) shows the good correlation that exists between the two datasets (coefficient of determination of the linear regression, R^2, is 0.77). Plotted monthly mean time-series (Figure 5- 6) confirm the overall consistency over time between the FTIR mean tropospheric mixing ratios and the AGAGE datasets.

As BASCOE CTM and WACCM simulations have the same lower boundary condition, the simulated tropospheric mean mixing ratios are close to each other with a BASCOE CTM-WACCM mean relative difference of 4.18±1.94% (not shown) for the whole simulation period. We also note good agreement between BASCOE CTM and MHD, with BASCOE CTM being 3.67±0.99% lower than MHD for the 1999–2014 time period. This result is not surprising as Meinshausen et al. (2017) included AGAGE measurements to build their historical greenhouse gas concentration dataset, but it gives confidence in the proper application of the lower boundary condition in both models.

Our tropospheric time-series displays a similar seasonal cycle in phase as the lower-stratospheric time-series (7% peak-to-peak amplitude; not shown). However, Xiang et al. (2014) demonstrated that the HCFC-22 surface concentration annual cycle has a weak amplitude, with broad minima in summer and broad maxima in winter. Chirkov et al. (2016) also noticed a significant tropospheric cycle in their MIPAS upper tropospheric mixing ratio time-series, in contrast with the in situ data considered in their paper. They attributed this difference to the fact that their time-series was capturing the intrusion of HCFC-22-poor stratospheric air into the mid- latitude upper troposphere/lower stratosphere (UTLS) at the time of the polar vortex breakdown (late winter/early spring). The effect of the polar vortex breakdown was also observed on nitrous oxide and chlorofluorocarbons in the UTLS by Nevison et al. (2004). This difference in the annual cycle between the situ and FTIR time-series could also be artificially amplified by the fact that our retrievals do not have a constant vertical sensitivity (see total averaging kernels in Figure 5- 2) and present a sensitivity peak in the UTLS, where the cycle is dominant compared to lower-altitude signals (see lower left frame of Fig. 15 in Chirkov et al., 2016). Note that this difference causes the layered structure (FTIR data spread around the in situ values) of the scatter plot in Figure 5- 6.

5.5 Trend analyses

Trend in this chapter are estimated applying the linear model described in Sect. 4.5.1 of the thesis manuscript. The uncertainty around the estimated trend values are obtained using the a posteriori correction for correlation (Santer et al., 2000; Sect. 4.5.3). Along with the absolute trend values, we also compute relative trend values, taking the yearly mean of the middle year of the considered period as a reference. The trend analysis is applied to all of our partial column subsets, i.e. total columns, tropospheric columns (from ground to 11.21 km) and lower-stratospheric columns (11.21 to 30 km).

The overall multidecadal 1988-2017 HCFC-22 total column trend is $8.13\pm0.08\times10^{13}$ molec cm^{-2}. The trends for the tropospheric and lower-stratospheric columns, computed over the same time period, are $5.1\pm0.1\times10^{13}$ molec cm^{-2} and $2.99\pm0.05\times10^{13}$ molec cm^{-2}, respectively.

Table 5- 2: HCFC-22 total columns trends over JFJ. The uncertainties are given for the 2σ level following the Santer et al. (2000) approach. Models trends are underlined when not significantly different from observations. Relative trends (% yr^{-1}) are given with respect to the yearly mean of the middle year of the considered period.

Total columns trends (10^{+13}molec cm^{-2} yr^{-1})	1988–2017	1988–1997	1996–2005	2005–2014	2008 –2017
FTIR	8.13 ± 0.08 (3.75 ± 0.04)%	8.52 ± 0.57 (5.88 ± 0.39)%	7.09 ± 0.37 (3.41 ± 0.18)%	8.6 ± 0.28 (3.03 ± 0.1)%	7.98 ± 0.29 (2.57 ± 0.09)%
BASCOE		7.21 ± 0.1 (5.3 ± 0.07)%	6.94 ± 0.15 (3.57 ± 0.08)%	8.98 ± 0.2 (3.35 ± 0.08)%	–
WACCM		6.63 ± 0.13 (5.16 ± 0.1)%	6.3 ± 0.12 (3.41 ± 0.07)%	8.53 ± 0.2 (3.36 ± 0.08)%	–

The decadal trends calculated on total columns (Table 5- 2) show relatively high values for the late 1980s and early 1990s, i.e. 8.52±0.57×10^{13} molec cm^{-2} for 1988–1997. The uncertainty is also greater due to the poorer sampling during this period. The models show significantly lower trends for the same time period. Temporarily lower trend values are then observed, 7.09±0.37×10^{13} molec cm^{-2} for 1996–2005, before again reaching the same values as during the late 1980s, i.e. 8.6±0.28×10^{13} molec cm^{-2} for 2005-2014. This evolution is well captured by the models, although WACCM shows systematically lower absolute trend values. Finally, the HCFC-22 accumulation rate seems to slow down in the most recent time period (2008-2017). The models cannot support this later observation as the simulations end in 2014 (see Sect. 5.4.1).

Trends calculated on our tropospheric mean mixing ratio time-series agree substantially well with trends calculated using AGAGE data (Table 5- 3). The results show, as for total columns trends, the decrease of trends over the last decade (trends ∼19% lower over 2008-2017 than over 1999-2008). For the overlapping period (2012-2017), the trends are also in good agreement within the uncertainties.

Table 5- 3: HCFC-22 tropospheric trends over JFJ. The uncertainties are given for the 2σ level following the Santer et al. (2000) approach. Trends are underlined when not significantly different from FTIR trends. Relative trends (% yr^{-1}) are given with respect to the yearly mean of the middle year of the considered period.

Tropospheric trends (ppt/year)	1988–2017 (10^{+13} molec cm^{-2})	1999-2008	2008-2017	2012-2017
FTIR Mean Tropospheric mixing ratio	5.1 ± 0.06 (3.41 ± 0.07)%	6.54 ± 0.35 (3.72 ± 0.2)%	5.31 ± 0.42 (2.29 ± 0.18)%	4.04 ± 0.73 (1.72 ± 0.31)% (2011-2017)*
AGAGE Mace Head		6.39 ± 0.1 (3.66 ± 0.06)%	5.36 ± 0.12 (2.27 ± 0.05)%	4.2 ± 0.08 (1.71 ± 0.03)%
AGAGE JFJ		-	-	4.05 ± 0.12 (1.65 ± 0.04)%

*Time frame enlarged in order to encompass the 2012 low-quality measurement period (see Sect. 5.3.3).

Concerning the lower-stratospheric time-series, we also include partial columns (from 11.21 to 30km at ±5° latitude around JFJ) from ACE-FTS (v3.6), pre-processed following the averaging kernel

smoothing method described in Sect. 4.3. Note that MIPAS data are available for the 2005-2012 period, which is a bit shorter than the 10-year period used for the other lower-stratospheric datasets (i.e. 2005-2014). Table 5- 4 reports excellent agreement within the uncertainties between the observational dataset trends, with a $2.99 \pm 0.05 \times 10^{13}$ molec cm^{-2} calculated trend for the JFJ time-series.

The WACCM lower-stratospheric absolute trend is more than 20% too low compared with the observations and BASCOE CTM. As the WACCM and BASCOE CTM simulations started from the same initial condition in 1984 and use the same lower boundary condition, this bias may be due to the unconstrained dynamical fields in WACCM, in contrast with the ERA-Interim dynamical fields used by the BASCOE CTM. Consequently, the lower absolute trend in WACCM results in a significant underestimation after 2002 (see Figure 5- 4 and Sect. 5.4.3). The corresponding relative trends, in comparison, do not significantly differ between observations and models.

Table 5- 4: HCFC-22 lower-stratospheric trends over JFJ. The uncertainties are given for the 2σ level following the Santer et al. (2000) approach. Relative trends (% yr^{-1}) are given with respect to the yearly mean of the middle year of the considered period. Trends are underlined when not significantly different from the FTIR trends.

	FTIR 1988-2017	FTIR JFJ 2005-2014	MIPAS 2005-2012	ACE-FTS 2005-2014	BASCOE CTM 2005-2014	WACCM 2005-2014
Lower-stratospheric trends	2.99 ± 0.05	3.11 ± 0.19	3.21 ± 0.11	2.96 ± 0.39	2.94 ± 0.11	2.53 ± 0.16
(10^{+13}molec cm^{-2} yr^{-1})	(4.11 ± 0.07)%	(3.29 ± 0.2)%	(3.32 ± 0.11)%	(3.17 ± 0.42)%	(3.5 ± 0.13)%	(3.47 ± 0.22)%

5.6 Conclusion

Using the narrow and well-isolated $2\nu_6$ Q-branch of HCFC- 22, we established an improved strategy to retrieve HCFC- 22 abundances from ground-based high-resolution FTIR solar spectra. Our new approach, using a Tikhonov regularization, retrieves enough information to distinguish two independent pieces of information that are representative of the troposphere and the lower stratosphere. We retrieve total columns with 66±6% (2σ) of tropospheric contribution. The main potential improvement that could be made to our retrieval strategy would be to build a new pseudo-linelist from recently determined cross-sections (Harrison, 2016). This could minimize the systematic uncertainty, and, moreover, the ν_3 feature (near 1100cm^{-1}) could be investigated again.

The comparison with independent datasets confirms the consistency and validity of these new time-series. We compared mean tropospheric mixing ratios, obtained from our retrievals, to AGAGE measurements performed at Mace Head (Ireland) and Jungfraujoch. Despite the larger variability found in the FTIR data, our mean tropospheric mixing ratios compare very well to the in situ time-series. Retrieved lower-stratospheric columns are also in excellent agreement with MIPAS observations. Relative differences between MIPAS and FTIR retrievals are indeed within the systematic uncertainty assessed on our time-series.

BASCOE CTM and WACCM outputs have been included in this study to support our comparisons. Analysis of tropospheric time-series showed that the lower boundary condition chosen (Meinshausen et al., 2017) drives the models' lower boundary through the simulation time period well. Nevertheless, WACCM lower-stratospheric columns are significantly too small compared with the observations and BASCOE CTM.

Bias aside, we showed that all of the stratospheric datasets used here depict the same seasonality in the lower stratosphere: high values in late summer (August) and low values in late winter/spring (February and March). This seasonality was also identified by Chirkov et al. (2016) using MIPAS global limb soundings, and it is neatly anti-correlated with the mean age of air derived from a BASCOE CTM simulation driven by ERA-Interim. Zhou et al. (2016) also noted this seasonality from ground-based FTIR measurements at 21°S (Reunion Island) despite the limited vertical resolution of their ground-based FTIR data (i.e. ~1 DOFS).

We also performed a trend analysis on the datasets used for the comparisons. The results are in good agreement for the datasets for the selected time frames. Total column and mean tropospheric mixing ratio trend analysis shows that HCFC-22 growth rates have changed significantly during the past 30 years. We confirm the decreasing of HCFC-22 growth rate during the last decade as observed by recent in situ studies (Montzka et al., 2015; Simmonds et al., 2017).

The fact that HCFC-22 emissions have been constant since 2007 and, therefore, that HCFC-22 growth rate has ceased to exhibit a continuous increase over the last decade, as highlighted in this paper and other works, seems to promise a fulfilment of the Montreal Protocol and its amendments in the years to come. Recent HCFC trends even suggest that the 2013 cap on global production (Montreal Protocol) has been respected well in advance (Montzka et al., 2015; Mahieu et al., 2017). Finally, this improvement in retrieval strategy, leading to the determination of partial columns, could be applied to other source gases essential for monitoring chlorine in the atmosphere (e.g. CFC-12 which presents relatively narrow features).

Additional discussion elements: update of the time-series and confirmation of the slowing down of HCFC-22 accumulation rates

Three supplemental years are now available (2018, 2019 and 2020) since the study presented in this chapter was published. We updated our time-series and reassessed trends to further emphasize the decreasing HCFC-22 accumulation rates in the recent years.

Figure 5- 7 shows the updated time-series of HCFC-22 total columns above Jungfraujoch. We also show total columns as simulated by BASCOE CTM driven by ERA-Interim (ending in August, 2019). Figure 5- 8 shows the time-series of tropospheric mixing ratios as obtained from FTIR (see Sect. 5.4.4) and AGAGE in situ measurements performed at Jungfraujoch. Table 5- 5 collects the results from a trend analysis, for the period 2012-2020, performed on time-series showed in this section (except for BASCOE CTM).

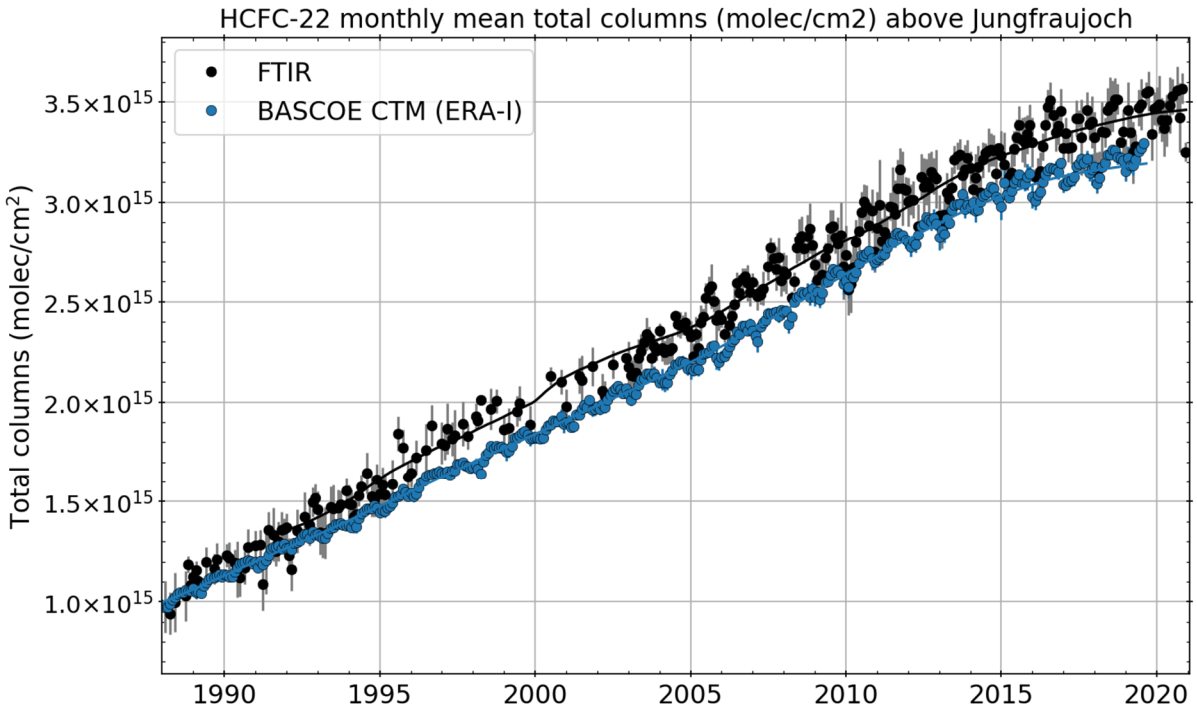

Figure 5- 7: FTIR monthly time-series of HCFC-22 total columns above Jungfraujoch. Vertical bars are the standard deviations around the monthly means. Due to pollution events starting in 1996 that mainly influenced the Bruker instrument, observations retrieved from the Bruker spectra are discarded before 2003. Smoothing lines are non-parametric trends obtained following Sect. 4.5.5.

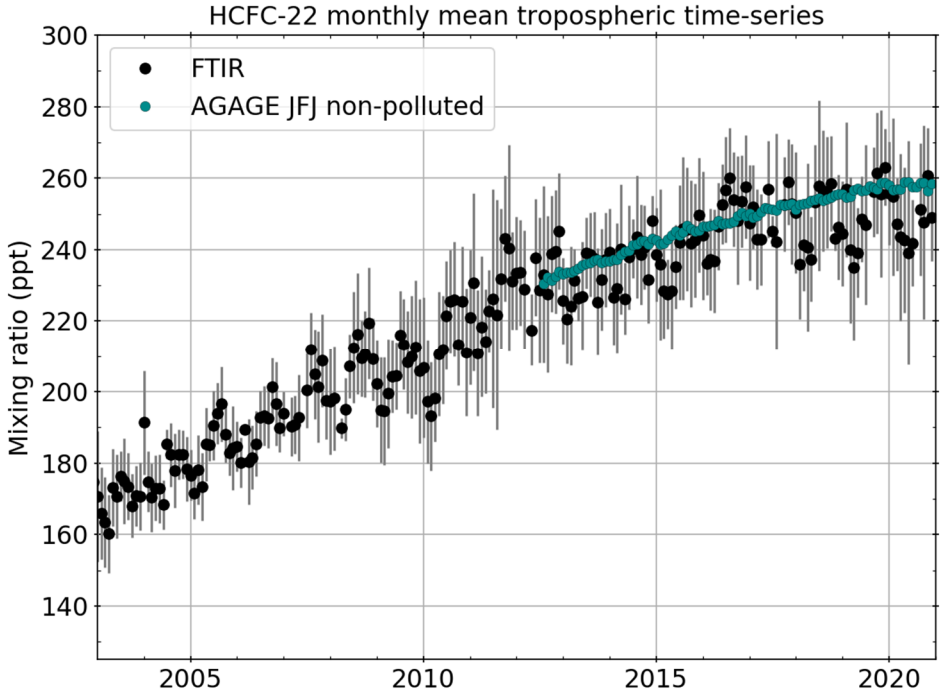

Figure 5- 8: Tropospheric monthly time-series at Jungfraujoch. The FTIR time-series is constructed by taking the average of all of the layers below 11.21 km, the altitude limit objectively defined by the retrieval information content. AGAGE in situ time-series from JFJ are baseline measurements (see Sect. 5.4.1.1). Vertical bars are the standard deviations around the monthly means.

Table 5- 5: HCFC-22 trends over JFJ. The uncertainties are given for the 2σ level following the Santer et al. (2000) approach. Trends are underlined when not significantly different from FTIR trends. Relative trends (% yr^{-1}) are given with respect to the yearly mean of the middle year of the considered period.

	Total columns (10^{13} molec cm^{-2} yr^{-1})	Tropospheric mean mixing ratio (ppt)	AGAGE JFJ (ppt)
2012-2020	5.28 ± 0.47	3.15 ± 0.43	<u>3.33 ± 0.09</u>
	(1.58 ± 0.14)%	(1.26 ± 0.18)%	<u>(1.34±0.03)%</u>
		(2011-2020)*	

*Time frame enlarged in order to encompass the 2012 low-quality measurement period (see Sect. 5.3.3).

From the time-series and the trend analysis presented in this section, we confirm the recent slowing down of HCFC-22 accumulation rates. Comparing trends values from Table 5- 3 and Table 5- 5, FTIR tropospheric trends have decreased by 0.89 ppt (−22%) between the periods 2011-2017 and 2011-2020. AGAGE JFJ trends have decreased by 0.72 ppt (−18%) between the periods 2012-2017 and 2012-2020.

Chapter 6

Stratospheric fluorine as a tracer of circulation changes: comparison between infrared remote-sensing observations and simulations with five modern reanalyses

Numbered sections of this chapter follow:

Prignon, M., Chabrillat, S., Friedrich, M., Smale, D., Strahan, S. E., Bernath, P. F., Chipperfield, M. P., Dhomse, S. S., Feng, W., Minganti, D., Servais, C. and Mahieu, E.: Stratospheric fluorine as a tracer of circulation changes: comparison between infrared remote-sensing observations and simulations with five modern reanalyses, J. Geophys. Res. Atmos. (*under review*), 2021.

Abstract. Using multidecadal time-series of ground-based and satellite Fourier transform infrared measurements of inorganic fluorine (i.e., total fluorine resident in stratospheric fluorine reservoirs), we investigate stratospheric circulation changes over the past 20 years. The representation of these changes in five modern reanalyses are further analysed through chemical-transport model (CTM) simulations. From the observations but also from all reanalyses, we show that the inorganic fluorine is accumulating less rapidly in the Southern Hemisphere than in the Northern Hemisphere during the twenty-first century. Comparisons with a study evaluating the age-of-air of these reanalyses using the same CTM allow us to link this hemispheric asymmetry to changes in the Brewer-Dobson circulation (BDC), with the age-of-air of the Southern Hemisphere getting younger relative to that of the Northern Hemisphere. Large differences in simulated total columns and absolute trend values are, nevertheless, depicted between our simulations driven by the five reanalyses. Superimposed on this multidecadal change, we, furthermore, confirm a 5-to-7-year variability of the BDC that was first described in a recent study analysing long-term time-series of hydrogen chloride (HCl) and nitric acid (HNO_3). It is important to stress that our results, based on observations and meteorological reanalyses, are in contrast with the projections of chemistry-climate models in response to the coupled increase of greenhouse gases and decrease of ozone depleting substances, calling for further investigations and the continuation of long-term observations.

Plain Language Summary. The overturning circulation of the stratosphere is projected to change in response to increases in greenhouse gases and decreases in ozone depleting substances, with the Southern Hemisphere branch expected to get weaker relative to the Northern Hemisphere. Here we use 30 year-time-series of observations and simulations of a long-lived tracer to investigate stratospheric circulation changes. The observations analysed are from ground-based and satellite instruments. We

compare them with simulations that use a chemical-transport model driven by winds from meteorological reanalyses of 1990-2019. A reanalysis assimilates meteorological measurements into a forecast model to simulate the best possible representation of the atmospheric state. All five simulations, which use different reanalyses, agree with the observational analysis showing that the analysed tracer is accumulating less rapidly in the Southern Hemisphere than in the Northern Hemisphere through 2019. This hemispheric asymmetry is attributed to changes in the stratospheric transport circulation, with the Southern Hemisphere branch getting stronger relative to the Northern Hemisphere. Our results support the conclusions of a recent observational study but do not support circulation changes projected by chemistry climate models. This work highlights the crucial importance of long-term observation time-series.

6.1 Introduction

The motivations of the study presented in this chapter are given in Chapter 2 (Sect. 2.5). Its objective is the general objective of this thesis, i.e., investigating the recently reported BDC changes, including the long-term change and the interannual variability, through an analysis of long-term time-series of observations and CTM simulations of inorganic fluorine.

A better characterization of the BDC and its interannual variability is crucial as it strongly influences ozone trend assessments (see Sect. 1.5.2). To scrutinize the onset of the ozone recovery and thus the success of the Montreal Protocol, reducing the uncertainty around the trend values of ozone is, in fact, a key requirement (WMO, 2018; SPARC/IO3C/GAW, 2019). Additionally, most of CCMs, employed for climate projections, still fail to correctly reproduce the observed midlatitude lower stratosphere trend of ozone due to enhanced mixing of tropical air into the midlatitudes (Ball et al., 2020). As concluded recently by Strahan et al. (2020), the disagreements between, on the one hand, observations and reanalyses and, on the other hand, CCMs, require additional studies assessing long-term trends from observational datasets as long-lived tracers. Finally, the BDC and its changes are also key drivers of variability observed in the tropospheric circulation and composition as highlighted in recent studies (e.g., Banerjee et al., 2020; Ray et al., 2020).

In this study, we investigate multidecadal trends of the BDC as well as its interannual variability most recently described in Strahan et al. (2020). Here we make use of time-series of total inorganic fluorine (F_y) as retrieved from ground-based Fourier-transform infrared (FTIR) measurements as well as FTIR satellite observations (Sect. 6.3.1 and Sect. 6.3.2). Outside the context of the BDC trends and multiyear variability, assessing long-term trends of inorganic fluorine is also of great interest in the framework of the Montreal Protocol. While the total inorganic chlorine was preferred to F_y because it is more directly related to the chlorinated (thus harmful for the ozone layer) source gases, the recent Kigali Amendment, entered into force on 1st January 2019, will gradually reduce the consumption and production of HFCs (not chlorinated but having large global warming potentials). With this respect, this will make F_y a relevant indicator of the fulfilment of the Montreal Protocol. In the framework of the SPARC S-RIP project we also include long-term simulations performed by the BASCOE CTM (Sect. 6.3.3.1) driven by the main modern reanalyses, i.e., ERA-Interim, JRA-55, MERRA, MERRA-2, as well as the new ECMWF reanalysis, ERA5(Hersbach et al., 2020).

Section 6.2 provides a brief theoretical introduction to the F_y budget. Section 6.3 describes the datasets and methods employed in this research. Section 6.4.1 describes the observed and simulated F_y budget

above Jungfraujoch (46°N) and Lauder (45°S) NDACC stations and discusses on the marginal contribution of COClF to F_y. Section 6.4.2 presents and describes the inorganic fluorine time-series used for the trend analyses of Section 6.5. These results are discussed in Section 6.6 in the context of recent studies and Section 6.7 draws the main conclusions and outcomes of this work.

6.2 Fluorine in the stratosphere

Fluorine in the stratosphere originates from the photochemical destruction of anthropogenic CFCs, HCFCs and hydrofluorocarbons HFCs (Harrison et al., 2016). The most abundant CFCs, HCFCs or HFCs (see hereafter) have long atmospheric lifetimes ranging from 10 to 100 years, although some HFCs may be short-lived with lifetimes of several days only. Consequently, these source gases largely reach the stratosphere where they undergo photolysis and oxidation by $O(^1D)$ or OH (HCFCs and HFCs) to form inorganic reservoirs. In atmospheric chemistry, organic fluorine refers to the fluorinated tropospheric source gases while inorganic fluorine refers to the chemical species resulting from the decomposition of these species. Figure 1 shows the increase of CFCs until the 1990's, followed by their gradual decrease and gradual replacement by HCFCs and HFCs. The global mixing ratios given in Fig. 1 are derived from in situ measurements and were compiled for CMIP6 (Meinshausen et al., 2017, 2020). Due to their very long lifetimes, CFCs are still the most abundant halocarbons, with CFC-12 (516.1 ppt), CFC-11 (229.6 ppt) and CFC-113 (71.4 ppt) the top three most-abundant CFCs in 2016 (the numerical values are the global volume mixing ratios at surface as given in WMO, 2018). HCFC-22 is by far the most abundant HCFC with a global mole fraction of 237.4 ppt in 2016 (WMO, 2018). CFC production and consumption are currently banned and HCFC consumption and production are banned in developed countries and are strongly regulated in developing countries by the Montreal Protocol (and its later adjustments). Consequently, the planned transition to HFCs has led to a rapid increase of HFC-134a, with its global mixing ratio reaching nearly 90 ppt in 2016 while being close to 0 in 1995 (WMO, 2018). It should be noted that the total abundance of fluorine at the surface increased almost linearly between 1993 and 2014 (Fig. 1).

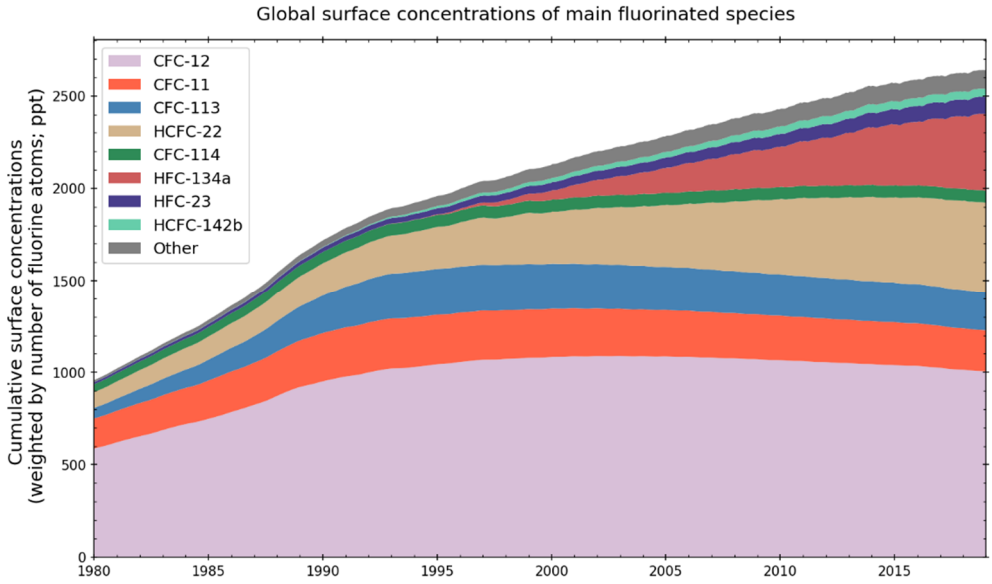

Figure 6- 1: Global means of the surface volume mixing ratios of the main fluorinated species as given in Meinshausen et al. (2017, 2020; see Sect. 5.3.3.1). Mixing ratios are weighted by the number of fluorine atoms in each species (e.g., 2×[CFC-12]). "Other" contributions (grey) comprise the species CFC-115, HCFC-141b, HFC-152a, Halon-1211 and Halon-1301.

For the major halocarbons, species with at least two fluorine atoms (i.e., CFC-12, HCFC-22 and HFC-134a) follow a reaction path leading to the formation of COF_2, while CFC-11, containing a single fluorine atom, follows another reaction path leading to the formation of COClF (Harrison et al., 2016). CFC-113 follows similar paths but degrades into both COClF and COF_2. These two fluorine reservoirs in turn undergo photolysis to release fluorine atoms which quickly react with methane, water or molecular hydrogen to form the ultimate, and very stable, fluorine reservoir, HF. With less abundant sources and a weaker stability, COClF is by far the least abundant inorganic fluorine reservoir and is decreasing in the atmosphere in line with its major sources (e.g., Bernath et al., 2020). Conversely, COF_2 is increasing because the positive trends in both HCFC-22 and HFC-134a more than compensate for the decreasing abundances of CFC-12 and CFC-113 (e.g., Harrison et al., 2014; Bernath et al., 2020). Finally, HF has no major chemical sink in the stratosphere and is slowly removed by transport (into both the troposphere and the mesosphere) and by rainout. Consequently, HF is still increasing in the atmosphere (i.e., 0.5% in 2004-2012) although less rapidly than before (i.e., 5% in 1991-1997; Harrison et al., 2016; WMO, 2018).

The total inorganic fluorine (F_y) is defined as the sum, weighted by the number of fluorine atoms, of either volume mixing ratios or total columns of HF, COF_2 and COClF:

$$[F_y] = [HF] + 2[COF_2] + [COClF]. \quad (6.1)$$

Due to the unavailability of COClF in the FTIR retrievals (see Sect. 6.3.1), we also define a budget of inorganic fluorine that excludes this reservoir:

$$[{}^{*}F_y] = [HF] + 2[COF_2]. \quad (6.2)$$

As the total inorganic fluorine is produced by the photolysis of halocarbons, minimum volume mixing ratios are encountered in the lower tropical stratosphere. Following the deep branch of the BDC and ascending in tropical stratosphere, the availability of high-energy ultraviolet photons increases and photolysis becomes more efficient, and the total inorganic volume mixing ratios become larger. The downwelling branches of the circulation transport air that is rich in F_y into the extratropical latitudes of the lower stratosphere.

6.3 Data and methods

6.3.1 Ground-based FTIR retrievals

This study relies on time-series from the Jungfraujoch (Switzerland, 46.55°N) and Lauder (New Zealand, 45.04°S) NDACC stations. Jungfraujoch and Lauder stations generated multidecadal and regular records of high-resolution (0.003-0.006 cm^{-1}) FTIR solar absorption spectra recorded under clear-sky conditions. Since the most striking BDC changes have been observed through differences between the northern and southern midlatitudes (see Sect. 6.1), these two stations are particularly suited for such investigations.

While HF is retrieved at most of the NDACC stations, COF_2 is a more challenging species to retrieve from ground-based FTIR spectra due to very weak absorption lines. The only published COF_2 retrieval methods from ground-based infrared solar spectra are in Melen et al. (1998) and in Duchatelet et al. (2009) and were only applied to the Jungfraujoch observations. Here, this strategy was applied to Lauder spectra as well. COClF is, to our knowledge, currently not retrieved at any FTIR NDACC sites due to

its very weak features blinded by water vapour strong interferences. Therefore, the inorganic budget as retrieved from ground-based FTIR ($^{*}F_y$; see Eq. 6.2) is not totally closed. Nassar et al. (2006) showed that the contribution of COClF to the total inorganic fluorine abundance is very small compared to HF and COF_2 hence the ground-based FTIR $^{*}F_y$ should be a very good approximation to F_y. This approximation will be further investigated in Section 6.4.1.

We apply the optimal estimation method developed by Rodgers (2000), implemented in the SFIT-4 v.0.9.4.4 algorithm, to perform the retrievals from the solar infrared spectra. At Jungfraujoch, spectra were recorded by a homemade instrument from 1984 to 2008 and have been recorded by a Bruker IFS 120HR spectrometer from the early 1990s to present (see Zander et al., 2008). At Lauder the spectrometers are a Bruker IFS 120M (1996-2002), a Bruker IFS 120HR (2002-2018) and a Bruker 125HR (2018 to present; Kohlhepp et al., 2012; Strahan et al., 2020).

6.3.1.1 HF

HF retrievals from the Jungfraujoch spectra are performed following the retrieval strategy described in Duchatelet et al. (2010). The microwindow considered is from 4038.80 cm^{-1} to 4039.11 cm^{-1} and includes water vapour (H_2O) and methane (CH_4) as interfering species (i.e., their vertical distributions are scaled during the spectrum inversion). A signal-to-noise ratio of 500 is assumed in all inversions, for both instruments. Diagonal elements of the covariance matrix are set to 70% km^{-1} along with a Gaussian interlayer correlation of 3 km at half-width. The total systematic error is estimated to be around 5.5% while the random error is estimated to be around 2% (estimated using the formalism of Rodgers, 2000).

For Lauder, a second microwindow is included for the spectrum inversion: 4109.77 cm^{-1} to 4110.07 cm^{-1}. Fixed signal-to-noise ratios of 230, 270 and 320 are assumed for the Bruker IFS 120M, the Bruker IFS 120HR, and the Bruker 125HR, respectively. Diagonal elements of the covariance matrix are set to 50% km^{-1} along with a Gaussian interlayer correlation of 4 km at half-width. The total systematic error is estimated to be around 2.5% while the random error is estimated to be around 1.25%.

For both sites, the mean vertical profile of HF computed from a WACCM version 4 40-year run (1980-2020) is used as the a priori profile for the inversion. Line-by-line spectroscopic parameters are taken from HITRAN 2008 (Rothman et al., 2009b).

6.3.1.2 COF2

To retrieve enough information despite the very weak absorption lines of COF_2 in the infrared spectral region, Duchatelet et al. (2009) proposed a multi-spectrum fitting approach. In this strategy, the microwindows taken from different spectra recorded during the same day or half-day are fitted simultaneously by the retrieval process. This way, the combined spectra allow the inverse method to retrieve more information from the measurement (i.e., lower dependence from the a priori, see Table 2 in Duchatelet et al., 2009).

For Jungfraujoch, we apply the multi-spectrum approach developed for the spectra recorded at the station. The strategy allows to retrieve COF_2 columns from spectra recorded by the two detectors of the Bruker instrument (MCT and InSb) as well as the InSb detector of the homemade FTS. We include the same microwindows as in Duchatelet et al. (2009). As Melen et al. (1998), we note a systematic

difference of around 6% between the total columns retrieved from spectra recorded by the InSb and the MCT detectors (MCT columns being higher). As there is no trend in the systematic differences, we applied a simple constant scaling factor (computed over daily mean coincidences) in order to scale the MCT time-series towards that of the InSb, thus avoiding the scaling of the homemade instrument time-series. We assume a fixed signal-to-noise ratio of 250 for the retrievals of COF_2.

COF_2 retrievals at Lauder are performed using a different approach. Rather than fitting simultaneously several spectra, the strategy applied at Lauder is based on co-adding of all spectra within a month over a defined solar zenith angle range (70-80 degrees) to increase the signal-to-noise ratio. The combination of spectra is performed using the approach outlined in Notholt and Lehmann (2003). Consequently, FTIR COF_2 retrievals from Lauder have a monthly sampling. At Lauder, only the spectra recorded by the MCT detectors are used to retrieve COF_2. The co-adding of spectra allows to approximately double the signal-to-noise ratio, thus a fixed signal-to-noise ratio of 400 is assumed for Lauder COF_2 retrievals.

For both stations, we have updated the a priori profile of COF_2 using ACE-FTS measurements (see Sect. 6.3.2) performed between 2004 and 2019. The a priori profile is completed with WACCM v4 outputs below 15 km. For Jungfraujoch (Lauder) we make use of ACE-FTS measurements included between 40°N and 50°N (40°S and 50°S). For the covariance matrix, we follow Duchatelet et al. (2009) and set the diagonal elements of the covariance matrix to 60% km^{-1} along with a Gaussian interlayer correlation of 2 km at half-width. As for HF, line-by-line spectroscopic parameters are taken from the HITRAN 2008 compilation.

Systematic errors are estimated to be relatively high for COF_2 retrievals as a large uncertainty of the spectroscopic parameters is assumed (15-20%) while the total random error is estimated to be around 10% (See also Duchatelet et al., 2009).

6.3.2 ACE-FTS

Observations from ACE-FTS on board the SCISAT satellite are also included in this work (Bernath et al., 2005; Bernath, 2017). Beside their involvement in the cross-validation between ground-based and satellite FTIR observations, ACE-FTS data are included to support the F_y budget evaluation (see Sect. 6.4.1) as well as to offer a global picture of F_y trends, thus supporting the reanalysis intercomparison.

Originally planned for a 2-year mission (Bernath et al., 2005), the successful SCISAT satellite, launched on August 12, 2003, has been orbiting the Earth and recording infrared solar occultation spectra for more than 17 years now. The three inorganic fluorine reservoirs, HF, COF_2 and COClF, are currently retrieved from ACE-FTS observations. Satellites benefit from a better geometry of observation (i.e., limb sounding in the case of ACE-FTS) compared to ground-based instruments and, consequently, molecules having very weak infrared absorption as COClF can be retrieved. HF retrievals are available from 12 km to 54 km, COF_2 from 12 km to 34 km and COClF from 13 km to 24 km. We use version 4.0 of ACE-FTS and we filter outliers following the method detailed in Sheese et al. (2015). Zonal mean trends are obtained from interpolations of the ACE-FTS retrievals from their constant altitude vertical grid to a constant vertical pressure grid employing a mass-conservative regridding method (see Sect. 4.3.1) followed by binning into 5-degree latitude intervals (e.g., Steffen et al., 2019). When compared to the ground-based FTIR time-series, we use all ACE-FTS measurements included between 40°S-50°S and 40°N-50°N for Lauder and Jungfraujoch, respectively.

6.3.3 Models

6.3.3.1 BASCOE CTM

BASCOE CTM (Skachko et al., 2016; Chabrillat et al., 2018; Errera et al., 2019) is included in this study to compare the representation of the BDC changes (see Sect. 6.1) in modern reanalyses (i.e., ERA-Interim, ERA5, JRA55, MERRA and MERRA-2; see Fujiwara et al., 2017 for a technical comparison of these reanalyses except ERA5; and Hersbach et al., 2020 for a comparison between ERA-Interim and ERA5). Its advection module is the FFSL scheme (Lin and Rood, 1996; see Sect. 3.2), configured as recommended in Rotman et al. (2001).

Chabrillat et al. (2018) conducted a comparison of advective transport in these reanalyses (except ERA5) through mean age of air evaluations performed by BASCOE CTM. In such a comparison the transport model is used as a transfer tool to accomplish a fair comparison between the reanalyses. The transport module of BASCOE and reanalysis forcing set-up is configured as in the study of Chabrillat et al (2018). BASCOE CTM is a kinematic transport model and is therefore only driven by the surface pressure and horizontal wind fields of the reanalyses. It is actually the FFSL algorithm that derives the vertical winds from mass conservation. The algorithm requires the input fields to be staggered on a relatively low resolution Arakawa-C grid (2°×2.5° latitude-longitude) while the native vertical grid of each reanalysis is kept. The pre-processing method needed to transfer the spectral or high resolution fields on the low resolution grid and to filter out the eventual dynamical imbalances of the reanalyses is described in Sect. 3.1.2.

The chemical scheme of BASCOE CTM is described is Sect. 3.3.1. The chemistry reactions related to the transformation of organic fluorine sources into inorganic fluorine reservoirs are simplified in BASCOE CTM. Consequently, rather than reacting through the main fluorine reservoirs (HF, COF_2 and COClF), the fluorine atoms, released by the degradation of halocarbons, are directly converted into the total inorganic fluorine tracer F_y (Eq. 6.1). The initial state (1st December 1984) of all simulations is based on a BASCOE reanalysis of Aura MLS (Microwave Limb Sounder) for the year 2010 that was scaled by global constants to obtain surface concentrations representative of 1984 (see Sect. 3.3.3).

The five simulations used here include the daily varying spectral solar irradiance as recommended for the Coupled Model Intercomparison Project phase 6 (CMIP6; Matthes et al., 2017). The age of air (AoA) derived from ERA-Interim, MERRA, MERRA-2 and JRA-55 by the BASCOE CTM (Chabrillat et al., 2018) apply exactly here because the grid and transport settings are strictly identical: time step set to 30 minutes, a 2°×2.5° latitude-longitude grid and the native hybrid sigma-pressure vertical grids of the driving reanalyses.

6.3.3.2 TOMCAT

TOMCAT/SLIMCAT (hereafter TOMCAT; Chipperfield, 2006) is a global CTM which can be used in a variety of configurations. In this study it is used with a detailed stratospheric chemistry scheme to calculate the partitioning of F_y species. The model chemistry scheme includes the main species of the O_x, NO_y, Cl_y, Br_y, HO_x and CHO_x chemical families, along with long-lived source gases. The TOMCAT Fy chemistry is as described in Harrison et al. (2014, 2016) who compared the model with ACE-FTS HF, COF_2 and COClF. COF_2 is assumed to be produced from the degradation of CFC-12, CFC-113, CFC-114, CFC-115, HCFC-22, HCFC-142b, HFC-23, HFC-134a, HFC-152a, Halon 1211 and Halon

1301, with COClF production from the degradation of CFC-11, CFC-113, and HCFC-141b. A very small amount of HF is assumed to form directly from the source gases, mainly arising from HFC-134a (Harrison et al., 2016). The primary loss of COF_2 and COClF in the stratosphere occurs via photolysis, with an additional secondary loss mechanism through reaction with $O(^1D)$.

In this study TOMCAT was run at a horizontal resolution of 2.8° × 2.8° with 32 levels from the surface to approximately 60 km in a setup similar to that used by Dhomse et al. (2019). The model used a hybrid sigma-pressure vertical coordinate and was forced by ECMWF ERA-Interim meteorological fields. The simulation was initialised in 1977 and uses specified global mean surface mixing ratios of the long-lived source gases from the 2018 WMO Ozone Assessment (WMO, 2018). The model also includes solar flux and aerosol Surface Area Density variations as described in Dhomse et al. (2015, 2016).

6.3.4 Trend methods

Trend estimates presented in this research are obtained from a classic linear trend model accounting for an annual cycle (see Sect. 4.5.1). We estimate the uncertainty around trend values following the autoregressive wild bootstrap method (see Sect. 4.5.4). This method is robust to the eventual heteroskedasticity (i.e., changing variance over time) and autocorrelation of the residuals.

Several time-series in this chapter display smoothed trend lines that are obtained using the nonparametric trend estimation technique described in Sect. 4.5.5.

6.3.5 Modified normalized mean bias

The mean relative differences of this study are expressed in term of modified normalized mean bias (MNMB), following Eq. (1) in Eskes et al. (2015):

$$MNMB = 100\ \% \times \frac{1}{N}\sum_i^N \frac{x_i - y_i}{(x_i + y_i)/2}, \tag{6.3}$$

with N the number of coincidences between both x and y datasets. MNMBs are given along with their 1σ standard deviation.

6.4 Inorganic fluorine above Jungfraujoch and Lauder

6.4.1 Partitioning of total inorganic fluorine F_y and marginal contribution of COClF

Figure 6- 2 shows the time-series of the total columns of the three major inorganic fluorine reservoirs above Jungfraujoch and Lauder. The ground-based FTIR retrievals of HF and COF_2 exhibit a very good agreement with both the retrievals of ACE-FTS and the outputs from TOMCAT. With respect to COClF no FTIR retrievals are available but we note large differences between the ACE-FTS retrievals and the TOMCAT results. Table 6- 1 displays the MNMB over the 2004-2018 period and the associated uncertainties. While the biases between the HF datasets are negligible and the larger biases between COF_2 datasets remain within the large systematic errors assessed for ground-based retrievals (reaching 20% due to large spectroscopic uncertainty; see Sect. 6.3.1.2), the large biases between the ACE-FTS and TOMCAT datasets indicate a systematic disagreement for COClF that is also noted and discussed in Harrison et al. (2016).

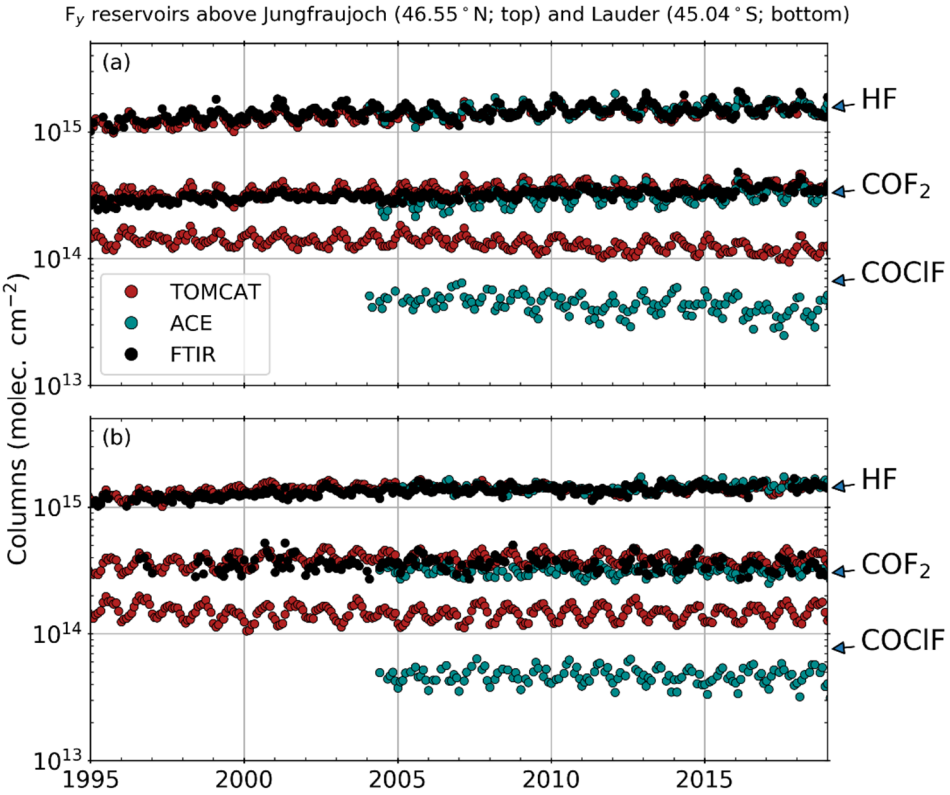

Figure 6- 2: Total columns (molec. cm^{-2}) of total inorganic fluorine (F$_y$) reservoirs observed above Jungfraujoch (**a**) and Lauder (**b**) by ground-based (black) and ACE-FTS (dark cyan) Fourier transform spectrometers as well as simulated by TOMCAT (red). Note that COClF is currently not retrieved at either ground-based station (see Sect. 6.3.1).

Table 6- 1: Relative difference (MNMB, Eq. 6.3) between ACE-FTS and FTIR, and between ACE-FTS and TOMCAT, for the total columns of the three major inorganic fluorine reservoirs, above Jungfraujoch and Lauder and for the period 2004-2018. Negative values indicate lower ACE-FTS total columns. See section 6.3.5 for the definitions of MNMB and the associated uncertainties.

2004-2018		Lauder		Jungfraujoch	
		FTIR	TOMCAT	FTIR	TOMCAT
ACE FTS	HF	2.79±7.4 %	2.74±7.5 %	-0.32±7.8 %	4.21±6.2 %
	COF$_2$	-9.82±12 %	-22.4±6.6%	-8.08±11 %	-16.5±8.5 %
	COClF	n.a.	-102 ± 8 %	n.a.	-98.1±12 %

Figure 6- 3 depicts the time-series of F$_y$ as computed from the reservoir time-series of Figure 6- 2 (see Eq. 6.1 and Eq. 6.2). The F$_y$ simulation of BASCOE CTM driven by ERA-Interim is also displayed for comparison. Despite the systematic difference between TOMCAT and BASCOE CTM, we show here that both model time-series present an almost identical interannual variability, thus giving confidence in the forcing methods of BASCOE CTM. Regarding the F$_y$ partitioning above both stations, from ACE-FTS retrievals, we compute that HF represents 69.6% and 68.4% of F$_y$ at Jungfraujoch and Lauder, respectively. TOMCAT simulates a lower relative contribution of HF to F$_y$, with HF ratio representing 60.2% and 58.7% at the two stations. The corresponding fractions for COF$_2$ (note that COF$_2$ total columns are multiplied by 2 to compute the F$_y$ budget, see Eq. 6.1) are 28.4% and 29.4% (ACE-FTS above Jungfraujoch and Lauder, respectively) and 33.0% and 34.1% (TOMCAT above Jungfraujoch and Lauder, respectively). Thanks to the success of the Montreal Protocol, chlorinated source gas

emissions have now been declining for several decades (WMO, 2018). As a result, COClF is decreasing in the atmosphere while HF and COF_2 are not, leading to a decreasing contribution of COClF to F_y. From ACE-FTS time-series we note, however, that between 2014 and 2018 the contribution of COClF has decreased by less than 1% above Jungfraujoch (Figure 6- 3b) and remained constant above Lauder (Figure 6- 3d). To evaluate the impact of the decreasing contribution of COClF to F_y, we have estimated ACE-FTS trends of F_y and $^*F_y$ (see Eq. 6.1 and Eq. 6.2, respectively) for the period 2004-2018. We noted only a marginal difference between F_y and $^*F_y$ trends (not shown) which is negligible when compared to the estimated uncertainty of these trends (as given by the ARW bootstrap method, see Sect. 6.3.4).

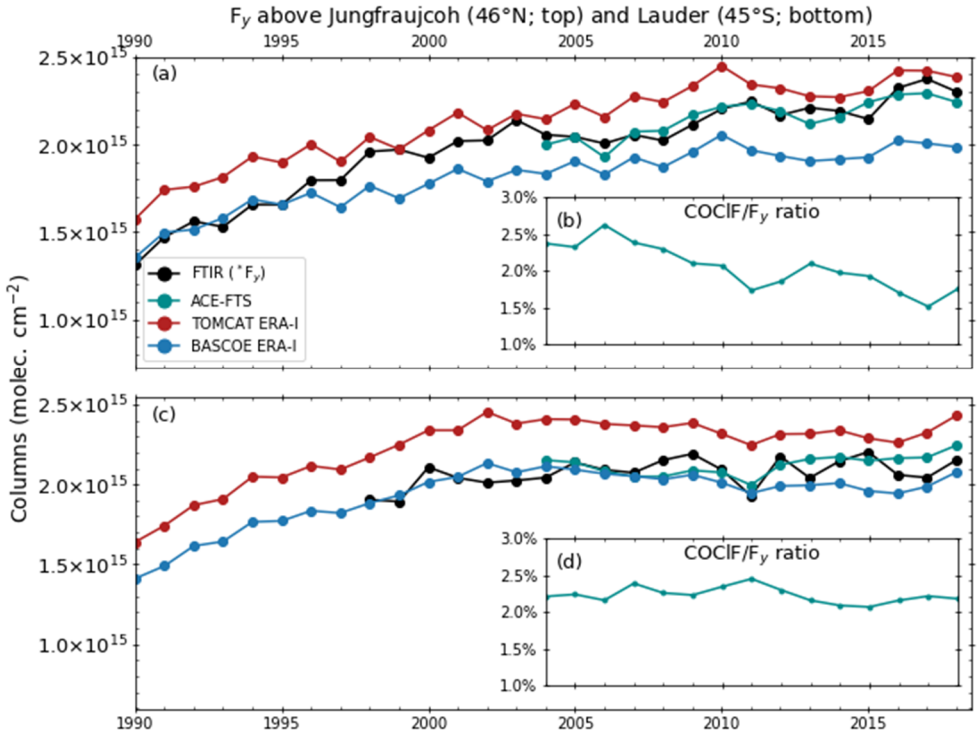

Figure 6- 3: Annual means of the total inorganic fluorine (F_y) total columns (molec. cm^{-2}) observed above Jungfraujoch (**a**) and Lauder (**c**) by ACE-FTS (dark cyan) or simulated by TOMCAT (red) and BASCOE CTM (blue). FTIR total columns (black) do not include COClF (see Sect 6.3.1) and correspond to $^*F_y$ (Eq. 6.2). Panels **b** and **d** depict the contribution of COClF to F_y (%) computed from ACE-FTS time-series.

In conclusion, we have shown that omitting COClF in the F_y budget should not induce large biases as HF and COF_2 taken together represent at least 93% (from TOMCAT), and even up to 98% (from ACE-FTS), of the closed F_y budget. The remaining contribution of COClF is moreover sufficiently stable over time to not induce any significant bias in the estimation of the F_y trend when it is approximated by the $^*F_y$ trend. Consequently, all trends of ACE-FTS in the following sections are computed over $^*F_y$ time-series.

6.4.2 Inorganic fluorine time-series

In Figure 6- 4, we show the time-series of $^*F_y$ observed by FTIR and ACE-FTS and F_y simulated by the BASCOE CTM above both NDACC stations. As already demonstrated in Figure 6- 2 and Figure 6- 3, ground-based FTIR and ACE-FTS retrievals are in good agreement at Lauder and Jungfraujoch (Figure 6- 4Figure 6- 3a and b, respectively).

F_y simulations performed by BASCOE CTM driven by five modern reanalyses show large differences in absolute values and trends (Figure 6- 4e, f). At both stations, MERRA-2 delivers the highest F_y columns, ERA-Interim and JRA-55 the lowest ones, with MERRA and ERA5 situated in between.

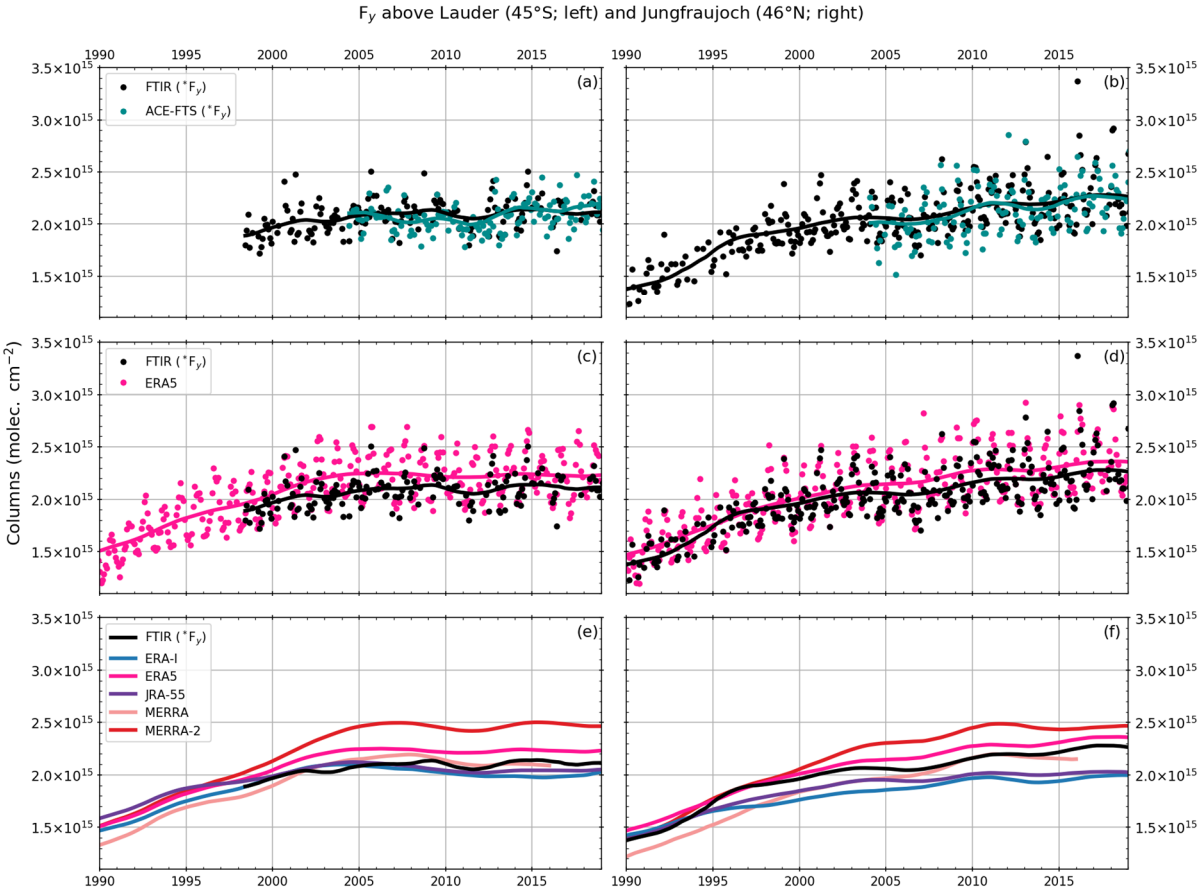

Figure 6- 4: Inorganic fluorine above Lauder (left panels **a**, **c**, **e**) and Jungfraujoch (right panels **b**, **d**, **f**). Panels **a** and **b** are observations from ground-based FTIR (black) and ACE-FTS (at site latitude ± 5°; dark cyan). For a direct comparison between observations, COClF is excluded from the inorganic fluorine of ACE-FTS (see Sect. 6.4.1). Panels **c**-**f** are the BASCOE CTM total inorganic fluorine simulations interpolated at the gridpoints closest to Lauder (**c**, **e**) and Jungfraujoch (**d**, **f**). Points are monthly means and lines are nonparametric smoothing trends (see Sect. 6.3.4).

Relative differences (MNMB, see Eq. 6.3) between observations and BASCOE CTM simulations computed on 2004-2018 daily mean coincidences for Jungfraujoch and monthly mean coincidences for Lauder (see Sect. 6.3.1.2) are shown in Table 6- 2. While observations show a remarkably good agreement at both sites, the performance of the BASCOE CTM depends on the forcing reanalysis and the evaluated station. Considering both stations for the period 2004-2018, ERA5 and MERRA (note that MERRA ends at the end of 2015) allow the best agreement between the CTM and the observations.

Table 6- 2: 2004-2018 relative difference (MNMB, Eq. 6.3) between Jungfraujoch (JFJ) and Lauder FTIR $^*F_y$, and ACE-FTS $^*F_y$ and BASCOE CTM F_y driven by ERA-Interim, ERA5, JRA-55, MERRA (ending in 2015) and MERRA-2. See section 6.3.5 for the definitions of MNMB and the associated uncertainties.

2004-2018	ACE-FTS	ERA-I	ERA5	JRA-55	MERRA	MERRA-2
FTIR JFJ	2.66 ± 12.9 %	12.43 ± 5.2%	-2.59 ± 6.3 %	9.66 ± 5.4 %	3.58 ± 6.9 %	-9.25 ± 5.2 %
FTIR Lauder	1.08 ± 7.3 %	2.88 ± 6.6 %	-6.96 ± 6.7 %	1.19 ± 6.0 %	-2.62 ± 7.4 %	-16.87 ± 6.4 %

6.5 Trends

6.5.1 Long-term and decadal trends

We now present an analysis, summarized in Figure 6- 5 and Figure 6- 6, of the long-term trends computed from observations (ground-based FTIR and ACE-FTS) and BASCOE CTM simulations. The longest time-period for which all datasets are available is 2004-2018 (except for MERRA which ends at the end of 2015). We determine trends over three time-periods:1990-2018, 1990-1999 and 2004-2018. 2004-2018 was chosen instead of 2000-2018 such as to accommodate the full ACE-FTS time range.

We first consider the trends computed above Lauder and Jungfraujoch (Figure 6- 5a and b, respectively). For the longest time-period 1990-2018, covered by the Jungfraujoch ground-based observations and BASCOE CTM, the differences qualitatively shown in Figure 6- 4 are confirmed quantitatively: MERRA and MERRA-2 deliver the largest trends while the trends obtained with ERA-Interim (1.85×10^{13} molec. cm^{-2} yr^{-1}) and JRA-55 (2.01×10^{13} molec. cm^{-2} yr^{-1}) are the smallest among the five BASCOE CTM simulations and also the closest to the trends derived from the Jungfraujoch FTIR (2.33×10^{13} molec. cm^{-2} yr^{-1}). Yet a separate inspection of the early (pre-2000) and recent (post-2000) periods delivers very different results. During the period of strongly increasing F_y 1990-1999, the ERA-Interim reanalysis delivers a trend value at Jungfraujoch that is twice smaller that the FTIR observations. This significant underestimation is corrected with the most recent ECMWF reanalysis, ERA5, and is not found with the three other CTM simulations. Regarding the 2004-2018 common time period, large differences are depicted between both sites as well as between datasets (especially between reanalyses) at each site. At Jungfraujoch, ground-based and ACE-FTS time-series reveal an excellent agreement. At Lauder, FTIR and ACE-FTS trends are not significantly different as their uncertainties overlap. An important result for this period is that observations and model simulations exhibit significantly higher trend values at Jungfraujoch than at Lauder. Additionally, all trends from BASCOE-CTM simulations are too low in comparison to observations at Lauder, even significantly negative for ERA-Interim and JRA-55 (the trend obtained with MERRA is also negative but over a different period that ends in 2015).

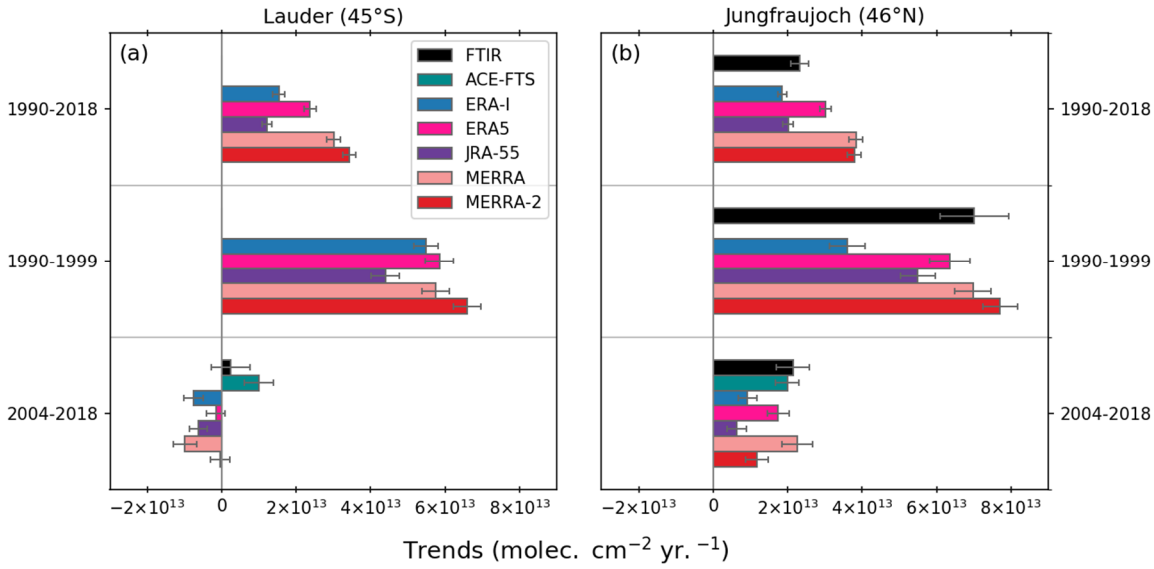

Figure 6- 5: Inorganic fluorine trends above Lauder (**a**) and Jungfraujoch (**b**) computed for ground-based FTIR and ACE-FTS observations ($^{*}F_y$) as well as for BASCOE CTM simulations (F_y). Horizontal thin error bars are the 95% uncertainty range around estimated trend values. Note that MERRA ends in December 2015.

Trends computed from zonal mean time-series (Figure 6- 6) expand these results to the whole stratosphere. During the 1990's MERRA, MERRA-2 and ERA5 deliver comparable trend values while those obtained from ERA-Interim and JRA-55 are much lower. For the common dataset period, 2004-2018 (except for MERRA, ending in 2015), interhemispheric differences in the lower stratosphere on zonal mean trends are noticeable, with larger trend values in the Northern Hemisphere than in the Southern Hemisphere. While ACE-FTS trends also show larger values for the Northern Hemisphere, the values for the Southern Hemisphere are not statistically significant at the 95% confidence level.

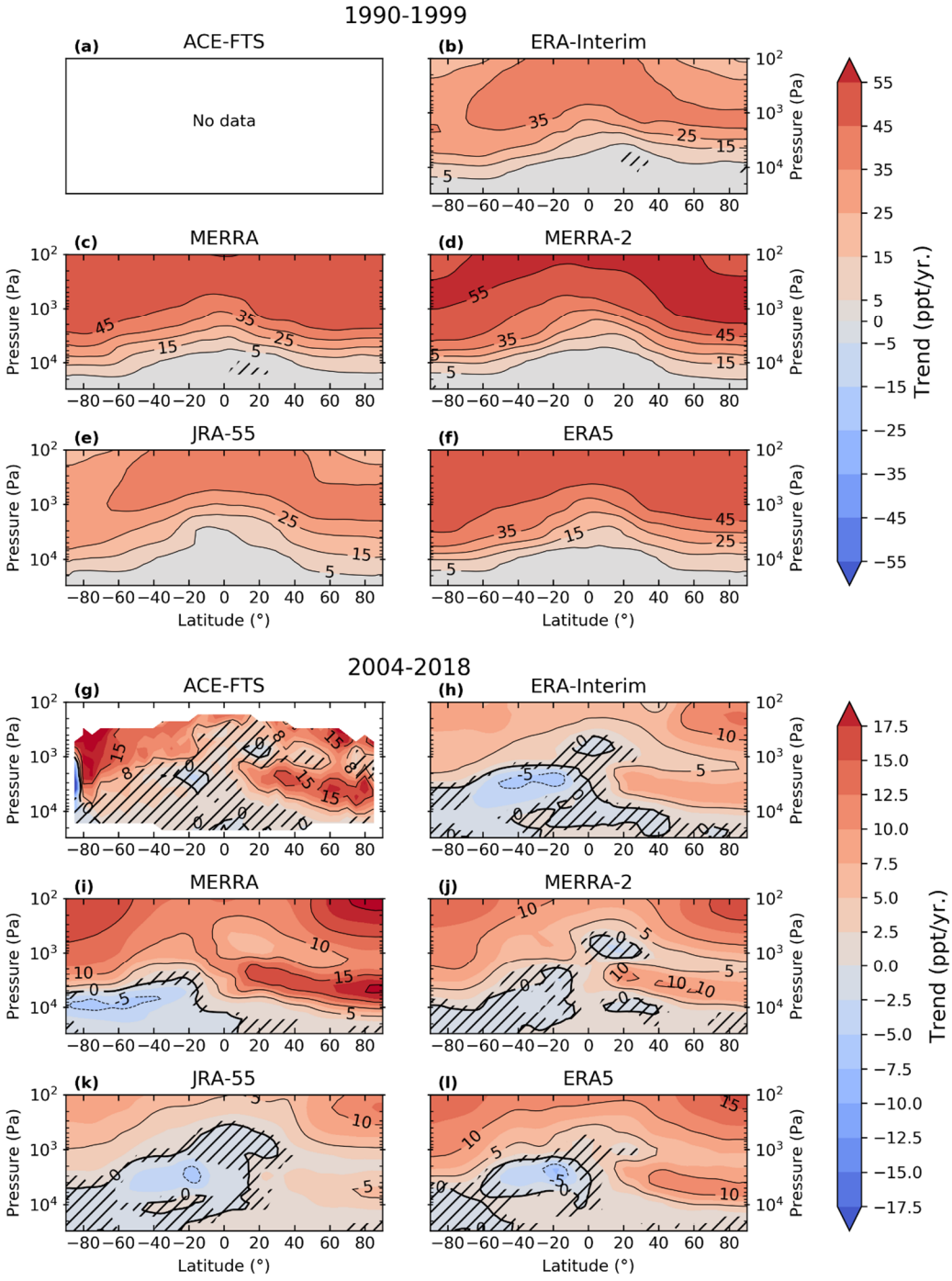

Figure 6- 6: Long-term trends of $^{*}F_y$ (ACE-FTS) and F_y (BASCOE CTM forced by ERA-Interim, MERRA, MERRA-2, JRA-55 and ERA5) for 1990-1999 (**a-f**) and 2004-2018 (**g-l**). Hashed areas indicate grid points where the trend is not significant at

the 95% confidence level. Note that MERRA ends in December 2015. Note the different colour scales for the early and later periods.

6.5.2 On the dipole interhemispheric pattern of shorter timescale trends

We highlighted in the introduction a body of studies reporting on the interhemispheric asymmetries in trends of long-lived tracers or AoA (see Sect. 2.5.4). In this section we investigate our inorganic fluorine time-series for these short-term modulations that are related to BDC changes. Strahan et al. (2020, Fig. 3) highlighted a periodic signal in the time-series of interhemispheric differences for deseasonalized AoA as well as for deseasonalized long-lived tracers (i.e., HNO_3 and HCl). From 1995 to 2018, 2011 stands out as the year with the strongest interhemispheric difference in their three analysed datasets, with AoA and tracer anomalies much smaller in the Southern Hemisphere than in the Northern Hemisphere. The years 2005 and 2014, on the other hand, stand out as years with opposite interhemispheric differences, i.e., AoA and tracer anomalis that are larger in the Southern Hemisphere than in the Northern Hemisphere. On the basis of this observation, we expect to find that the interhemispheric asymmetries in our inorganic fluorine trends are clearest for the period 2004-2011. Due to the relatively short time-series considered for this section, we emphasize that the following shorter term trend analysis is focused on the interhemispheric asymmetries rather than the computed absolute trend values.

As expected, a clear and significant hemispheric asymmetry in ${}^{*}F_y$ trends is found from ACE-FTS observations for the period 2004-2011, with positive trend values in the Northern Hemisphere and negative trend values in the Southern Hemisphere (Figure 6- 7a). The negative ${}^{*}F_y$ trend of the Southern Hemisphere is unexpected as organic fluorine sources are accumulating linearly in the troposphere during this period (Figure 6- 1). In the Northern Hemisphere, the positive trend area stretches from around 10°N up to the pole with a vertical extent from 100 hPa to 10 hPa. In the Southern Hemisphere, the area with negative trends is more limited than in the Northern Hemisphere, ranging from 20°S to -50°S and from 20 hPa to 10 hPa. Moreover, a second negative trend area is seen above the South Pole. All reanalyses reproduce well the spatial pattern depicted by ACE-FTS in the Northern Hemisphere but the interhemispheric differences are not as clear as in the observations because the negative trends in the Southern Hemisphere are weaker and not significant in the case of MERRA (Figure 6- 7c).

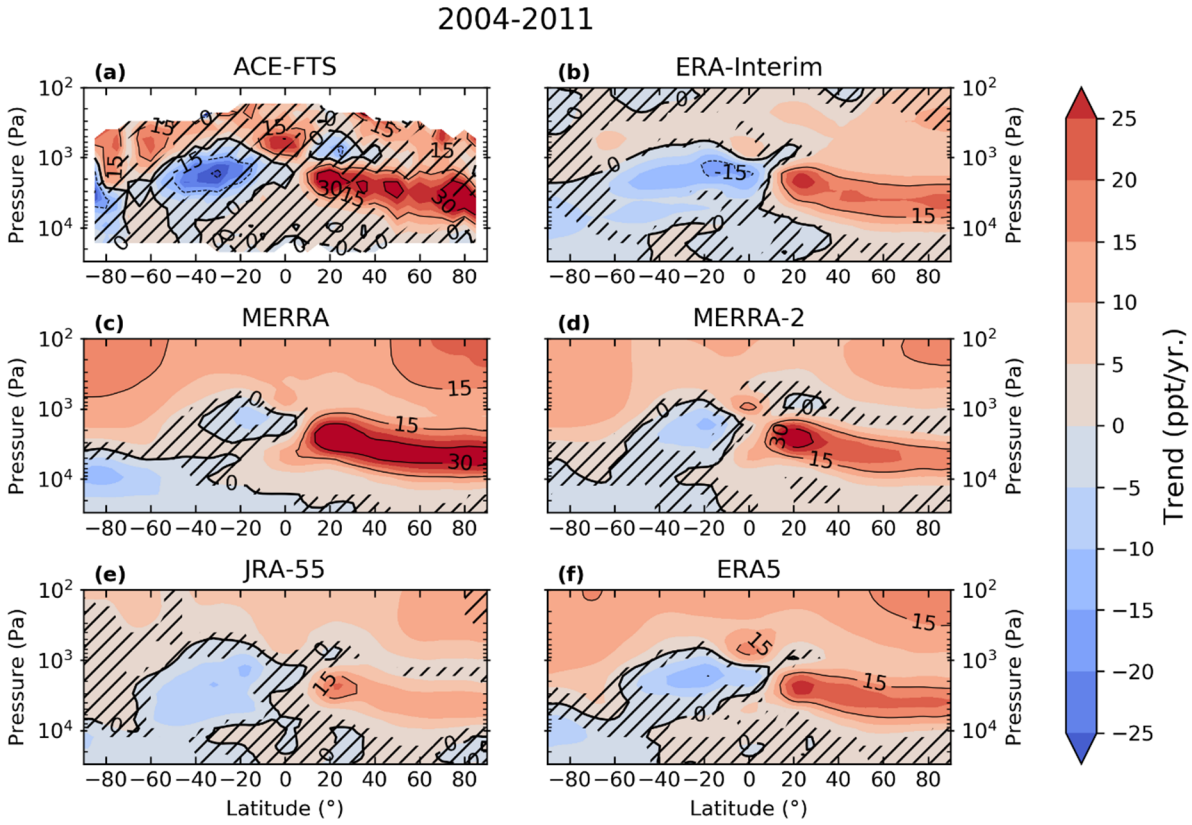

Figure 6- 7: Trends of *Fy (ACE-FTS) and Fy (BASCOE CTM forced by ERA-Interim, MERRA, MERRA-2, JRA-55 and ERA5 for 2004-2011. Hashed areas indicate grid points where the trend is not significant at the 95% confidence level.

From ground-based FTIR retrievals, we also note contrasting $^{*}F_y$ trend values between Lauder and Jungfraujoch for the period 2004-2011. The trends are 3.23 (2.4 – 4.1) $\times 10^{13}$ molec. cm^{-2} yr.$^{-1}$ at Jungfraujoch and -0.43 (-1.9 – 1.1) $\times 10^{13}$ molec. cm^{-2} yr.$^{-1}$ at Lauder. Although the uncertainty for the Lauder trend is quite large due to the monthly sampling, we note a non-significant trend at Lauder (45°S) and a large positive trend at Jungfraujoch (46°N). ACE-FTS shows even more contrasted results. In the Northern Hemisphere midlatitudes (40°N-50°N), the total column trend is 3.42 (2.6 – 4.2) $\times 10^{13}$ molec. cm^{-2} yr.$^{-1}$. In the Southern Hemisphere midlatitudes (40°S-50°S), it is -1.63 (-2.4 – -0.9) $\times 10^{13}$ molec. cm^{-2} yr.$^{-1}$.

6.6 Discussion

The analysis of inorganic fluorine time-series and their long-term trends highlights substantial differences between the reanalyses. From Figure 6- 4, Figure 6- 5 and Figure 6- 6, it is, as one would expect, clear that large trend values (i.e., MERRA and MERRA-2) result in high-biased time-series and inversely for low trend values (i.e., ERA-Interim and JRA-55). A comparison of this result with AoA studies can be drawn. In both studies of Chabrillat et al. (2018) and Ploeger et al. (2019), MERRA-2 is the reanalysis with the oldest AoA while JRA-55 and ERA-Interim, being close to each other, have the youngest AoA. MERRA, which is only compared in Chabrillat et al. (2018), has a mean AoA that is slightly younger than MERRA-2. An older mean AoA in the midlatitudes means a longer transit time from the tropical tropopause to the midlatitudes (i.e., slower residual circulation) and/or more time spent in large-scale eddies (i.e., irreversible mixing) in the midlatitudes. In the case of F_y, longer transit to – or residency times in – the midlatitudes allow for larger faction of the source gases to be converted into

inorganic fluorine reservoirs (i.e., HF, COF_2 and COClF; see Sect. 6.2). Hence the older AoA obtained from MERRA-2 is directly responsible for the larger F_y total columns when this reanalysis is used to drive BASCOE CTM and the steeper AoA trends with MERRA-2 are reflected in the stronger F_y trends obtained with that reanalysis. The same reasoning applies to the other reanalyses since their respective mean AoA, as determined by Chabrillat et al. (2018), are identical in this study (see Sect. 6.3.3.1).

Long-term trend analysis of the FTIR observations at Jungfraujoch also revealed significantly smaller trends of $^{*}F_y$ for the period 2004-2018 than for the period 1990-1999. This is reproduced by all CTM simulations, independently of the driving reanalysis (Figure 6- 5 and Figure 6- 6). From HF satellite observations and a TOMCAT/SLIMCAT ERA-Interim driven simulation, Harrison et al. (2016) also noted larger trend values during the end of the twentieth century (1991-1997) than the beginning of the twenty-first century (2004-2012). This reduced inorganic fluorine trend for the twenty-first century is expected as the total organic fluorine growing rate at surface peaked in the early 1990's (Figure 6- 1). Interestingly, all reanalyses except ERA-Interim show comparable trend values at Jungfraujoch and at Lauder for the period 1990-1999. Indeed, at Jungfraujoch, the BASCOE CTM simulation driven by ERA-Interim produces F_y trend values that are too small compared to ground-based FTIR observations and the other BASCOE CTM simulations. Harrison et al. (2016) also noted a disagreement for this period between HF global trends from their SLIMCAT run driven by ERA-interim and from HALOE (HALogen Occultation Experiment) satellite observations, with ERA-Interim trend being too small compared to that from HALOE. An unrealistic representation of the stratospheric dynamics in ERA-Interim in the end of the twentieth century is likely producing the biased F_y trends (Harrison et al., 2016). The new ECMWF reanalysis, ERA5, does not reproduce this bias and thus, seems to correct this issue in the former ERA-Interim reanalysis.

A key result of this study is the statistically smaller inorganic fluorine trend values at Lauder than at Jungfraujoch for all datasets for the period 2004-2018 (Figure 6- 5 and Figure 6- 6). Ground-based FTIR and ACE-FTS trend values are in agreement at both stations despite the larger uncertainty in the ground-based FTIR trend of Lauder due to the poorer sampling caused by the retrieval method (see Sect. 6.3.1.2). At Lauder, all BASCOE CTM simulations show small trend values for this period with even negative values for ERA-Interim and JRA-55. Using NDACC ground-based FTIR measurements, Strahan et al. (2020) also noted smaller HNO_3 and HCl trend values in the Southern Hemisphere compared to the Northern Hemisphere for the period 1994-2018. Moreover, estimating AoA trends from the NDACC measurements as well as using a CTM AoA simulation driven by MERRA-2, they concluded that the HNO_3 and HCl interhemispheric differences in trend were caused by a strengthening of the deep branch of the BDC (corresponding to lower AoA values) occurring in the Southern Hemisphere. While we do not assess any AoA trends in the present study, a comparison with our results showing lower F_y trend values in the Southern Hemisphere than in the Northern Hemisphere for the 21st century, confirms the conclusions of Strahan et al. (2020), using another stratospheric reservoir.

By subtracting each respective non-parametric fit (see Sect. 6.3.4 for methods and lines in Figure 6-4) of the Northern Hemisphere time-series to that of the Southern Hemisphere (e.g., Lauder minus Jungfraujoch FTIR or ACE-FTS 40°S to 50°S minus ACE-FTS 40°N to 50°N), Figure 6- 8 mimics Fig. 3 in Strahan et al. (2020) and reveals the dynamical signature of the discussed trends as the tropospheric trend of F_y sources should affect both hemispheres equally (Strahan et al., 2020). Figure 6- 8 confirms the overall building-up asymmetry between midlatitudes of both hemispheres in terms of inorganic

fluorine and thus AoA for the period 2000-2018. Moreover, it shows again that, despite the noted large differences between reanalyses, all of them capture that the AoA of the Southern Hemisphere midlatitudes is getting younger relative to that of the Northern Hemisphere midlatitudes. Figure 6- 8 furthermore highlights years of strong interhemispheric differences (i.e., 2005-2006, 2011, 2014-2015, 2017). Here we note again that all reanalyses reproduce, more or less strongly, the observed (ground-based FTIR and ACE-FTS) 5-to-7-year interhemispheric variability discussed in Strahan et al. (2020) and more specifically the considerable drop leading to the local minimum of the year 2011, followed by the local maximum of the year 2014. This variability seems to be more strongly reproduced by MERRA and MERRA-2 than by the other reanalyses (Figure 6- 7 and Figure 6- 8).

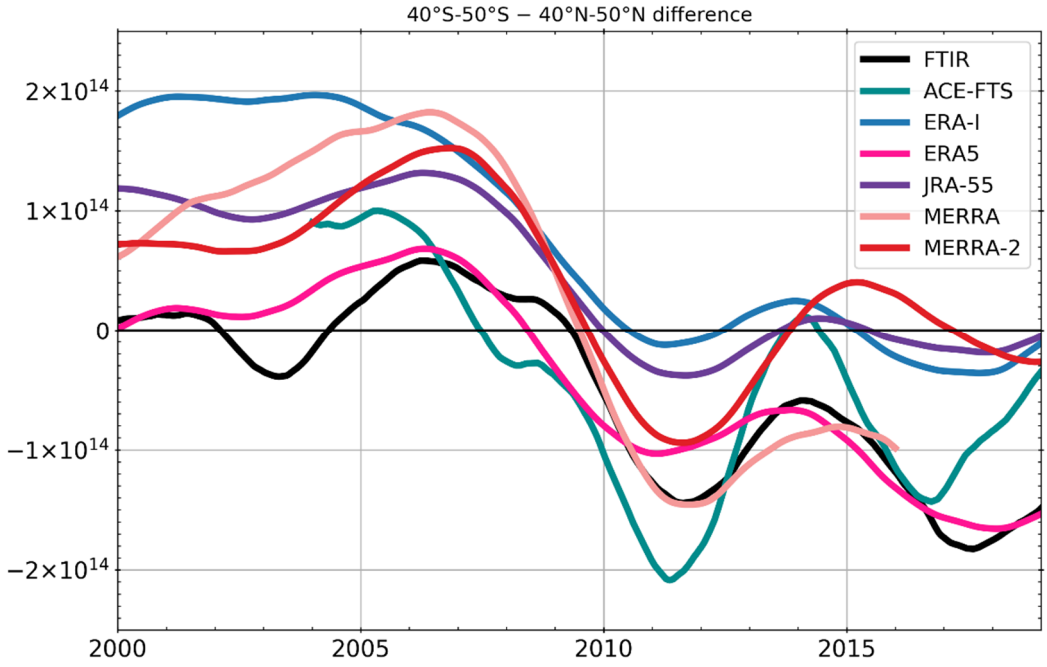

Figure 6- 8: Midlatitude differences (40°S-50°S minus 40°N-50°N) between respective observations of $^{*}F_y$ (ground-based FTIR and ACE-FTS) and BASCOE CTM simulation of F_y. The ground-based FTIR (black) difference is computed from Lauder (45°S) and Jungfraujoch (46°N). See text in Sect. 6.6 for methods.

The dipole structure in trends of the first two decades of the 21st century of long-lived tracers or AoA that has been discussed in the past years (see Sect 2.5.4 and references therein) is also noted in the trends of inorganic fluorine (Figure 6- 7). The time-period considered, often limited by data availability, is similar among the noted studies, e.g., 2005-2012 in Stiller et al. (2017) or 2002-2015 in Chabrillat et al. (2018) and Ploeger et al. (2019). Moreover, long-lived tracer studies generally limit their CTM simulation to a unique forcing reanalysis, which is often the ERA-Interim reanalysis (e.g., Harrison et al., 2014, 2016; Mahieu et al., 2014; Stiller et al., 2017; Han et al., 2019). As in Strahan et al. (2020), we show here that considering a sufficiently long time period allows for the detection of succeeding minima and maxima in the time-series of interhemispheric difference (Figure 6- 8). In this context, the dipole structure in trends of long-lived tracers firstly described by Mahieu et al. (2014) and followed by a number of other studies is actually situated between two years of large (actually among the largest) opposite extremes in interhemispheric differences (i.e., 2005, with older AoA in the Southern Hemisphere relative to the Northern Hemisphere, to 2011 or 2012, with younger AoA in the Southern Hemisphere relative to the Northern Hemisphere). On the other hand, the period 2002-2015, chosen by Chabrillat et al. (2018) and Ploeger et al. (2019), might not be adequate to detect this dipole as the local

minimum or maximum interhemispheric anomalies are missed by a few years at both limits of the time period. Moreover, these two studies concluded that only ERA-Interim showed a dipole structure in AoA trends (i.e., opposite hemispheric trends) over the 2002-2015 period. Chabrillat et al. (2018) further mentioned that the Northern Hemisphere positive AoA trend was larger and significant at more grid points for the 2002-2012 period. Zonal mean trends computed on our F_y simulations for the period 2002-2015 only show a dipole structure for ERA-Interim (not shown).

While recent studies agree on the role of the QBO in the midlatitude BDC multiyear-variability, it is still unclear if the observed periodicity is actually caused by the same phenomenon or if it is a succession or alignment of more or less independent phenomena. The QBO itself is inherently unpredictable as it has, on the one hand, a variable period of ~22 to ~36 months (e.g., Osprey et al., 2016) and, on the other hand, an intrinsic variability as illustrated by the unprecedented QBO disruption in 2015-2016 (Osprey et al., 2016; Tweedy et al., 2017; Diallo et al., 2018). In addition to the interaction between the BDC and the QBO, the El Niño–Southern Oscillation (ENSO) is also at play and its alignment with QBO phases can lead to large stratospheric water vapour and O_3 anomalies (Diallo et al., 2018, 2019). As in earlier studies (see e.g., Fig. 13 in Ploeger and Birner, 2016; Fig. 4 in Diallo et al., 2018 or Fig. 3 in Strahan et al., 2020), the 2010-2011 period stands out in Figure 6- 8 as a period of particularly strong interhemispheric difference, whether in long-lived tracer or in AoA spectrum time-series. The 2009-2013 period saw peculiarities in the QBO winds, with an intense QBO easterly wind phase starting in mid-2009 and ending in mid-2010, followed by a relatively weak westerly phase (Nedoluha et al., 2015). The strong easterly phase, starting in austral winter, could have built-up low F_y anomalies in the Southern Hemisphere midlatitudes due to enhanced poleward advection from the tropics (Baldwin et al., 2001; Strahan et al., 2015). As explained in Strahan et al. (2015), a transport pathway allows the QBO-generated trace gas variability to reach the poles and persist in midlatitudes through recirculation (Ploeger and Birner, 2016). Moreover, as noted by Diallo et al. (2018), the Arctic stratospheric vortex was exceptionally strong and lasted until April 2011 (Manney et al., 2011), which corresponds to a weaker wave activity (Hurwitz et al., 2011) and thus, weaker BDC in the Northern Hemisphere. The more stable poleward transport of easterly QBO phase anomalies in the Southern Hemisphere (Strahan et al., 2015) coupled to the weak BDC in the Northern Hemisphere would then explain the strong interhemispheric difference (i.e., high and low F_y values in the Northern and Southern Hemispheres, respectively) of the period 2010-2011. Detailed quantitative analysis needs to be done in the future to support or reject this hypothesis.

6.7 Conclusions

Using inorganic fluorine, as retrieved ($^{*}F_y$, see Eq. 6.2) from ground-based FTIR solar spectra recorded at the NDACC stations of Jungfraujoch (Switzerland, 46°N) and Lauder (New Zealand, 45°S) as well as from ACE-FTS occultation measurements and simulated (F_y, see Eq. 6.1) by BASCOE CTM driven by 5 modern reanalyses, we investigated the BDC variability and long-term changes over the last 30 years. The long-term trends of inorganic fluorine analysed in this research suggest that the midlatitude lower stratosphere of the Southern Hemisphere is getting younger relative to that of the Northern Hemisphere during the first decades of the twenty-first century (2004-2018; Figure 6- 6g-i and Figure 6- 8). While we noted large differences between the reanalyses, we showed that all of them capture this interhemispheric asymmetry. This result, based on observations and CTM simulations driven by meteorological reanalyses, are in contrast with the CCM projections for the twenty-first century in

response to the coupled increase of greenhouse gases and decrease of ODS (See Sect. 2.5.2). Indeed, CCMs simulate a much less accelerated BDC in response to the greenhouse gases increase when the forcing of the ODS decrease is taken into account, with a larger impact of the latter in the Southern Hemisphere due to the ozone hole recovery, i.e., a decelerated BDC in the Southern Hemisphere (Polvani et al., 2019). These conflicting results, between observed and CCM-modelled BDC long-term trends, were also recently noted by Strahan et al. (2020) from global and multidecadal observations of HCl and HNO_3. These disagreements between observations and CCMs, also highlighted recently in Ball et al. (2020) for midlatitude ozone trends, await further investigations as these same models are used to project the health of the ozone layer as ODS decline and climate changes.

The large differences in stratospheric transport evaluated in modern reanalyses were noted in previous studies. A direct comparison between earlier AoA results (Chabrillat et al., 2018) and the present work highlights the relation between the assessed AoA of reanalyses and our F_y time-series, with older AoA causing larger F_y columns in the midlatitudes. Our comparison with FTIR observations shows that the F_y trend produced by ERA-Interim above Jungfraujoch is unrealistically low for the 1990-1999 period. An important original result of this study is that ERA5, the new ECMWF reanalysis, seems more suitable than ERA-Interim to drive kinematic CTMs such as the BASCOE CTM (Figure 6- 4, Figure 6- 5, Figure 6- 6 and Figure 6- 8). This suggests an overall better representation of transport variability in ERA5 than in ERA-Interim over the whole period 1990-2018 investigated here.

While we did not investigate the cause of the BDC circulation changes, we emphasize here the importance of multidecadal time-series of observations as proposed today by the FTIR NDACC network as well as by the ACE-FTS or the AURA-MLS satellite instruments. Large disagreements or differences are indeed depicted between CCMs simulations, reanalyses and observations (see Sect. 2.5). The differences between reanalyses are not limited to the 20th century when observations were sparser and less precise (e.g., vertically resolved) than they are today. Disagreements between reanalyses can, in fact, be larger for the last two decades than for the 1990s. Moreover, seeing these large discrepancies, it seems that studies assessing trends in the last decades (e.g., estimations of the current status of ozone layer healing) should not rely on only one reanalysis and should choose the periods for the trend evaluation with care.

Beside their utility in this study, we demonstrate that the multidecadal $^{*}F_y$ time-series of inorganic fluorine as retrieved from the ground-based FTIR stations of Lauder and Jungfraujoch are a very good approximation of the total inorganic fluorine F_y. This is important as these long-term time-series are needed to scrutinize the fulfilment of the Montreal Protocol on Substances that Deplete the Ozone Layer, now that HFCs are also regulated (See Sect. 6.1).

Chapter 7

Conclusions and outlook

Five years ago, following the recent study discussing the unexpected Northern Hemisphere stratospheric HCl increase (Mahieu et al., 2014a), a research project was submitted to investigate the BDC changes, since they were believed to be at the origin of this HCl variability. The ACCROSS (Atmospheric Composition and Circulation investigated with meteorological Reanalyses, Observational datasets and models for the Study of the Stratosphere and its changes) project was then launched. During the four years and a half of this project and thesis, I had the opportunity to broaden my knowledge about the stratosphere –my Master's courses were principally focused on the troposphere–, familiarized on site with the FTS installed at the scientific station of the Jungfraujoch, get acquainted with the BASCOE CTM and the modelling of the stratospheric chemistry and transport, or play (a lot) with Python to carry out the needed analyses for the project. My initial expectations were to help in the characterization of the temporary BDC asymmetric change first detected by Mahieu et al. (2014). With the time passing, we progressively discovered that this asymmetry in BDC trends was part of, what seems to be, an interannual variability of the BDC. Something I did not expect was also to determine that, for the past twenty years, the BDC has been changing asymmetrically, with a relative strengthening of the Southern Hemisphere branch relative that of the Northern Hemisphere.

This chapter summarizes the objectives (Sect. 7.1) and the major results (Sect. 7.2) of this thesis. Section 7.3 finally presents the outlook, i.e., the potential future studies and the importance of the datasets we generated in the framework of this thesis for the monitoring of the Montreal Protocol on Substances that Deplete the Ozone Layer.

7.1 Motivations and objectives

In Chapter 2, we drew a state of the art of the observed and simulated BDC changes over the past decades. We also presented the main results from CCM projections for the twenty-first century in response to the increase of greenhouse gases and to the decrease of ODSs: CCMs project an overall acceleration of the BDC, although large hemispheric asymmetries are simulated. Due to the ozone hole recovery, the BDC in the Southern Hemisphere is, indeed, expected to increase much less than in the Northern Hemisphere. From this state of the art, we retained three main results which were later investigated in Chapter 6: (1) recent long-term trends of observed (i.e., as estimated from observations of CO_2 and SF_6) age of air and long-lived tracers oppose, or at least do not confirm, results of CCMs,

calling for further investigations. In fact, the long-term age of air time-series of Engel et al. (2017) shows a positive but not statistically significant trend in the Northern Hemisphere midlatitudes for the period 1975-2016. Long-term global observations of HCl and HNO_3 suggest that the age of air in the Southern Hemisphere is getting younger relative to that of the Northern Hemisphere during the first decades of the twenty-first century (Strahan et al., 2020); (2) Decadal trends of age of air (e.g., Haenel et al., 2015) and long-lived stratospheric tracers (e.g., Mahieu et al., 2014; Nedoluha et al., 2015) are strongly perturbed by a 5-to-7-year interannual variability of the BDC (Strahan et al., 2020); (3) Evaluation of the representation of the BDC in reanalyses, through age of air simulation performed by CTMs, has revealed substantial differences between modern reanalyses (Chabrillat et al., 2018; Ploeger et al., 2019), suggesting that these datasets may not be adequate to assess BDC trends.

Facing these highlighted results, we proposed, in this work, to investigate the BDC changes through an analysis of long-term time-series of inorganic fluorine. To this end, we updated the ground-based FTIR time-series of HF and COF_2 from Lauder and Jungfraujoch, constructed a total inorganic fluorine (F_y) dataset from ACE-FTS retrievals of HF, COF_2 and COClF, and prepared and performed five 35-year simulations of F_y using the BASCOE CTM driven by five modern meteorological reanalyses (ERA-Interim, ERA5, JRA-55, MERRA and MERRA-2).

Before this effort, BASCOE CTM has been principally employed to perform reanalyses of the stratospheric chemical composition (e.g., Skachko et al., 2016; Errera et al., 2019) or long-term simulations of mean age of air (Chabrillat et al., 2018). It is the first time that this CTM is used for multidecadal simulations aiming at the accurate modelling of a long-lived tracer such as F_y. Therefore, new developments were needed in order to carry out the five experiments (see Chapter 3). Thus, new features, such as the reading of historical lower boundary conditions for surface concentrations and their oxidation by OH in the troposphere, were implemented just before the beginning of this project. Moreover, important F_y sources, such as HFC-134a, were missing from the chemical scheme of BASCOE CTM. Therefore, we had to include these species, along with their degradation schemes. In the same time, all reaction rates of F_y sources were updated.

In this work, we first presented a new strategy to retrieve HCFC-22, currently the second source of F_y and the most abundant HCFC, from infrared solar spectra recorded at the scientific station of the Jungfraujoch. Besides the obvious motivation to assess recent trends of a major source of F_y and an important ODS, with production and consumption practically banned at the present time, this study was also the occasion to perform a first evaluation of our BASCOE CTM set-up. Indeed, before evaluating the simulated time-series of F_y, it was necessary to first evaluate and validate the behaviour of the model regarding F_y sources.

7.2 Summary of the main conclusions

7.2.1 HCFC-22 lower accumulation rates and BASCOE CTM first evaluation

We developed an improved strategy to retrieve for the first time partial columns of HCFC-22 from infrared solar spectra recorded by the FTIR instruments operated at the Jungfraujoch scientific station (Chapter 5). Thus far, only total columns of HCFC-22 were available from our observations or from any other ground-based stations, without any information on the tropospheric and stratospheric partitioning of this important source of fluorine and chlorine. Our work allowed to derive partial columns

representative of the troposphere (<11.21 km) and of the lower to mid stratosphere (11.21 to 30 km), with only a minor influence of the a priori state. The new retrieval strategy uses a Tikhonov regularization to inverse the relatively narrow $2\nu_6$ Q-branch feature (~829.1 cm^{-1}) of HCFC-22. To our knowledge, this remains the sole study retrieving partial columns of HCFC-22 with a reasonable information content.

The major result of Chapter 5 is the **slowing down of the HCFC-22 accumulation rate in the atmosphere**. Each new year included reduces the last decade trend. This supports the perspective of a new success of the Montreal Protocol on Substances that Deplete the Ozone Layer in the years to come.

We demonstrated the validity of our total and partial columns by realizing an intercomparison with independent datasets. Stratospheric columns showed a good agreement with retrievals of MIPAS in absolute values, trends and seasonality. The retrieved mean tropospheric mixing ratios (average of the vertical levels below 11.21 km) were compared to AGAGE in situ measurements performed at Mace Head (Ireland) and Jungfraujoch, confirming the soundness of our tropospheric time-series, both in absolute values and trends. However, a disagreement for the seasonality was depicted. While our tropospheric time-series showed a seasonal cycle similar to that of the lower-stratospheric partial columns, the in situ time-series were not showing any cycles. It was attributed to the different vertical sensitivities between the two measurement techniques. Indeed, contrary to surface in situ measurements, our tropospheric retrievals have a sensitivity up to the tropopause. At this altitude, intrusions of HCFC-22-poor polar air masses in late winter/early spring may indeed cause a seasonal cycle in our tropospheric time-series.

Concerning BASCOE CTM, we showed that HCFC-22 total and partial simulated columns were also in good agreement with the observations, giving us confidence in the validity of the chosen lower boundary conditions (see Chapter 3) as well as in their handling by BASCOE CTM. The fact that the lower-stratospheric time-series were also in good agreement with the observations also gave us confidence in the implemented chemistry of F_y sources.

7.2.2 Hemispheric asymmetry in trends of inorganic fluorine related to BDC changes: qualitative agreement between observations and all of the five modern reanalyses

In Chapter 6, we presented the results from our investigations on the BDC long-term change and interannual variability as indirectly diagnosed from observed and simulated time-series of inorganic fluorine. We included three different types of datasets: ground-based FTIR retrievals of HF and COF_2 from Lauder (New Zealand, 45°S) and Jungfraujoch (Switzerland, 46°N) NDACC stations, global time-series of HF, COF_2 and COClF from ACE-FTS and five F_y simulations of BASCOE CTM driven by the five modern meteorological reanalyses (ERA-Interim, ERA5, JRA-55, MERRA and MERRA-2).

For ground-based FTIR time-series, HF is a standard target of the NDACC network and is thus currently retrieved at most NDACC sites. However, before this work, COF_2 had only been retrieved from infrared solar spectra recorded at the scientific station of the Jungfraujoch. This is mostly owing to the fact that COF_2 is a challenging species to retrieve because of its very weak and relatively broad absorptions. The strategy, developed by Duchatelet et al. (2009), enhances the information content by simultaneously fitting several spectra recorded over the same day (with 3 retrieval windows considered in each spectrum). It was originally developed for the SFIT-2 retrieval algorithm. For this work, we developed a processing environment to prepare and process multiple spectra with SFIT-4, the current

algorithm in use in NDACC. The retrieval strategy now includes a new a priori calculated from ACE-FTS COF_2 vertical profiles, offering a better representativeness thanks to larger statistics. For the first time, COF_2 total columns were retrieved from infrared solar spectra recorded at Lauder. Thanks to a fruitful collaboration with Dan Smale (National Institute of Water and Atmospheric Research, Lauder), the Jungfraujoch retrieval strategy was adapted for Lauder spectra (see Sect. 6.3.1.2).

A major finding is the **slower F_y accumulation rate in the Southern Hemisphere** relative to the Northern Hemisphere **as seen from observations and from all of the five reanalyses for the period 2004-2018**. Linking our results with the recent study of Strahan et al. (2020) on HCl and HNO_3 global time-series, we concluded that this hemispheric asymmetry in trends of F_y is **caused by a strengthening of the BDC in the Southern Hemisphere relative to the Northern Hemisphere**. This result opposes the CCM projections in response to the increase of greenhouse gases and the decrease of ODSs. Superimposed to this long-term change of the BDC, we also detected the 5-to-7-year variability leading to strong dipole in global stratospheric trends and influencing very strongly decadal trends of long-lived tracers and age of air. These conclusions stress out the need to pursue long-term observational experiments such as in the frameworks of the NDACC network and of satellite missions as ACE-FTS.

While the agreement between ground-based and satellites measurements of long-lived tracers for this hemispheric asymmetry is already a chief result, the fact that we showed that all of the five modern reanalyses were qualitatively in agreement with this conclusion is as big and, somehow, unexpected. Indeed, recent studies, assessing the age of air of these same reanalyses (Chabrillat et al., 2018; Ploeger et al., 2019; note that Chabrillat et al., 2018, used the BASCOE CTM in the exact same configuration) revealed large differences in the reanalysis BDC decadal trends.

Finally, we demonstrated that inorganic fluorine time-series derived from ground-based FTIR retrievals of HF and COF_2 are a very good proxy of the total inorganic fluorine F_y. Indeed, the evaluation of the F_y budget from ACE-FTS and the CTM TOMCAT showed that COClF in only accounting for 2% (from ACE-FTS) to 7% (from TOMCAT) of the F_y budget above the stations of Lauder and Jungfraujoch.

7.2.3 First long-term simulations of BASCOE CTM

It is important to stress out again that, in this work, we performed the first long-term experiments of BASCOE CTM aiming at the accurate simulation of a long-term tracer such as F_y. The major developments were: (1) the construction of a model initial state valid for 1985, a period where global observations of atmospheric constituents are sparse; (2) the addition of missing important F_y sources (e.g., HFC-134a) and their corresponding degradation pathways in the model chemical scheme; (3) the update of all fluorine-related reaction rates. All these improvements were conducted and tested continuously during this project. The fact that we finally managed to accurately simulate F_y in the stratosphere, both in absolute values and trends (in general aspects), is a key achievement of this work that should not be ignored or forgotten when discussing the general conclusions of Chapters 5 and 6.

7.3 Outlook

7.3.1 Future work on BDC changes

Concerning the observed BDC changes we diagnosed in this thesis, next research topics should focus on the determination of their causes. Our simulations were recently used to evaluate the climatological impact of the BDC on the meridional distribution of N_2O, through an evaluation of their TEM budget (i.e., a separation of the residual mean advection and the isentropic mixing from the BDC; Minganti et al., 2020). In the study of Minganti et al. (2020), which I co-authored, the TEM budget of modern reanalyses (except ERA5 whose BASCOE CTM simulation was not completed yet) were also compared to that of a chemical reanalysis of Aura MLS performed by BASCOE and to that of a free-running simulation of WACCM. A follow-up of this study is currently in progress. This time, it is planned to analyse the separated time-series of residual mean advection and isentropic mixing (as derived from the TEM framework), derived from the same datasets, to assess their respective contribution to the observed BDC changes.

All reanalyses are qualitatively in agreement for the hemispheric asymmetry building up during the first decades of the twenty-first century and the BDC 5-to-7-year variability. Therefore, these datasets could be further used to investigate the cause of the BDC changes we highlighted in the present thesis. This could be done, for example, by assessing the wave forcing of the reanalyses (e.g., Pahlavan et al., 2021) and see if the observed asymmetry of the BDC is related to an eventual asymmetry in the wave forcing.

Future works could also include proper comparisons of our observational and reanalysis datasets with CCM results. The suggested disagreement between observations and CCM BDC trends could be this way investigated more deeply. This was for example done in the recent study of Ball et al. (2020) for lower-stratospheric ozone trends. It is crucial to evaluate the CCM performances against observations for historical periods as these models are used to project future changes, such as the recovery of the ozone layer, as greenhouse gases increase and ODSs decrease.

7.3.2 Monitoring the success of the Montreal Protocol and the WMO's Scientific Assessment of Ozone Depletion 2022

All observational time-series produced during this thesis are essential for the monitoring of the fulfilment of the Montreal Protocol.

Notably, the ground-based inorganic fluorine ($= \mathrm{HF} + 2 \times \mathrm{COF_2}$) time-series are now a mandatory indicator of the success of the Montreal Protocol since HFC production and consumption are now regulated by the protocol through the Kigali Amendment. While, the time-series of inorganic fluorine were already available for the Jungfraujoch NDACC station, it is the first time that such time-series are available and published for the Lauder station. Two time-series of inorganic fluorine are, therefore, now available for the northern and southern midlatitudes. That is particularly relevant given the contrasted evolutions of the atmospheric circulation and composition in both hemispheres. We also demonstrated that ACE-FTS F_y data were in very good agreement with the ground-based FTIR time-series.

HCFC-22 is obviously a key anthropogenic gas to monitor as it is, by far, the most abundant HCFCs. Moreover, HCFC production and consumption are now banned in developed countries (since 1st January

2020; with a 10-year 0.5% allowance) and will be banned in developing countries on 1st January 2030 (with a 10-year 2.5% allowance). HCFCs are the last ODSs targeted by the Montreal Protocol that are still produced and consumed today. It would be interesting in the future to establish a retrieval strategy for HFC-134a. Indeed, this greenhouse gas is strongly increasing since the mid-1990s and will certainly rapidly overcome HCFC-22 as the second source of F_y. This last perspective is actually planned in an ongoing thesis project in our group at the University of Liège.

The two first-author studies published in the framework of this thesis, along with their corresponding produced datasets, will thus provide good supports for the production of the upcoming WMO's Scientific Assessment of Ozone Depletion 2022.

References

Abalos, M., Polvani, L., Calvo, N., Kinnison, D., Ploeger, F., Randel, W. and Solomon, S.: New Insights on the Impact of Ozone-Depleting Substances on the Brewer-Dobson Circulation, J. Geophys. Res. Atmos., 124(5), 2435–2451, https://doi.org/10.1029/2018JD029301, 2019.

Andrews, A. E., Boering, K. A., Daube, B. C., Wofsy, S. C., Loewenstein, M., Jost, H., Podolske, J. R., Webster, C. R., Herman, R. L., Scott, D. C., Flesch, G. J., Moyer, E. J., Elkins, J. W., Dutton, G. S., Hurst, D. F., Moore, F. L., Ray, E. A., Romashkin, P. A. and Strahan, S. E.: Mean ages of stratospheric air derived from in situ observations of CO2, CH4 , and N2O, J. Geophys. Res. Atmos., 106(D23), 32295–32314, https://doi.org/10.1029/2001JD000465, 2001.

Andrews, D. G. and Mcintyre, M. E.: Generalized Eliassen-Palm and Charney-Drazin Theorems for Waves oin Axismmetric Mean Flows in Compressible Atmospheres, J. Atmos. Sci., 35(2), 175–185, https://doi.org/10.1175/1520-0469(1978)035<0175:GEPACD>2.0.CO;2, 1978.

Andrews, D. G. and McIntyre, M. E.: Planetary Waves in Horizontal and Vertical Shear: The Generalized Eliassen-Palm Relation and the Mean Zonal Acceleration, J. Atmos. Sci., 33(11), 2031–2048, https://doi.org/10.1175/1520-0469(1976)033<2031:PWIHAV>2.0.CO;2, 1976.

Bader, W., Bovy, B., Conway, S., Strong, K., Smale, D., Turner, A. J., Blumenstock, T., Boone, C., Collaud Coen, M., Coulon, A., Garcia, O., Griffith, D. W. T., Hase, F., Hausmann, P., Jones, N., Krummel, P., Murata, I., Morino, I., Nakajima, H., O'Doherty, S., Paton-Walsh, C., Robinson, J., Sandrin, R., Schneider, M., Servais, C., Sussmann, R. and Mahieu, E.: The recent increase of atmospheric methane from 10 years of ground-based NDACC FTIR observations since 2005, Atmos. Chem. Phys., 17(3), 2255–2277, https://doi.org/10.5194/acp-17-2255-2017, 2017.

Baldwin, M. P., Gray, L. J., Dunkerton, T. J., Hamilton, K., Haynes, P. H., Randel, W. J., Holton, J. R., Alexander, M. J., Hirota, I., Horinouchi, T., Jones, D. B. A., Kinnersley, J. S., Marquardt, C., Sato, K. and Takahashi, M.: The quasi-biennial oscillation, Rev. Geophys., 39(2), 179–229, https://doi.org/10.1029/1999RG000073, 2001.

Ball, W. T., Chiodo, G., Abalos, M., Alsing, J. and Stenke, A.: Inconsistencies between chemistry–climate models and observed lower stratospheric ozone trends since 1998, Atmos. Chem. Phys., 20(16), 9737–9752, https://doi.org/10.5194/acp-20-9737-2020, 2020.

Baltensperger, U., Gäggeler, H. W., Jost, D. T., Lugauer, M., Schwikowski, M., Weingartner, E. and Seibert, P.: Aerosol climatology at the high-alpine site Jungfraujoch, Switzerland, J. Geophys. Res. Atmos., 102(D16), 19707–19715, https://doi.org/10.1029/97JD00928, 1997.

Banerjee, A., Fyfe, J. C., Polvani, L. M., Waugh, D. and Chang, K. L.: A pause in Southern Hemisphere circulation trends due to the Montreal Protocol, Nature, 579(7800), 544–548, https://doi.org/10.1038/s41586-020-2120-4, 2020.

Barret, B.: Inversion et caractérisation de profils de constituants atmosphériques à partir de mesures FTIR sol, Université Libre de Bruxelles, 2003.

Barret, B., De Mazière, M. and Demoulin, P.: Retrieval and characterization of ozone profiles from solar infrared spectra at the Jungfraujoch, J. Geophys. Res., 107(D24), 4788, https://doi.org/10.1029/2001JD001298, 2002.

Bates, D. R. and Nicolet, M.: Atmospheric hydrogen, Publ. Astron. Soc. Pacific, 62(365), 106–110, 1950.

Bednarek, G., Breil, M., Hoffmann, A., Kohlmann, J. P., Mörs, V. and Zellner, R.: Rate and Mechanism of the Atmospheric Degradation of 1,1,1,2-Tetrafluoroethane (HFC-134a), Berichte der

Bunsengesellschaft für Phys. Chemie, 100(5), 528–539, https://doi.org/10.1002/bbpc.19961000503, 1996.

Bernath, P. F.: The Atmospheric Chemistry Experiment (ACE), J. Quant. Spectrosc. Radiat. Transf., 186, 3–16, https://doi.org/10.1016/j.jqsrt.2016.04.006, 2017.

Bernath, P. F., McElroy, C. T., Abrams, M. C., Boone, C. D., Butler, M., Camy-Peyret, C., Carleer, M., Clerbaux, C., Coheur, P. F., Colin, R., DeCola, P., DeMazière, M., Drummond, J. R., Dufour, D., Evans, W. F. J., Fast, H., Fussen, D., Gilbert, K., Jennings, D. E., Llewellyn, E. J., Lowe, R. P., Mahieu, E., McConnell, J. C., McHugh, M., McLeod, S. D., Michaud, R., Midwinter, C., Nassar, R., Nichitiu, F., Nowlan, C., Rinsland, C. P., Rochon, Y. J., Rowlands, N., Semeniuk, K., Simon, P., Skelton, R., Sloan, J. J., Soucy, M. A., Strong, K., Tremblay, P., Turnbull, D., Walker, K. A., Walkty, I., Wardle, D. A., Wehrle, V., Zander, R. and Zou, J.: Atmospheric chemistry experiment (ACE): Mission overview, Geophys. Res. Lett., 32(15), L15S01, https://doi.org/10.1029/2005GL022386, 2005.

Bernath, P. F., Steffen, J., Crouse, J. and Boone, C. D.: Atmospheric Chemistry Experiment SciSat Level 2 Processed Data, v4.0 [Dataset], , https://doi.org/10.20383/101.0291, 2020a.

Bernath, P. F., Steffen, J., Crouse, J. and Boone, C. D.: Sixteen-year trends in atmospheric trace gases from orbit, J. Quant. Spectrosc. Radiat. Transf., 253, 107178, https://doi.org/10.1016/j.jqsrt.2020.107178, 2020b.

Birner, T. and Bönisch, H.: Residual circulation trajectories and transit times into the extratropical lowermost stratosphere, Atmos. Chem. Phys., 11(2), 817–827, https://doi.org/10.5194/acp-11-817-2011, 2011.

Bloom, S. C., Takacs, L. L., da Silva, A. M. and Ledvina, D.: Data Assimilation Using Incremental Analysis Updates, Mon. Weather Rev., 124(6), 1256–1271, https://doi.org/10.1175/1520-0493(1996)124<1256:DAUIAU>2.0.CO;2, 1996.

Boering, K. A., Wofsy, S. C., Daube, B. C., Schneider, H. R., Loewenstein, M., Podolske, J. R. and Conway, T. J.: Stratospheric Mean Ages and Transport Rates from Observations of Carbon Dioxide and Nitrous Oxide, Science (80-.)., 274(5291), 1340–1343, https://doi.org/10.1126/science.274.5291.1340, 1996.

Bönisch, H., Engel, A., Birner, T., Hoor, P., Tarasick, D. W. and Ray, E. A.: On the structural changes in the Brewer-Dobson circulation after 2000, Atmos. Chem. Phys., 11(8), 3937–3948, https://doi.org/10.5194/acp-11-3937-2011, 2011.

Brasseur, G. P. and Jacob, D. J.: Numerical Methods for Advection, in Modeling of Atmospheric Chemistry, pp. 275–341, Cambridge University Press, Cambridge, https://doi.org/10.1017/9781316544754.008, , 2017.

Brasseur, G. P. and Solomon, S.: Aeronomy of the Middle Atmosphere, 3rd ed., edited by L. A. Mysak and K. Hamilton, Springer Netherlands, Dordrecht., 2005.

Brewer, A. W.: Evidence for a world circulation provided by the measurements of helium and water vapour distribution in the stratosphere, Q. J. R. Meteorol. Soc., 75(326), 351–363, https://doi.org/10.1002/qj.49707532603, 1949.

Burkholder, J. B., Cox, R. A. and Ravishankara, A. R.: Atmospheric Degradation of Ozone Depleting Substances, Their Substitutes, and Related Species, Chem. Rev., 115(10), 3704–3759, https://doi.org/10.1021/cr5006759, 2015a.

Burkholder, J. B., Sander, S. P., Abbatt, J., Barker, J. R., Huie, R. E., Kolb, C. E., Kurylo, M. J., Orkin, V. L., Wilmouth, D. M. and Wine, P. H.: Chemical Kinetics and Photochemical Data for Use in Atmospheric Studies, Evaluation No. 18, JPL Publ., 15–10 https://jpldataeval.jpl.nasa.gov/, 2015b.

Butchart, N.: The Brewer-Dobson circulation, Rev. Geophys., 52(2), 157–184,

https://doi.org/10.1002/2013RG000448, 2014.

Butchart, N., Cionni, I., Eyring, V., Shepherd, T. G., Waugh, D. W., Akiyoshi, H., Austin, J., Brühl, C., Chipperfield, M. P., Cordero, E., Dameris, M., Deckert, R., Dhomse, S., Frith, S. M., Garcia, R. R., Gettelman, A., Giorgetta, M. A., Kinnison, D. E., Li, F., Mancini, E., McLandress, C., Pawson, S., Pitari, G., Plummer, D. A., Rozanov, E., Sassi, F., Scinocca, J. F., Shibata, K., Steil, B. and Tian, W.: Chemistry–Climate Model Simulations of Twenty-First Century Stratospheric Climate and Circulation Changes, J. Clim., 23(20), 5349–5374, https://doi.org/10.1175/2010JCLI3404.1, 2010.

Chabrillat, S., Vigouroux, C., Christophe, Y., Engel, A., Errera, Q., Minganti, D., Monge-Sanz, B. M., Segers, A. and Mahieu, E.: Comparison of mean age of air in five reanalyses using the BASCOE transport model, Atmos. Chem. Phys., 18(19), 14715–14735, https://doi.org/10.5194/acp-18-14715-2018, 2018.

Chapman, S.: XXXV. On ozone and atomic oxygen in the upper atmosphere, London, Edinburgh, Dublin Philos. Mag. J. Sci., 10(64), 369–383, https://doi.org/10.1080/14786443009461588, 1930.

Chipperfield, M. P.: New version of the TOMCAT/SLIMCAT off-line chemical transport model: Intercomparison of stratospheric tracer experiments, Q. J. R. Meteorol. Soc., 132(617), 1179–1203, https://doi.org/10.1256/qj.05.51, 2006.

Chipperfield, M. P., Burton, M., Bell, W., Walsh, C. P., Blumenstock, T., Coffey, M. T., Hannigan, J. W., Mankin, W. G., Galle, B., Mellqvist, J., Mahieu, E., Zander, R., Notholt, J., Sen, B. and Toon, G. C.: On the use of HF as a reference for the comparison of stratospheric observations and models, J. Geophys. Res. Atmos., 102(D11), 12901–12919, https://doi.org/10.1029/96JD03964, 1997.

Chirkov, M., Stiller, G. P., Laeng, A., Kellmann, S., von Clarmann, T., Boone, C. D., Elkins, J. W., Engel, A., Glatthor, N., Grabowski, U., Harth, C. M., Kiefer, M., Kolonjari, F., Krummel, P. B., Linden, A., Lunder, C. R., Miller, B. R., Montzka, S. A., Mühle, J., O'Doherty, S., Orphal, J., Prinn, R. G., Toon, G., Vollmer, M. K., Walker, K. A., Weiss, R. F., Wiegele, A. and Young, D.: Global HCFC-22 measurements with MIPAS: retrieval, validation, global distribution and its evolution over 2005–2012, Atmos. Chem. Phys., 16(5), 3345–3368, https://doi.org/10.5194/acp-16-3345-2016, 2016.

von Clarmann, T., Glatthor, N., Grabowski, U., Höpfner, M., Kellmann, S., Kiefer, M., Linden, A., Tsidu, G. M., Milz, M., Steck, T., Stiller, G. P., Wang, D. Y. and Fischer, H.: Retrieval of temperature and tangent altitude pointing from limb emission spectra recorded from space by the Michelson Interferometer for Passive Atmospheric Sounding (MIPAS), J. Geophys. Res., 108(D23), 4736, https://doi.org/10.1029/2003JD003602, 2003.

Collaud Coen, M., Weingartner, E., Furger, M., Nyeki, S., Prévôt, A. S. H., Steinbacher, M. and Baltensperger, U.: Aerosol climatology and planetary boundary influence at the Jungfraujoch analyzed by synoptic weather types, Atmos. Chem. Phys., 11(12), 5931–5944, https://doi.org/10.5194/acp-11-5931-2011, 2011.

Courtier, P., Thépaut, J.-N. and Hollingsworth, A.: A strategy for operational implementation of 4D-Var, using an incremental approach, Q. J. R. Meteorol. Soc., 120(519), 1367–1387, https://doi.org/10.1002/qj.49712051912, 1994.

Crutzen, P. J.: The influence of nitrogen oxides on the atmospheric ozone content, Q. J. R. Meteorol. Soc., 96(408), 320–325, https://doi.org/10.1002/qj.49709640815, 1970.

Cunnold, D. M., Steele, L. P., Fraser, P. J., Simmonds, P. G., Prinn, R. G., Weiss, R. F., Porter, L. W., O'Doherty, S., Langenfelds, R. L., Krummel, P. B., Wang, H. J., Emmons, L., Tie, X. X. and Dlugokencky, E.: In situ measurements of atmospheric methane at GAGE/AGAGE sites during 1985–2000 and resulting source inferences, J. Geophys. Res., 107(D14), 4225, https://doi.org/10.1029/2001JD001226, 2002.

Daniel, J. S., Solomon, S., Portmann, R. W. and Garcia, R. R.: Stratospheric ozone destruction: The

importance of bromine relative to chlorine, J. Geophys. Res. Atmos., 104(D19), 23871–23880, https://doi.org/10.1029/1999JD900381, 1999.

Dee, D. P., Uppala, S. M., Simmons, a. J., Berrisford, P., Poli, P., Kobayashi, S., Andrae, U., Balmaseda, M. a., Balsamo, G., Bauer, P., Bechtold, P., Beljaars, a. C. M., van de Berg, L., Bidlot, J., Bormann, N., Delsol, C., Dragani, R., Fuentes, M., Geer, a. J., Haimberger, L., Healy, S. B., Hersbach, H., Hólm, E. V., Isaksen, L., Kållberg, P., Köhler, M., Matricardi, M., McNally, A. P., Monge-Sanz, B. M., Morcrette, J.-J., Park, B.-K., Peubey, C., de Rosnay, P., Tavolato, C., Thépaut, J.-N. and Vitart, F.: The ERA-Interim reanalysis: configuration and performance of the data assimilation system, Q. J. R. Meteorol. Soc., 137(656), 553–597, https://doi.org/10.1002/qj.828, 2011.

Dhomse, S. S., Chipperfield, M. P., Feng, W., Hossaini, R., Mann, G. W. and Santee, M. L.: Revisiting the hemispheric asymmetry in midlatitude ozone changes following the Mount Pinatubo eruption: A 3-D model study, Geophys. Res. Lett., 42(8), 3038–3047, https://doi.org/10.1002/2015GL063052, 2015.

Dhomse, S. S., Chipperfield, M. P., Damadeo, R. P., Zawodny, J. M., Ball, W. T., Feng, W., Hossaini, R., Mann, G. W. and Haigh, J. D.: On the ambiguous nature of the 11 year solar cycle signal in upper stratospheric ozone, Geophys. Res. Lett., 43(13), 7241–7249, https://doi.org/10.1002/2016GL069958, 2016.

Dhomse, S. S., Kinnison, D., Chipperfield, M. P., Salawitch, R. J., Cionni, I., Hegglin, M. I., Abraham, N. L., Akiyoshi, H., Archibald, A. T., Bednarz, E. M., Bekki, S., Braesicke, P., Butchart, N., Dameris, M., Deushi, M., Frith, S., Hardiman, S. C., Hassler, B., Horowitz, L. W., Hu, R.-M., Jöckel, P., Josse, B., Kirner, O., Kremser, S., Langematz, U., Lewis, J., Marchand, M., Lin, M., Mancini, E., Marécal, V., Michou, M., Morgenstern, O., O'Connor, F. M., Oman, L., Pitari, G., Plummer, D. A., Pyle, J. A., Revell, L. E., Rozanov, E., Schofield, R., Stenke, A., Stone, K., Sudo, K., Tilmes, S., Visioni, D., Yamashita, Y. and Zeng, G.: Estimates of ozone return dates from Chemistry-Climate Model Initiative simulations, Atmos. Chem. Phys., 18(11), 8409–8438, https://doi.org/10.5194/acp-18-8409-2018, 2018.

Dhomse, S. S., Feng, W., Montzka, S. A., Hossaini, R., Keeble, J., Pyle, J. A., Daniel, J. S. and Chipperfield, M. P.: Delay in recovery of the Antarctic ozone hole from unexpected CFC-11 emissions, Nat. Commun., 10, 5781, https://doi.org/10.1038/s41467-019-13717-x, 2019.

Diallo, M., Riese, M., Birner, T., Konopka, P., Müller, R., Hegglin, M. I., Santee, M. L., Baldwin, M., Legras, B. and Ploeger, F.: Response of stratospheric water vapor and ozone to the unusual timing of El Niño and the QBO disruption in 2015-2016, Atmos. Chem. Phys., 18(17), 13055–13073, https://doi.org/10.5194/acp-18-13055-2018, 2018.

Diallo, M., Konopka, P., Santee, M. L., Müller, R., Tao, M., Walker, K. A., Legras, B., Riese, M., Ern, M. and Ploeger, F.: Structural changes in the shallow and transition branch of the Brewer–Dobson circulation induced by El Niño, Atmos. Chem. Phys., 19(1), 425–446, https://doi.org/10.5194/acp-19-425-2019, 2019.

Dlugokencky, E. J., Myers, R. C., Lang, P. M., Masarie, K. A., Crotwell, A. M., Thoning, K. W., Hall, B. D., Elkins, J. W. and Steele, L. P.: Conversion of NOAA atmospheric dry air CH4 mole fractions to a gravimetrically prepared standard scale, J. Geophys. Res., 110(D18), 1–8, https://doi.org/10.1029/2005JD006035, 2005.

Dobson, G. M. B.: Observations of the amount of ozone in the earth's atmosphere, and its relation to other geophysical conditions.—Part IV, Proc. R. Soc. London. Ser. A, Contain. Pap. a Math. Phys. Character, 129(811), 411–433, https://doi.org/10.1098/rspa.1930.0165, 1930.

Dobson, G. M. B.: Origin and distribution of the polyatomic molecules in the atmosphere, Proc. R. Soc. London. Ser. A. Math. Phys. Sci., 236(1205), 187–193, https://doi.org/10.1098/rspa.1956.0127, 1956.

Duchatelet, P.: Fluorine in the atmosphere: Inorganic fluorine budget and long-term trends based on

FTIR measurements at Jungfraujoch, University of Liège http://hdl.handle.net/2268/91413, 2011.

Duchatelet, P., Mahieu, E., Ruhnke, R., Feng, W., Chipperfield, M., Demoulin, P., Bernath, P., Boone, C. D., Walker, K. A., Servais, C. and Flock, O.: An approach to retrieve information on the carbonyl fluoride (COF2) vertical distributions above Jungfraujoch by FTIR multi-spectrum multi-window fitting, Atmos. Chem. Phys., 9(22), 9027–9042, https://doi.org/10.5194/acp-9-9027-2009, 2009.

Duchatelet, P., Demoulin, P., Hase, F., Ruhnke, R., Feng, W., Chipperfield, M. P., Bernath, P. F., Boone, C. D., Walker, K. A. and Mahieu, E.: Hydrogen fluoride total and partial column time series above the Jungfraujoch from long-term FTIR measurements: Impact of the line-shape model, characterization of the error budget and seasonal cycle, and comparison with satellite and model data, J. Geophys. Res. Atmos., 115(22), 1–20, https://doi.org/10.1029/2010JD014677, 2010.

Engel, A., Möbius, T., Bönisch, H., Schmidt, U., Heinz, R., Levin, I., Atlas, E., Aoki, S., Nakazawa, T., Sugawara, S., Moore, F., Hurst, D., Elkins, J., Schauffler, S., Andrews, A. and Boering, K.: Age of stratospheric air unchanged within uncertainties over the past 30 years, Nat. Geosci., 2(1), 28–31, https://doi.org/10.1038/ngeo388, 2009.

Engel, A., Bönisch, H., Ullrich, M., Sitals, R., Membrive, O., Danis, F. and Crevoisier, C.: Mean age of stratospheric air derived from AirCore observations, Atmos. Chem. Phys., 17(11), 6825–6838, https://doi.org/10.5194/acp-17-6825-2017, 2017.

Engel, A., Bönisch, H., Ostermöller, J., Chipperfield, M. P., Dhomse, S. and Jöckel, P.: A refined method for calculating equivalent effective stratospheric chlorine, Atmos. Chem. Phys., 18(2), 601–619, https://doi.org/10.5194/acp-18-601-2018, 2018.

EPICA community members., EPICA community members (participants are listed alphabetically)., Augustin, L. et al.: Eight glacial cycles from an Antarctic ice core, Nature, 429(6992), 623–628, https://doi.org/10.1038/nature02599, 2004.

Errera, Q., Chabrillat, S., Christophe, Y., Debosscher, J., Hubert, D., Lahoz, W., Santee, M. L., Shiotani, M., Skachko, S., von Clarmann, T. and Walker, K.: Technical note: Reanalysis of Aura MLS chemical observations, Atmos. Chem. Phys., 19(21), 13647–13679, https://doi.org/10.5194/acp-19-13647-2019, 2019.

Eskes, H., Huijnen, V., Arola, A., Benedictow, A., Blechschmidt, A.-M., Botek, E., Boucher, O., Bouarar, I., Chabrillat, S., Cuevas, E., Engelen, R., Flentje, H., Gaudel, A., Griesfeller, J., Jones, L., Kapsomenakis, J., Katragkou, E., Kinne, S., Langerock, B., Razinger, M., Richter, A., Schultz, M., Schulz, M., Sudarchikova, N., Thouret, V., Vrekoussis, M., Wagner, A. and Zerefos, C.: Validation of reactive gases and aerosols in the MACC global analysis and forecast system, Geosci. Model Dev., 8(11), 3523–3543, https://doi.org/10.5194/gmd-8-3523-2015, 2015.

Etheridge, D. M., Steele, L. P., Langenfelds, R. L., Francey, R. J., Barnola, J.-M. and Morgan, V. I.: Natural and anthropogenic changes in atmospheric CO 2 over the last 1000 years from air in Antarctic ice and firn, J. Geophys. Res. Atmos., 101(D2), 4115–4128, https://doi.org/10.1029/95JD03410, 1996.

Etheridge, D. M., Steele, L. P., Francey, R. J. and Langenfelds, R. L.: Atmospheric methane between 1000 A.D. and present: Evidence of anthropogenic emissions and climatic variability, J. Geophys. Res. Atmos., 103(D13), 15979–15993, https://doi.org/10.1029/98JD00923, 1998.

Farman, J. C., Gardiner, B. G. and Shanklin, J. D.: Large losses of total ozone in Antarctica reveal seasonal ClOx/NOx interaction, Nature, 315(6016), 207–210, https://doi.org/10.1038/315207a0, 1985.

Farmer, C. B., Raper, O. F. and O'Callaghan, F. G.: Final Report on the First Flight of the ATMOS Instrument during the Spacelab-3 Mission, April 29 through May 6, 1985, JPL Publ., 87–32 https://ntrs.nasa.gov/api/citations/19880005100/downloads/19880005100.pdf, 1987.

Fischer, H., Birk, M., Blom, C., Carli, B., Carlotti, M., von Clarmann, T., Delbouille, L., Dudhia, A., Ehhalt, D., Endemann, M., Flaud, J. M., Gessner, R., Kleinert, A., Koopman, R., Langen, J., López-Puertas, M., Mosner, P., Nett, H., Oelhaf, H., Perron, G., Remedios, J., Ridolfi, M., Stiller, G. and Zander, R.: MIPAS: an instrument for atmospheric and climate research, Atmos. Chem. Phys., 8(8), 2151–2188, https://doi.org/10.5194/acp-8-2151-2008, 2008.

Franco, B., Bader, W., Toon, G. C., Bray, C., Perrin, A., Fischer, E. V., Sudo, K., Boone, C. D., Bovy, B., Lejeune, B., Servais, C. and Mahieu, E.: Retrieval of ethane from ground-based FTIR solar spectra using improved spectroscopy: Recent burden increase above Jungfraujoch, J. Quant. Spectrosc. Radiat. Transf., 160, 36–49, https://doi.org/10.1016/j.jqsrt.2015.03.017, 2015.

Friedrich, M., Beutner, E., Reuvers, H., Smeekes, S., Urbain, J.-P., Bader, W., Franco, B., Lejeune, B. and Mahieu, E.: A statistical analysis of time trends in atmospheric ethane, Clim. Change, 162(1), 105–125, https://doi.org/10.1007/s10584-020-02806-2, 2020a.

Friedrich, M., Smeekes, S. and Urbain, J. P.: Autoregressive wild bootstrap inference for nonparametric trends, J. Econom., 214(1), 81–109, https://doi.org/10.1016/j.jeconom.2019.05.006, 2020b.

Froidevaux, L., Kinnison, D. E., Wang, R., Anderson, J. and Fuller, R. A.: Evaluation of CESM1 (WACCM) free-running and specified-dynamics atmospheric composition simulations using global multi-species satellite data records, Atmos. Chem. Phys. Discuss., (June), 1–70, https://doi.org/10.5194/acp-2018-546, 2018.

Fu, Q., Lin, P., Solomon, S. and Hartmann, D. L.: Observational evidence of strengthening of the Brewer-Dobson circulation since 1980, J. Geophys. Res. Atmos., 120(19), 10,214-10,228, https://doi.org/10.1002/2015JD023657, 2015.

Fu, Q., Solomon, S., Pahlavan, H. A. and Lin, P.: Observed changes in Brewer–Dobson circulation for 1980–2018, Environ. Res. Lett., 14(11), https://doi.org/10.1088/1748-9326/ab4de7, 2019.

Fujiwara, M., Wright, J. S., Manney, G. L., Gray, L. J., Anstey, J., Birner, T., Davis, S., Gerber, E. P., Harvey, V. L., Hegglin, M. I., Homeyer, C. R., Knox, J. A., Krüger, K., Lambert, A., Long, C. S., Martineau, P., Monge-Sanz, B. M., Santee, M. L., Tegtmeier, S., Chabrillat, S., Tan, D. G. H., Jackson, D. R., Polavarapu, S., Compo, G. P., Dragani, R., Ebisuzaki, W., Harada, Y., Kobayashi, C., McCarty, W., Onogi, K., Pawson, S., Simmons, A., Wargan, K., Whitaker, J. S. and Zou, C.-Z.: Introduction to the SPARC Reanalysis Intercomparison Project (S-RIP) and overview of the reanalysis systems, Atmos. Chem. Phys. Discuss., 17(2), 1417–1452, https://doi.org/10.5194/acp-2016-652, 2017.

Garcia, R. R., Marsh, D. R., Kinnison, D. E., Boville, B. A. and Sassi, F.: Simulation of secular trends in the middle atmosphere, 1950-2003, J. Geophys. Res. Atmos., 112(9), 1–23, https://doi.org/10.1029/2006JD007485, 2007.

Garcia, R. R., Randel, W. J. and Kinnison, D. E.: On the determination of age of air trends from atmospheric trace species, J. Atmos. Sci., 68(1), 139–154, https://doi.org/10.1175/2010JAS3527.1, 2011.

Garcia, R. R., Smith, A. K., Kinnison, D. E., Cámara, Á. de la and Murphy, D. J.: Modification of the Gravity Wave Parameterization in the Whole Atmosphere Community Climate Model: Motivation and Results, J. Atmos. Sci., 74(1), 275–291, https://doi.org/10.1175/JAS-D-16-0104.1, 2017.

Gardiner, T., Forbes, A., de Mazière, M., Vigouroux, C., Mahieu, E., Demoulin, P., Velazco, V., Notholt, J., Blumenstock, T., Hase, F., Kramer, I., Sussmann, R., Stremme, W., Mellqvist, J., Strandberg, A., Ellingsen, K. and Gauss, M.: Trend analysis of greenhouse gases over Europe measured by a network of ground-based remote FTIR instruments, Atmos. Chem. Phys., 8(22), 6719–6727, https://doi.org/10.5194/acp-8-6719-2008, 2008.

Garfinkel, C. I., Aquila, V., Waugh, D. W. and Oman, L. D.: Time-varying changes in the simulated structure of the Brewer–Dobson Circulation, Atmos. Chem. Phys., 17(2), 1313–1327,

https://doi.org/10.5194/acp-17-1313-2017, 2017.

Gelaro, R., McCarty, W., Suárez, M. J., Todling, R., Molod, A., Takacs, L., Randles, C. A., Darmenov, A., Bosilovich, M. G., Reichle, R., Wargan, K., Coy, L., Cullather, R., Draper, C., Akella, S., Buchard, V., Conaty, A., da Silva, A. M., Gu, W., Kim, G.-K., Koster, R., Lucchesi, R., Merkova, D., Nielsen, J. E., Partyka, G., Pawson, S., Putman, W., Rienecker, M., Schubert, S. D., Sienkiewicz, M. and Zhao, B.: The Modern-Era Retrospective Analysis for Research and Applications, Version 2 (MERRA-2), J. Clim., 30(14), 5419–5454, https://doi.org/10.1175/JCLI-D-16-0758.1, 2017.

Glatthor, N., Höpfner, M., Leyser, A., Stiller, G. P., von Clarmann, T., Grabowski, U., Kellmann, S., Linden, A., Sinnhuber, B.-M., Krysztofiak, G. and Walker, K. A.: Global carbonyl sulfide (OCS) measured by MIPAS/Envisat during 2002–2012, Atmos. Chem. Phys., 17(4), 2631–2652, https://doi.org/10.5194/acp-17-2631-2017, 2017.

Haenel, F. J., Stiller, G. P., von Clarmann, T., Funke, B., Eckert, E., Glatthor, N., Grabowski, U., Kellmann, S., Kiefer, M., Linden, A. and Reddmann, T.: Reassessment of MIPAS age of air trends and variability, Atmos. Chem. Phys., 15(22), 13161–13176, https://doi.org/10.5194/acp-15-13161-2015, 2015.

Hall, T. M. and Waugh, D. W.: Influence of nonlocal chemistry on tracer distributions: Inferring the mean age of air from SF 6, J. Geophys. Res. Atmos., 103(D11), 13327–13336, https://doi.org/10.1029/98JD00170, 1998.

Han, Y., Tian, W., Chipperfield, M. P., Zhang, J., Wang, F., Sang, W., Luo, J., Feng, W., Chrysanthou, A. and Tian, H.: Attribution of the Hemispheric Asymmetries in Trends of Stratospheric Trace Gases Inferred From Microwave Limb Sounder (MLS) Measurements, J. Geophys. Res. Atmos., 124(12), 6283–6293, https://doi.org/10.1029/2018JD029723, 2019.

Hardiman, S. C., Butchart, N. and Calvo, N.: The morphology of the Brewer-Dobson circulation and its response to climate change in CMIP5 simulations, Q. J. R. Meteorol. Soc., 140(683), 1958–1965, https://doi.org/10.1002/qj.2258, 2014.

Hardiman, S. C., Lin, P., Scaife, A. A., Dunstone, N. J. and Ren, H. L.: The influence of dynamical variability on the observed Brewer-Dobson circulation trend, Geophys. Res. Lett., 44(6), 2885–2892, https://doi.org/10.1002/2017GL072706, 2017.

Harrison, J. J.: New and improved infrared absorption cross sections for chlorodifluoromethane (HCFC-22), Atmos. Meas. Tech., 9(6), 2593–2601, https://doi.org/10.5194/amt-9-2593-2016, 2016.

Harrison, J. J., Chipperfield, M. P., Dudhia, A., Cai, S., Dhomse, S., Boone, C. D. and Bernath, P. F.: Satellite observations of stratospheric carbonyl fluoride, Atmos. Chem. Phys., 14(21), 11915–11933, https://doi.org/10.5194/acp-14-11915-2014, 2014.

Harrison, J. J., Chipperfield, M. P., Boone, C. D., Dhomse, S. S., Bernath, P. F., Froidevaux, L., Anderson, J. and Russell, J.: Satellite observations of stratospheric hydrogen fluoride and comparisons with SLIMCAT calculations, Atmos. Chem. Phys., 16(16), 10501–10519, https://doi.org/10.5194/acp-16-10501-2016, 2016.

Hase, F., Demoulin, P., Sauval, A. J., Toon, G. C., Bernath, P. F., Goldman, A., Hannigan, J. W. and Rinsland, C. P.: An empirical line-by-line model for the infrared solar transmittance spectrum from 700 to 5000cm-1, J. Quant. Spectrosc. Radiat. Transf., 102(3), 450–463, https://doi.org/10.1016/j.jqsrt.2006.02.026, 2006.

Haynes, P.: Stratospheric dynamics, Annu. Rev. Fluid Mech., 37, 263–293, https://doi.org/10.1146/annurev.fluid.37.061903.175710, 2005.

Henne, S., Dommen, J., Neininger, B., Reimann, S., Staehelin, J. and Prévôt, A. S. H.: Influence of mountain venting in the Alps on the ozone chemistry of the lower free troposphere and the European pollution export, J. Geophys. Res., 110(D22), D22307, https://doi.org/10.1029/2005JD005936,

2005.

Henne, S., Brunner, D., Folini, D., Solberg, S., Klausen, J. and Buchmann, B.: Assessment of parameters describing representativeness of air quality in-situ measurement sites, Atmos. Chem. Phys., 10(8), 3561–3581, https://doi.org/10.5194/acp-10-3561-2010, 2010.

Hersbach, H., Bell, B., Berrisford, P., Hirahara, S., Horányi, A., Nicolas, J., Peubey, C., Radu, R., Bonavita, M., Dee, D., Dragani, R., Flemming, J., Forbes, R., Geer, A., Hogan, R. J., Janisková, H. M., Keeley, S., Laloyaux, P., Cristina, P. L. and Thépaut, J.: The ERA5 global reanalysis, Q. J. R. Meteorol. Soc., 146(730), 1999–2049, https://doi.org/10.1002/qj.3803, 2020.

Holton, J. R.: Wave propagation and transport in the middle atmosphere, Philos. Trans. R. Soc. London. Ser. A, Math. Phys. Sci., 296(1418), 73–85, https://doi.org/10.1098/rsta.1980.0157, 1980.

Holton, J. R. and Hakim, G. J.: An Introduction to Dynamic Meteorology, Fifth Edit., Academic Press Inc., 2013.

Horowitz, L. W., Walters, S., Mauzerall, D. L., Emmons, L. K., Rasch, P. J., Granier, C., Tie, X., Lamarque, J.-F., Schultz, M. G., Tyndall, G. S., Orlando, J. J. and Brasseur, G. P.: A global simulation of tropospheric ozone and related tracers: Description and evaluation of MOZART, version 2, J. Geophys. Res. Atmos., 108(D24), 1–18, https://doi.org/10.1029/2002JD002853, 2003.

Hurwitz, M. M., Newman, P. A. and Garfinkel, C. I.: The Arctic vortex in March 2011: a dynamical perspective, Atmos. Chem. Phys., 11(22), 11447–11453, https://doi.org/10.5194/acp-11-11447-2011, 2011.

IPCC: Climate change 2013: The Physical Science Basis. Contribution of Working Group I to the Fifth Assessment Report of the Intergovernmental Panel on Climate Change, edited by T. F. Stocker, D. Qin, G.-K. Plattner, M. Tignor, S. K. Allen, J. Boschung, A. Nauels, Y. Xia, V. Bex, and P. M. Midgley, Cambridge University Press, Cambridge, United Kingdom and New York, NY, USA., 2013.

IPCC: Climate Change 2014: Impacts, Adaptation, and Vulnerability. Part A: Global and Sectoral Aspects. Contribution of Working Group II to the Fifth Assessment Report of the Intergovernmental Panel on Climate Change, edited by C. B. Field, V. R. Barros, D. J. Dokken, K. J. Mach, M. D. Mastrandrea, T. E. Bilir, M. Chatterjee, K. L. Ebi, Y. O. Estrada, R. C. Genova, B. Girma, E. S. Kissel, A. N. Levy, S. MacCracken, P. R. Mastrandrea, and L. L. White, Cambridge University Press, Cambridge, United Kingdom and New York, NY, USA., 2014.

Irion, F. W., Brown, M., Toon, G. C. and Gunson, M. R.: Increase in atmospheric CHF 2 Cl (HCFC-22) over southern California from 1985 to 1990, Geophys. Res. Lett., 21(16), 1723–1726, https://doi.org/10.1029/94GL01323, 1994.

Jablonowski, C. and Williamson, D. L.: The Pros and Cons of Diffusion, Filters and Fixers in Atmospheric General Circulation Models, in Numerical Techniques for Global Atmospheric Models. Lecture Notes in Computational Science and Engineering, vol 80, edited by P. Lauritzen, C. Jablonowski, M. Taylor, and R. Nair, pp. 381–493, Springer, Berlin, Heidelberg, https://doi.org/10.1007/978-3-642-11640-7_13, , 2011.

Jacob, D. J.: Introduction to atmospheric chemistry, Princeton University Press, Princeton, New Jersey., 1999.

Johnston, H.: Reduction of Stratospheric Ozone by Nitrogen Oxide Catalysts from Supersonic Transport Exhaust, Science (80-.)., 173(3996), 517–522, https://doi.org/10.1126/science.173.3996.517, 1971.

Julian, P. R. and Labitzke, K. B.: A Study of Atmospheric Energetics During the January–February 1963 Stratospheric Warming, J. Atmos. Sci., 22(6), 597–610, https://doi.org/10.1175/1520-0469(1965)022<0597:ASOAED>2.0.CO;2, 1965.

Kalnay, E., Kanamitsu, M., Kistler, R., Collins, W., Deaven, D., Gandin, L., Iredell, M., Saha, S., White,

G., Woollen, J., Zhu, Y., Leetmaa, A., Reynolds, R., Chelliah, M., Ebisuzaki, W., Higgins, W., Janowiak, J., Mo, K. C., Ropelewski, C., Wang, J., Jenne, R. and Joseph, D.: The NCEP/NCAR 40-Year Reanalysis Project, Bull. Am. Meteorol. Soc., 77(3), 437–471, https://doi.org/10.1175/1520-0477(1996)077<0437:TNYRP>2.0.CO;2, 1996.

Karion, A., Sweeney, C., Tans, P. and Newberger, T.: AirCore: An Innovative Atmospheric Sampling System, J. Atmos. Ocean. Technol., 27(11), 1839–1853, https://doi.org/10.1175/2010JTECHA1448.1, 2010.

Kasting, J.: Earth's early atmosphere, Science (80-.)., 259(5097), 920–926, https://doi.org/10.1126/science.11536547, 1993.

Kida, H.: General Circulation of Air Parcels and Transport Characteristics Derived from a Hemispheric GCM, J. Meteorol. Soc. Japan. Ser. II, 61(4), 510–523, https://doi.org/10.2151/jmsj1965.61.4_510, 1983.

Kinnison, D. E., Brasseur, G. P., Walters, S., Garcia, R. R., Marsh, D. R., Sassi, F., Harvey, V. L., Randall, C. E., Emmons, L., Lamarque, J. F., Hess, P., Orlando, J. J., Tie, X. X., Randel, W., Pan, L. L., Gettelman, A., Granier, C., Diehl, T., Niemeier, U. and Simmons, A. J.: Sensitivity of chemical tracers to meteorological parameters in the MOZART-3 chemical transport model, J. Geophys. Res., 112(D20), D20302, https://doi.org/10.1029/2006JD007879, 2007.

Kobayashi, S., Ota, Y., Harada, Y., Ebita, A., Moriya, M., Onoda, H., Onogi, K., Kamahori, H., Kobayashi, C., Endo, H., Miyaoka, K. and Takahashi, K.: The JRA-55 Reanalysis: General Specifications and Basic Characteristics, J. Meteorol. Soc. Japan. Ser. II, 93(1), 5–48, https://doi.org/10.2151/jmsj.2015-001, 2015.

Kohlhepp, R., Ruhnke, R., Chipperfield, M. P., De Mazière, M., Notholt, J., Barthlott, S., Batchelor, R. L., Blatherwick, R. D., Blumenstock, T., Coffey, M. T., Demoulin, P., Fast, H., Feng, W., Goldman, A., Griffith, D. W. T., Hamann, K., Hannigan, J. W., Hase, F., Jones, N. B., Kagawa, A., Kaiser, I., Kasai, Y., Kirner, O., Kouker, W., Lindenmaier, R., Mahieu, E., Mittermeier, R. L., Monge-Sanz, B., Morino, I., Murata, I., Nakajima, H., Palm, M., Paton-Walsh, C., Raffalski, U., Reddmann, T., Rettinger, M., Rinsland, C. P., Rozanov, E., Schneider, M., Senten, C., Servais, C., Sinnhuber, B.-M., Smale, D., Strong, K., Sussmann, R., Taylor, J. R., Vanhaelewyn, G., Warneke, T., Whaley, C., Wiehle, M. and Wood, S. W.: Observed and simulated time evolution of HCl, ClONO2, and HF total column abundances, Atmos. Chem. Phys., 12(7), 3527–3556, https://doi.org/10.5194/acp-12-3527-2012, 2012.

Konopka, P., Ploeger, F., Tao, M., Birner, T. and Riese, M.: Hemispheric asymmetries and seasonality of mean age of air in the lower stratosphere: Deep versus shallow branch of the Brewer-Dobson circulation, J. Geophys. Res. Atmos., 120(5), 2053–2066, https://doi.org/10.1002/2014JD022429, 2015.

Langerock, B., De Mazière, M., Hendrick, F., Vigouroux, C., Desmet, F., Dils, B. and Niemeijer, S.: Description of algorithms for co-locating and comparing gridded model data with remote-sensing observations, Geosci. Model Dev., 8(3), 911–921, https://doi.org/10.5194/gmd-8-911-2015, 2015.

Lejeune, B., Mahieu, E., Vollmer, M. K., Reimann, S., Bernath, P. F., Boone, C. D., Walker, K. A. and Servais, C.: Optimized approach to retrieve information on atmospheric carbonyl sulfide (OCS) above the Jungfraujoch station and change in its abundance since 1995, J. Quant. Spectrosc. Radiat. Transf., 186, 81–95, https://doi.org/10.1016/j.jqsrt.2016.06.001, 2017.

Levin, I., Naegler, T., Heinz, R., Osusko, D., Cuevas, E., Engel, A., Ilmberger, J., Langenfelds, R. L., Neininger, B., Rohden, C. V., Steele, L. P., Weller, R., Worthy, D. E. and Zimov, S. A.: The global SF6 source inferred from long-term high precision atmospheric measurements and its comparison with emission inventories, Atmos. Chem. Phys., 10(6), 2655–2662, https://doi.org/10.5194/acp-10-2655-2010, 2010.

Li, F., Waugh, D. W., Douglass, A. R., Newman, P. A., Strahan, S. E., Ma, J., Nielsen, J. E. and Liang,

Q.: Long-term changes in stratospheric age spectra in the 21st century in the Goddard earth observing system chemistry-climate model (GEOSCCM), J. Geophys. Res. Atmos., 117(20), 1–15, https://doi.org/10.1029/2012JD017905, 2012.

Li, F., Newman, P., Pawson, S. and Perlwitz, J.: Effects of Greenhouse Gas Increase and Stratospheric Ozone Depletion on Stratospheric Mean Age of Air in 1960-2010, J. Geophys. Res. Atmos., 123(4), 2098–2110, https://doi.org/10.1002/2017JD027562, 2018.

Lin, P. and Fu, Q.: Changes in various branches of the Brewer-Dobson circulation from an ensemble of chemistry climate models, J. Geophys. Res. Atmos., 118(1), 73–84, https://doi.org/10.1029/2012JD018813, 2013.

Lin, S.-J. and Rood, R. B.: Multidimensional Flux-Form Semi-Lagrangian Transport Schemes, Mon. Weather Rev., 124(9), 2046–2070, https://doi.org/10.1175/1520-0493(1996)124<2046:MFFSLT>2.0.CO;2, 1996.

Lindzen, R. S. and Holton, J. R.: A Theory of the Quasi-Biennial Oscillation, J. Atmos. Sci., 25(6), 1095–1107, https://doi.org/10.1175/1520-0469(1968)025<1095:ATOTQB>2.0.CO;2, 1968.

Lüthi, D., Le Floch, M., Bereiter, B., Blunier, T., Barnola, J.-M., Siegenthaler, U., Raynaud, D., Jouzel, J., Fischer, H., Kawamura, K. and Stocker, T. F.: High-resolution carbon dioxide concentration record 650,000–800,000 years before present, Nature, 453(7193), 379–382, https://doi.org/10.1038/nature06949, 2008.

Mahieu, E., Duchatelet, P., Zander, R., Demoulin, P., Servais, C., Rinsland, C. P., Chipperfield, M. P. and De Mazière, M.: The Evolution of Inorganic Chlorine above the Jungfraujoch Station: an update, in Proceedings Quadrennial Ozone Symposium, vol. 2, edited by C. S. Zerefos, pp. 997–998, Kos (Greece), , 2004.

Mahieu, E., Chipperfield, M. P., Notholt, J., Reddmann, T., Anderson, J., Bernath, P. F., Blumenstock, T., Coffey, M. T., Dhomse, S. S., Feng, W., Franco, B., Froidevaux, L., Griffith, D. W. T., Hannigan, J. W., Hase, F., Hossaini, R., Jones, N. B., Morino, I., Murata, I., Nakajima, H., Palm, M., Paton-Walsh, C., Iii, J. M. R., Schneider, M., Servais, C., Smale, D. and Walker, K. A.: Recent Northern Hemisphere stratospheric HCl increase due to atmospheric circulation changes, Nature, 515(7525), 104–107, https://doi.org/10.1038/nature13857, 2014a.

Mahieu, E., Zander, R., Toon, G. C., Vollmer, M. K., Reimann, S., Mühle, J., Bader, W., Bovy, B., Lejeune, B., Servais, C., Demoulin, P., Roland, G., Bernath, P. F., Boone, C. D., Walker, K. A. and Duchatelet, P.: Spectrometric monitoring of atmospheric carbon tetrafluoride (CF₄) above the Jungfraujoch station since 1989: evidence of continued increase but at a slowing rate, Atmos. Meas. Tech., 7(1), 333–344, https://doi.org/10.5194/amt-7-333-2014, 2014b.

Mahieu, E., Lejeune, B., Bovy, B., Servais, C., Toon, G. C., Bernath, P. F., Boone, C. D., Walker, K. A., Reimann, S., Vollmer, M. K. and O'Doherty, S.: Retrieval of HCFC-142b (CH 3 CClF 2) from ground-based high-resolution infrared solar spectra: Atmospheric increase since 1989 and comparison with surface and satellite measurements, J. Quant. Spectrosc. Radiat. Transf., 186, 96–105, https://doi.org/10.1016/j.jqsrt.2016.03.017, 2017.

Mahieu, E., Flock, O., Notholt, J., Palm, M., Cantos, I., Prignon, M., Roland, G., Servais, C. and Verma, A.: Surveillance à long terme de l'atmosphère terrestreà la station du Jungfraujoch, Bull. la Société R. des Sci. Liège, 88, 31–41, https://doi.org/10.25518/0037-9565.9136, 2019.

Manney, G. L., Santee, M. L., Rex, M., Livesey, N. J., Pitts, M. C., Veefkind, P., Nash, E. R., Wohltmann, I., Lehmann, R., Froidevaux, L., Poole, L. R., Schoeberl, M. R., Haffner, D. P., Davies, J., Dorokhov, V., Gernandt, H., Johnson, B., Kivi, R., Kyrö, E., Larsen, N., Levelt, P. F., Makshtas, A., McElroy, C. T., Nakajima, H., Parrondo, M. C., Tarasick, D. W., von der Gathen, P., Walker, K. A. and Zinoviev, N. S.: Unprecedented Arctic ozone loss in 2011, Nature, 478(7370), 469–475, https://doi.org/10.1038/nature10556, 2011.

Matsuno, T.: Lagrangian motion of air parcels in the stratosphere in the presence of planetary waves, Pure Appl. Geophys., 118, 189–216, https://doi.org/10.1007/BF01586451, 1980.

Matthes, K., Funke, B., Andersson, M. E., Barnard, L., Beer, J., Charbonneau, P., Clilverd, M. A., Dudok de Wit, T., Haberreiter, M., Hendry, A., Jackman, C. H., Kretzschmar, M., Kruschke, T., Kunze, M., Langematz, U., Marsh, D. R., Maycock, A. C., Misios, S., Rodger, C. J., Scaife, A. A., Seppälä, A., Shangguan, M., Sinnhuber, M., Tourpali, K., Usoskin, I., van de Kamp, M., Verronen, P. T. and Versick, S.: Solar forcing for CMIP6 (v3.2), Geosci. Model Dev., 10(6), 2247–2302, https://doi.org/10.5194/gmd-10-2247-2017, 2017.

De Mazière, M., Thompson, A. M., Kurylo, M. J., Wild, J. D., Bernhard, G., Blumenstock, T., Braathen, G. O., Hannigan, J. W., Lambert, J.-C., Leblanc, T., McGee, T. J., Nedoluha, G., Petropavlovskikh, I., Seckmeyer, G., Simon, P. C., Steinbrecht, W. and Strahan, S. E.: The Network for the Detection of Atmospheric Composition Change (NDACC): history, status and perspectives, Atmos. Chem. Phys., 18(7), 4935–4964, https://doi.org/10.5194/acp-18-4935-2018, 2018.

McDaniel, A. H., Cantrell, C. A., Davidson, J. A., Shetter, R. E. and Calvert, J. G.: The temperature dependent, infrared absorption cross-sections for the chlorofluorocarbons: CFC-11, CFC-12, CFC-13, CFC-14, CFC-22, CFC-113, CFC-114, and CFC-115, J. Atmos. Chem., 12(3), 211–227, https://doi.org/10.1007/BF00048074, 1991.

Meijer, E. W., Bregman, B., Segers, A. and van Velthoven, P. F. J.: The influence of data assimilation on the age of air calculated with a global chemistry-transport model using ECMWF wind fields, Geophys. Res. Lett., 31(23), 1–4, https://doi.org/10.1029/2004GL021158, 2004.

Meinshausen, M., Vogel, E., Nauels, A., Lorbacher, K., Meinshausen, N., Etheridge, D. M., Fraser, P. J., Montzka, S. A., Rayner, P. J., Trudinger, C. M., Krummel, P. B., Beyerle, U., Canadell, J. G., Daniel, J. S., Enting, I. G., Law, R. M., Lunder, C. R., O'Doherty, S., Prinn, R. G., Reimann, S., Rubino, M., Velders, G. J. M., Vollmer, M. K., Wang, R. H. J. and Weiss, R.: Historical greenhouse gas concentrations for climate modelling (CMIP6), Geosci. Model Dev., 10(5), 2057–2116, https://doi.org/10.5194/gmd-10-2057-2017, 2017.

Meinshausen, M., Nicholls, Z. R. J., Lewis, J., Gidden, M. J., Vogel, E., Freund, M., Beyerle, U., Gessner, C., Nauels, A., Bauer, N., Canadell, J. G., Daniel, J. S., John, A., Krummel, P. B., Luderer, G., Meinshausen, N., Montzka, S. A., Rayner, P. J., Reimann, S., Smith, S. J., van den Berg, M., Velders, G. J. M., Vollmer, M. K. and Wang, R. H. J.: The shared socio-economic pathway (SSP) greenhouse gas concentrations and their extensions to 2500, Geosci. Model Dev., 13(8), 3571–3605, https://doi.org/10.5194/gmd-13-3571-2020, 2020.

Melen, F., Mahieu, E., Zander, R., Rinsland, C. P., Demoulin, P., Roland, G., Delbouille, L. and Servais, C.: Vertical Column Abundances of COF2 Above the Jungfraujoch Station, Derived from Ground-Based Infrared Solar Observations, J. Atmos. Chem., 29(2), 119–134, https://doi.org/10.1023/A:1005847829686, 1998.

Membrive, O., Crevoisier, C., Sweeney, C., Danis, F., Hertzog, A., Engel, A., Bönisch, H. and Picon, L.: AirCore-HR: a high-resolution column sampling to enhance the vertical description of CH4 and CO2, Atmos. Meas. Tech., 10(6), 2163–2181, https://doi.org/10.5194/amt-10-2163-2017, 2017.

Ménard, R., Chabrillat, S., Robichaud, A., de Grandpré, J., Charron, M., Rochon, Y., Batchelor, R., Kallaur, A., Reszka, M. and Kaminski, J. W.: Coupled Stratospheric Chemistry–Meteorology Data Assimilation. Part I: Physical Background and Coupled Modeling Aspects, Atmosphere (Basel)., 11(2), 1–39, https://doi.org/10.3390/atmos11020150, 2020.

Miller, B. R., Weiss, R. F., Salameh, P. K., Tanhua, T., Greally, B. R., Mühle, J. and Simmonds, P. G.: Medusa: A Sample Preconcentration and GC/MS Detector System for in Situ Measurements of Atmospheric Trace Halocarbons, Hydrocarbons, and Sulfur Compounds, Anal. Chem., 80(5), 1536–1545, https://doi.org/10.1021/ac702084k, 2008.

Minganti, D., Chabrillat, S., Christophe, Y., Errera, Q., Abalos, M., Prignon, M., Kinnison, D. E. and

Mahieu, E.: Climatological impact of the Brewer–Dobson circulation on the N2O budget in WACCM, a chemical reanalysis and a CTM driven by four dynamical reanalyses, Atmos. Chem. Phys., 20(21), 12609–12631, https://doi.org/10.5194/acp-20-12609-2020, 2020.

Minschwaner, K., Su, H. and Jiang, J. H.: The upward branch of the Brewer-Dobson circulation quantified by tropical stratospheric water vapor and carbon monoxide measurements from the Aura Microwave Limb Sounder, J. Geophys. Res. Atmos., 121(6), 2790–2804, https://doi.org/10.1002/2015JD023961, 2016.

Molina, M. J. and Rowland, F. S.: Stratospheric sink for chlorofluoromethanes: chlorine atom-catalysed destruction of ozone, Nature, 249(5460), 810–812, https://doi.org/10.1038/249810a0, 1974.

Montzka, S. A., Hall, B. D. and Elkins, J. W.: Accelerated increases observed for hydrochlorofluorocarbons since 2004 in the global atmosphere, Geophys. Res. Lett., 36(3), 1–5, https://doi.org/10.1029/2008GL036475, 2009.

Montzka, S. A., McFarland, M., Andersen, S. O., Miller, B. R., Fahey, D. W., Hall, B. D., Hu, L., Siso, C. and Elkins, J. W.: Recent Trends in Global Emissions of Hydrochlorofluorocarbons and Hydrofluorocarbons: Reflecting on the 2007 Adjustments to the Montreal Protocol, J. Phys. Chem. A, 119(19), 4439–4449, https://doi.org/10.1021/jp5097376, 2015.

Montzka, S. A., Dutton, G. S., Yu, P., Ray, E., Portmann, R. W., Daniel, J. S., Kuijpers, L., Hall, B. D., Mondeel, D., Siso, C., Nance, J. D., Rigby, M., Manning, A. J., Hu, L., Moore, F., Miller, B. R. and Elkins, J. W.: An unexpected and persistent increase in global emissions of ozone-depleting CFC-11, Nature, 557(7705), 413–417, https://doi.org/10.1038/s41586-018-0106-2, 2018.

Morgenstern, O., Stone, K. A., Schofield, R., Akiyoshi, H., Yamashita, Y., Kinnison, D. E., Garcia, R. R., Sudo, K., Plummer, D. A., Scinocca, J., Oman, L. D., Manyin, M. E., Zeng, G., Rozanov, E., Stenke, A., Revell, L. E., Pitari, G., Mancini, E., Di Genova, G., Visioni, D., Dhomse, S. S. and Chipperfield, M. P.: Ozone sensitivity to varying greenhouse gases and ozone-depleting substances in CCMI-1 simulations, Atmos. Chem. Phys., 18(2), 1091–1114, https://doi.org/10.5194/acp-18-1091-2018, 2018.

Mote, P. W., Rosenlof, K. H., McIntyre, M. E., Carr, E. S., Gille, J. C., Holton, J. R., Kinnersley, J. S., Pumphrey, H. C., Russell, J. M. and Waters, J. W.: An atmospheric tape recorder: The imprint of tropical tropopause temperatures on stratospheric water vapor, J. Geophys. Res. Atmos., 101(D2), 3989–4006, https://doi.org/10.1029/95JD03422, 1996.

Müller, R., Grooß, J.-U., Zafar, A. M., Robrecht, S. and Lehmann, R.: The maintenance of elevated active chlorine levels in the Antarctic lower stratosphere through HCl null cycles, Atmos. Chem. Phys., 18(4), 2985–2997, https://doi.org/10.5194/acp-18-2985-2018, 2018.

Murgatroyd, R. J. and Singleton, F.: Possible meridional circulations in the stratosphere and mesosphere, Q. J. R. Meteorol. Soc., 87(372), 125–135, https://doi.org/10.1002/qj.49708737202, 1961.

Nassar, R., Bernath, P. F., Boone, C. D., Clerbaux, C., Coheur, P. F., Dufour, G., Froidevaux, L., Mahieu, E., McConnell, J. C., McLeod, S. D., Murtagh, D. P., Rinsland, C. P., Semeniuk, K., Skelton, R., Walker, K. A. and Zander, R.: A global inventory of stratospheric chlorine in 2004, J. Geophys. Res. Atmos., 111(22), 1–13, https://doi.org/10.1029/2006JD007073, 2006a.

Nassar, R., Bernath, P. F., Boone, C. D., McLeod, S. D., Skelton, R., Walker, K. A., Rinsland, C. P. and Duchatelet, P.: A global inventory of stratospheric fluorine in 2004 based on Atmospheric Chemistry Experiment Fourier transform spectrometer (ACE-FTS) measurements, J. Geophys. Res. Atmos., 111(22), 1–10, https://doi.org/10.1029/2006JD007395, 2006b.

Neale, R. B., Richter, J., Park, S., Lauritzen, P. H., Vavrus, S. J., Rasch, P. J. and Zhang, M.: The Mean Climate of the Community Atmosphere Model (CAM4) in Forced SST and Fully Coupled Experiments, J. Clim., 26(14), 5150–5168, https://doi.org/10.1175/JCLI-D-12-00236.1, 2013.

Nedoluha, G. E., Boyd, I. S., Parrish, A., Gomez, R. M., Allen, D. R., Froidevaux, L., Connor, B. J. and

Querel, R. R.: Unusual stratospheric ozone anomalies observed in 22 years of measurements from Lauder, New Zealand, Atmos. Chem. Phys., 15(12), 6817–6826, https://doi.org/10.5194/acp-15-6817-2015, 2015.

Nevison, C. D., Kinnison, D. E. and Weiss, R. F.: Stratospheric influences on the tropospheric seasonal cycles of nitrous oxide and chlorofluorocarbons, Geophys. Res. Lett., 31(20), L20103, https://doi.org/10.1029/2004GL020398, 2004.

Newman, P. A., Daniel, J. S., Waugh, D. W. and Nash, E. R.: A new formulation of equivalent effective stratospheric chlorine (EESC), Atmos. Chem. Phys., 7(17), 4537–4552, https://doi.org/10.5194/acp-7-4537-2007, 2007.

Newman, P. A., Coy, L., Pawson, S. and Lait, L. R.: The anomalous change in the QBO in 2015–2016, Geophys. Res. Lett., 43(16), 8791–8797, https://doi.org/10.1002/2016GL070373, 2016.

Notholt, J. and Lehmann, R.: The moon as light source for atmospheric trace gas observations: measurement technique and analysis method, J. Quant. Spectrosc. Radiat. Transf., 76(3–4), 435–445, https://doi.org/10.1016/S0022-4073(02)00069-9, 2003.

O'Doherty, S., Simmonds, P. G., Cunnold, D. M., Wang, H. J., Sturrock, G. A., Fraser, P. J., Ryall, D., Derwent, R. G., Weiss, R. F., Salameh, P., Miller, B. R. and Prinn, R. G.: In situ chloroform measurements at Advanced Global Atmospheric Gases Experiment atmospheric research stations from 1994 to 1998, J. Geophys. Res. Atmos., 106(D17), 20429–20444, https://doi.org/10.1029/2000JD900792, 2001.

Oberländer-Hayn, S., Meul, S., Langematz, U., Abalichin, J. and Haenel, F.: A chemistry-climate model study of past changes in the Brewer-Dobson circulation, J. Geophys. Res. Atmos., 120(14), 6742–6757, https://doi.org/10.1002/2014JD022843, 2015.

Oberländer-Hayn, S., Gerber, E. P., Abalichin, J., Akiyoshi, H., Kerschbaumer, A., Kubin, A., Kunze, M., Langematz, U., Meul, S., Michou, M., Morgenstern, O. and Oman, L. D.: Is the Brewer-Dobson circulation increasing or moving upward?, Geophys. Res. Lett., 43(4), 1772–1779, https://doi.org/10.1002/2015GL067545, 2016.

Oberländer, S., Langematz, U. and Meul, S.: Unraveling impact factors for future changes in the Brewer-Dobson circulation, J. Geophys. Res. Atmos., 118(18), 10,296-10,312, https://doi.org/10.1002/jgrd.50775, 2013.

Oman, L., Waugh, D. W., Pawson, S., Stolarski, R. S. and Newman, P. A.: On the influence of anthropogenic forcings on changes in the stratospheric mean age, J. Geophys. Res., 114(D3), D03105, https://doi.org/10.1029/2008JD010378, 2009.

Osprey, S. M., Butchart, N., Knight, J. R., Scaife, A. A., Hamilton, K., Anstey, J. A., Schenzinger, V. and Zhang, C.: An unexpected disruption of the atmospheric quasi-biennial oscillation, Science (80-.)., 353(6306), 1424–1427, https://doi.org/10.1126/science.aah4156, 2016.

Ossó, A., Sola, Y., Rosenlof, K., Hassler, B., Bech, J. and Lorente, J.: How Robust Are Trends in the Brewer–Dobson Circulation Derived from Observed Stratospheric Temperatures?, J. Clim., 28(8), 3024–3040, https://doi.org/10.1175/JCLI-D-14-00295.1, 2015.

Pahlavan, H. A., Wallace, J. M., Fu, Q. and Kiladis, G. N.: Revisiting the Quasi-Biennial Oscillation as Seen in ERA5. Part II: Evaluation of Waves and Wave Forcing, J. Atmos. Sci., 78(3), 693–707, https://doi.org/10.1175/JAS-D-20-0249.1, 2021.

Ploeger, F. and Birner, T.: Seasonal and inter-annual variability of lower stratospheric age of air spectra, Atmos. Chem. Phys., 16(15), 10195–10213, https://doi.org/10.5194/acp-16-10195-2016, 2016.

Ploeger, F., Abalos, M., Birner, T., Konopka, P., Legras, B., Müller, R. and Riese, M.: Quantifying the effects of mixing and residual circulation on trends of stratospheric mean age of air, Geophys. Res. Lett., 42(6), 2047–2054, https://doi.org/10.1002/2014GL062927, 2015a.

Ploeger, F., Riese, M., Haenel, F., Konopka, P., Müller, R. and Stiller, G.: Variability of stratospheric mean age of air and of the local effects of residual circulation and eddy mixing, J. Geophys. Res. Atmos., 120(2), 716–733, https://doi.org/10.1002/2014JD022468, 2015b.

Ploeger, F., Legras, B., Charlesworth, E., Yan, X., Diallo, M., Konopka, P., Birner, T., Tao, M., Engel, A. and Riese, M.: How robust are stratospheric age of air trends from different reanalyses?, Atmos. Chem. Phys., 19(9), 6085–6105, https://doi.org/10.5194/acp-19-6085-2019, 2019.

Plumb, R. A.: The quasi-biennial oscillation, in Dynamics of the Middle Atmosphere, edited by J. R. Holton and T. Matsuno, pp. 217–251, Springer Netherlands, Tokyo, , 1984.

Plumb, R. A.: Stratospheric Transport, J. Meteorol. Soc. Japan. Ser. II, 80(4B), 793–809, https://doi.org/10.2151/jmsj.80.793, 2002.

Polvani, L. M., Wang, L., Aquila, V. and Waugh, D. W.: The impact of ozone-depleting substances on tropical upwelling, as revealed by the absence of lower-stratospheric cooling since the late 1990s, J. Clim., 30(7), 2523–2534, https://doi.org/10.1175/JCLI-D-16-0532.1, 2017.

Polvani, L. M., Abalos, M., Garcia, R., Kinnison, D. and Randel, W. J.: Significant Weakening of Brewer-Dobson Circulation Trends Over the 21st Century as a Consequence of the Montreal Protocol, Geophys. Res. Lett., 45(1), 401–409, https://doi.org/10.1002/2017GL075345, 2018.

Polvani, L. M., Wang, L., Abalos, M., Butchart, N., Chipperfield, M. P., Dameris, M., Deushi, M., Dhomse, S. S., Jöckel, P., Kinnison, D., Michou, M., Morgenstern, O., Oman, L. D., Plummer, D. A. and Stone, K. A.: Large impacts, past and future, of ozone-depleting substances on Brewer-Dobson circulation trends: A multi-model assessment, J. Geophys. Res. Atmos., 124(13), 6669–6680, https://doi.org/10.1029/2018JD029516, 2019.

Prather, M. J., Holmes, C. D. and Hsu, J.: Reactive greenhouse gas scenarios: Systematic exploration of uncertainties and the role of atmospheric chemistry, Geophys. Res. Lett., 39(9), 1–5, https://doi.org/10.1029/2012GL051440, 2012.

Ray, E. A., Portmann, R. W., Yu, P., Daniel, J., Montzka, S. A., Dutton, G. S., Hall, B. D., Moore, F. L. and Rosenlof, K. H.: The influence of the stratospheric Quasi-Biennial Oscillation on trace gas levels at the Earth's surface, Nat. Geosci., 13(1), 22–27, https://doi.org/10.1038/s41561-019-0507-3, 2020.

Reed, R. J., Wolfe, J. L. and Nishimoto, H.: A Spectral Analysis of the Energetics of the Stratospheric Sudden Warming of Early 1957, J. Atmos. Sci., 20(4), 256–275, https://doi.org/10.1175/1520-0469(1963)020<0256:ASAOTE>2.0.CO;2, 1963.

Reimann, S.: Halogenated greenhouse gases at the Swiss High Alpine Site of Jungfraujoch (3580 m asl): Continuous measurements and their use for regional European source allocation, J. Geophys. Res., 109(D5), D05307, https://doi.org/10.1029/2003JD003923, 2004.

Rienecker, M. M., Suarez, M. J., Gelaro, R., Todling, R., Bacmeister, J., Liu, E., Bosilovich, M. G., Schubert, S. D., Takacs, L., Kim, G.-K., Bloom, S., Chen, J., Collins, D., Conaty, A., da Silva, A., Gu, W., Joiner, J., Koster, R. D., Lucchesi, R., Molod, A., Owens, T., Pawson, S., Pegion, P., Redder, C. R., Reichle, R., Robertson, F. R., Ruddick, A. G., Sienkiewicz, M. and Woollen, J.: MERRA: NASA's Modern-Era Retrospective Analysis for Research and Applications, J. Clim., 24(14), 3624–3648, https://doi.org/10.1175/JCLI-D-11-00015.1, 2011.

Rinsland, C. P.: Trends of HF, HCl, CCl 2 F 2 , CCl 3 F, CHClF 2 (HCFC-22), and SF 6 in the lower stratosphere from Atmospheric Chemistry Experiment (ACE) and Atmospheric Trace Molecule Spectroscopy (ATMOS) measurements near 30°N latitude, Geophys. Res. Lett., 32(16), L16S03, https://doi.org/10.1029/2005GL022415, 2005.

Rinsland, C. P., Jones, N. B., Connor, B. J., Logan, J. A., Pougatchev, N. S., Goldman, A., Murcray, F. J., Stephen, T. M., Pine, A. S., Zander, R., Mahieu, E. and Demoulin, P.: Northern and southern hemisphere ground-based infrared spectroscopic measurements of tropospheric carbon monoxide and ethane, J. Geophys. Res. Atmos., 103(D21), 28197–28217, https://doi.org/10.1029/98JD02515,

1998.

Rodgers, C. D.: Inverse methods for atmospheric sounding, World Scientific, Singapore., 2000.

Rothman, L. S., Gordon, I. E., Barbe, A., Benner, D. C., Bernath, P. F., Birk, M., Boudon, V., Brown, L. R., Campargue, A., Champion, J.-P., Chance, K., Coudert, L. H., Dana, V., Devi, V. M., Fally, S., Flaud, J.-M., Gamache, R. R., Goldman, A., Jacquemart, D., Kleiner, I., Lacome, N., Lafferty, W. J., Mandin, J.-Y., Massie, S. T., Mikhailenko, S. N., Miller, C. E., Moazzen-Ahmadi, N., Naumenko, O. V., Nikitin, A. V., Orphal, J., Perevalov, V. I., Perrin, A., Predoi-Cross, A., Rinsland, C. P., Rotger, M., Šimečková, M., Smith, M. A. H., Sung, K., Tashkun, S. A., Tennyson, J., Toth, R. A., Vandaele, A. C. and Vander Auwera, J.: The HITRAN 2008 molecular spectroscopic database, J. Quant. Spectrosc. Radiat. Transf., 110(9–10), 533–572, https://doi.org/10.1016/j.jqsrt.2009.02.013, 2009a.

Rothman, L. S., Gordon, I. E., Barbe, A., Benner, D. C., Bernath, P. F., Birk, M., Boudon, V., Brown, L. R., Campargue, A., Champion, J.-P., Chance, K., Coudert, L. H., Dana, V., Devi, V. M., Fally, S., Flaud, J.-M., Gamache, R. R., Goldman, A., Jacquemart, D., Kleiner, I., Lacome, N., Lafferty, W. J., Mandin, J.-Y., Massie, S. T., Mikhailenko, S. N., Miller, C. E., Moazzen-Ahmadi, N., Naumenko, O. V., Nikitin, A. V., Orphal, J., Perevalov, V. I., Perrin, A., Predoi-Cross, A., Rinsland, C. P., Rotger, M., Šimečková, M., Smith, M. A. H., Sung, K., Tashkun, S. A., Tennyson, J., Toth, R. A., Vandaele, A. C. and Vander Auwera, J.: The HITRAN 2008 molecular spectroscopic database, J. Quant. Spectrosc. Radiat. Transf., 110(9–10), 533–572, https://doi.org/10.1016/j.jqsrt.2009.02.013, 2009b.

Rotman, D. A., Tannahill, J. R., Kinnison, D. E., Connell, P. S., Bergmann, D., Proctor, D., Rodriguez, J. M., Lin, S. J., Rood, R. B., Prather, M. J., Rasch, P. J., Considine, D. B., Ramaroson, R. and Kawa, S. R.: Global Modeling Initiative assessment model: Model description, integration, and testing of the transport shell, J. Geophys. Res. Atmos., 106(D2), 1669–1691, https://doi.org/10.1029/2000JD900463, 2001.

Šácha, P., Eichinger, R., Garny, H., Pišoft, P., Dietmüller, S., De La Torre, L., Plummer, D. A., Jöckel, P., Morgenstern, O., Zeng, G., Butchart, N. and Añel, J. A.: Extratropical age of air trends and causative factors in climate projection simulations, Atmos. Chem. Phys., 19(11), 7627–7647, https://doi.org/10.5194/acp-19-7627-2019, 2019.

Santer, B. D., Wigley, T. M. L., Boyle, J. S., Gaffen, D. J., Hnilo, J. J., Nychka, D., Parker, D. E. and Taylor, K. . E.: Statistical significance of trends and trend differences in layer-average atmospheric temperature time series, J. Geophys. Res. Atmos., 105(D6), 7337–7356, https://doi.org/10.1029/1999JD901105, 2000.

Santer, B. D., Wehner, M. F., Wigley, T. M. L., Sausen, R., Meehl, G. A., Taylor, K. . E., Ammann, C., Arblaster, J., Washington, W. M., Boyle, J. S. and Brüggemann, W.: Contributions of Anthropogenic and Natural Forcing to Recent Tropopause Height Changes, Science (80-.)., 301(5632), 479–483, https://doi.org/10.1126/science.1084123, 2003.

Scinocca, J. F., McFarlane, N. A., Lazare, M., Li, J. and Plummer, D.: Technical Note: The CCCma third generation AGCM and its extension into the middle atmosphere, Atmos. Chem. Phys., 8(23), 7055–7074, https://doi.org/10.5194/acp-8-7055-2008, 2008.

Shao, X.: The dependent wild bootstrap, J. Am. Stat. Assoc., 105(489), 218–235, https://doi.org/10.1198/jasa.2009.tm08744, 2010.

Sheese, P. E., Boone, C. D. and Walker, K. A.: Detecting physically unrealistic outliers in ACE-FTS atmospheric measurements, Atmos. Meas. Tech., 8(2), 741–750, https://doi.org/10.5194/amt-8-741-2015, 2015.

Shepherd, T. G.: Large-Scale Atmospheric Dynamics for Atmospheric Chemists, Chem. Rev., 103(12), 4509–4532, https://doi.org/10.1021/cr020511z, 2003.

Shepherd, T. G. and McLandress, C.: A Robust Mechanism for Strengthening of the Brewer–Dobson Circulation in Response to Climate Change: Critical-Layer Control of Subtropical Wave Breaking, J. Atmos. Sci., 68(4), 784–797, https://doi.org/10.1175/2010JAS3608.1, 2011.

Sherlock, V. J., Jones, N. B., Matthews, W. A., Murcray, F. J., Blatherwick, R. D., Murcray, D. G., Goldman, A., Rinsland, C. P., Bernardo, C. and Griffith, D. W. T.: Increase in the vertical column abundance of HCFC-22 (CHClF 2) above Lauder, New Zealand, between 1985 and 1994, J. Geophys. Res. Atmos., 102(D7), 8861–8865, https://doi.org/10.1029/96JD01012, 1997.

Simmonds, P. G., O'Doherty, S., Nickless, G., Sturrock, G. A., Swaby, R., Knight, P., Ricketts, J., Woffendin, G. and Smith, R.: Automated Gas Chromatograph/Mass Spectrometer for Routine Atmospheric Field Measurements of the CFC Replacement Compounds, the Hydrofluorocarbons and Hydrochlorofluorocarbons, Anal. Chem., 67(4), 717–723, https://doi.org/10.1021/ac00100a005, 1995.

Simmonds, P. G., Rigby, M., McCulloch, A., O'Doherty, S., Young, D., Mühle, J., Krummel, P. B., Steele, P., Fraser, P. J., Manning, A. J., Weiss, R. F., Salameh, P. K., Harth, C. M., Wang, R. H. J. and Prinn, R. G.: Changing trends and emissions of hydrochlorofluorocarbons (HCFCs) and their hydrofluorocarbon (HFCs) replacements, Atmos. Chem. Phys., 17(7), 4641–4655, https://doi.org/10.5194/acp-17-4641-2017, 2017.

Skachko, S., Ménard, R., Errera, Q., Christophe, Y. and Chabrillat, S.: EnKF and 4D-Var data assimilation with chemical transport model BASCOE (version 05.06), Geosci. Model Dev., 9(8), 2893–2908, https://doi.org/10.5194/gmd-9-2893-2016, 2016.

Smeekes, S. and Urbain, J.-P.: A multivariate invariance principle for modified wild bootstrap methods with an application to unit root testing, Maastricht Univ. Grad. Sch. Bus. Econ. GSBE Res. Memo., 008, https://doi.org/10.26481/umagsb.2014008, 2014.

Solomon, S., Garcia, R. R., Rowland, F. S. and Wuebbles, D. J.: On the depletion of Antarctic ozone, Nature, 321(6072), 755–758, https://doi.org/10.1038/321755a0, 1986.

Solomon, S., Kinnison, D., Bandoro, J. and Garcia, R.: Simulation of polar ozone depletion: An update, J. Geophys. Res. Atmos., 120(15), 7958–7974, https://doi.org/10.1002/2015JD023365, 2015.

SPARC/IO3C/GAW: SPARC/IO3C/GAW Report on Long-term Ozone Trends and Uncertainties in the Stratosphere, SPARC Repo., edited by I. Petropavlovskikh, S. Godin-Beekmann, D. Hubert, R. Damadeo, B. Hassler, and V. Sofieva., 2019.

SPARC: Lifetimes of Stratospheric Ozone-Depleting Substances, Their Replacements, and Related Species, in SPARC Report No. 6, WCRP-15/2013, edited by M. K. W. Ko, P. A. Newman, S. Reimann, and S. E. Strahan, Zürich, , 2013.

Spivakovsky, C. M., Logan, J. A., Montzka, S. A., Balkanski, Y. J., Foreman-Fowler, M., Jones, D. B. A., Horowitz, L. W., Fusco, A. C., Brenninkmeijer, C. A. M., Prather, M. J., Wofsy, S. C. and McElroy, M. B.: Three-dimensional climatological distribution of tropospheric OH: Update and evaluation, J. Geophys. Res. Atmos., 105(D7), 8931–8980, https://doi.org/10.1029/1999JD901006, 2000.

Steck, T.: Methods for determining regularization for atmospheric retrieval problems, Appl. Opt., 41(9), 1788, https://doi.org/10.1364/AO.41.001788, 2002.

Steck, T. and Clarmann, T. von: Constrained profile retrieval applied to the observation mode of the Michelson Interferometer for Passive Atmospheric Sounding, Appl. Opt., 40(21), 3559, https://doi.org/10.1364/AO.40.003559, 2001.

Steffen, J., Bernath, P. F. and Boone, C. D.: Trends in halogen-containing molecules measured by the Atmospheric Chemistry Experiment (ACE) satellite, J. Quant. Spectrosc. Radiat. Transf., 238, 106619, https://doi.org/10.1016/j.jqsrt.2019.106619, 2019.

Stiller, G. P., Von Clarmann, T., Haenel, F., Funke, B., Glatthor, N., Grabowski, U., Kellmann, S., Kiefer, M., Linden, A., Lossow, S. and López-Puertas, M.: Observed temporal evolution of global mean age of stratospheric air for the 2002 to 2010 period, Atmos. Chem. Phys., 12(7), 3311–3331, https://doi.org/10.5194/acp-12-3311-2012, 2012.

Stiller, G. P., Fierli, F., Ploeger, F., Cagnazzo, C., Funke, B., Haenel, F. J., Reddmann, T., Riese, M. and von Clarmann, T.: Shift of subtropical transport barriers explains observed hemispheric asymmetry of decadal trends of age of air, Atmos. Chem. Phys., 17(18), 11177–11192, https://doi.org/10.5194/acp-17-11177-2017, 2017.

Stolarski, R. S. and Cicerone, R. J.: Stratospheric Chlorine: a Possible Sink for Ozone, Can. J. Chem., 52(8), 1610–1615, https://doi.org/10.1139/v74-233, 1974.

Strahan, S. E., Douglass, A. R., Newman, P. A. and Steenrod, S. D.: Inorganic chlorine variability in the Antarctic vortex and implications for ozone recovery, J. Geophys. Res. Atmos., 119(24), 14,098-14,109, https://doi.org/10.1002/2014JD022295, 2014.

Strahan, S. E., Oman, L. D., Douglass, A. R. and Coy, L.: Modulation of Antarctic vortex composition by the quasi-biennial oscillation, Geophys. Res. Lett., 42(10), 4216–4223, https://doi.org/10.1002/2015GL063759, 2015.

Strahan, S. E., Smale, D., Douglass, A. R., Blumenstock, T., Hannigan, J. W., Hase, F., Jones, N. B., Mahieu, E., Notholt, J., Oman, L. D., Ortega, I., Palm, M., Prignon, M., Robinson, J., Schneider, M., Sussmann, R. and Velazco, V. A.: Observed Hemispheric Asymmetry in Stratospheric Transport Trends From 1994 to 2018, Geophys. Res. Lett., 47(17), 1–9, https://doi.org/10.1029/2020GL088567, 2020.

Strong, K., Wolff, M. A., Kerzenmacher, T. E., Walker, K. A., Bernath, P. F., Blumenstock, T., Boone, C., Catoire, V., Coffey, M., De Mazière, M., Demoulin, P., Duchatelet, P., Dupuy, E., Hannigan, J., Höpfner, M., Glatthor, N., Griffith, D. W. T., Jin, J. J., Jones, N., Jucks, K., Kuellmann, H., Kuttippurath, J., Lambert, A., Mahieu, E., McConnell, J. C., Mellqvist, J., Mikuteit, S., Murtagh, D. P., Notholt, J., Piccolo, C., Raspollini, P., Ridolfi, M., Robert, C., Schneider, M., Schrems, O., Semeniuk, K., Senten, C., Stiller, G. P., Strandberg, A., Taylor, J., Tétard, C., Toohey, M., Urban, J., Warneke, T. and Wood, S.: Validation of ACE-FTS N_2O measurements, Atmos. Chem. Phys., 8(16), 4759–4786, https://doi.org/10.5194/acp-8-4759-2008, 2008.

Sussmann, R., Borsdorff, T., Rettinger, M., Camy-Peyret, C., Demoulin, P., Duchatelet, P., Mahieu, E. and Servais, C.: Technical Note: Harmonized retrieval of column-integrated atmospheric water vapor from the FTIR network - first examples for long-term records and station trends, Atmos. Chem. Phys., 9(22), 8987–8999, https://doi.org/10.5194/acp-9-8987-2009, 2009.

Toon, G. C., Blavier, J.-F., Sen, B., Margitan, J. J., Webster, C. R., May, R. D., Fahey, D., Gao, R., Del Negro, L., Proffitt, M., Elkins, J., Romashkin, P. A., Hurst, D. F., Oltmans, S., Atlas, E., Schauffler, S., Flocke, F., Bui, T. P., Stimpfle, R. M., Bonne, G. P., Voss, P. B. and Cohen, R. C.: Comparison of MkIV balloon and ER-2 aircraft measurements of atmospheric trace gases, J. Geophys. Res. Atmos., 104(D21), 26779–26790, https://doi.org/10.1029/1999JD900379, 1999.

Tweedy, O. V., Kramarova, N. A., Strahan, S. E., Newman, P. A., Coy, L., Randel, W. J., Park, M., Waugh, D. W. and Frith, S. M.: Response of trace gases to the disrupted 2015–2016 quasi-biennial oscillation, Atmos. Chem. Phys., 17(11), 6813–6823, https://doi.org/10.5194/acp-17-6813-2017, 2017.

Uglietti, C., Leuenberger, M. and Brunner, D.: European source and sink areas of CO_2 retrieved from Lagrangian transport model interpretation of combined O_2 and CO_2 measurements at the high alpine research station Jungfraujoch, Atmos. Chem. Phys., 11(15), 8017–8036, https://doi.org/10.5194/acp-11-8017-2011, 2011.

Varanasi, P., Li, Z., Nemtchinov, V. and Cherukuri, A.: Spectral absorption-coefficient data on HCFC-22 and SF6 for remote-sensing applications, J. Quant. Spectrosc. Radiat. Transf., 52(3–4), 323–332,

https://doi.org/10.1016/0022-4073(94)90162-7, 1994.

Vigouroux, C., Augusto Bauer Aquino, C., Bauwens, M., Becker, C., Blumenstock, T., De Mazière, M., García, O., Grutter, M., Guarin, C., Hannigan, J., Hase, F., Jones, N., Kivi, R., Koshelev, D., Langerock, B., Lutsch, E., Makarova, M., Metzger, J. M., Müller, J. F., Notholt, J., Ortega, I., Palm, M., Paton-Walsh, C., Poberovskii, A., Rettinger, M., Robinson, J., Smale, D., Stavrakou, T., Stremme, W., Strong, K., Sussmann, R., Té, Y. and Toon, G.: NDACC harmonized formaldehyde time series from 21 FTIR stations covering a wide range of column abundances, Atmos. Meas. Tech., 11(9), 5049–5073, https://doi.org/10.5194/amt-11-5049-2018, 2018.

Vincent, G.: Mean meridional circulations in the Northern Hemisphere lower stratosphere during 1964 and 1965, Q. J. R. Meteorol. Soc., 94(401), 333–349, https://doi.org/10.1002/qj.49709440109, 1968.

Waugh, D. W. and Hall, T. M.: Age of stratospheric air: Theory, observations, and models, Rev. Geophys., 40(4), 1-1-1–10, https://doi.org/10.1029/2000RG000101, 2002.

Weber, M., Coldewey-Egbers, M., Fioletov, V. E., Frith, S. M., Wild, J. D., Burrows, J. P., Long, C. S. and Loyola, D.: Total ozone trends from 1979 to 2016 derived from five merged observational datasets – the emergence into ozone recovery, Atmos. Chem. Phys., 18(3), 2097–2117, https://doi.org/10.5194/acp-18-2097-2018, 2018.

WMO (World Meteorological Organization): Scientific Assessment of Ozone Depletion: 2014, Organization, Global Ozone Research and Monitoring Project—Report No. 55, Geneva, Switzerland., 2014.

WMO (World Meteorological Organization): Scientific Assessment of Ozone Depletion: 2018, Global Ozone Research and Monitoring Project–Report No. 58, Geneva, Switzerland., 2018.

Wofsy, S. C., McElroy, M. B. and Yung, Y. L.: The chemistry of atmospheric bromine, Geophys. Res. Lett., 2(6), 215–218, https://doi.org/10.1029/GL002i006p00215, 1975.

Xiang, B., Patra, P. K., Montzka, S. A., Miller, S. M., Elkins, J. W., Moore, F. L., Atlas, E. L., Miller, B. R., Weiss, R. F., Prinn, R. G. and Wofsy, S. C.: Global emissions of refrigerants HCFC-22 and HFC-134a: Unforeseen seasonal contributions, Proc. Natl. Acad. Sci., 111(49), 17379–17384, https://doi.org/10.1073/pnas.1417372111, 2014.

Zander, R.: Présence de HF dans la stratosphere supérieure, Comptes Rendus Hebd. des Séances l'Académie des Sci. Séries A B. Série B, Sci. Phys., 281(12), 213–214, 1975.

Zander, R., Roland, G. and Delbouille, L.: Confirming the presence of hydrofluoric acid in the upper stratosphere, Geophys. Res. Lett., 4(3), 117–120, https://doi.org/10.1029/GL004i003p00117, 1977.

Zander, R., Gunson, M. R., Farmer, C. B., Rinsland, C. P., Irion, F. W. and Mahieu, E.: The 1985 chlorine and fluorine inventories in the stratosphere based on ATMOS observations at 30° north latitude, J. Atmos. Chem., 15(2), 171–186, https://doi.org/10.1007/BF00053758, 1992.

Zander, R., Mahieu, E., Demoulin, P., Rinsland, C. P., Weisenstein, D. K., Ko, M. K. W., Sze, N. D. and Gunson, M. R.: Secular evolution of the vertical column abundances of CHCIF2 (HCFC-22) in the Earth's atmosphere inferred from ground-based IR solar observations at the Jungfraujoch and at Kitt Peak, and comparison with model calculations, J. Atmos. Chem., 18(2), 129–148, https://doi.org/10.1007/BF00696811, 1994.

Zander, R., Mahieu, E., Gunson, M. R., Abrams, M. C., Chang, A. Y., Abbas, M., Aellig, C., Engel, A., Goldman, A., Irion, F. W., Kämpfer, N., Michelson, H. A., Newchurch, M. J., Rinsland, C. P., Salawitch, R. J., Stiller, G. P. and Toon, G. C.: The 1994 northern midlatitude budget of stratospheric chlorine derived from ATMOS/ATLAS-3 observations, Geophys. Res. Lett., 23(17), 2357–2360, https://doi.org/10.1029/96GL01792, 1996.

Zander, R., Mahieu, E., Demoulin, P., Duchatelet, P., Roland, G., Servais, C., Mazière, M. De, Reimann, S. and Rinsland, C. P.: Our changing atmosphere: Evidence based on long-term infrared solar

observations at the Jungfraujoch since 1950, Sci. Total Environ., 391(2–3), 184–195, https://doi.org/10.1016/j.scitotenv.2007.10.018, 2008.

Zellweger, C., Ammann, M., Buchmann, B., Hofer, P., Lugauer, M., Rüttimann, R., Streit, N., Weingartner, E. and Baltensperger, U.: Summertime NO_y speciation at the Jungfraujoch, 3580 m above sea level, Switzerland, J. Geophys. Res. Atmos., 105(D5), 6655–6667, https://doi.org/10.1029/1999JD901126, 2000.

Zellweger, C., Forrer, J., Hofer, P., Nyeki, S., Schwarzenbach, B., Weingartner, E., Ammann, M. and Baltensperger, U.: Partitioning of reactive nitrogen (NO_y) and dependence on meteorological conditions in the lower free troposphere, Atmos. Chem. Phys., 3(3), 779–796, https://doi.org/10.5194/acp-3-779-2003, 2003.

Zhou, M., Vigouroux, C., Langerock, B., Wang, P., Dutton, G., Hermans, C., Kumps, N., Metzger, J.-M., Toon, G. and De Mazière, M.: CFC-11, CFC-12 and HCFC-22 ground-based remote sensing FTIR measurements at Réunion Island and comparisons with MIPAS/ENVISAT data, Atmos. Meas. Tech., 9(11), 5621–5636, https://doi.org/10.5194/amt-9-5621-2016, 2016.

Zhou, M., Langerock, B., Vigouroux, C., Wang, P., Hermans, C., Stiller, G., Walker, K. A., Dutton, G., Mahieu, E. and De Mazière, M.: Ground-based FTIR retrievals of SF6 on Reunion Island, Atmos. Meas. Tech., 11(2), 654–662, https://doi.org/10.5194/amt-11-651-2018, 2018.

Appendix: list of relevant publications

Prignon, M., Chabrillat, S., Minganti, D., O'Doherty, S., Servais, C., Stiller, G., Toon, G. C., Vollmer, M. K. and Mahieu, E.: Improved FTIR retrieval strategy for HCFC-22 (CHClF2), comparisons with in situ and satellite datasets with the support of models, and determination of its long-term trend above Jungfraujoch, Atmos. Chem. Phys., 19(19), 12309–12324, https://doi.org/10.5194/acp-19-12309-2019, 2019.

Minganti, D., Chabrillat, S., Christophe, Y., Errera, Q., Abalos, M., **Prignon, M.**, Kinnison, D. E. and Mahieu, E.: Climatological impact of the Brewer–Dobson circulation on the N2O budget in WACCM, a chemical reanalysis and a CTM driven by four dynamical reanalyses, Atmos. Chem. Phys., 20(21), 12609–12631, https://doi.org/10.5194/acp-20-12609-2020, 2020.

Strahan, S. E., Smale, D., Douglass, A. R., Blumenstock, T., Hannigan, J. W., Hase, F., Jones, N. B., Mahieu, E., Notholt, J., Oman, L. D., Ortega, I., Palm, M., **Prignon, M.**, Robinson, J., Schneider, M., Sussmann, R. and Velazco, V. A.: Observed Hemispheric Asymmetry in Stratospheric Transport Trends From 1994 to 2018, Geophys. Res. Lett., 47(17), 1–9, https://doi.org/10.1029/2020GL088567, 2020.

Prignon, M., Chabrillat, S., Friedrich, M., Smale, D., Strahan, S. E., Bernath, P. F., Chipperfield, M. P., Dhomse, S. S., Feng, W., Minganti, D., Servais, C. and Mahieu, E.: Stratospheric fluorine as a tracer of circulation changes: comparison between infrared remote-sensing observations and simulations with five modern reanalyses, J. Geophys. Res. Atmos. (*under review*), 2021.